

University of Southampton Research Repository

Copyright © and Moral Rights for this thesis and, where applicable, any accompanying data are retained by the author and/or other copyright owners. A copy can be downloaded for personal non-commercial research or study, without prior permission or charge. This thesis and the accompanying data cannot be reproduced or quoted extensively from without first obtaining permission in writing from the copyright holder/s. The content of the thesis and accompanying research data (where applicable) must not be changed in any way or sold commercially in any format or medium without the formal permission of the copyright holder/s.

When referring to this thesis and any accompanying data, full bibliographic details must be given, e.g.

Thesis: Author (Year of Submission) "Full thesis title", University of Southampton, name of the University Faculty or School or Department, PhD Thesis, pagination.

Data: Author (Year) Title. URI [dataset]

UNIVERSITY OF SOUTHAMPTON

Mathematical Modelling of Evaporation Mechanisms
and Instabilities in Cryogenic Liquids

Angeli Elizabeth Thomas

Doctor of Philosophy

Faculty of Mathematical Studies

January, 1999

UNIVERSITY OF SOUTHAMPTON

ABSTRACT

FACULTY OF MATHEMATICAL STUDIES
MATHEMATICS

Doctor of Philosophy

MATHEMATICAL MODELLING OF EVAPORATION MECHANISMS AND
INSTABILITIES IN CRYOGENIC LIQUIDS

by Angeli Elizabeth Thomas

In this thesis we propose a model for laminar natural convection within a mixture of two cryogenic fluids with preferential evaporation.

This full model was developed after a number of smaller models of the behaviour of the surface of the fluid had been examined. Throughout we make careful comparison between our analytical and computational work and existing experimental and theoretical results.

The coupled differential equations for the main model were solved using an explicit upwind scheme for the vorticity-transport, temperature and concentration equations and the multigrid method for the Poisson equation. From plots of the evolution of the system, it is found that convection becomes stronger when preferential evaporation is included.

This new model demonstrates how to include preferential evaporation, and can be applied to other fluid systems.

Contents

1	Introduction	1
1.1	Literature Review	5
1.1.1	The La Spezia rollover incident	5
1.1.2	Experimental and theoretical models of rollover and evaporation	6
1.2	Thesis Layout	21
2	Temperature Models For Rollover	23
2.1	Initial Time Dependent Model	23
2.1.1	Description of the initial mathematical model	23
2.1.2	Properties of mixtures for two specific cases	26
2.1.3	Results of the initial model	29
2.1.4	Discussion of results obtained from initial model	34
2.2	The Inclusion of Evaporation	34
2.2.1	Basic model including evaporation	34
2.2.2	Results of the model with the inclusion of evaporation	34
2.2.3	Discussion of results with evaporation	41
2.3	Conclusions of Temperature Models for Rollover	41
3	Analytical Models Of Evaporation	43
3.1	The Stefan Model	43
3.1.1	The One-Dimensional Stefan Condition	44
3.1.2	The Basic Unsteady, Stefan Problem	45
3.1.3	Similarity solution	47

3.1.4	Travelling wave solution	54
3.1.5	The unsteady Stefan problem with a different boundary condition	58
3.1.6	Discussion of the Stefan problem	62
3.2	Model of Flow in a Mixture	63
3.2.1	Governing differential equations	63
3.2.2	Initial and boundary conditions	65
3.2.3	Discussion of the two component model	65
3.3	Conclusions of the Analytical Models of Evaporation	66
4	Instabilities At The Surface	67
4.1	Model of Convective Instability with Couette Flow	73
4.1.1	Governing differential equations	73
4.1.2	Linearising the governing differential equations	75
4.1.3	Non-dimensionalisation of the governing equations	76
4.1.4	Boundary conditions	77
4.1.5	Simplification of the main equations	78
4.1.6	Numerical procedure	80
4.1.7	Numerical Results for the Rayleigh number	88
4.1.8	Predicted velocity and temperature profiles above the critical Rayleigh number	93
4.1.9	Discussion of thermal instability	96
4.2	Micro Convection Eddies near the Surface	106
4.2.1	Discussion of temperature fluctuations	109
4.3	Conclusions of the Instabilities at the Surface	110
5	Numerical Modelling Of An Evaporative Mixture	111
5.1	One-Component Model in Cartesian Coordinates	112
5.1.1	Construction of problem and basic assumptions	112
5.1.2	Governing differential equations	114
5.1.3	Non-dimensionalising the governing equations	115
5.1.4	Boundary and initial conditions	116

5.2	Numerical Procedure	116
5.2.1	Discretisation method	116
5.2.2	General differential equation	118
5.2.3	Stability criterion	119
5.2.4	Outline of the solution procedure	121
5.2.5	Solution of the discretised Poisson equation	122
5.2.6	Validation of code for thermal induced convection	128
5.3	Two-Component Model in Cartesian Coordinates	131
5.3.1	Modifications for the two-component model	131
5.3.2	Solution procedure	133
5.3.3	Validation of code for double-diffusive convection	134
5.4	Rollover Model	137
5.4.1	Governing differential equations	137
5.4.2	Boundary and initial conditions	138
5.5	Properties of Liquid Nitrogen and Liquid Oxygen	141
5.5.1	Validation of code for rollover model	142
5.6	Preferential Evaporation Model	143
5.6.1	Modifications for the evaporation model	150
5.6.2	Normalisation of the concentration equation	154
5.6.3	Boundary and initial conditions	154
5.6.4	Solution procedure	156
5.6.5	Results of the preferential evaporation model	156
5.7	Rollover with Preferential Evaporation	170
5.8	Conclusions from Numerical Modelling an Evaporative Mixture	175

6 Discussion

177

List of Figures

1.1	A schematic diagram of a typical LNG storage tank containing two stratified layers.	3
1.2	Morphology of surface layers during evaporation reproduced from Beduz and Scurlock(1994).	8
1.3	Temperature and oxygen concentration measurement apparatus reproduced from Agbabi(1987).	10
2.1	Diagram depicting vessel used experimentally by Agbabi(1987), illustrating the heat gain/loss from the system.	24
2.2	Graph showing densities of LIN and LOX against temperature at a constant pressure of 1 atmosphere.	28
2.3	Comparison between the numerical and experimental solutions of the bulk temperatures for case (1).	30
2.4	Comparison between the numerical and experimental solutions of the bulk temperatures for case (2).	31
2.5	Numerical solutions of the bulk densities of the upper and lower layers for case (1).	32
2.6	Numerical solutions of the bulk densities of the upper and lower layers for case (2).	33
2.7	Numerical and experimental solutions of bulk temperature with the inclusion of evaporation for case (1).	37
2.8	Numerical and experimental solutions of bulk temperature with the inclusion of evaporation for case (2).	38
2.9	Numerical solutions of the bulk density of the upper and lower layers with the inclusion of evaporation for case (1).	39

2.10	Numerical solutions of the bulk density of the upper and lower layers with the inclusion of evaporation for case (2).	40
3.1	A simple example of the use of the Stefan condition - the problem of heat entering ice reproduced from Tayler(1986).	44
3.2	Graph of the Stefan number against λ for $f(\lambda) = 0$	51
4.1	Diagram depicting shear effect caused by convection in the bulk liquid on the surface layer.	71
4.2	Typical temperature profile through the surface of a cryogenic mixture reproduced from Beduz and Scurlock(1996).	72
4.3	Surface plot of the log of the determinant (det) as α_x and Ra vary with Pr=0.0, Re=200 and $n=50$	82
4.4	Plan view of Figure 4.3.	83
4.5	Surface plot of the log of the determinant (det) as α_x and Ra vary with Pr=0.0, Re=200 and $n=60$	84
4.6	Plan view of Figure 4.5.	85
4.7	Convergence to a minimum by inverse parabolic interpolation.	87
4.8	Graph of the critical Rayleigh number against the Reynolds Number for Pr=0.0, for various boundary conditions on the upper and lower boundary of the fluid.	89
4.9	Graph of the critical Rayleigh number against the Reynolds number for Pr=0.71 (air), for various boundary conditions on the upper and lower boundary of the fluid.	90
4.10	Graph of the critical Rayleigh number against the Reynolds Number for Pr=2.32 (LIN), for various boundary conditions on the upper and lower boundary of the fluid.	91
4.11	Temperature profile through a cross-section at four fixed points of the fluid at $t=0.0$	96
4.12	Temperature profile through a cross-section at four fixed points of the fluid at $t=0.2$	97
4.13	Temperature profile through a cross-section at four fixed points of the fluid at $t=0.4$	98

4.14	Temperature profile through a cross-section at four fixed points of the fluid at $t=0.6$	99
4.15	Temperature profile through a cross-section at four fixed points of the fluid at $t=0.8$	100
4.16	Temperature profile through a cross-section at four fixed points of the fluid at $t=1.0$	101
4.17	Velocity profile at $t=0.0$	102
4.18	Velocity profile at $t=0.4$	103
4.19	Velocity profile at $t=0.8$	104
4.20	Velocity profile at $t=1.0$	105
4.21	The Maxwellian distribution.	107
5.1	Solution domain for problem studied by De Vahl Davis(1968,1983). . .	113
5.2	Representation of the Forward Time Centred Space (FTCS) differencing scheme.	117
5.3	Representation of upwind scheme.	118
5.4	Structure of multigrid cycles.	126
5.5	Structure of cycles for the full multigrid (FMG) method.	127
5.6	Comparison of contour maps and isotherms with De Vahl Davis(1968) for case (1).	129
5.7	Comparison of contour maps and isotherms with De Vahl Davis(1968) for case(2).	130
5.8	Solution domain for problem studied by Béghein <i>et al.</i> (1992).	132
5.9	Comparison of streamlines, isotherms and isopleths of concentration with Béghein <i>et at.</i> (1992) for case (1).	135
5.10	Comparison of streamlines and isotherms with Béghein <i>et at.</i> (1992) for case (2).	136
5.11	Comparison of isopleths of concentration with Béghein <i>et at.</i> (1992) for case (3).	137
5.12	Solution domain for problem studied by Shi(1990).	138
5.13	Diagram depicting the cavity flow in the vessel which is used to calculate the wall vorticity.	140

5.14	Comparison of isotherms, isopleths of concentration and contour maps with Shi(1990) at non-dimensionalised time, $t=0.005$	144
5.15	Comparison of isotherms, isopleths of concentration and contour maps with Shi(1990) at non-dimensionalised time, $t=0.01$	145
5.16	Comparison of isotherms, isopleths of concentration and contour maps with Shi(1990) at non-dimensionalised time, $t=0.2$	146
5.17	Comparison of isotherms, isopleths of concentration and contour maps with Shi(1990) at non-dimensionalised time, $t=0.04$	147
5.18	Comparison of isotherms, isopleths of concentration and contour maps with Shi(1990) at non-dimensionalised time, $t=0.06$	148
5.19	Comparison of isotherms, isopleths of concentration and contour maps with Shi(1990) at non-dimensionalised time, $t=0.10$	149
5.20	An element at the surface of the fluid.	152
5.21	Graph showing the relationship between the concentration at the surface of the liquid and the concentration of the vapour where the crosses mark the data points and the line is the best fit line through those points. . .	153
5.22	Graph showing relationship between the saturation temperature and the concentration where the crosses mark the data points and the line is the best fit line through those points.	155
5.23	Isopleths of concentration, the stream function and temperature for flow with preferential evaporation at $t=0.1$	157
5.24	Isopleths of concentration, the stream function and temperature for flow with preferential evaporation at $t=0.5$	159
5.25	Isopleths of concentration, the stream function and temperature for flow with preferential evaporation at $t=0.9$	160
5.26	Isopleths of concentration, the stream function and temperature for flow with preferential evaporation at $t=1.3$	161
5.27	Isopleths of concentration, the stream function and temperature for flow with preferential evaporation at $t=1.7$	162
5.28	Isopleths of concentration, the stream function and temperature for flow with preferential evaporation at $t=2.1$	163

5.29	Isopleths of concentration, the stream function and temperature for flow with preferential evaporation at $t=2.3$	164
5.30	Graph showing average bulk temperature and average surface temperature over time.	165
5.31	Graph showing average bulk concentration and average surface concentration over time.	166
5.32	Graph showing the total mass flux over time.	167
5.33	Graph of temperature profile through the vessel at non-dimensionalised time, $t=0.5$	169
5.34	Graph of temperature profile through the vessel at non-dimensionalised time, $t=1.7$	171
5.35	Graph of temperature profile through the vessel at non-dimensionalised time, $t=2.3$	172
5.36	Graph of temperature profile through the vessel at $x=0.0063\text{m}$ over time.	173

List of Tables

1.1	Approximate Values of Thermo-Physical Properties of Cryogenic Fluids	15
2.1	Properties of mixtures in upper and lower layers for two specific experimental cases.	27
5.1	Comparison of present model (P.M.) to benchmark solutions(B.M.). . .	128
5.2	Comparison of properties of LIN and LOX.	142

Acknowledgements

I would like to thank my supervisors, Alistair Fitt and Alison Keary, for their patience and guidance over the past four years. I very much appreciate the support given to me by a number of research groups at Southampton - especially from members of the Applied Mathematics Group past and present! In particular I am grateful for many useful discussions with Carlo Beduz and Ralph Scurlock (Institute of Cryogenics, Mechanical Engineering) and Ken Thomas (Electronics and Computer Science).

I also acknowledge the Engineering and Physical Sciences Research Council, for their financial support.

Finally I would like to thank my friends and family for their continued support and encouragement, in particular my parents and Simon Cox without whose constant enthusiasm this work would never have been completed.

Chapter 1

Introduction

Demand for cryogenic fluids such as oxygen, nitrogen and natural gas is increasing with applications in power generation, medicine, refrigeration and chemical processes.

These fluids are normally stored and transported in their liquid state, owing to the smaller volumes involved. Storage containers may be unpressurised or pressurised to a maximum value set by a relief valve or a bursting disc. The liquid will therefore be stored at around 200K below ambient temperature, and, despite using a high level of insulation, heat leak will be inevitable. In an unpressurised container it is quite normal for the liquid to become superheated due to a lack of suitable nucleation sites. The level of superheat which is reached depends on the nucleation sites present and may reach several degrees.

These liquids are potentially hazardous in terms of causing cold burns and of causing and aiding combustion (liquid natural gas, termed LNG and liquid oxygen, termed LOX). They may also lead to suffocation (LIN). Another hazard involved in storing liquid cryogens is the uncontrolled, almost explosive, release of the superheat energy. Problems are also associated with liquid mixtures due to the possible formation of stratified layers and the consequences of the rapid destruction of these layers. This is termed rollover.

Rollover may occur when a cryogenic fluid is added to a partially-filled storage vessel containing fluid of a different density. This is a particular problem for LNG since its composition of methane, heavier hydrocarbons, nitrogen and some lighter gases, can vary considerably. For example, Libyan LNG may consist of 65% methane, 25% ethane and 10% propane or higher hydrocarbons whilst pipeline gas in the North-East

of the U.S.A. may be composed of up to 95% methane (Shi, 1990). Furthermore, the composition of the fluid may alter whilst it is in the tank due to preferential evaporation, a process which we will consider in more detail later.

If the lighter fluid is added on top of the denser fluid, they will not mix and two stratified layers will result, as shown in Figure 1.1. A convection circulation pattern will be established in each layer with heat entering from the surroundings into both layers. The interface between the layers possesses a steep density gradient and acts as a barrier, preventing the lower layer from reaching the liquid/vapour surface. The lower layer is able to release only a small amount of heat through conduction to the upper layer and this causes a build-up of superheat in the lower fluid. The density of the lower layer thus decreases. In contrast, although the upper layer receives heat from the surroundings and the bottom layer, it is able to lose a substantial amount of heat through evaporation at the surface causing the temperature of the upper layer to increase less quickly than the lower layer. In addition, evaporation of the lighter hydrocarbons may occur which increases the density of the upper layer. Therefore the densities of the two layers become progressively closer until they are equal. At this point, the layers mix, allowing the highly superheated liquid in the lower layer to reach the surface. This is accompanied by both a sudden release of heat and a sharp increase in the surface evaporation rate, termed enhanced vapour generation (EVG), which can lead to overpressurisation problems in the storage tank and/or the loss of large quantities of fluid.

For LNG containing nitrogen the added problem of spontaneous stratification of the liquid arises. This is due to the preferential evaporation of nitrogen, rather than the lighter component, methane, due to nitrogen's lower saturation temperature. This causes an immediate low density fraction to float on the bulk liquid creating two stratified layers. After rollover, the mixed fluid may still contain enough nitrogen for auto-stratification and for the whole process to be repeated. Fortunately however, most sources of LNG contain less than 3% nitrogen.

Some preventative measures have been developed to stop rollover occurring. These include adding the new liquid by top or bottom loading, depending on whether it is more or less dense than the fluid in the container at the time of loading (Drake, 1976). This should, in theory, encourage mixing, although cases have been reported of incomplete mixing after the correct choice of load point. Since a lowering in the rate of

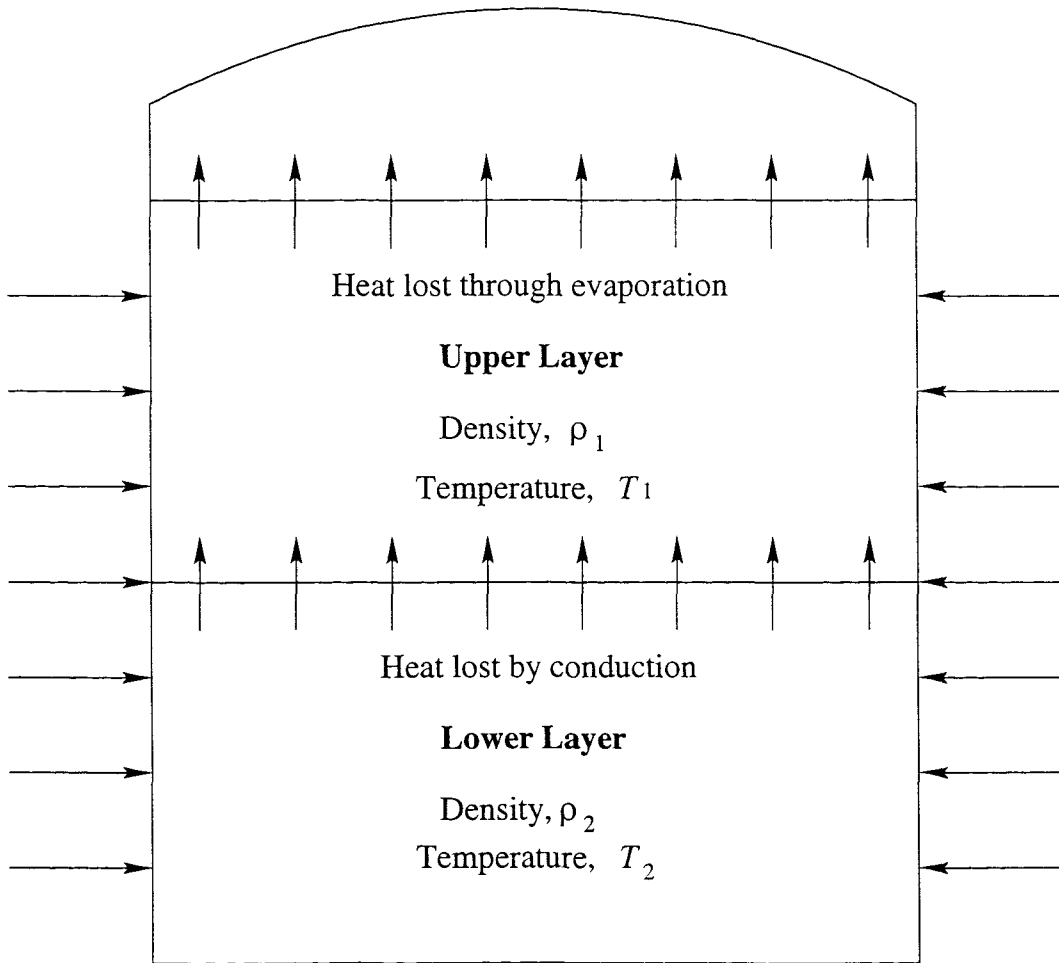


Figure 1.1: A schematic diagram of a typical LNG storage tank containing two stratified layers. The arrows mark the direction of the heat flux.

generation of vapour is a characteristic of stratification, a reduction of the cumulative vapour release to 90% of that expected during tank loading is taken as a warning of stratification and guidelines on the handling of cryogenic liquids suggest that tank loading should be ceased if there is a reduction to 70% of that expected. Limiting the range of composition of LNG added to the tank or using a mechanical device to mix the liquids in the tank may also help.

These measures may not, however, always be enough to prevent rollover, so storage tanks are fitted with adequate venting and other vapour handling equipment which is designed to cope with the maximum amount of vapour that might be generated (MacKenzie, 1986). Density, temperature and vapour generation sensors may also be used to scan the liquid and enable layering to be detected.

Understanding evaporation is essential to follow the convection process within the liquid and rollover and this will be our main concern in this thesis. Heat flux through the sides and bottom of vessels cause the temperature of the liquid to increase and lead to convection within the liquid. Whilst boiling is not generally experienced under most storage conditions, the liquid will evaporate at the top free surface. If the storage container is closed with a finite vapour space, evaporation will increase the pressure in the vapour space and therefore increase the saturation temperature, suppressing evaporation. With small vapour spaces, a small amount of evaporation will cause a large increase in pressure and therefore in the saturation conditions; evaporation will drop markedly with the result that the entire bulk of the liquid will be isothermal at the saturation temperature. With a large head space or with an open vessel, the pressure increase will be small or zero. Heat leak will increase the temperature within the bulk of the liquid, with the top surface, which is maintained at the saturation temperature, losing heat by evaporation. The situation considered throughout this thesis is the unpressurised case.

The conditions become further complicated when the liquid is a mixture with different densities and saturation temperatures. Preferential evaporation is the evaporation of one component of a mixture in preference to the other. The more volatile component may be less dense than the other, causing the formation of a denser, unstable surface layer; alternatively it may be heavier, causing a lighter surface layer. Preferential evaporation changes the liquid composition and therefore will drive convection due to buoyancy effects.

The main aims of our work are

1. To discover the important variables affecting evaporation in superheated liquids and their influence on the process;
2. To gain a physical understanding of the effects of evaporation on a low temperature fluid;
3. To model the development of preferential evaporation, which occurs in mixtures of cryogenic fluids and see whether this effect is significant in rollover.

1.1 Literature Review

In this section, we will discuss previous work on rollover and evaporation in low-temperature mixtures and give details of a particular rollover incident. The available literature falls into two categories and will be discussed in the following order:

1. Details of a rollover incident;
2. Experimental and theoretical models of rollover and evaporation firstly from the University of Southampton and secondly those reported in published literature.

1.1.1 The La Spezia rollover incident

Sarsten(1972) reported the La Spezia rollover incident, which occurred on 21 August 1971, in the Esso designed LNG terminal in La Spezia, Italy. It began 18 hours after a tank containing LNG was topped up with LNG cargo which had travelled from Marsa El Brega, Libya. This cargo spent more than a month at the La Spezia harbour where it became hotter and denser than when it was first loaded into the ship, due to the continued evaporation of light components. The storage tank had a side entering bottom nozzle so that when the heavier, hotter cargo was transferred to the tank, it stayed at the bottom. The less dense, colder fluid already in the storage tank was displaced upwards with only minimal mixing with the off-loaded cargo. The static pressure of the initial fluid in the tank suppressed vaporisation of the higher vapour pressure cargo in the tank bottom. After about 18 hours the storage tank experienced a sudden increase in pressure causing a discharge from the tank safety valves. These

valves discharged LNG vapour for approximately one and a quarter hours and the vent released vapour at high rates for about three and a quarter hours. The data of the mass of vapour lost throughout this event and in the aftermath was recorded. Although this is not the only case of rollover to have occurred, it is the biggest one reported.

1.1.2 Experimental and theoretical models of rollover and evaporation

We will begin this subsection by describing thermal overflow, termed TO , a concept first introduced by Maher and Van Gelder(1972) to explain boil-off variations in the isobaric storage of cryogenic liquids. TO (J) was defined by Beduz *et al.*(1984) as the sum, taken over all the elements of the stored liquid, of the excess enthalpy ($H - H_0$) (Jmol^{-1}) of the stored liquid in relation to the value H_0 (Jmol^{-1}) defined for the surface of a homogeneous liquid in thermodynamic equilibrium (at T_0 (K)) with its saturated vapour at a prescribed pressure P_0 (Pa). Mathematically,

$$TO = \sum_{i=1}^n (H_i - (H_0)_i).$$

where n is the total number of elements of the stored liquid. The rate of change of TO is the net difference between the total heat flux into the stored liquid and the surface vaporisation,

$$\frac{\partial(TO)}{\partial t} = \dot{Q} - \dot{m}L, \quad (1.1)$$

where \dot{m} is the vapour flowrate (kgs^{-1}), \dot{Q} is the rate of heat input (W) and L is the latent heat of vaporisation (Jkg^{-1}) of the liquid.

If the rate at which heat is removed is less than that at which heat enters, the right-hand side of equation (1.1) is positive and thermal energy is accumulated in the liquid. A build-up of this energy over a period of time is likely to cause a hazardous situation and can be used to explain the build-up of superheat prior to rollover.

Also in this paper, micro-thermometer studies were carried out on mixtures of liquid nitrogen, LIN and liquid oxygen, LOX, in order to study surface evaporation. Similar experiments were later performed by Atkinson-Barr(1989) and these will be described in more detail later in this subsection. Briefly, these studies were performed in a double-walled glass dewar surrounded by a bath of LIN to minimise uncontrolled heat leaks and the heat leak was controlled with a uniform heat flux electrical heater mounted

in the vacuum space around the inner wall. From this, it was shown that cryogenic liquids become superheated in storage. For a set heat leak, the bulk temperature and the evaporation rate increase to a steady level where the heat lost through evaporation balances the heat leak. The bulk temperature is uniform to within $\pm 0.1\text{K}$ throughout the liquid, apart from the boundary layer region at the wall and near the surface. The temperature drop from the bulk temperature to the surface temperature occurs over a distance of less than 1mm close to the surface. This layer, sometimes termed a conduction layer, contains a steep temperature gradient of $1000\text{-}5000\text{Km}^{-1}$, which provides a large thermal impedance for heat transfer at the surface.

Micro-thermometer studies on LIN, LOX, liquid argon termed LAr, liquid methane (LCH_4) and LNG were also carried out by Agbabi *et al.* (1990) to again study the surface evaporation. Results showed that if the thin surface layer separating the interface from the bulk superheated liquid is penetrated by the bulk liquid, due to any agitation at the surface, the molecular evaporative impedance is lowered. This destroys the delicate impedance mechanism and the instability causes a rise in the evaporation rate, shown to be as much as 30-fold. The overall impedance equation was obtained for surface evaporation for LIN as

$$\Delta T = (T_b - T_0) = \dot{m} \left(\overbrace{\frac{1}{(90\alpha)}}^{\text{I}} + \underbrace{440}_{\text{II}} + \overbrace{4}^{\text{III}} \right) \quad (1.2)$$

where ΔT is the temperature difference (K) between the bulk liquid (T_b), measured at a depth of 5mm or more below the surface, and the surface saturation temperature (T_0), \dot{m} is the surface mass flux ($\text{kgm}^{-2}\text{s}^{-1}$), α is the evaporation coefficient and where the impedance terms represent contributions from

- I. Molecular evaporation including impurity effects;
- II. The thermal conduction layer;
- III. The intermediate layer.

Although equation (1.2) is over simplistic, in that the thickness of the layers are assumed to be invariant with heat flux, it enabled the authors to consider the relative importance of the three impedance contributions.

Under equilibrium, the evaporation is largely controlled by impedance term II of the thermal conduction layer which is 30 times greater than the sum of impedance terms I

and III and a relatively large bulk liquid superheat is required to drive the evaporation. However, if there are impurities at the surface, which reduce the evaporation coefficient by an order of 10^2 , impedance term I dominates. In Chapter 3, we shall neglect the effect of surface impurities and attempt to find a similar analytical relationship between the rate of mass flux through evaporation and temperature.

Beduz and Scurlock(1994) also examined the surface evaporation and provided more details of the three previously described mechanisms within 5-10mm of the surface which control evaporation: molecular evaporation at the surface, thermal conduction in a thin layer $100\text{--}500\mu\text{m}$ thick with a steep temperature gradient and vortex convection lines in the liquid with axes parallel to the surface. Rollover arises when the three mechanisms are disturbed by bulk liquid motion and/or mono-molecular surface layers of impurities. The lower thick layer, known as the intermittent surface convection layer, between the superheated bulk layer and the thermal conduction layer is said to contain the mechanism whereby superheated bulk liquid is carried into the thermally conducting surface layer from which latent heat and evaporative mass transfer takes place. We shall investigate the conduction layer described in these studies in Chapter 3. Figure 1.2, obtained from Beduz and Scurlock (1994) illustrates the morphology of surface layers during evaporation.

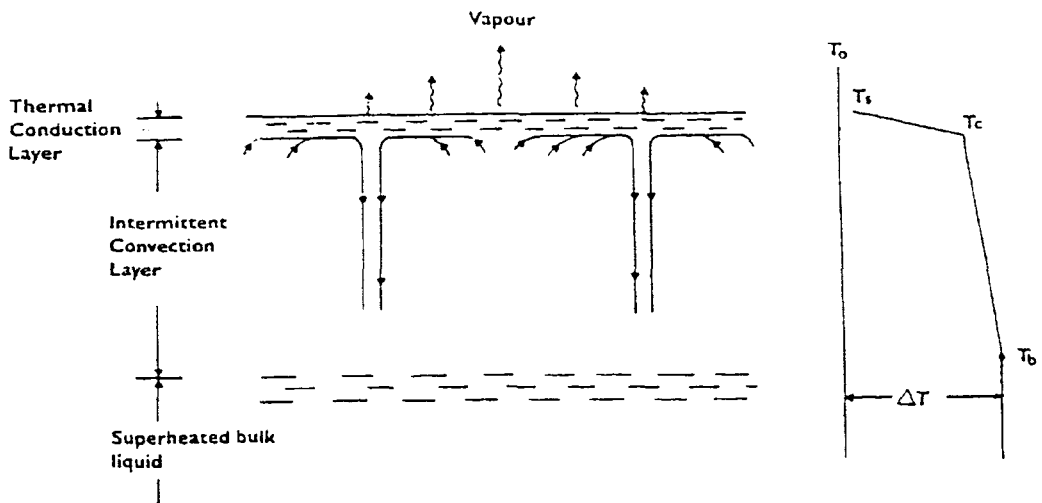


Figure 1.2: Morphology of surface layers during evaporation reproduced from Beduz and Scurlock(1994).

We will now describe the experimental investigations performed by Agbabi(1987),

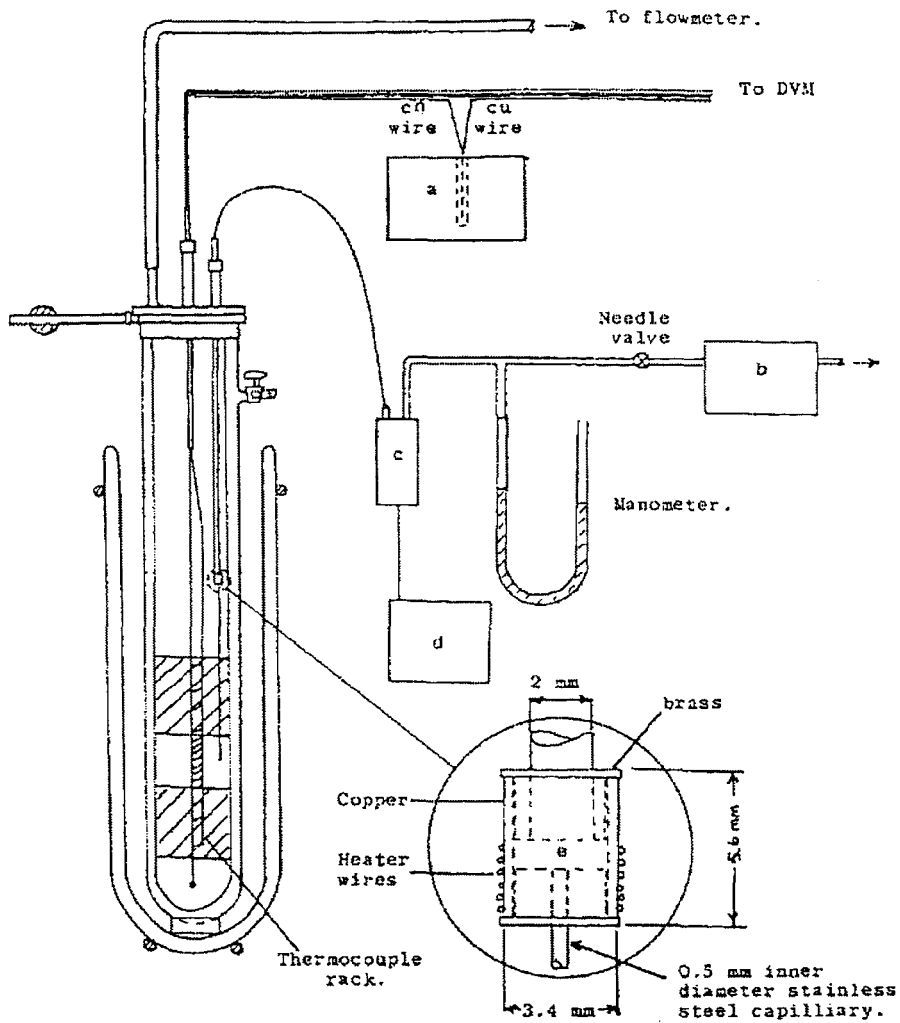
which will be used to compare the results from our models in Chapter 2. A number of studies were carried out using a two-layered system to reproduce, on a smaller scale, the mixing stages in an initially poorly mixed LNG tank. These experiments were conducted with LIN and LOX mixtures to form the two stratified layers.

To allow flow visualisation during an experimental run, a vacuum insulated glass vessel was constructed. Two semi-transparent metal oxide coatings were formed on the outside of the inner jacket of the dewar to serve as electrical heaters, and temperature profiles were measured using copper-constantan (an alloy of copper and nickel) thermocouples. A concentration probe was constructed which extracted liquid, vaporised it and measured the concentration continuously. The flowrate of the evaporated liquid was measured using a flowmeter connected to the dewar outlet. The equipment is shown in Figure 1.3.

Two layers of different composition were formed in the dewar. A constant heat input was applied to the top and bottom layers and temperature, concentration and flowrate plots were obtained from data recorded at 2 minute intervals up to the point of rollover when the layers mixed, with a consequent increase in flowrate. This procedure was performed for various concentrations and with different heat fluxes applied to the layers in the system.

The experiments showed that the peak flowrate at the point of rollover is a function of the initial difference in the densities of the layers. This is reasonable since the greater the initial density difference conditions, the longer the time taken for the layers to reach the same density, giving the bottom layer more opportunity to build up a larger thermal overfill which is released through evaporation. A mass flux equation was derived empirically to estimate the variations in flowrate based on the bulk fluid superheat. This, however, does not apply to transient flowrate behaviour which is a function of the heat input into the vessel as well. The mass flux correlation cannot predict the peak flowrates observed in incidents like the one at La Spezia based on a reasonable bulk fluid superheat value. The only way that an extremely high flowrate can be produced is by destroying the surface thermal resistance layer, which can be done by either assuming flash evaporation or boundary layer penetration from the bottom to the top layer surface.

Experimental simulations to study the liquid/vapour interface have been reported by Atkinson-Barr(1989). Initially, micro-thermometer studies were carried out on



- a: constant temperature source
- b: rotary pump
- c: oxygen analyser sensor head
- d: oxygen analyser meter display
- e: mixture vaporising chamber

Figure 1.3: Temperature and oxygen concentration measurement apparatus reproduced from Agbabi(1987).

liquids such as LIN, LOX, LAr and LNG, in a double-walled bath which was surrounded by a second LIN/LOX bath. The micro-thermometer consisted of a $25\mu\text{m}$ copper/constantan thermocouple which was fixed rigidly with respect to the dewar and positioned such that it was initially below the surface. As the liquid level fell by evaporation, the micro-thermometer measured the temperature in the thin conduction layer, at the surface and finally in the vapour.

Thermal fluctuations ('spikes') with a frequency of 1-2 per second and a range of heights up to $\pm 0.5\text{K}$ were found to dominate the profile of the plot. The significance of these profiles will be discussed in more detail in section 4.2. The thermal conduction region was also observed in the plot.

Schlieren visualisations of the liquid/vapour interface were also carried out in the aforementioned thesis, to give a qualitative interpretation of the structures seen in the temperature scans. Schlieren visualisation is a method which provides an image of the horizontal gradient of the density field in a horizontal slice. These images showed that at all evaporation rates, the single most pervasive thermal structure in the fluid appears to be the streamer. Streamers can be thought of as long circulating loops which move cold liquid to the bulk and allow hot liquid to rise. The frequency of these streamers appeared to be linearly proportional to the evaporation rate.

Finally in this work, Atkinson-Barr performed flow visualisation experiments on mixtures of LAr and LIN at the liquid/vapour and more particularly, the liquid/liquid interface. Since the image could not be seen clearly in photographs, the experiments were videoed. At the start of the experiment, it was observed that the heat flux into the vessel was very small and convective motions were not evident in either the upper or lower layers. As heat was applied into the base of the vessel, convective circulation developed in the lower layer and a small distortion was seen at the interface. The core, which formed a downward flow, stayed in general near the centre of the vessel.

As the temperature of the lower layer increased, the interface between the two layers developed an oscillatory form with the greatest disturbances near the wall where boundary layer flow was evident. Plumes in the lower layer entrained fluid from the upper layer and returned under their own buoyancy causing the liquid/liquid interface to move upwards slightly. This is termed penetrative convection. As the experiment progressed, the wave motions in the interfacial region grew in amplitude and after about two hours, convection in the upper layer became apparent. This motion devel-

oped strongly causing the interfacial level to fall slightly as liquid from the lower layer was entrained into the upper layer. The boil-off mass flux increased sharply at this stage and its peak occurred whilst the layers were clearly visible. This is not in agreement with the theoretical models of Chatterjee and Geist(1972) and Germeles(1975) (described later) which show the peak mass flux occurring at the same time as the destruction of the layers.

The movement of the interface grew in amplitude and in wavelength and the interface displayed oscillations of a large amplitude, comparable to the depth of the liquid. The disappearance of the interface was not evident until about four hours after the experiment had started, at which time the boil-off reached an equilibrium, at an elevated level from that associated with similar heating in an unstratified fluid. This experiment showed that rollover begins with convection in both layers, followed by waves on the liquid/liquid interface and finally a migration of this interface.

Shi(1990) formed models of rollover for fluid in two types of vessels. The first was for that in a rectangular vessel which required Cartesian coordinates and the second used cylindrical polar coordinates to describe flow in a cylindrical storage vessel. Two basic assumptions were made about the flow medium:

1. The fluid is Newtonian;
2. The fluid is incompressible.

The Boussinesq approximation was also assumed. This states that if density variations are small, they may be neglected in so far as they affect inertia but must be retained in the buoyancy terms. A model for two-dimensional homogeneous flows, termed the one-component model, was then constructed, the governing differential equations being the two-dimensional Navier-Stokes equations,

$$\begin{aligned}\frac{\partial u}{\partial t} + u \frac{\partial u}{\partial x} + w \frac{\partial u}{\partial z} &= -\frac{1}{\rho_0} \frac{\partial p}{\partial x} + \nu \left(\frac{\partial^2 u}{\partial x^2} + \frac{\partial^2 u}{\partial z^2} \right) \\ \frac{\partial w}{\partial t} + u \frac{\partial w}{\partial x} + w \frac{\partial w}{\partial z} &= -\frac{1}{\rho_0} \frac{\partial p}{\partial z} + \nu \left(\frac{\partial^2 w}{\partial x^2} + \frac{\partial^2 w}{\partial z^2} \right) + g\beta_T T\end{aligned}$$

the energy equation (in conservative form),

$$\frac{\partial T}{\partial t} + \frac{\partial(uT)}{\partial x} + \frac{\partial(wT)}{\partial z} = \kappa \left(\frac{\partial^2 T}{\partial x^2} + \frac{\partial^2 T}{\partial z^2} \right)$$

and the continuity equation,

$$\frac{\partial u}{\partial x} + \frac{\partial w}{\partial z} = 0.$$

Here $u(x, z, t)$ is the horizontal velocity component (ms^{-1}), $w(x, z, t)$ is the vertical velocity component (ms^{-1}), ρ_0 is the density in a reference state of hydrostatic equilibrium (kgm^{-3}), $p(x, z, t)$ is the pressure (Pa), ν is the kinematic viscosity (m^2s^{-1}), g is the gravitational acceleration (ms^{-2}), β_T is the thermal expansion coefficient (K^{-1}), $T(x, z, t)$ is the temperature (K) and κ is the thermal diffusivity (m^2s^{-1}) of the fluid.

Two assumptions were made about the the liquid surface in order to propose boundary conditions at the surface. Firstly, the surface was considered non-evaporating (i.e. not moving); secondly it was assumed to be stress free, i.e. a free surface. Though these assumptions are not strictly valid, they greatly simplify the computation. It was argued that although there will be continuous evaporation of liquid at the surface in the storage of cryogenic liquids since heat leak is inevitable, for well insulated tanks the daily loss of liquid is trivial (order of 0.5%) compared with the whole content. The second assumption was based upon the fact that for cryogenic liquids, the vapours have a much lower viscosity than the liquids. Furthermore, the temperature at the surface was fixed at the saturation temperature.

The governing equations were non-dimensionalised and discretised before being solved numerically for temperature and density. This model was expanded to deal with heterogeneous flows, which are flows containing two (or more) miscible components. For simplicity, only two-component flows were considered where the major constituent is referred to as the solvent and the other the solute. The behaviour of the solute was included by the addition of the equation

$$\frac{\partial S}{\partial t} + \frac{\partial(uS)}{\partial x} + \frac{\partial(wS)}{\partial z} = \alpha_s \left(\frac{\partial^2 S}{\partial x^2} + \frac{\partial^2 S}{\partial z^2} \right)$$

where $S(x, z, t)$ is the concentration (kgm^{-3}) of the solute and α_s is the diffusivity (m^2s^{-1}) of the solute in the solvent. Since the surface was considered to be non-evaporating, it was assumed that the composition of the liquid remained unchanged at all times so preferential evaporation, which has a greater effect the greater the difference between the saturation temperatures of the solvent and the solute, was not included in the problem. Further, there was assumed to be no exchange of the solute between the liquid and the walls. Therefore

$$\frac{\partial S}{\partial n} = 0$$

was taken to hold at all four boundaries, where \vec{n} is the direction normal to the boundary.

These equations were solved initially in Cartesian coordinates, for a two-layer system of LIN, with LOX as the solute. They were then adapted for cylindrical polar coordinates. The numerical results showed that the mixing process of two initially stratified layers is characterised by two continuing processes: steady downward penetration by the core flow into the convective loop in the upper layer and the process of entrainment whereby higher density liquid is entrained and mixed into the upper layer. These two processes work together until, eventually, the lower layer is completely mixed into the upper layer and the whole liquid became one single layer.

Also in this work, flow visualisation experiments were conducted in a cylindrical double-walled glass dewar in order to qualitatively verify these predictions. Ideally, LIN and LOX should have been used as the testing liquids since these were the fluids in which the numerical simulations were performed. However, this experiment demanded controllable uniform wall heating. To meet this requirement for this mixture was not easy. Instead, Freon 11 and Freon 113 were chosen. These fluids have a higher saturation temperature, making them less volatile and easier to handle at room temperature. The observations from these experiments agreed with the predictions from the numerical model, showing that the merging of the two stratified layers is characterised first by a gradual descent of the interface level as a result of the entrainment mixing at the interface facilitated on the core flow as it impinges on a density interface, and then by a rapid mixing of the layers. The main conclusion of Shi's thesis was that in a two-layer system of cryogenic liquids under atmospheric pressure, the free surface is almost isothermal, unlike the quasi-adiabatic liquid-liquid interface. So the buoyancy-induced convective flows in the two layers are distinctly different. Due to the cooling action of the isothermal surface, a strong core exists in the upper layer whereas high fluid velocities are confined to the boundary layer in the lower layer. This work will be used as a foundation for our work in chapter 5 involving preferential evaporation in mixtures of cryogenic fluids.

Table 1.1 lists the cryogenic liquids which will be used in our models, along with approximate values of T_{sat} , the saturation temperature (K), ρ_l , the density (kgm^{-3}) in liquid form at the saturation temperature and L , the latent heat of vaporisation (Jkg^{-1}) at the saturation temperature.

Cryogenic Liquid	T_{sat} (K)	ρ_l (kgm^{-3})	L (kJkg^{-1})
Nitrogen (LIN)	77.4	808	199
Oxygen (LOX)	90.2	1140	213
Argon (LAr)	87.3	1400	158
Methane (CH_4)	112	425	512

Table 1.1: Approximate Values of Thermo-Physical Properties of Cryogenic Fluids

There has been some previous interest in the evaporation of mixtures. A report by Beduz and Scurlock(1996) described experimental investigations into, amongst other things, the relationship between the evaporation rate of both pure LIN and mixtures of LIN, including LIN/LOX and LIN/LA mixtures, and the temperature difference between the bulk fluid and the surface. From this, it was found that the evaporation mass flux at a fixed superheat is some 30-50% greater for mixtures than for pure LIN. This is thought to be associated with the more intense convection which occurs as a result of the two additive components on the local density. More recently, Keary *et al.*(1998) investigated concentration changes in liquid air evaporating in an open dewar. Their results implied the existence of a surface layer which was richer in LOX due to the preferential evaporation of LIN. These results were obtained in a long (1-1.7m long), narrow (70mm diameter) double-walled glass dewar using temperature and concentration probes which could be moved up and down. The work showed a non-linear relationship between the evaporative mass flux and the concentration difference between the surface and the bulk of the liquid.

There have been several other experimental and theoretical investigations of rollover. For example, Nakano *et al.*(1982) conducted studies on the mixing of stratified layers using mixtures of Freon-11 and Freon-113 since their saturation temperatures are around room temperature, making them easier to handle. After the stratified layers were formed, heat was applied to the tank to initiate rollover. It was noted that for fluid in a tank which was heated from the bottom, rapid mixing patterns could be observed. However, when the tank was heated from the side, boundary layer penetration patterns could be seen. These formed because of the gradual penetration of upward convective flows along the wall and into the upper layer. Peak evaporation flowrates were not observed for either of these methods of heating the tank but were found to be present when the tank was heated from both the side and bottom.

Sugawara *et al.*(1983) performed various tests including one which used a full size LNG tank. LNG from two different sources was used to simulate the stratification in the tank and the temperature and density of the layers were measured. A mixed layer was found to exist between the upper and lower layers caused by a mixing effect due to the addition of cargo at the vessel bottom. In this ‘intermediate layer’, a temperature gradient was observed. However the density profile proved impossible to measure. The thickness of the layer gradually decreased with time because of the convective flows in the upper and lower layers and a sharp interface was formed. Initially, the interface descended gradually, but just before rollover, it descended more rapidly. Finally the upper and lower layers were mixed. Whilst the intermediate layer was present, the rate at which the mixture evaporated was small but this increased significantly shortly after the layer disappeared.

Experiments with liquid petroleum gas (LPG) performed by Morrison and Richardson(1990) provided a good qualitative description of the development of stratified layers with time. In brief, the results confirmed the presence of an initially stationary interface with heat/mass exchanges akin to double-diffusive convection between the layers. However interface migration dominated in the later stages when penetrative convection was seen to exist. As fluid was removed from the lower layer, the interface between the two layers moved perceptibly upward and their relative densities decreased.

The Kelvin-Helmholtz instability mechanism (see Milne-Thomson, 1968, for more details) may be used to explain the instability in the interface between stratified layers in storage containers. This instability affects the interface between two layers of inviscid fluids of different densities and perhaps velocities. Modelling the pressure at the surface with Bernoulli’s equation for unsteady potential flow and examining the stability of this interface suggests that the system will become unstable if

$$\frac{\rho_1\rho_2U^2}{\rho_1 + \rho_2} > 2[(\rho_2 - \rho_1)g\sigma]^{\frac{1}{2}}$$

where ρ_1 and ρ_2 are the densities (kgm^{-3}) of the upper and lower layer respectively, U is the convective velocity difference (ms^{-1}) between the two layers, g is gravity (ms^{-2}) and σ is the surface tension (Nm^{-1}) between the two fluids.

Gravity and surface tension therefore play a stabilising role; the larger g or σ , the larger U would need to be before the instability occurs. In the absence of surface tension, σ , there will be instability for any U , however small. This equation also indicates that when the two densities, which are variables, become equal, the instability

comes into existence. This agrees with the concept of rollover which occurs when the densities of the upper and lower layers become equal.

Hashemi and Wesson(1971) formed the following equation for the rate of evaporation, \dot{m} ($\text{kgm}^{-2}\text{s}^{-1}$):

$$\dot{m} = C_1 \left(\frac{k}{\lambda} \right) \left(\frac{\beta g}{\alpha \nu} \right)^{1/3} \Delta T^{4/3}$$

where C_1 is a dimensionless constant, k is the thermal conductivity ($\text{Wm}^{-1}\text{K}^{-1}$), λ is the latent heat of vaporisation (Jkg^{-1}), β is the coefficient of thermal expansion (K^{-1}), g is the acceleration due to gravity (ms^{-2}), α is the thermal diffusivity (m^2s^{-1}), ν is the kinematic viscosity (m^2s^{-1}) and ΔT is the temperature difference between the bulk of the liquid and the surface (K). C_1 can be obtained from data on the fluid which is being modelled.

By comparing the theoretical evaporation rate for water to that found experimentally, the authors concluded that surface evaporation is essentially controlled by heat transfer through the liquid boundary layer rather than mass transfer through the gaseous boundary layer over the free surface.

Chatterjee and Geist(1972) examined the effects of stratification on boil-off rates in LNG tanks. A mathematical model of rollover, with n homogeneous layers of LNG of given heights and physical properties, at a constant tank pressure, was proposed. The model included double-diffusive convection, the behaviour of fluids in which there are gradients of two properties with different diffusivities, to describe the interfacial transportation of heat and methane. The differential equations produced to model the process were solved numerically as an initial value problem. For a set of initial conditions and tank properties, the temperature, composition and densities of each layer and the boil-off rates were calculated at finite time intervals. When two adjacent layers had insignificantly small compositional differences they were considered mixed and the number of layers was decreased one by one until only one layer remained. For three widely different and well-known cases, the mathematical model predicted with satisfactory accuracy both the time required to reach maximum boil-off rates and the magnitudes of these peaks. However, the accuracy was limited by uncertainties in the interfacial heat and mass transfer coefficients incorporated in the model and by the assumption that density differences always lead to complete stratification, thus neglecting the effects of mixing that always occur to some extent during filling. Also, the differential equations formed in this paper were for a tank containing many different

layers. Multi-layers have never been shown to exist in real storage containers so we may only take qualitative results for a two-layer system.

Germeles(1975) formulated a similar model to Chatterjee and Geist(1976) to describe rollover, considering two mixtures of LNG with slightly different compositions of methane (the solvent) and other solutes (impurities) and/or different temperatures T_1 and T_2 , and corresponding densities ρ_1 and ρ_2 . This was simplified to a fictitious two-component mixture representing LNG compounds. Differential equations were then formed to describe the conservation of energy and solute material for a number of adjacent convection layers, known as cells. The Hashemi-Wesson model(1971) was used for the computation of boil-off of the solvent and the solute was assumed not to evaporate. In the model, when any two adjacent cells reached density equilibration within a specified small difference, they were assumed to be mixed and were transformed into a single cell of average characteristics. The final rollover of the tank took place when the last two cells were mixed, and the entire tank became one single cell. A computer program was written which, given the number of cells, the cell thicknesses and the initial values of the temperatures and concentrations for each cell, integrated the conservation equations of the model forward in time. The computed time histories of boil-off mass flux, temperature, concentration and density for each cell were plotted. The results of this model were compared to the data from the La Spezia rollover incident (Sarsten, 1972), in which rollover actually occurred in an LNG storage tank, and were shown to give reasonable predictions. This model is slightly more realistic than the Chatterjee and Geist model, because unlike in the latter, it does not assume that there is equimolar counter-diffusion across the interfaces and therefore that the number of moles in each layer is constant until mixing occurs. The transport coefficients used in both models, however, were for salt solutions rather than for LNG mixtures and the model could again only give qualitative results for a two-layer system.

Chatterjee and Geist(1976) extended this model to incorporate the presence of nitrogen. This required various alterations to their former model including:

1. LNG was treated as a mixture of nitrogen, methane and ethane, rather than a two-component mixture of methane and ethane;
2. The original model assumed that the boil-off vapour from the top layer was pure methane. In the new model, the boil-off vapour was taken to be a mixture of nitrogen, methane and ethane and the model incorporated a detailed flash

calculation to calculate the boil-off rate.

Computer simulations were carried out using the model, to improve understanding of the factors that influence the intensity and duration of this type of rollover. They indicated that with 1-3% nitrogen, the peak flowrate associated with rollover will be about 2-3 times the normal boil-off rate.

A computer program ('ROLLO') was developed by Heestand *et al.*(1983). For given initial temperatures and compositions, ROLLO computes the evolution of stratified LNG by numerically solving a set of differential equations, which are formed with the conditions of material and energy balance between the N liquid strata with stationary interfaces. A modified Hashemi-Wesson(1971) model, which assumed that the vapour evolved is in thermodynamic equilibrium with an arbitrarily thin film of liquid on the surface, was used to describe the weathering of the stored LNG. However no spatial dimensions were used in each strata so the effects of weathering were assumed to be convected immediately, maintaining a uniform liquid composition throughout the top layer.

In chapter 5, we consider the natural convection of concentration and temperature in mixtures of cryogenic fluids with preferential evaporation and double-diffusive convection. A review of the developments and applications in double-diffusive convection was given by Huppert and Turner(1981). This type of convection was first associated with salt fingers, which are long narrow convection cells that are set up when warm salty water lies above cold fresh water. Renardy and Schmitt(1996) explored the influence of non-linear profiles of salinity, as might arise due to surface evaporation, on the linear stability problem in a salt-fingering regime. The asymmetry observed experimentally in the salt fingers has been attributed to evaporation due to a dry atmosphere leading to a salty layer at the top with the salinity varying little over the rest of the fluid. A model was constructed of double-diffusive convection with a sharp, non-linear concentration gradient applied at the upper boundary, to model the surface evaporation of the solute. This gradient was found to drive a motion that was confined to a depth of a few boundary layers. No significant motion was found lower in the layer. The instability which operated in the boundary was stabilised by the temperature gradient in the bulk.

Sévédér and Petit(1989) studied the natural convection caused by combined heat and mass transfer on a single layer of LNG in a two-dimensional square closed cavity

with insulated, horizontal walls. This LNG was assumed to be composed of methane, taken as the solvent, and ethane, as the diffusing species. The steady-state equations for the problem were formed and solved numerically for thermal and solutal Rayleigh numbers of 5.5×10^3 and -1.3×10^5 respectively. Various boundary conditions were applied on the two vertical walls, including the case of uniform temperatures and molar fractions, where the thermal buoyancy force counteracts the compositional buoyancy force. The computed streamlines were shown to be similar to those obtained for natural convection due to heat transfer only, with an upward flow induced along the hot side wall and fluid descending down the opposite wall. The effects of evaporation were not considered in this model.

A more recent paper by Nishimura *et al.*(1998) investigated the effect of a buoyancy ratio, N , on the flow structure of a binary mixture gas in a rectangular enclosure, subject to opposing horizontal thermal and compositional buoyancy. The buoyancy ratio, $N = \beta_C(c_h - c_l)/\beta_T(T_h - T_c)$ where β_C is the compositional expansion coefficient, c_h is the high concentration, c_l is the low concentration, β_T is the thermal expansion coefficient, T_h is the hot wall temperature and T_c is the cold wall temperature. The unsteady problem was solved numerically using a finite element model and predicted that oscillatory double-diffusive convection occurs for a certain range of buoyancy ratios.

In this section we have concentrated on previous work which we feel to be closely related to our studies. There are a number of other papers which also consider various phenomena in multi-component fluid systems which are of less relevance.

Turner(1965) performed experiments to examine the stability of cold fresh water resting on top of hot salty water with a sharp density interface between them. Both the heat transfer and the ratio of the rates of turbulent transport of salt and heat were found to depend systematically on the ratio of the density difference due to salinity differences to the density difference due to temperature differences between the layers. Bose and Palmer(1983) used linear hydrodynamic stability theory to examine the extent to which key mass-transfer properties affect the interfacial stability of a binary mixture evaporating under vacuum. Results indicated that the stability criteria for interfacial convection were extremely sensitive to the difference in volatility between the two components. Lin *et al.*(1990) carried out a detailed numerical study to investigate transient natural convection in a binary mixture in a square enclosure with temperature and concentration fixed on both opposing walls. The effects of the buoyancy ratio were

found to be significant on the flow pattern and heat and mass transfer. Kamakura and Ozoe(1993) examined the evolution of the concentration distribution for double-diffusive natural convection within a fluid heated and cooled from opposing walls and with an initially linear concentration gradient. Multi-layered roll cells separated by sharp interfaces were observed numerically. Bates and Morrison(1997) modelled the evolution of stratified liquid natural gas in storage tanks from formation to breakdown, due to rollover. The behaviour of the fluid was described in two phases, the first of which followed the model proposed by Heestand *et al.*(1983) and the second which modelled the migrating interface. The results compared well with experimental data.

1.2 Thesis Layout

A simple model, dependent only on time, for the rate of increase in temperature of two stratified layers of cryogenic fluids up to the point of rollover is proposed and solved in Section 2.1. The effects of evaporation are included in Section 2.2 and the results are compared with two specific experimental cases studied by Agbabi(1987). We discuss the important variables in this initial model in Section 2.3.

The rate at which a one-component fluid evaporates is discussed in Chapter 3. A model is proposed which examines the thin conduction region at the surface observed in experiments (e.g. Beduz *et al.*, 1984), assuming that away from the surface, the temperature of the fluid is uniform. The Stefan condition is applied at the surface to describe the rate at which the surface moves downward. In 3.1.3, we find a similarity solution which satisfies the equations of the model. Since we require one mass flux rate to describe the process over all time, to make a direct comparison to experimental work, we examine the stability of the solution in order to see whether it is capable of damping out small perturbations to which any physical system is subjected. A time-dependent mass flux rate is calculated in 3.1.3. We then examine the long-term behaviour of the fluid by examining a travelling wave solution. A more realistic boundary condition is proposed for the model in 3.1.5, such that the temperature of the bulk of fluid remains a fixed distance from the moving surface. The long-term behaviour of the fluid is again examined using a travelling wave solution. With knowledge of the thickness of the conduction region, we obtain a mass flux rate which is independent of time. The result agrees qualitatively with previous experimental correlations. In Section 3.2, we

propose a model for a two-component liquid with evaporation of only one component at the surface.

We obtain numerical predictions of the thickness of the conduction region in Chapter 4. This model is constructed using the assumption made in previous studies; this considers the unstable temperature gradient close to the surface and proposes a Bénard-type instability criterion for the thickness of the surface layer, characterised by a critical Rayleigh number, above which convection is initiated. Equations are formed which model convective instability in the surface layer with Couette flow at the lower boundary to describe the effect of convection in a cell in the bulk of the liquid on the conduction region. Numerical results obtained with the model suggest that the minimum thickness of the layer is larger than that observed in experiments. In Section 4.2, we construct a simple model to investigate the theory that thermal fluctuations, observed close to the surface of cryogenic fluids, particularly mixtures (Atkinson-Barr, 1989), could be due to micro-convection eddies, which replenish the fluid lost at the surface. The comparison between our estimated frequency and experimental results supports such a theory.

Finally in Chapter 5, we propose what we believe to be the first model to include preferential evaporation with laminar natural convection within a mixture of two cryogenic fluids, in a square vessel. We begin this work by constructing a model for the laminar natural convection within a one-component fluid in Section 5.1. The equations from this model are discretised by an upwind scheme and solved numerically, with the Poisson equation being solved using the multigrid method, described in 5.2.5. After carefully validating our code with previous results for one and two-component flows, we derive a new term for the preferential evaporation of the mixture in Section 5.6. The equations used in the model are solved numerically to obtain the first plots of the evolution of this type of evaporation.

Chapter 2

Temperature Models For Rollover

In this chapter, we will examine the bulk temperature in a two layer system, up to the onset of rollover. The results will be compared to the experimental work of Agbabi(1987), described in detail in Section 1.1, in which rollover is observed using two different LIN/LOX mixtures to form the two layers and applying different heat fluxes to the upper and lower layers. Although we shall only propose and solve elementary mathematical models in this section, we shall see that they give initial qualitative results of the behaviour of the system.

2.1 Initial Time Dependent Model

2.1.1 Description of the initial mathematical model

We begin by constructing a model to describe rollover which has no space dimensions and only time dependency. The vessel used in the work of Agbabi(1987) is depicted in Figure 2.1, showing the heat flux in and out of the system. For the initial model, we shall assume that there are bulk heating sources in both layers of the fluid which heat up the particles individually, rather than model the problem with external heaters around the cylinder, as performed experimentally. In this way we can avoid introducing any space dimensions to the problem. The vessel is otherwise assumed to be well insulated and all other heat transfer between the system and the surroundings is ignored. The lower layer, therefore, gains heat from the bulk heater and releases some of this heat by conduction to the upper layer. In this initial model, evaporation is neglected since

it is assumed to be insignificant. So, the upper layer simply gains heat, both from the bulk heater and from the lower layer by conduction.

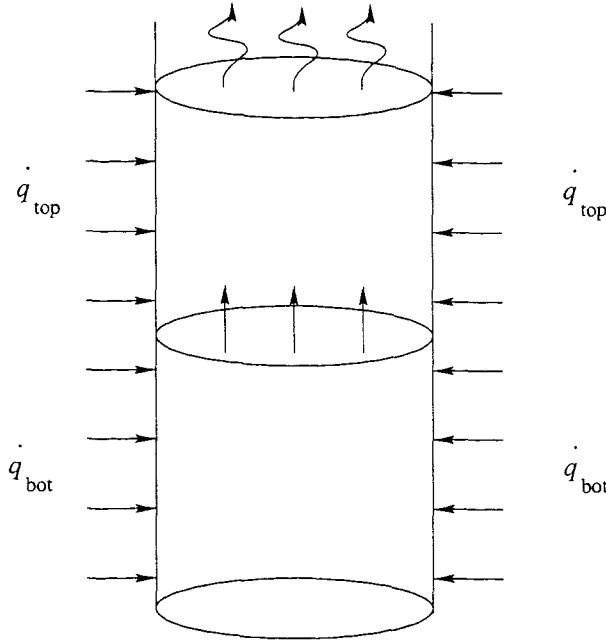


Figure 2.1: Diagram depicting vessel used experimentally by Agbabi(1987), illustrating the heat gain/loss from the system. The arrows indicate the direction of the heat flow.

Suppose \dot{q}_{top} and \dot{q}_{bot} are the thermal powers per unit area (Wm^{-2}) applied to the top and bottom wall heaters respectively. These values are required to find the powers of the bulk heaters in both layers. Let $T_{\text{top}}(t)$ and $T_{\text{bot}}(t)$ be the temperatures (K) of the top and bottom layers respectively which are dependent on time, t . This leads to two equations:

$$\rho_{\text{top}}(t)c_{\text{top}}\dot{T}_{\text{top}}(t) = f_1(t) + f_3(t) \quad (2.1)$$

$$\rho_{\text{bot}}(t)c_{\text{bot}}\dot{T}_{\text{bot}}(t) = f_2(t) - f_3(t) \quad (2.2)$$

where $f_1(t)$ and $f_2(t)$ are the heating powers per unit volume (Wm^{-3}) due to the bulk heater and so are dependent on \dot{q}_{top} and \dot{q}_{bot} respectively and $f_3(t)$ represents the thermal power per unit volume (Wm^{-3}) transferred through the layers by conduction; $\rho_{\text{top}}(t)$ and $\rho_{\text{bot}}(t)$ are the time-dependent densities (kgm^{-3}) and c_{top} and c_{bot} are the

specific heat capacities ($\text{Jkg}^{-1}\text{K}^{-1}$) of the upper and lower layers respectively.

$$\begin{aligned} \text{Heat entering top layer per unit time} &= \text{Heat flux per unit area into vessel} \\ &\quad \times \text{Area in contact with heater} \\ &= 2\dot{q}_{\text{top}}\pi ah_{\text{top}} \end{aligned}$$

where a is the radius (m) of the cylinder, and h_{top} is the height (m) of the top layer.

$$\text{So the heat entering the top layer per unit time per unit volume} = \frac{2\dot{q}_{\text{top}}\pi ah_{\text{top}}}{\pi a^2 h_{\text{top}}}$$

Therefore, we have found one of the terms in equation (2.1), namely:

$$f_1(t) = \frac{2\dot{q}_{\text{top}}}{a}. \quad (2.3)$$

The term $f_2(t)$ in equation (2.2) is found similarly to be:

$$f_2(t) = \frac{2\dot{q}_{\text{bot}}}{a}. \quad (2.4)$$

The thermal conductivity equation gives,

$$J_v = \frac{k(T_{\text{bot}}(t) - T_{\text{top}}(t))}{l} \quad (2.5)$$

where J_v is the heat flux (Wm^{-2}) between the two layers, k is the thermal conductivity ($\text{Wm}^{-1}\text{K}^{-1}$), assumed to be equal for the two fluids and l (m) is the thickness of the interface seen to exist between the two layers obtained from experimental data. This interface exists to prevent the lower layer from penetrating through to the surface and so by its very nature has a steep temperature gradient. We can estimate its thickness from the experimental data of temperature profiles through the vessel and it is found to be about 2cm.

It is assumed that the thermal conductivity does not vary significantly with concentration. This is reasonable for small differences in concentration since the thermal conductivity of LIN is $0.1396\text{Wm}^{-1}\text{K}^{-1}$ and the thermal conductivity of LOX is $0.1514\text{Wm}^{-1}\text{K}^{-1}$.

Using equation (2.5), the thermal power per unit volume transferred from the lower layer to the upper layer is found to be:

$$\begin{aligned} f_3(t) &= J_v \times \frac{\text{surface area in contact with both layers}}{\text{volume of interface layer}} \\ &= \frac{J_v \pi a^2}{\pi a^2 l} \\ &= \frac{k(T_{\text{bot}}(t) - T_{\text{top}}(t))}{l^2}. \end{aligned} \quad (2.6)$$

Using equation 2.3, 2.4 and 2.6 in equation 2.1 and 2.2 yields the following differential equations for $\dot{T}_{\text{top}}(t)$ and $\dot{T}_{\text{bot}}(t)$:

$$\dot{T}_{\text{top}}(t) = \frac{2\dot{q}_{\text{top}}}{\rho_{\text{top}}(t)c_{\text{top}}a} + \frac{k}{\rho_{\text{top}}(t)c_{\text{top}}l^2} (T_{\text{bot}}(t) - T_{\text{top}}(t)) \quad (2.7)$$

$$\dot{T}_{\text{bot}}(t) = \frac{2\dot{q}_{\text{bot}}}{\rho_{\text{bot}}(t)c_{\text{bot}}a} - \frac{k}{\rho_{\text{bot}}(t)c_{\text{bot}}l^2} (T_{\text{bot}}(t) - T_{\text{top}}(t)). \quad (2.8)$$

The densities, $\rho_{\text{top}}(t)$ and $\rho_{\text{bot}}(t)$, can be expressed as functions of temperature for a constant pressure of 1 atmosphere, using experimental data (Younglove, 1982). Thus we have two differential equations in two unknowns, namely $T_{\text{top}}(t)$ and $T_{\text{bot}}(t)$.

Equations (2.7) and (2.8) are solved numerically, for the temperatures of the upper and lower layers, $T_{\text{top}}(t)$ and $T_{\text{bot}}(t)$ and these results are compared to experimental results for two specific cases performed by Agbabi(1987).

2.1.2 Properties of mixtures for two specific cases

For our work, we select two specific cases from Agbabi(1987) to compare with our numerical results. Case (1) is the simplest case of heat only entering the lower layer and case (2) has fairly similar heat fluxes entering the two layers. Table 2.1 shows the properties of the mixtures for these two cases where L_{top} and L_{bot} are the latent heat of vaporisation of the fluid in the top and bottom layers respectively and $C_{\text{top}}^{\text{LOX}}$, and $C_{\text{bot}}^{\text{LOX}}$ are the initial percentage concentrations of LOX in the upper and lower layers respectively. $C_{\text{top}}^{\text{LIN}}$ and $C_{\text{bot}}^{\text{LIN}}$, the initial percentage concentrations of LIN in the upper and lower layers respectively, can be found using $C_{\text{top}}^{\text{LIN}} = 1 - C_{\text{top}}^{\text{LOX}}$ and $C_{\text{bot}}^{\text{LIN}} = 1 - C_{\text{bot}}^{\text{LOX}}$. Figure 2.2 shows the graph of density against temperature at a constant pressure of 1 atmosphere obtained for LIN and LOX where the crosses and circles mark the actual values given in the experimental data (Younglove, 1982) and the straight lines represent the best fit line through the points. From these, we find the following linear relationships between density and temperature for both fluids:

$$\begin{aligned} \rho_{\text{LIN}} &= -3.80T + 1106.2 \\ \text{and} \quad \rho_{\text{LOX}} &= -4.59T + 1556.0 \end{aligned}$$

where ρ_{LIN} and ρ_{LOX} are the densities (kgm^{-3}) and T is the temperature (K) of the fluid.

Case	1	2
\dot{q}_{top} ($\text{Jmin}^{-1}\text{m}^{-2}$)	0	9.9×60
\dot{q}_{bot} ($\text{Jmin}^{-1}\text{m}^{-2}$)	67.1×60	16.8×60
a (m)	0.0325	0.0325
c_{top} ($\text{Jkg}^{-1}\text{K}^{-1}$)	2×10^3	2×10^3
c_{bot} ($\text{Jkg}^{-1}\text{K}^{-1}$)	2×10^3	2×10^3
L_{top} (Jkg^{-1})	2×10^5	2×10^5
L_{bot} (Jkg^{-1})	2×10^5	2×10^5
k ($\text{Jmin}^{-1}\text{m}^{-1}\text{K}^{-1}$)	0.1×60	0.1×60
l (m)	0.02	0.02
$T_{\text{top}}(0)$ (K)	77.40	77.50
$T_{\text{bot}}(0)$ (K)	77.60	77.50
$\rho_{\text{top}}(t)$ (kgm^{-3})	$-3.81T_{\text{top}}(t) + 1114.4$	$-3.81T_{\text{top}}(t) + 1111.1$
$\rho_{\text{bot}}(t)$ (kgm^{-3})	$-3.84T_{\text{bot}}(t) + 1127.3$	$-3.81T_{\text{bot}}(t) + 1114.7$
$C_{\text{top}}^{\text{LOX}}$ (%)	1.8	1.1
$C_{\text{bot}}^{\text{LOX}}$ (%)	4.7	1.85

Table 2.1: Properties of mixtures in upper and lower layers for two specific experimental cases.

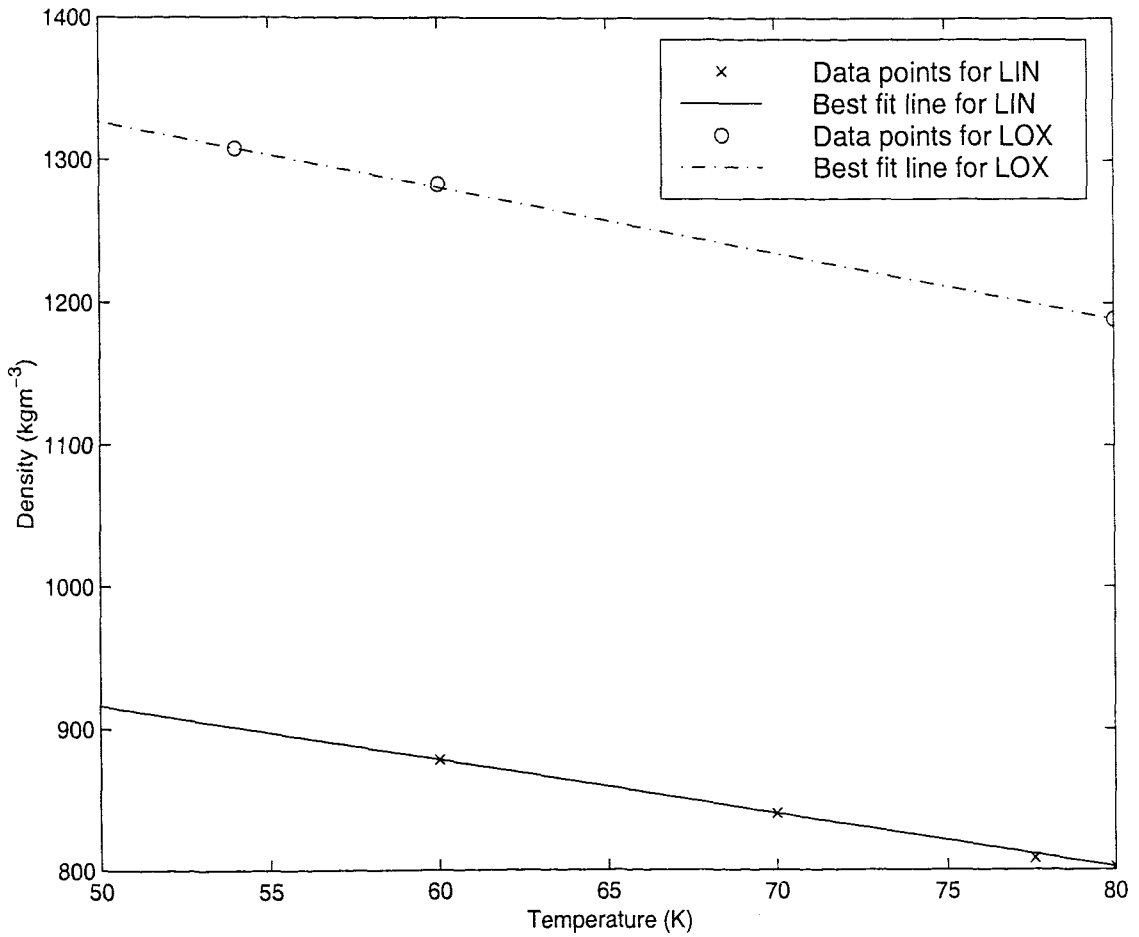


Figure 2.2: Graph showing densities of LIN and LOX against temperature at a constant pressure of 1 atmosphere.

The densities of the upper and lower layers, $\rho_{top}(t)$ and $\rho_{bot}(t)$ respectively, are assumed to be linear combinations of the densities of LIN and LOX, based on the concentration of the fluid in each layer.

2.1.3 Results of the initial model

The coupled differential equations (2.7) and (2.8) are solved numerically using a simple Runge-Kutta routine with adaptive stepsize control (Smith, 1965) for the two cases. The bulk temperatures in the upper and lower layers for the two cases are compared to those found experimentally and are shown in Figures 2.3 and 2.4 respectively. Although experimental evidence shows that rollover is initiated by increased convective mixing, we will examine the use of a simple 'equal density' criterion for predicting the onset of rollover. Thus although we do not have any experimental data with which to compare the density, we find the densities of the upper and lower layers for the two cases and these are shown in Figures 2.5 and 2.6 respectively. The time measurements are calculated in minutes to allow for an easier comparison with the experimental work.

Figure 2.3 shows that the numerical solution of the temperature for the upper layer initially agrees well with experimental data but after approximately 4 minutes starts to increase more rapidly than the measured temperature suggests. The numerical solution of the temperature for the lower layer immediately increases at a faster rate than the experimental result and, after 20 minutes, there is a temperature difference of almost 2K between the two values. Figure 2.4 shows that the predicted temperatures for both the upper and lower layers, for case (2), immediately increase at a much faster rate than the experimental results and after 30 minutes there is approximately a 0.7K difference in both layers. Although this does not sound very much, this difference in temperature causes a change in the density. Assuming that rollover occurs when the two layers become an equal density, this density difference could mean the difference between rollover occurring or not.

The numerical results for the density of both the top and bottom layers are shown in Figure 2.5 for case (1) and in Figure 2.6 for case (2). Initially the density of the lower layer is higher than that of the upper layer for both cases. However we see that in Figure 2.5, the density of the lower layer decreases quite rapidly whilst that of the upper layer only decreases slowly and at the end of the run, there is only a 1kgm^{-3} (0.1%) density difference. However, although the density of the lower layer

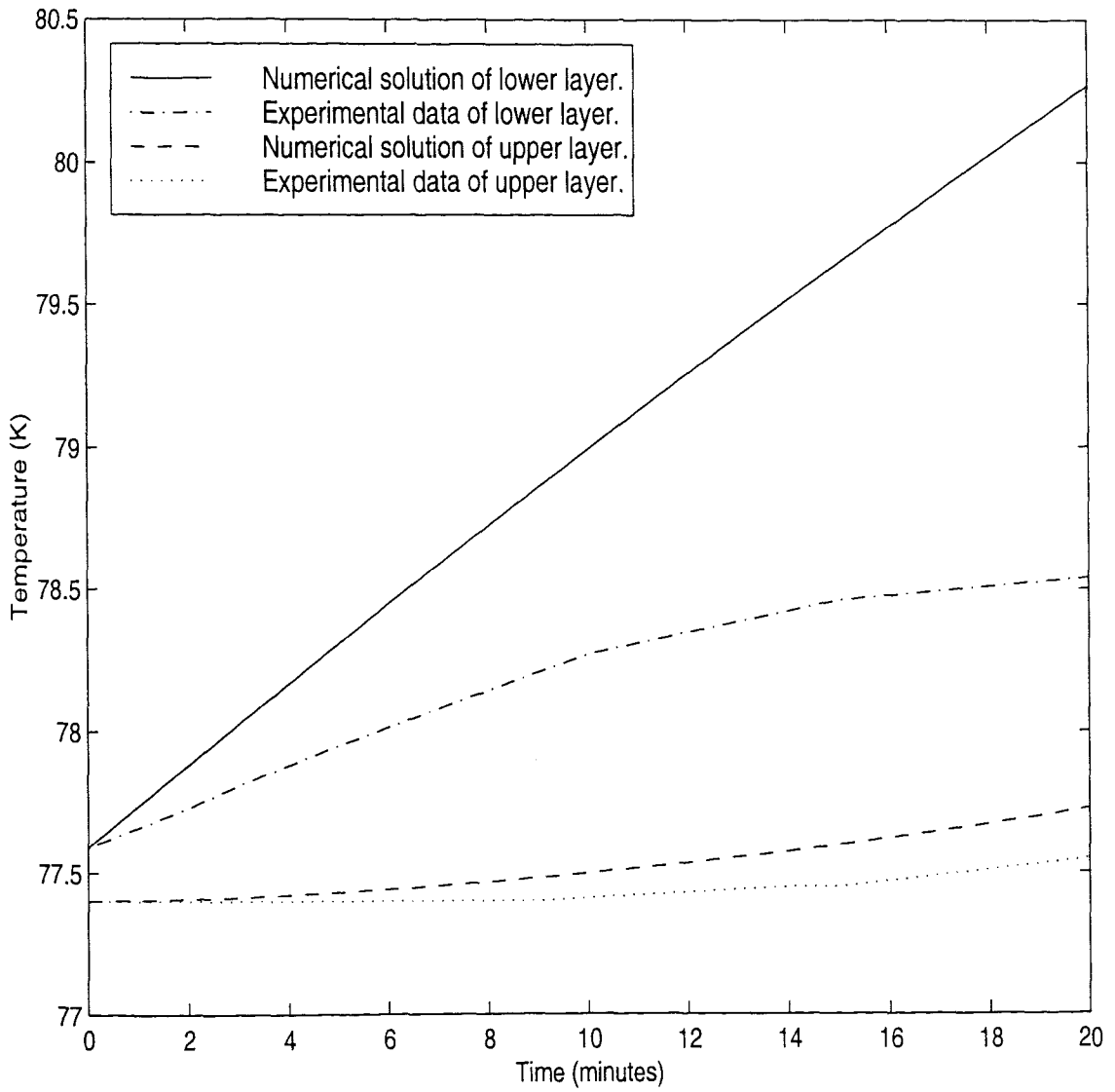


Figure 2.3: Comparison between the numerical solutions of the bulk temperatures of the upper and lower layers and those found experimentally for case (1).

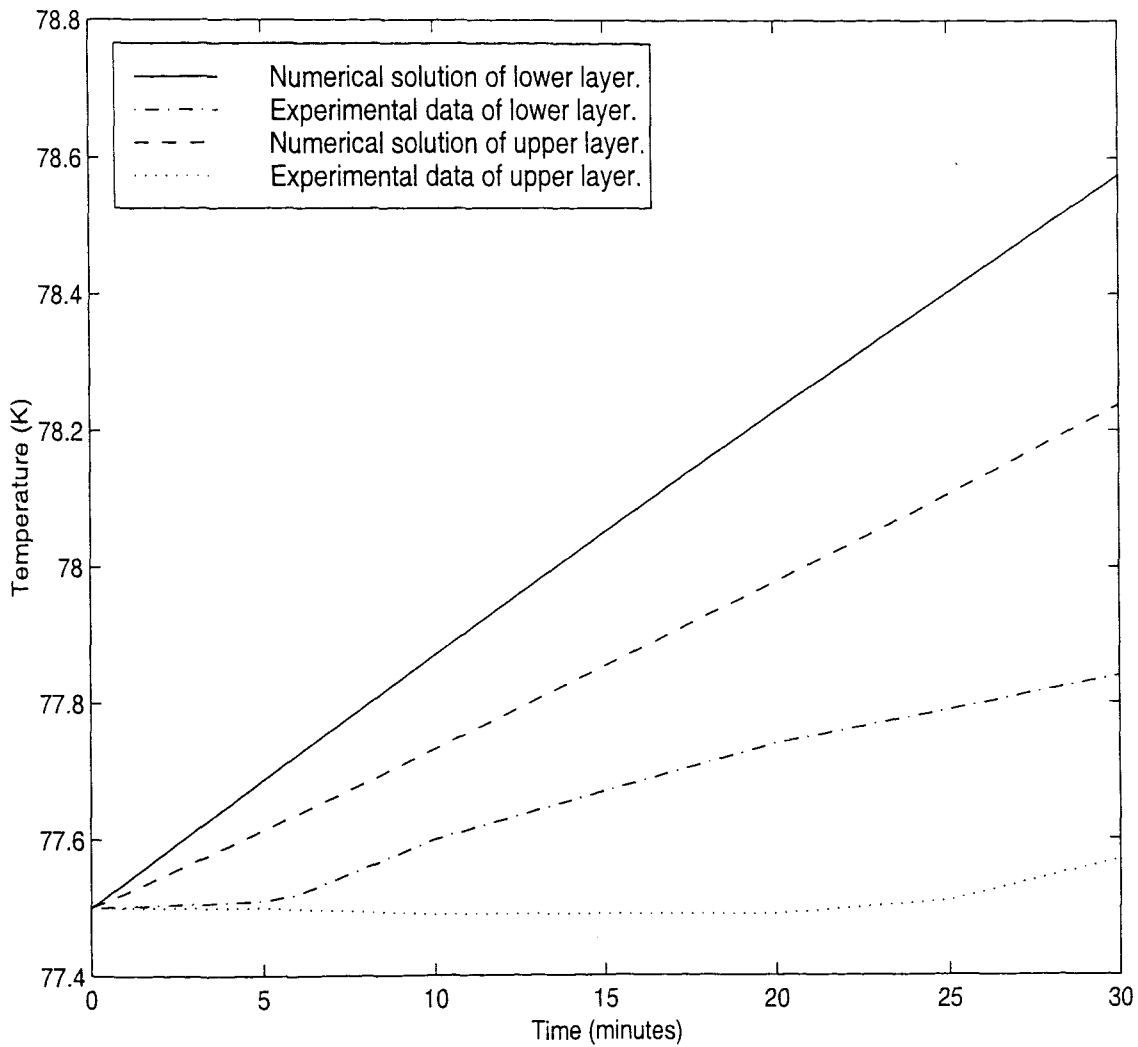


Figure 2.4: Comparison between the numerical solutions of the bulk temperatures of the upper and lower layers and those found experimentally for case (2).

is decreasing more rapidly than that of the upper layer in Figure 2.6, there is still a 2.5kgm^{-3} (0.3%) density difference after 20 minutes. In both cases, the system is still bottom heavy at the end of the run by which time it appears that the penetrative convection was becoming dominant in Agbabi's experiments.

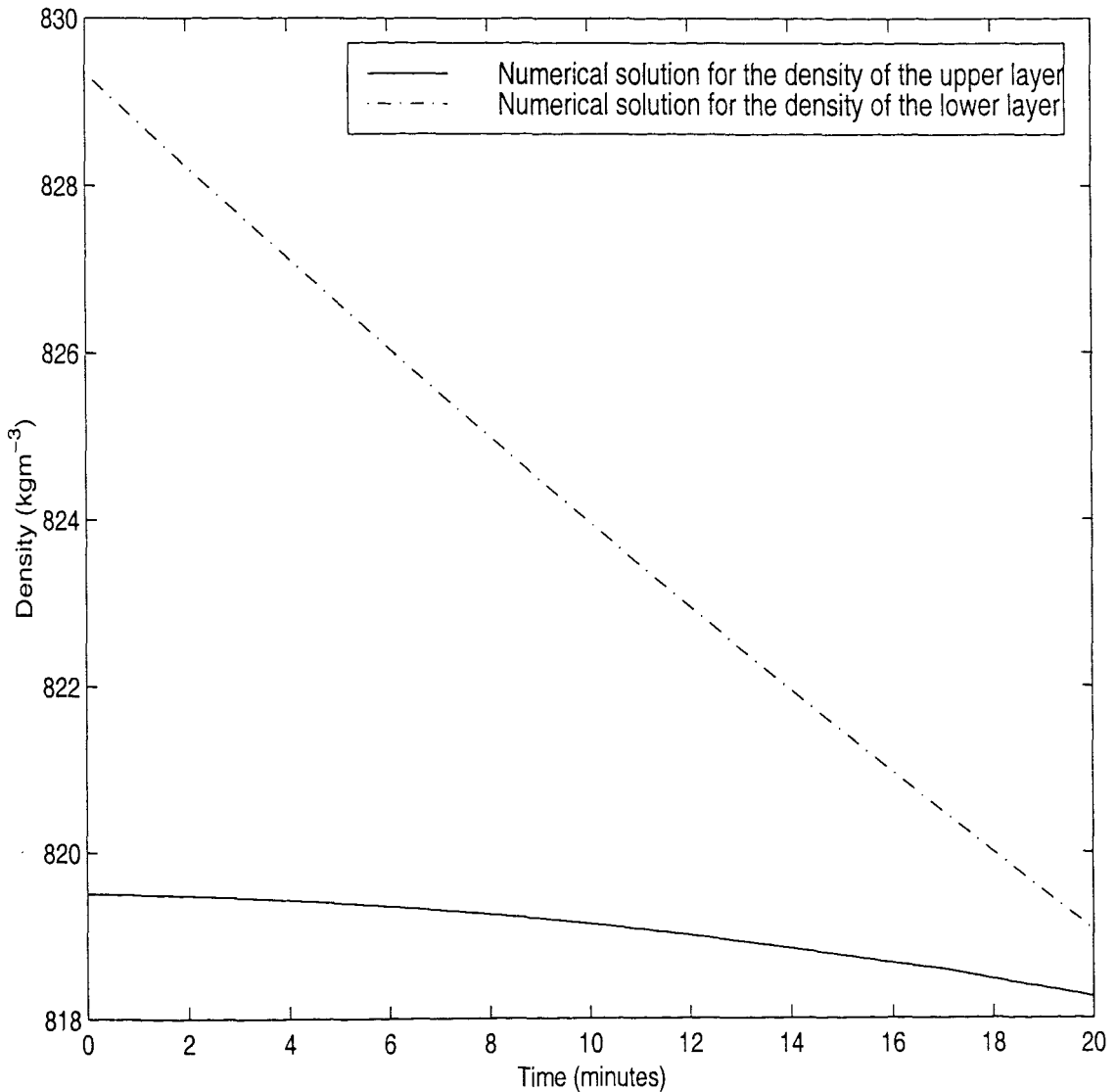


Figure 2.5: Numerical solutions of the bulk densities of the upper and lower layers for case (1).

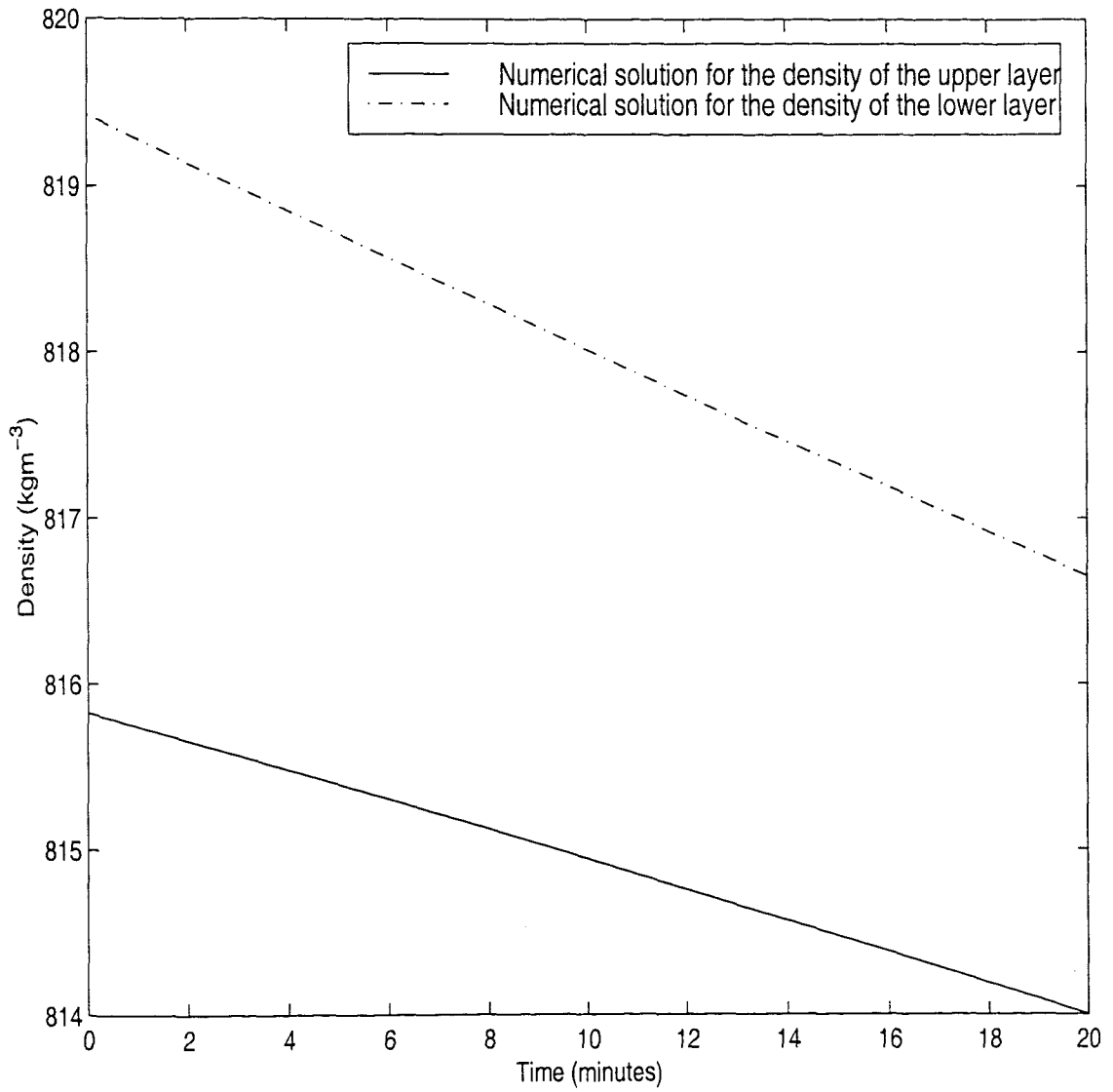


Figure 2.6: Numerical solutions of the bulk densities of the upper and lower layers for case (2).

2.1.4 Discussion of results obtained from initial model

The assumption of an adiabatic upper surface, neglecting heat loss through evaporation can be used to explain some of the difference between the numerical and experimental solutions for the upper layer in both cases. Its effect, however, would be greater on case (2) than on case (1) since more fluid evaporates in case (2), due to the greater superheat of the upper layer which drives evaporation. This inaccuracy will directly affect the density of the layers and shall be addressed in the next section.

2.2 The Inclusion of Evaporation

2.2.1 Basic model including evaporation

Evaporation cools the upper layer and therefore neglecting the effects of evaporation causes the temperature of the upper layer to increase too rapidly as we saw from our previous results. In this section, evaporation will be included to study the effect of this phenomena on the temperature. The mass flux equation, given below, which was obtained experimentally for LIN by Agbabi(1987) will be included in the model

$$\dot{m} = 2.88 \times 10^{-3} \Delta T^{1.6}$$

where \dot{m} is the mass flux ($\text{kgm}^{-2}\text{s}^{-1}$) caused by evaporation and $\Delta T = T_{\text{top}}(t) - T_{\text{sat}}$ is the difference in temperature (K) between the upper layer and the saturation temperature, for our cases 77.36K.

We may then form new differential equations for $\dot{T}_{\text{top}}(t)$ and $\dot{T}_{\text{bot}}(t)$ by introducing the mass flux equation to the previous set of differential equations.

2.2.2 Results of the model with the inclusion of evaporation

We will now find $f_4(t)$, an additional term on the right hand side of equation (2.7) which represents evaporation in the differential equation for the upper layer.

$$\begin{aligned} \text{Heat flux out of the surface} &= \text{Mass flux out of surface} \\ &\quad \times \text{Latent heat of vaporisation} \\ &= \dot{m}L \end{aligned}$$

where L is the latent heat of vaporisation (Jkg^{-1}) for the fluid.

$$\begin{aligned} \text{Then the heat leaving per unit time} &= \text{Heat flux out of surface} \\ &\quad \times \text{Area of surface} \\ &= \dot{m}L\pi a^2. \end{aligned}$$

$$\text{So the heat entering the top surface per unit time per unit volume} = -\frac{\dot{m}L\pi a^2}{\pi a^2 h_{\text{top}}}.$$

Although the height of the upper layer will change over time as the fluid evaporates, we shall assume that this change is small enough to be neglected, such that $h_{\text{top}} = 0.13\text{m}$ for both cases. So we have found the new term in the differential equation for the upper layer, namely:

$$f_4(t) = -\frac{\dot{m}L}{h_{\text{top}}}.$$

Thus we obtain the following ordinary differential equations:

$$\begin{aligned} \dot{T}_{\text{top}}(t) &= \frac{2\dot{q}_{\text{top}}}{\rho_{\text{top}}(t)c_{\text{top}}a} + \frac{k}{\rho_{\text{top}}(t)c_{\text{top}}l^2}(T_{\text{bot}}(t) - T_{\text{top}}(t)) \\ &\quad - \frac{60 \times \dot{m}L}{h_{\text{top}}\rho_{\text{top}}(t)c_{\text{top}}} \\ \dot{T}_{\text{bot}}(t) &= \frac{2\dot{q}_{\text{bot}}}{\rho_{\text{bot}}(t)c_{\text{bot}}a} - \frac{k}{\rho_{\text{bot}}(t)c_{\text{bot}}l^2}(T_{\text{bot}}(t) - T_{\text{top}}(t)). \end{aligned}$$

The steady-state solution of the problem can be found by solving

$$\begin{aligned} \frac{2\dot{q}_{\text{top}}}{\rho_{\text{top}}c_{\text{top}}a} + \frac{k}{\rho_{\text{top}}c_{\text{top}}l^2}(T_{\text{bot}} - T_{\text{top}}) - \frac{60 \times \dot{m}L}{h_{\text{top}}\rho_{\text{top}}c_{\text{top}}} &= 0 \\ \text{and} \quad \frac{2\dot{q}_{\text{bot}}}{\rho_{\text{bot}}c_{\text{bot}}a} - \frac{k}{\rho_{\text{bot}}c_{\text{bot}}l^2}(T_{\text{bot}} - T_{\text{top}}) &= 0 \end{aligned}$$

which gives the temperature of the upper layer to be

$$T_{\text{top}} = \left\{ \frac{2(\dot{q}_{\text{top}} + \dot{q}_{\text{bot}})h_{\text{top}}}{a\lambda} \right\}^{1/1.6} + T_{\text{sat}}$$

and the temperature of the lower layer to be

$$T_{\text{bot}} = \frac{2\dot{q}_{\text{bot}}l^2}{ak} + \left\{ \frac{(\dot{q}_{\text{top}} + \dot{q}_{\text{bot}})h_{\text{top}}}{a\lambda} \right\}^{1/1.6} + T_{\text{sat}}$$

where

$$\lambda = 60 \times 2.88 \times 10^{-3}L.$$

The steady state solutions for case (1) are

$$T_{\text{top}} = 78.32\text{K}$$

$$T_{\text{bot}} = 86.58\text{K}$$

and for case (2) are

$$T_{\text{top}} = 77.90\text{K}$$

$$T_{\text{bot}} = 82.04\text{K}$$

Both the temperature of the upper and lower layers are higher for case (1) than for case (2). Although there is an absence of heat entering from the side of the vessel into the upper layer for the former case, the high heat flux into the lower layer must have a fairly significant effect on the temperature in the upper.

The new differential equations are again solved numerically for $T_{\text{top}}(t)$ and $T_{\text{bot}}(t)$ and the results are shown in Figures 2.7 and 2.8, with the experimental results superimposed for cases (1) and (2) respectively. Figure 2.7 shows the numerical solution of temperature for case (1). The rate of increase of the numerical solution of temperature for the lower layer has not changed noticeably. However, the temperature of the upper layer is far more accurate than that in Figure 2.3 for the 20 minute run. Similarly, although the accuracy of the numerical solution of the temperature of the lower layer for case (2), shown in Figure 2.8, has increased slightly, the main difference from Figure 2.4 is in the temperature of the upper layer which is now far closer to the temperature found experimentally.

The numerical results for the density of both the top and bottom layers are shown in Figures 2.9 and 2.10 for cases (1) and (2) respectively. The plot for case (1) shows that the density of the upper and lower layers are equal at the end of the 20 minute run, due to the slower rate of decrease of the density of the upper layer. Although the numerical solution for the density of the lower layer in case (2) has changed slightly, the more significant change in density is in the upper layer which again has a slower rate of decrease than that obtained using the original model, leaving less than a 0.5kgm^{-3} (0.06%) difference.

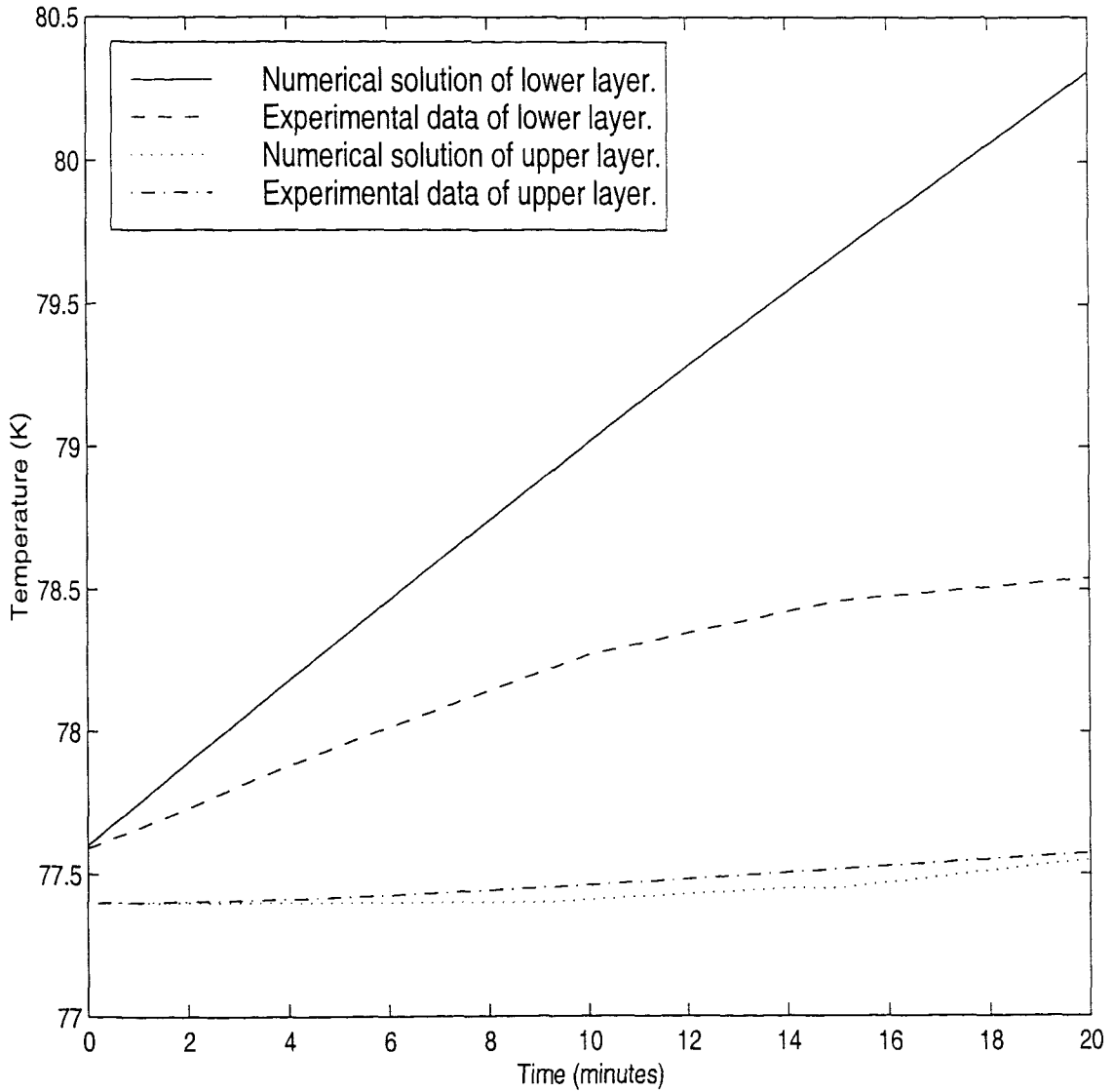


Figure 2.7: Comparison between the numerical solutions of the bulk temperatures of the upper and lower layers with the inclusion of evaporation, and those found experimentally for case (1).

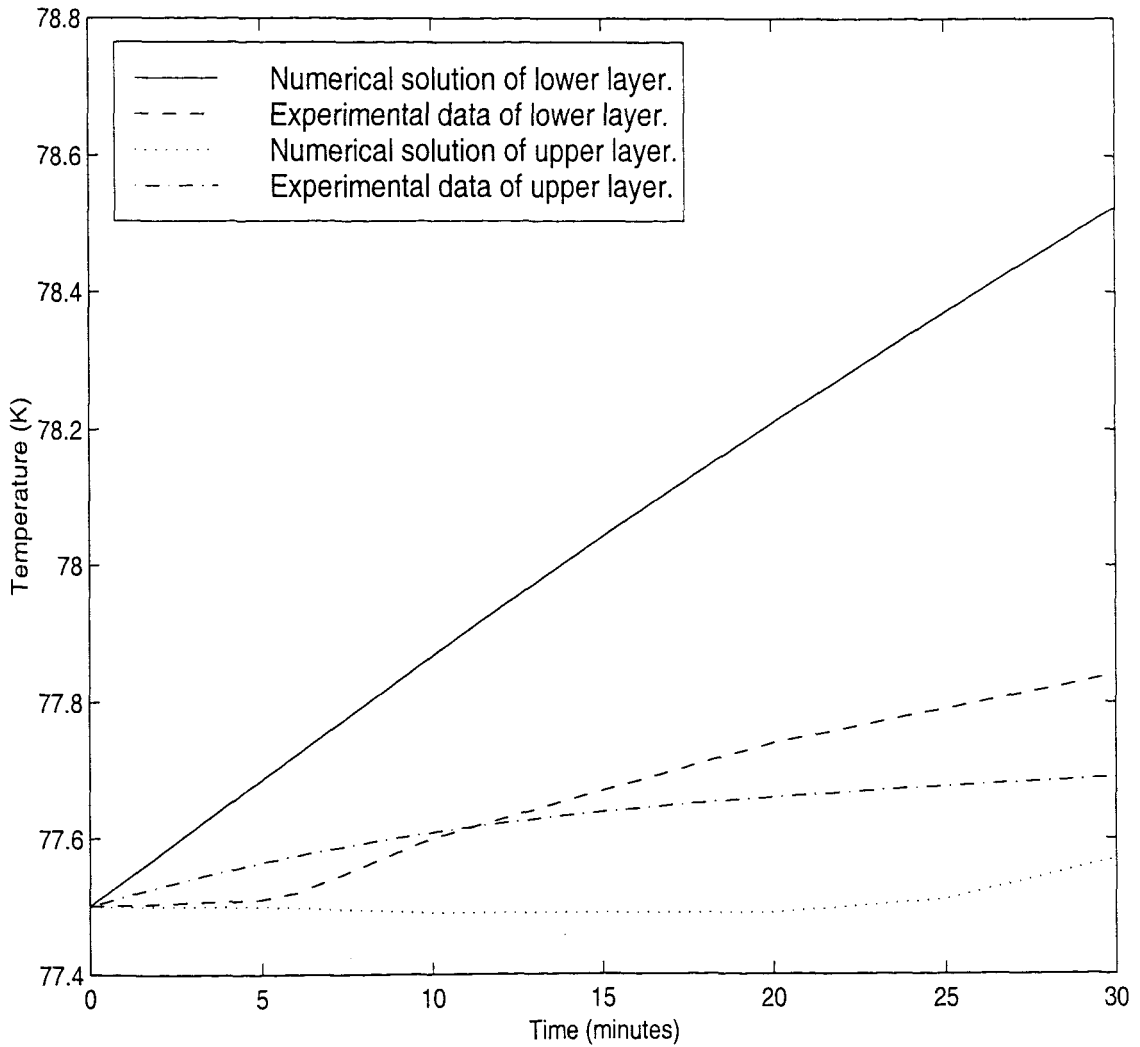


Figure 2.8: Comparison between the numerical solutions of the bulk temperatures of the upper and lower layers with the inclusion of evaporation, and those found experimentally for case (2).

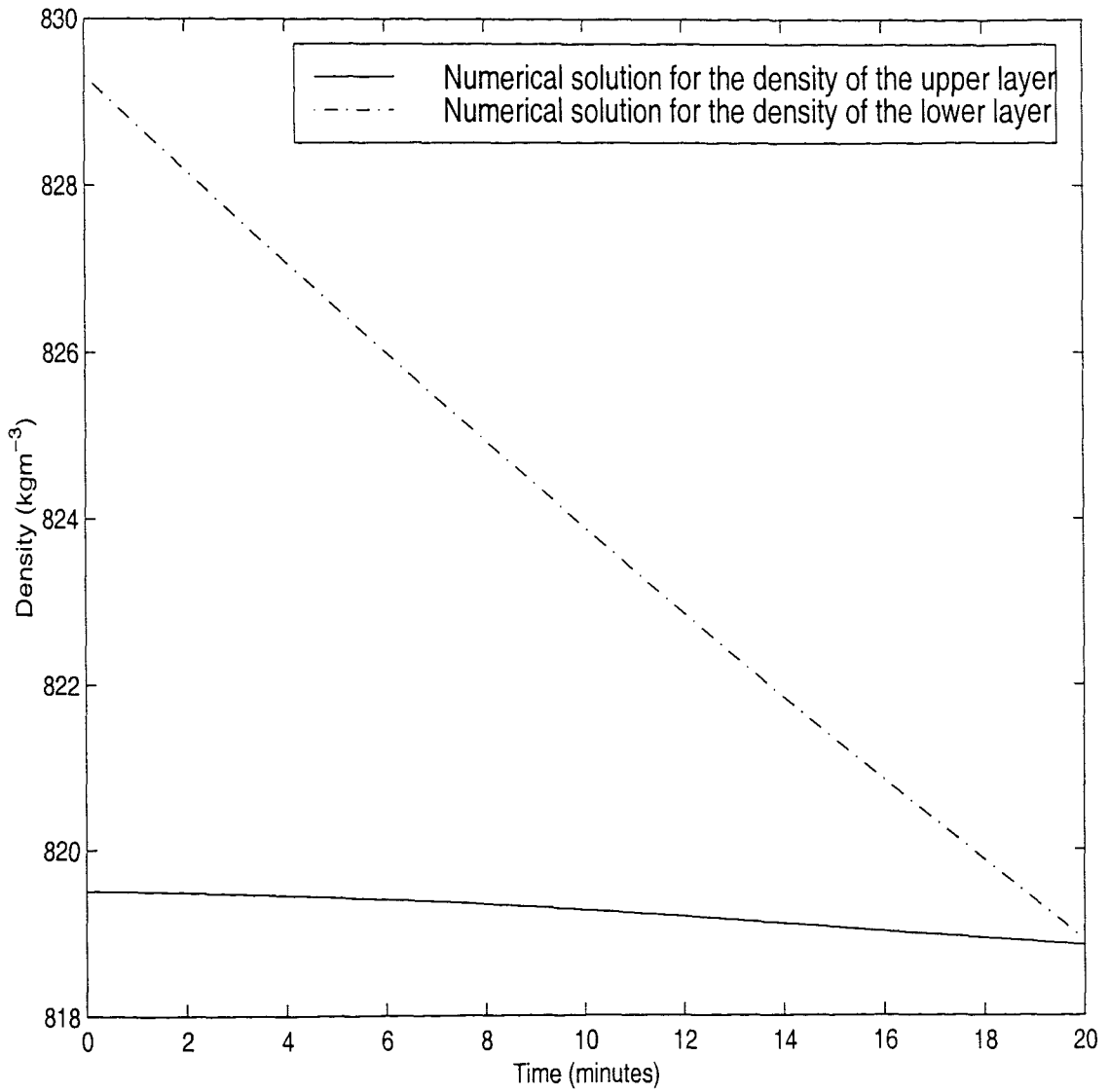


Figure 2.9: Numerical solutions of the bulk density of the upper and lower layers with the inclusion of evaporation for case (1).

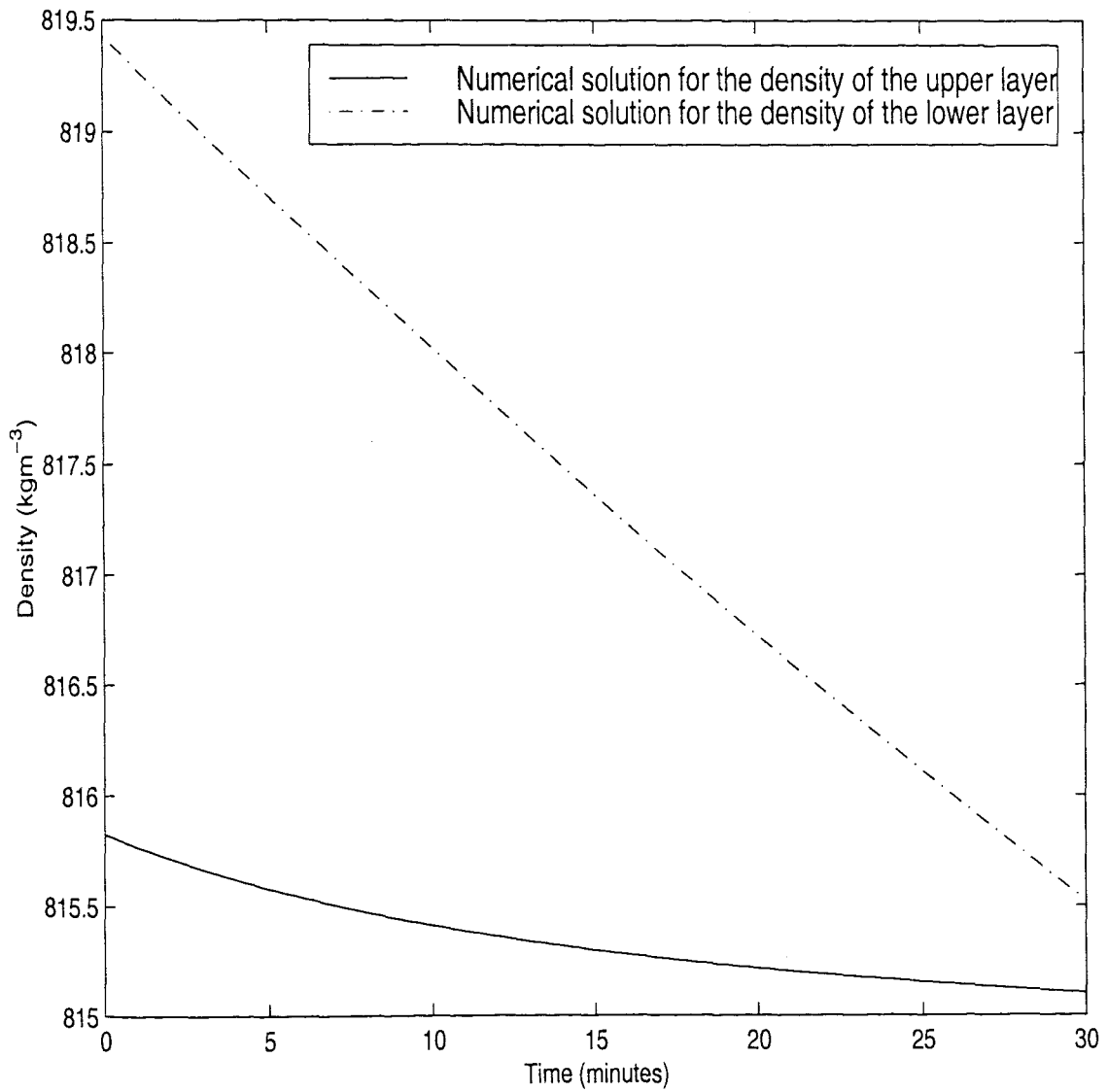


Figure 2.10: Numerical solutions of the bulk density of the upper and lower layers with the inclusion of evaporation for case (2).

2.2.3 Discussion of results with evaporation

The predictions obtained using the model with evaporation are far more accurate than those found previously. However, the lower layer is still hotter than the experiments suggest. This is largely due to the simple relationship of heat transfer between the layers. The temperature of the upper layer in turn should increase more rapidly because it should gain more heat from the lower layer but this will cause a higher temperature difference between the upper layer and the saturation temperature which will then increase the heat lost at the surface by evaporation.

2.3 Conclusions of Temperature Models for Rollover

In this chapter, we proposed and solved a simple mathematical model which examined the rate of increase of the bulk temperatures in two layers, due to heat entering the vessel and heat transfer by conduction between the layers. We found that the results were too high and included a term for the heat loss at the surface through evaporation in Section 2.2. The final model gave temperatures for the upper layer fairly close to those found experimentally, with all the numerical solutions for the temperature predicting the experimental data to within 1.5K for the run. With the ‘equal density’ theory, our numerical solutions for the densities of both layers at the end of the run time would suggest that rollover is just about to occur in case (1) but has not yet occurred in case (2). However, experimental results suggest that the rollover process has begun before this point in both cases thus indicating that ‘rollover’ is controlled by penetrative convection rather than a simple ‘equal density’ criterion.

Our model assumed that the concentrations in the two layers remain constant. However, concentration measurements over time for the two cases obtained by Agbabi(1987) show that the concentration of LOX in the lower layer decreases over time and that in the upper layer increases. This is due to entrainment of fluid from the lower layer to the upper layer and preferential evaporation of LIN at the surface leaving enriched LOX fluid. Changes in concentration will cause changes in density which were not included in our model. These effects will further increase the density of the upper layer, promoting a rollover situation.

Finally, the only method of heat transfer between the layers was assumed to be conduction. However, flow visualisation experiments by Atkinson-Barr(1989) have de-

scribed the interface developing an oscillatory form suggesting that heat is also transferred by convection. More detailed predictions of the processes involved could therefore be obtained by developing a model which included natural convection.

Chapter 3

Analytical Models Of Evaporation

In this chapter, we shall start by examining the ‘very thin’ surface region of the fluid more closely. The behaviour of this part of the fluid is likely to have a significant influence on evaporation and vice versa. Unlike in Chapter 2, where we considered the behaviour of two layers of fluid, here we will consider a single layer only.

This fluid is present in both its liquid and its gaseous form due to evaporation across a moving boundary. We shall determine the position of this moving boundary as part of the solution of the temperature distribution. Such problems are known as Stefan Problems (see Tayler, 1986, for more details). The stability of the solution will be assessed. Once the position of the moving boundary has been calculated, a mathematical equation for the mass flux at the surface can be found, which may be compared to that predicted from experimental data.

Having found the mass flux at the surface for a single fluid, we shall develop our work to model the behaviour of a two component fluid.

3.1 The Stefan Model

Experiments, such as Atkinson *et al.*(1984), show that cryogenic fluids, when stored in clean vessels, with a minimal number of nucleation sites, become superheated. This means that $T_{\text{bulk}} > T_{\text{sat}}$; where T_{bulk} is the temperature (K) of the bulk liquid underneath the surface layer and T_{sat} is the saturation temperature (K) of the fluid at the evaporating surface. This liquid surface is described from experimental studies using a combination of Schlieren flow visualisation and temperature measurements using a

micro-thermocouple ($25\mu\text{m}$ thick) by Beduz and Scurlock (1994) as being controlled by three delicate mechanisms within 5-10mm of the surface: molecular evaporation at the surface, thermal conduction in a thin liquid region $100\text{-}500\mu\text{m}$ thick with a steep temperature gradient and vortex convection lines in the liquid which form a radial pattern parallel to the surface.

In this section, we shall construct a model to describe the time and position dependent temperature distribution in the thermal conduction part of a one-component fluid. A Stefan condition will be imposed on the boundary. Using this model, we will evaluate the mass flux at the surface which will be compared to that estimated experimentally.

3.1.1 The One-Dimensional Stefan Condition

We begin by describing a simple example of a one-dimensional Stefan problem, that of melting ice, shown in Figure 3.1, in order to show the general method which will be used. The ice is at a temperature of 0°C on its boundary surface, $x = s(t)$. A heat flux, $-k_w\partial T_w/\partial x$, enters the shaded element in the diagram from the water phase and a heat flux, $-k_i\partial T_i/\partial x$ escapes into the ice, where k_w is the thermal conductivity ($\text{Wm}^{-1}\text{K}^{-1}$) of the water, $T_w(x, t)$ is the temperature (K) of the water, k_i is the thermal conductivity ($\text{Wm}^{-1}\text{K}^{-1}$) of the ice, and $T_i(x, t)$ is the temperature (K) of the ice.

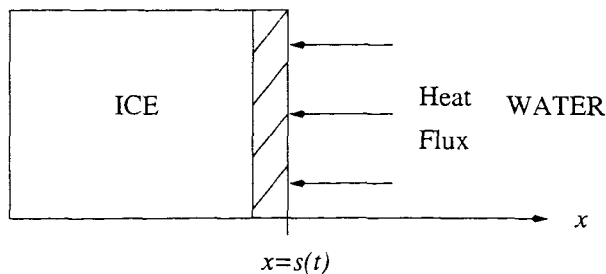


Figure 3.1: A simple example of the use of the Stefan condition - the problem of heat entering ice reproduced from Tayler(1986).

The heat flux absorbed by the shaded element

$$\begin{aligned}
 &= -k_w\partial T_w/\partial x - (-k_i\partial T_i/\partial x) \\
 &= k_i\partial T_i/\partial x - k_w\partial T_w/\partial x.
 \end{aligned} \tag{3.1}$$

This heat is used to melt the ice.

$$\text{But the heat used to melt the ice contained per unit area} = \rho_i \lambda \dot{s}(t) \quad (3.2)$$

where ρ_i is the density (kgm^{-3}) of the ice and λ is the latent heat of fusion (Jkg^{-1}).

So equating equations (3.1) and (3.2) gives

$$\rho_i \lambda \dot{s}(t) = k_i \frac{\partial T_i}{\partial x} - k_w \frac{\partial T_w}{\partial x}$$

and thus finally

$$\rho_i \lambda \dot{s}(t) = \left[k \frac{\partial T}{\partial x}(x, t) \right]_{x=s^-}^{x=s^+}.$$

This is known as the one-dimensional Stefan condition.

By an obvious generalization, the three-dimensional Stefan condition may be given as

$$[-k \nabla T]_{s^-}^{s^+} \cdot \nabla F = \rho \lambda \frac{\partial F}{\partial t}$$

where

$$F(x, y, z, t) = x - s(y, z, t).$$

and $s(y, z, t)$ is now the surface.

3.1.2 The Basic Unsteady, Stefan Problem

Now that we have derived the Stefan condition, we will apply the one-dimensional case to the problem of the conduction region of a liquid evaporating into freely convecting vapour above. Unlike general problems posed in this field, the boundary conditions in our situation are unclear. We shall discuss these in a moment but first we shall describe the flow in the two states.

In the vapour

We shall assume that the temperature in the vapour is uniform initially, at the saturation temperature of the fluid, T_{sat} . If we further assume that the pressure in the vapour remains constant, then T_{sat} does not change and the vapour may be assumed to remain at this temperature. Therefore we have

$$T_{\text{vp}}(x, t) = T_{\text{sat}}$$

where $T_{\text{vp}}(x, t)$ is the temperature (K) of the vapour.

In the thin conduction layer

Since there is no convection in this part of the fluid, the diffusion equation may be used to describe the temperature:

$$\rho_1 c_1 \frac{\partial T_1(x, t)}{\partial t} = k_1 \frac{\partial^2 T_1(x, t)}{\partial x^2},$$

where ρ_1 is the density (kgm^{-3}) of the liquid, c_1 is the specific heat capacity ($\text{Jkg}^{-1}\text{K}^{-1}$) of the liquid, k_1 is the thermal conductivity ($\text{Wm}^{-1}\text{K}^{-1}$) of the liquid and $T_1(x, t)$ is the temperature (K) of the liquid.

So

$$\frac{\partial T_1(x, t)}{\partial t} = \kappa_1 \frac{\partial^2 T_1(x, t)}{\partial x^2}$$

where $\kappa_1 = k_1/(\rho_1 c_1)$ is the thermal diffusivity (m^2s^{-1}) of the fluid.

Initial and Boundary conditions

We shall now discuss the initial and boundary conditions for the liquid phase. At the surface, the liquid is at a fixed temperature, known as the saturation temperature.

$$T_1(s(t), t) = T_{\text{sat}}, \quad \text{for } t > 0.$$

An initial condition is placed on the surface

$$s(0) = 0.$$

We know that below the thin conduction region, convection exists which maintains the bulk of the liquid at the uniform and constant temperature, T_{bulk} . However it is unclear if

1. the bulk temperature is fixed far away from the evaporating surface, such that

$$T_1(-\infty, t) = T_{\text{bulk}}$$

2. the bulk temperature remains a certain fixed distance from the moving surface, such that

$$T_1(s(t) - d, t) = T_{\text{bulk}}$$

where d is the thickness of the conduction region.

We shall consider boundary condition 1 in 3.1.3 and 3.1.4 and boundary condition 2 in 3.1.5. Finally, we have the Stefan condition at the boundary:

$$\rho_1 L \dot{s} = \left(-k_{vp} \frac{\partial T_{vp}(x, t)}{\partial x} + k_1 \frac{\partial T_1(x, t)}{\partial x} \right) \Big|_{x=s(t)}$$

where L is the latent heat of vaporisation (Jkg^{-1}) of the liquid and k_{vp} is the thermal conductivity ($\text{Wm}^{-1}\text{K}^{-1}$) of the fluid. But $T_{vp} = T_{\text{sat}}$ so

$$\rho_1 L \dot{s} = k_1 \frac{\partial T_1(x, t)}{\partial x} \Big|_{x=s(t)}$$

3.1.3 Similarity solution

Examining the diffusion equation, it is evident that a similarity solution exists (Dewynne *et al.*, 1989). Suppose $T_1(x, t) - T_{\text{sat}} = F(\eta)$ where $\eta = x/(2\sqrt{t})$ and $s(t) = -2\beta\sqrt{t}$ where β is a positive constant. Then $\eta \leq 0$ since $x \leq 0$.

We have

$$\begin{aligned} \frac{\partial T_1(x, t)}{\partial t} &= \frac{-xt^{-3/2}}{4} F'(\eta) \\ &= \kappa_1 \frac{\partial^2 T_1(x, t)}{\partial x^2} \\ &= \frac{\kappa_1}{4t} F''(\eta). \end{aligned}$$

So the diffusion equation becomes

$$\kappa_1 F''(\eta) + 2\eta F'(\eta) = 0.$$

Now let $G(\eta) = F'(\eta)$. Then we can solve for $G(\eta)$ to find that

$$G(\eta) = A \exp\left(-\frac{\eta^2}{\kappa_1}\right).$$

Therefore

$$F(\eta) = \int_0^\eta A \exp(-\eta^2/\kappa_1) d\eta + B$$

with the following initial and boundary conditions:

$$F(-\infty) = T_{\text{bulk}} - T_{\text{sat}} \tag{3.3}$$

$$\text{and } F(-\beta) = 0. \tag{3.4}$$

From equation (3.3)

$$B = T_{\text{bulk}} - T_{\text{sat}} + A \frac{\sqrt{\pi \kappa_1}}{2}$$

and so

$$F(\eta) = \int_0^\eta A \exp\left(\frac{-\eta^2}{\kappa_1}\right) d\eta + T_{\text{bulk}} - T_{\text{sat}} + A \frac{\sqrt{\pi \kappa_1}}{2}.$$

Also from equation (3.4),

$$A = -\frac{2}{\sqrt{\pi \kappa_1}} \frac{(T_{\text{bulk}} - T_{\text{sat}})}{(1 - \text{erf}(\beta/\sqrt{\kappa_1}))}$$

where the error function $\text{erf}(\mu)$ is defined by

$$\text{erf}(\mu) = \frac{2}{\sqrt{\pi}} \int_0^\mu \exp(-t^2) dt.$$

Thus

$$F(\eta) = T_{\text{bulk}} - T_{\text{sat}} - \frac{(T_{\text{bulk}} - T_{\text{sat}})}{(1 - \text{erf}(\beta/\sqrt{\kappa_1}))} (1 - \text{erf}(-\eta/\sqrt{\kappa_1})).$$

So we obtain the following temperature distribution

$$T_1(x, t) = T_{\text{bulk}} - \frac{(T_{\text{bulk}} - T_{\text{sat}})}{(1 - \text{erf}(\beta/\sqrt{\kappa_1}))} (1 - \text{erf}(-\eta/\sqrt{\kappa_1})).$$

Now from the Stefan condition,

$$-\rho_1 L \frac{\beta}{\sqrt{t}} = \frac{-k_1}{2\sqrt{t}} \frac{2(T_{\text{bulk}} - T_{\text{sat}})}{\sqrt{\pi \kappa_1}} \exp\left(-\frac{(-2\beta\sqrt{t})^2}{(2\sqrt{t})^2 \kappa_1}\right).$$

Therefore, the temperature in the thin conduction layer is described by

$$T_1(x, t) = T_{\text{bulk}} - \frac{(T_{\text{bulk}} - T_{\text{sat}})}{(1 - \text{erf}(\beta/\sqrt{\kappa_1}))} \text{erfc}(-\eta/\sqrt{\kappa_1})$$

where

$$\beta \text{erfc}(\beta/\sqrt{\kappa_1}) = \frac{k_1}{\rho_1 L \sqrt{\pi \kappa_1}} (T_{\text{bulk}} - T_{\text{sat}}) \exp(-\beta^2/\kappa_1) \quad (3.5)$$

and the complementary error function $\text{erfc}(\mu)$ is defined by

$$\text{erfc}(\mu) = 1 - \text{erf}(\mu).$$

The similarity solution used to find the temperature is valid only when the transcendental equation for β has a real solution. Let us suppose that $\lambda = \beta/\sqrt{\kappa_1}$. Then since $\beta > 0$, λ must be a positive constant.

Equation (3.5) would then become

$$\lambda \text{erfc}(\lambda) = \frac{\text{St}}{\sqrt{\pi}} e^{-\lambda^2} \quad (3.6)$$

where St is the Stefan number defined as

$$\begin{aligned} St &= \frac{c_l}{L}(T_{\text{bulk}} - T_{\text{sat}}) \\ &> 0 \text{ for superheated liquids.} \end{aligned}$$

Suppose

$$f(\lambda) = \lambda \operatorname{erfc}(\lambda) - \frac{St}{\sqrt{\pi}} e^{-\lambda^2}. \quad (3.7)$$

Then if there exists a λ for which $f(\lambda) = 0$, a solution for β exists and so the similarity solution is valid.

Now

$$\begin{aligned} f(0) &= -\frac{St}{\sqrt{\pi}} \\ &< 0 \text{ for superheated liquids.} \end{aligned}$$

So if there is a λ for which $f(\lambda) > 0$, then the function must be zero at some point. We can see that the optimal way to search for a solution is to solve the problem graphically, finding the value of the function at its stationary points and inspecting the gradient of $f(\lambda)$ over the domain.

$$\begin{aligned} f'(\lambda) &= \operatorname{erfc}(\lambda) + (St - 1) \frac{2\lambda}{\sqrt{\pi}} e^{-\lambda^2} \\ &= 0 \quad \text{at a stationary point.} \end{aligned}$$

So we shall divide the problem into three cases which are dependent on the Stefan number.

When $St > 1$:

The constraint is that

$$\lambda \operatorname{erfc}(\lambda) < \frac{1}{\sqrt{\pi}} e^{-\lambda^2}$$

and the stationary points can be found when

$$\operatorname{erfc}(\lambda) = -(St - 1) \frac{2\lambda}{\sqrt{\pi}} e^{-\lambda^2}.$$

But $\operatorname{erfc}(\lambda) \geq 0$ and $-(St - 1)2\lambda e^{-\lambda^2}/\sqrt{\pi} \leq 0$, for all λ in the domain so the only possible solution to this equation is when

$$\begin{aligned}\operatorname{erfc}(\lambda) &= -(St - 1)\frac{2\lambda}{\sqrt{\pi}}e^{-\lambda^2} \\ &= 0.\end{aligned}$$

Thus, the only stationary point is at $\lambda = \infty$ when $f(\lambda) = 0$. Also, $f'(\lambda) > 0$ for all λ in the domain given, except at $\lambda = \infty$. With this λ , the liquid would instantly evaporate. Excluding this case, there is no solution of the transcendental equation with $St > 1$.

When $St=1$:

The transcendental equation can be written as

$$\lambda \operatorname{erfc}(\lambda) = \frac{1}{\sqrt{\pi}} e^{-\lambda^2}$$

and

$$\begin{aligned}f'(\lambda) &= \operatorname{erfc}(\lambda) \\ &= 0 \quad \text{at a stationary point.}\end{aligned}$$

Then, again, the only stationary point of this function is at $\lambda = \infty$ when $f(\lambda) = 0$. Also $f'(\lambda) > 0$ for all λ in the domain given, except at $\lambda = \infty$. So, similarly to the previous case, excluding the case where all the fluid evaporates instantly, there is no solution of the transcendental equation with $St=1$.

When $St < 1$:

Since $f(0) < 0$ and $f(\lambda)$ is monotonically increasing, there is one and only one solution of λ . Figure 3.2 shows a graph of equation (3.7) with $f(\lambda) = 0$.

From this analysis we see that there is only a solution to the transcendental equation when $St < 1$. The temperature distribution for the conduction layer is thus only valid when $St < 1$. For $St \geq 1$, the fluid will evaporate instantly. In fact, considering the case for $St \geq 1$, since $c_1 = O(10^3) \text{Jkg}^{-1}\text{K}^{-1}$ and $L = O(10^5) \text{Jkg}^{-1}$, we would require the difference between the temperature in the bulk of the fluid and the saturation

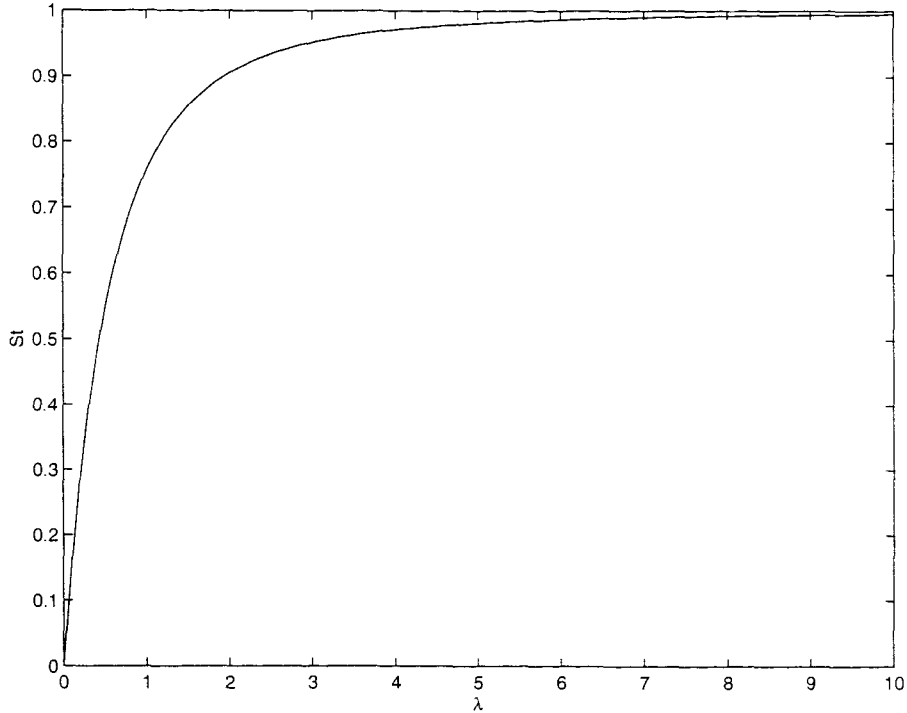


Figure 3.2: Graph of the Stefan number against λ for $f(\lambda) = 0$.

temperature to be 100K which would not be possible in practice as there are always some nucleation sites, even in the cleanest of vessels, which would cause boiling. Since $T_{\text{bulk}} - T_{\text{sat}}$ is typically at most 10K for cryogenic fluids, $St < 1$.

Before calculating an equation for the mass flux at the surface from this model, we shall discuss the stability of the problem.

The stability of the similarity solution

In experiments (e.g. Beduz *et al.*, 1984), a single correlation is found to model the mass flux over all time for each cryogenic fluid. To obtain a similar theoretical equation for the mass flux, we require our solutions of the temperature distribution and the position of the surface to be stable.

The stability of the similarity solution used to find the temperature distribution and the position of the surface for $0 < St < 1$ is discussed next, to see whether the model is capable of damping out small perturbations to which any physical system is subjected. This stability analysis can be directly compared to that of the temperature of a melting solid, as discussed by Chadam and Ortoleva(1983) and Strain(1988).

Chadam and Ortoleva(1983) made a change of variables such that the form of the equations in the stability proof were similar to those treated by Rubinstein(1982), whereby they were able to show that planar melting is asymptotically stable. Therefore the temperature distribution and the position of the surface found is stable for the problem.

Calculating a mass flux equation for the model found using a similarity solution

Now that we know that the temperature distribution is stable for $St < 1$, we shall return to the original problem in order to calculate the mass flux at the surface for $St < 1$. To find this, we require β , since the time-dependent position of the surface is determined by

$$s(t) = -2\beta t^{1/2}. \quad (3.8)$$

Assuming that λ is small, which is justified if the storage vessel is well insulated (daily loss of liquid would be approximately 0.5%), we may expand equation (3.6) as a series such that, up to $O(\lambda^2)$,

$$\lambda \left(1 - \frac{2}{\sqrt{\pi}} \lambda\right) = \frac{St}{\sqrt{\pi}} (1 - \lambda^2).$$

Solving this for β yields the solutions

$$\beta_1 = \frac{\sqrt{\kappa_1 \pi} \left(-1 + \sqrt{1 + 4St(St - 2)/\pi}\right)}{2(St - 2)}$$

and

$$\beta_2 = \frac{\sqrt{\kappa_1 \pi} \left(-1 - \sqrt{1 + 4St(St - 2)/\pi}\right)}{2(St - 2)}$$

Both these solutions for β in equation 3.8 give reasonable physical solutions for the position of the surface.

So the two equations for the mass flux at the surface from this method are

$$\begin{aligned} \dot{m} &= -\rho_1 \dot{s} \\ &= -\frac{\rho_1 \beta_1}{\sqrt{t}}, -\frac{\rho_1 \beta_2}{\sqrt{t}} \end{aligned}$$

where ρ_1 is the density of the fluid.

Unfortunately, this model does not predict the time-independent mass flux correlation found experimentally. We are able, however to make an averaged comparison of the

mass flux over a certain length of time. Given that we have two solutions for the mass flux at the surface, we shall calculate two average mass fluxes over an hour, M_1 and M_2 .

Thus

$$\begin{aligned} M_1 &= -\frac{1}{3600} \int_0^{3600} \frac{\rho_1 \beta_1}{\sqrt{t}} dt \\ &= -\frac{\rho_1 \beta_1}{30} \end{aligned}$$

and

$$\begin{aligned} M_2 &= -\frac{1}{3600} \int_0^{3600} \frac{\rho_1 \beta_2}{\sqrt{t}} dt \\ &= -\frac{\rho_1 \beta_2}{30}. \end{aligned}$$

For LNG (assuming a high concentration of liquid methane), $L \approx 5 \times 10^5 \text{Jkg}^{-1}$, $\rho_l \approx 425 \text{kgm}^{-3}$, $\kappa_l \approx 1.32 \times 10^{-7} \text{m}^2 \text{s}^{-1}$ and $c_l \approx 3.45 \times 10^3 \text{Jkg}^{-1} \text{K}^{-1}$. So, for a temperature difference of 2K (a typical value in the experiments of Rebiai, 1985), we find that

$$M_1 = -4.0 \times 10^{-5} \text{kgm}^{-2} \text{s}^{-1}$$

and

$$M_2 = -0.0046 \text{kgm}^{-2} \text{s}^{-1}.$$

The experimental equation for the mass flux for LNG is given (Beduz and Scurlock, 1995) as

$$\dot{m} = -1.7 \times 10^{-3} (T_{\text{bulk}} - T_{\text{sat}}) \text{kgm}^{-2} \text{s}^{-1}$$

such that with the conditions stated above

$$\dot{m} = -0.0034 \text{kgm}^{-2} \text{s}^{-1}.$$

This value compares well to the average mass flux, M_2 , found theoretically with β_2 . Although our model agrees well with experiments, the form of the solution suggests that we must consider the case $t \rightarrow 0$. It may be better therefore to disregard $t \rightarrow 0$ and look at the long-term behaviour of the fluid. We will therefore search for a travelling wave solution to the problem next. This type of solution will also give a mass flux equation which is independent of time so we will be able to make a direct comparison with experimental data.

3.1.4 Travelling wave solution

We will now search for a travelling wave solution to describe the long-term behaviour of the temperature distribution and the position of the moving boundary in the thin conduction region of the fluid. Suppose $T_1 = f(z)$ where $z = x + Vt$ and $s(t) = -Vt$, where V is the positive velocity (ms^{-1}) of the wave. Substituting this into the diffusion equation, we obtain

$$Vf'(z) = \kappa_1 f''(z).$$

Integrating this, we find that

$$f(z) = A + Be^{Vz/\kappa_1},$$

where A and B are constants of integration.

The boundary conditions applied on $f(z)$ become

$$f(0) = T_{\text{sat}}, \quad (3.9)$$

$$f(-\infty) = T_{\text{bulk}}, \quad (3.10)$$

$$\text{and the Stefan condition, } -\rho_1 LV = k_1 f'(z)|_{z=-Vt}. \quad (3.11)$$

Equation (3.10) gives

$$A = T_{\text{bulk}}$$

and, from equation (3.9), we obtain

$$B = T_{\text{sat}} - T_{\text{bulk}}.$$

Thus

$$f(z) = T_{\text{bulk}} - (T_{\text{bulk}} - T_{\text{sat}})e^{Vz/\kappa_1}$$

and so the temperature is described by

$$T_1(x, t) = T_{\text{bulk}} - (T_{\text{bulk}} - T_{\text{sat}})e^{V(x+Vt)/\kappa_1}.$$

Substituting this into the Stefan condition (3.11), we get

$$-\rho_1 LV = -\frac{k_1 V}{\kappa_1} (T_{\text{bulk}} - T_{\text{sat}}) \exp\left(\frac{V}{\kappa_1}(-Vt + Vt)\right).$$

So

$$T_{\text{bulk}} - T_{\text{sat}} = \frac{L}{c_1}.$$

But the Stefan number is defined by

$$\text{St} = \frac{c_1(T_{\text{bulk}} - T_{\text{sat}})}{L}$$

and so this travelling wave solution is only valid for the case $\text{St}=1$. Unfortunately the mass flux cannot be determined for this model since we cannot obtain any information about V , the speed with which the surface moves downward.

Although we are not generally interested in this Stefan number for our work (the Stefan numbers of the cryogenic fluids which we are investigating are less than unity) we will follow this work through and again examine the stability of the solution.

Examining the stability of the travelling wave solution

We will now examine the stability of the one-dimensional travelling wave solution for the Stefan problem with the Stefan number, $\text{St}=1$, in order to see whether the solution, found above, is valid when the problem is subjected to small perturbations of order ϵ , that exist in any physical system. Suppose

$$s(y, t) = -Vt + \epsilon e^{\sigma t} \sin ny$$

and

$$\begin{aligned} T_1(x, y, t) &= T_0(x, t) + \epsilon T_1(x, y, t) \\ &= T_{\text{bulk}} - (T_{\text{bulk}} - T_{\text{sat}}) \exp\left(\frac{V}{\kappa_1}(x + Vt)\right) + \epsilon a e^{\sigma t + p(x + Vt)} \sin ny \end{aligned}$$

where $\epsilon \ll 1$ and $n > 0$. If $p < V/\kappa_1$, the perturbations will remain small compared to the undisturbed solutions for large $(x + Vt)$.

The diffusion equation with the perturbations becomes

$$\frac{\partial T_0(x, t)}{\partial t} + \epsilon \frac{\partial T_1(x, y, t)}{\partial t} = \kappa_1 \left(\frac{\partial^2 T_0(x, t)}{\partial x^2} + \epsilon \frac{\partial^2 T_1(x, y, t)}{\partial x^2} + \epsilon \frac{\partial^2 T_1(x, y, t)}{\partial y^2} \right),$$

and with the substitutions for T_0 and T_1 , we get

$$\begin{aligned} \rho_1 c_1 \left\{ -\frac{(T_{\text{bulk}} - T_{\text{sat}})}{\kappa_1} V^2 \exp\left(\frac{V}{\kappa_1}(x + Vt)\right) + \epsilon a(\sigma + pV) e^{\sigma t + p(x + Vt)} \sin ny \right\} = \\ \kappa_1 \left\{ -\frac{V^2}{\kappa_1^2} (T_{\text{bulk}} - T_{\text{sat}}) \exp\left(\frac{V}{\kappa_1}(x + Vt)\right) \right. \\ \left. + \epsilon a p^2 e^{\sigma t + p(x + Vt)} \sin ny - \epsilon n^2 a e^{\sigma t + p(x + Vt)} \sin ny \right\}. \end{aligned}$$

So

$$\sigma + pV = \kappa_1(p^2 - n^2). \quad (3.12)$$

The boundary conditions for the problem are

$$T_0(-\infty, t) + \varepsilon T_1(-\infty, y, t) = T_{\text{bulk}} \quad (3.13)$$

$$T_0(s(y, t), t) + \varepsilon T_1(s(y, t), y, t) = T_{\text{sat}} \quad (3.14)$$

$$\text{and the Stefan condition } [-k\nabla T]_1^v \cdot \nabla F = -\rho_1 L \frac{\partial F}{\partial t} \quad (3.15)$$

$$\text{where } F(x, y, t) = x - s(y, t) \text{ on } x = s(y, t).$$

So from equation (3.13),

$$\begin{aligned} T_1(-\infty, y, t) &= \lim_{x \rightarrow -\infty} a e^{\sigma t + p(x + Vt)} \sin ny \\ &= 0 \end{aligned}$$

and from equation (3.14),

$$T_{\text{bulk}} - (T_{\text{bulk}} - T_{\text{sat}}) \exp\left(\frac{V}{\kappa_1} \varepsilon e^{\sigma t} \sin ny\right) + \varepsilon a e^{\sigma t} \exp\left(\varepsilon p e^{\sigma t} \sin ny\right) \sin ny = T_{\text{sat}}$$

from which we obtain

$$a = \frac{V(T_{\text{bulk}} - T_{\text{sat}})}{\kappa_1}.$$

But since the Stefan number is unity for this travelling wave solution,

$$\begin{aligned} (T_{\text{bulk}} - T_{\text{sat}}) &= \frac{\kappa_1 a}{V} \\ &= \frac{L}{c_1}. \end{aligned}$$

Therefore

$$a = \frac{VL}{\kappa_1 c_1}.$$

Finally from the Stefan condition (3.15), we get

$$\begin{aligned} \rho_1 L(-V + \varepsilon \sigma e^{\sigma t} \sin ny) &= k_1 \left\{ -\frac{V(T_{\text{bulk}} - T_{\text{sat}})}{\kappa_1} \exp\left(\frac{V}{\kappa_1} \varepsilon e^{\sigma t} \sin ny\right) \right. \\ &\quad \left. + \varepsilon a p e^{\sigma t} \exp(\varepsilon p e^{\sigma t} \sin ny) \sin ny \right\} \end{aligned}$$

which simplifies to

$$\rho_1 L \sigma = -\frac{V k_1}{\kappa_1} a + a p k_1. \quad (3.16)$$

Substituting σ from equation (3.12) into equation (3.16) yields,

$$\rho_1 L(\kappa_1(p^2 - n^2) - pV) = -\frac{Vk_1}{\kappa_1}a + apk_1.$$

Expanding this and simplifying gives,

$$(\kappa_1 p - V)^2 = \kappa_1^2 n^2.$$

Therefore

$$\kappa_1 p - V = \pm \kappa_1 n$$

and so

$$p = \frac{V}{\kappa_1} - n \text{ since } p < \frac{V}{\kappa_1}.$$

Substituting this solution into equation (3.16) gives

$$\sigma = -Vn.$$

Therefore

$$\begin{aligned} T_1(x, y, t) = & T_{\text{bulk}} - (T_{\text{bulk}} - T_{\text{sat}}) \exp\left(\frac{V}{\kappa_1}(x + Vt)\right) \\ & + \epsilon \frac{VL}{\kappa_1 c_1} e^{-Vnt} \exp\left(\left(\frac{V}{\kappa_1} - n\right)(x + Vt)\right) \sin ny \end{aligned}$$

and

$$s(y, t) = -Vt + \epsilon e^{-Vnt} \sin ny.$$

So, since σ is negative, if $V > 0$ as in the problem posed, any small disturbances will decay with time and the plane phase-change surface can be considered to be stable. Thus for a Stefan number of 1, there is a stable temperature distribution

$$T_1(x, t) = T_{\text{bulk}} - (T_{\text{bulk}} - T_{\text{sat}})e^{V(x+Vt)/\kappa_1}$$

and a stable equation for the position of the surface

$$s(y, t) = -Vt$$

The travelling wave solution gave the required form for the position of the surface such that we could have made a qualitative comparison with experimental results. However, the solution gave no information about the velocity of the surface since it was removed from the problem. We will next examine the other possible boundary condition, described in 3.1.2.

3.1.5 The unsteady Stefan problem with a different boundary condition

Although 3.1.3 and 3.1.4 have both produced reasonable models for the flow in the fluid, we shall now discuss the possibility of a different boundary condition

$$T_1(s(t) - d, t) = T_{\text{bulk}}$$

which may be even more realistic. We shall again examine the long-term behaviour of the fluid and therefore search for a travelling wave solution of the form $T_1 = f(\eta)$ where $\eta = x - At$ and $s(t) = At$, where A is the negative velocity (ms^{-1}) of the wave. The problem may be written as:

$$\rho_1 c_1 \frac{T_1(x, t)}{\partial t} = k_1 \frac{\partial^2 T_1(x, t)}{\partial x^2}$$

with boundary conditions:

$$T_1(s(t), t) = T_{\text{sat}}, \quad t > 0 \quad (3.17)$$

$$\text{the Stefan condition, } \rho_1 L \dot{s} = k_1 \left. \frac{\partial T_1(x, t)}{\partial x} \right|_{x=s(t)} \quad (3.18)$$

$$\text{and } T_1(s(t) - d, t) = T_{\text{bulk}} \quad (3.19)$$

where, as before, we shall assume that

$$T_{\text{vp}} = T_{\text{sat}}.$$

The diffusion equation becomes

$$-Af'(\eta) = \kappa_1 f''(\eta)$$

and so

$$f(\eta) = \alpha e^{-A\eta/\kappa_1} + \beta$$

where α and β are constants of integration.

Therefore

$$T_1(x, t) = \alpha \exp\left(-\frac{A}{\kappa_1}(x - At)\right) + \beta.$$

Using condition (3.17), we get

$$\alpha + \beta = T_{\text{sat}}.$$

So

$$T_1(x, t) = \alpha \exp\left(\frac{-A}{\kappa_1}(x - At)\right) + T_{\text{sat}} - \alpha.$$

and from the new boundary condition (3.19),

$$\alpha \exp\left(\frac{Ad}{\kappa_1}\right) - \alpha = T_{\text{bulk}} - T_{\text{sat}}.$$

So

$$T_1(x, t) = \frac{(T_{\text{bulk}} - T_{\text{sat}})}{(\exp(Ad/\kappa_1) - 1)} \left\{ \exp\left(-\frac{A}{\kappa_1}(x - At)\right) - 1 \right\} + T_{\text{sat}}.$$

Finally, from the Stefan condition (3.18), we obtain

$$\rho_1 L \dot{s} = k_1 \frac{\partial T_1(x, t)}{\partial x} \Big|_{x=s(t)}$$

which gives,

$$\rho_1 LA = \frac{-kA}{\kappa_1} \frac{(T_{\text{bulk}} - T_{\text{sat}})}{\exp(Ad/\kappa_1) - 1}.$$

So

$$\exp\left(\frac{Ad}{\kappa_1}\right) - 1 = -\text{St}.$$

Therefore

$$\frac{Ad}{\kappa_1} = \ln\left(1 - \frac{c_1}{L}(T_{\text{bulk}} - T_{\text{sat}})\right).$$

This solution is only valid if

$$1 - \frac{c_1}{L}(T_{\text{bulk}} - T_{\text{sat}}) > 0$$

and so

$$\text{St} < 1.$$

For our situation, St is calculated to be $\approx 10^{-2}$. For small x, $\ln(1 - x)$ may be written as a series and so can be approximated to $\ln(1 - x) \approx -x$. With this we find that

$$A = -\frac{\kappa_1 c_1}{dL}(T_{\text{bulk}} - T_{\text{sat}}).$$

So

$$s(t) = \frac{-\kappa_1 c_1}{dL}(T_{\text{bulk}} - T_{\text{sat}})t. \quad (3.20)$$

Stability of the travelling wave solution for the problem with a different boundary condition

We will now examine the stability of the one-dimensional travelling wave solution, in order to see whether the new model is valid when the problem is subjected to small perturbations, that exist in any physical system. Suppose

$$s(y, t) = At + \epsilon e^{\sigma t} \sin ny$$

and

$$\begin{aligned} T_1(x, y, t) &= T_0(x, t) + \epsilon T_1(x, y, t) \\ &= T_{\text{sat}} + \frac{(T_{\text{bulk}} - T_{\text{sat}})}{(\exp(Ad/\kappa_l) - 1)} \left\{ \exp\left(-\frac{A}{\kappa_l}(x - At)\right) - 1 \right\} \\ &\quad + \epsilon a e^{\sigma t + p(x - At)} \sin ny \end{aligned}$$

where $\epsilon \ll 1$ and $n > 0$. The diffusion equation with the perturbations becomes

$$\frac{\partial T_0(x, t)}{\partial t} + \epsilon \frac{\partial T_1(x, y, t)}{\partial t} = \kappa_l \left(\frac{\partial^2 T_0(x, t)}{\partial x^2} + \epsilon \frac{\partial^2 T_1(x, y, t)}{\partial x^2} + \epsilon \frac{\partial^2 T_1(x, y, t)}{\partial y^2} \right),$$

and with the substitutions for T_0 and T_1 , we get

$$\begin{aligned} &\left\{ -\frac{(T_{\text{bulk}} - T_{\text{sat}})A^2}{\kappa_l(\exp(Ad/\kappa_l) - 1)} \exp\left(-\frac{A}{\kappa_l}(x - At)\right) + \epsilon a(\sigma - pA)e^{\sigma t + p(x - At)} \sin ny \right\} = \\ &\kappa_l \left\{ \frac{A^2}{\kappa_l^2(\exp(Ad/\kappa_l) - 1)} (T_{\text{bulk}} - T_{\text{sat}}) \exp\left(-\frac{A}{\kappa_l}(x - At)\right) \right. \\ &\quad \left. + \epsilon a p^2 e^{\sigma t + p(x - At)} \sin ny - \epsilon n^2 a e^{\sigma t + p(x - At)} \sin ny \right\}. \end{aligned}$$

So

$$\sigma - pA = \kappa_l(p^2 - n^2). \quad (3.21)$$

The boundary conditions for the problem are

$$T_0(s(y, t) - d, t) + \epsilon T_1(s(y, t), y, t) = T_{\text{bulk}} \quad (3.22)$$

$$T_0(s(y, t), t) + \epsilon T_1(s(y, t), y, t) = T_{\text{sat}} \quad (3.23)$$

$$\text{and the Stefan condition } [-k\nabla T]_1^y \cdot \nabla F = -\rho_l L \frac{\partial F}{\partial t} \quad (3.24)$$

$$\text{where } F(x, y, t) = x - s(y, t) \text{ on } x = s(y, t).$$

So from equation (3.22),

$$\begin{aligned} &\frac{(T_{\text{bulk}} - T_{\text{sat}})}{(\exp(Ad/\kappa_l) - 1)} \left\{ e^{Ad/\kappa_l} \exp\left(-\frac{A}{\kappa_l}(\epsilon e^{\sigma t} \sin ny)\right) - 1 \right\} + T_{\text{sat}} \\ &\quad + \epsilon a e^{(\sigma t - pd)} \exp(\epsilon p e^{\sigma t} \sin ny) \sin ny = T_{\text{bulk}} \end{aligned}$$

from which we find that

$$ae^{-pd} = \frac{(T_{\text{bulk}} - T_{\text{sat}})A}{\kappa_1(\exp(Ad/\kappa_1) - 1)} e^{Ad/\kappa_1}. \quad (3.25)$$

Also from equation (3.23),

$$\begin{aligned} T_{\text{sat}} &+ \frac{(T_{\text{bulk}} - T_{\text{sat}})}{\kappa_l} \left\{ \exp\left(-\frac{A}{\kappa_l} \epsilon e^{\sigma t} \sin ny\right) - 1 \right\} \\ &+ \epsilon a e^{\sigma t} \exp(\epsilon p e^{\sigma t} \sin ny) \sin ny = T_{\text{sat}} \end{aligned}$$

from which we obtain

$$a = \frac{A(T_{\text{bulk}} - T_{\text{sat}})}{\kappa_l (\exp(Ad/\kappa_1) - 1)}. \quad (3.26)$$

Equating equations (3.25) and (3.26) we find that

$$p = -\frac{A}{\kappa_l}$$

and substituting this into equation (3.21), gives

$$\sigma = -\kappa_l n^2.$$

Therefore

$$\begin{aligned} T_1(x, t) &= \frac{(T_{\text{bulk}} - T_{\text{sat}})}{(\exp(Ad/\kappa_1) - 1)} \left\{ \exp\left(-\frac{A}{\kappa_l}(x - At)\right) - 1 \right\} + T_{\text{sat}} \\ &+ \epsilon \frac{A(T_{\text{bulk}} - T_{\text{sat}})}{\kappa_l (\exp(Ad/\kappa_1) - 1)} e^{\sigma t + p(x - At)} \sin ny \end{aligned}$$

and

$$s(y, t) = At + \epsilon e^{-\kappa_l n^2 t} \sin ny.$$

So, since σ is negative, any small disturbances will decay with time and the plane phase-change surface can be considered to be stable. Thus there is a stable temperature distribution

$$T_1(x, t) = \frac{(T_{\text{bulk}} - T_{\text{sat}})}{(\exp(Ad/\kappa_1) - 1)} \left\{ \exp\left(-\frac{A}{\kappa_l}(x - At)\right) - 1 \right\} + T_{\text{sat}}$$

and a stable position for the moving boundary

$$s(t) = At.$$

Calculating an equation for the mass flux for the model with a different boundary condition

Now that we have shown that the temperature distribution and the position of the surface moves is stable, we may proceed to calculate the mass flux at the surface. The mass flux is defined by

$$\dot{m} = \rho_1 \dot{s}.$$

So using (3.20) we find that

$$\begin{aligned}\dot{m} &= -\frac{\rho_1 \kappa_1 c_1}{dL} (T_{\text{bulk}} - T_{\text{sat}}) \\ &= -\frac{k_1}{dL} (T_{\text{bulk}} - T_{\text{sat}}).\end{aligned}$$

According to Scurlock and Beduz(1994), for LIN, LOX, LAr and LNG the thickness of the conduction layer, $d \approx 100 - 500\mu\text{m}$. For LNG, we know values of the thermal conductivity and latent heat of vaporisation of the fluid, namely (assuming that they are the properties of methane since methane is the main constituent of LNG), $k = 0.19\text{Wm}^{-1}\text{K}^{-1}$ and $L = 5 \times 10^5\text{Jkg}^{-1}$. Substituting these values into the equation, with an average thickness of say, $d = 300\mu\text{m}$, for the conducting layer gives

$$\dot{m} = -1.3 \times 10^{-3} (T_{\text{bulk}} - T_{\text{sat}}).$$

In fact with $d = 224\mu\text{m}$, the analytical result gives the equation found experimentally for LNG (Beduz and Scurlock, 1995):

$$\dot{m} = -1.7 \times 10^{-3} (T_{\text{bulk}} - T_{\text{sat}}).$$

Therefore, with knowledge of the thickness of the conduction region, the mass flux rate can be modelled mathematically and gives a good comparison with experimental data.

3.1.6 Discussion of the Stefan problem

In this section, we have explained and then applied the Stefan condition to the problem of evaporation in cryogenic fluids. At first we considered the situation where the temperature in the bulk of the fluid (assumed to be a uniform temperature due to convection) is fixed at a point far below the surface. The temperature distribution

was found initially using a similarity solution and then we examined the long-term behaviour of the fluid using a travelling wave solution. We considered the stability of both these results in order to assess whether there was a single solution for the mass flux at the surface over time, as has been found experimentally. Both initial models were proved to be stable. The mass flux found from the first model provided reasonable results when compared with experimental results. Unfortunately, we could not find a mass flux equation for the second model since it gave no information about the velocity of the surface.

We then examined a similar model but with the convecting fluid remaining a fixed distance from the surface where this distance is the thickness of the conduction region. The equations in our model were modified and the problem was again solved using a travelling wave solution for the long-term behaviour of the fluid. With an experimental value for the thickness of the conduction region, a time-independent mass flux equation was calculated which was compared to that calculated experimentally for LNG. The results compared favourably. This work showed that the steady mass flux rate used in rough calculations

$$\dot{m} = -\frac{k_1}{Ld}\Delta T$$

can be applied to the moving boundary problem.

3.2 Model of Flow in a Mixture

We have so far proposed models, all with degrees of success, for the behaviour of one-component fluid. However we have not yet included two-component flow for which we could consider a two phase model. Although this work is beyond the scope of our thesis, we shall discuss it briefly next.

3.2.1 Governing differential equations

We choose to examine a mixture of LIN and LOX, since the significant difference in their saturation temperatures makes analysis easier. The fluids are governed by the mass conservation equations

$$(\rho_1\alpha_1)_t + (\rho_1\alpha_1u_1)_x = 0 \tag{3.27}$$

$$(\rho_2\alpha_2)_t + (\rho_2\alpha_2u_2)_x = 0 \tag{3.28}$$

where $\rho_1(x, t)$ is the density (kgm^{-3}) of LOX, $\rho_2(x, t)$ is the density (kgm^{-3}) of LIN, $u_1(x, t)$ is the velocity (ms^{-1}) of the LOX in the liquid, $u_2(x, t)$ is the velocity (ms^{-1}) of the LIN in the liquid, $\alpha_1(x, t)$ is the volume fraction of LOX in the liquid and $\alpha_2(x, t)$ is the volume fraction of LIN in the liquid, such that

$$\alpha_1 + \alpha_2 = 1. \quad (3.29)$$

The loss of fluid through evaporation will be included as a boundary condition at the surface.

The temperature of the mixture may be described using the convection-diffusion equation:

$$((\rho_1\alpha_1c_1 + \rho_2\alpha_2c_2)T)_t + (\rho_1\alpha_1c_1 + \rho_2\alpha_2c_2)(\alpha_1u_1 + \alpha_2u_2)T_x = (kT_x)_x \quad (3.30)$$

where $T(x, t)$ is the temperature (K) of the mixture, $c_1(x, t)$ is the specific heat capacity ($\text{Jkg}^{-1}\text{K}^{-1}$) of LOX, $c_2(x, t)$ is the specific heat capacity ($\text{Jkg}^{-1}\text{K}^{-1}$) of LIN and $k(x, t)$ is the thermal conductivity ($\text{Wm}^{-1}\text{K}^{-1}$) of the mixture.

Note that we have four equations in five unknowns, where we have assumed that the density, specific heat capacity and thermal conductivity of the mixture can be calculated as linear combinations of those measurements of LIN and LOX weighted with the fraction of each in the layer.

We must therefore infer another equation governing the flow. In fact, we form two more equations for the flow which are dependent on one new variable:

$$u_1 = q - D_1\alpha_{1x} \quad (3.31)$$

$$u_2 = q - D_2\alpha_{2x} \quad (3.32)$$

where q is the velocity (ms^{-1}) that a single particle would travel at without any diffusive forces acting on it, D_1 is the mass diffusivity (m^2s^{-1}) of LOX in the mixture of LIN/LOX and D_2 is the mass diffusivity (m^2s^{-1}) of LIN in the mixture of LIN/LOX.

We now have six equations in six unknowns and may proceed to look at the initial and boundary conditions.

3.2.2 Initial and boundary conditions

We will now discuss the initial and boundary conditions of the system of equations. The initial values, i.e. at $t=0$, are taken to be

$$\left. \begin{aligned} T &= T_{\text{bulk}} \\ \alpha_1 &= 1/5, \alpha_2 = 4/5 \\ s(0) &= 0 \end{aligned} \right\} \quad (3.33)$$

Also at the surface, i.e. on $x = s(t)$:

$$\left. \begin{aligned} u_1 &= \dot{s} \\ \rho_2 L_2 (u_2 - \dot{s}) &= -k T_x \\ T &= T_{\text{sat}} \end{aligned} \right\} \quad (3.34)$$

where $s(t)$ is the surface position (m) and L_2 is the latent heat of vaporisation (Jkg^{-1}) of LIN.

The first of these equations defines the LOX at the surface to be moving at the same rate as the boundary moves down. This indicates that the LOX stays at the surface and none of its molecules evaporate. The second condition is the Stefan condition for LIN and as before, the saturation temperature is placed at the boundary.

Finally, as in 3.1.5, the bulk temperature is positioned a fixed distance from the moving boundary surface, such that

$$T = T_{\text{bulk}} \text{ at } x = s(t) - d. \quad (3.35)$$

3.2.3 Discussion of the two component model

As stated at the beginning of this section, we shall not attempt to solve this model, which would have shown us the development of a LOX enriched layer when all the LIN at the surface had evaporated.

In this model, we have assumed that only LIN evaporated. Although a larger proportion of LIN would evaporate, some LOX will always evaporate (see 4.2 for more details). We cannot, at this stage, derive a condition for the preferential evaporation at the surface. A further drawback with the model is that it also, similar to Section 3.1, requires knowledge of the thickness of the conduction layer.

3.3 Conclusions of the Analytical Models of Evaporation

In this chapter we obtained an equation for the mass flux of a single component superheated fluid in terms of the saturation temperature, the temperature in the bulk of the fluid, the thickness of the conduction region and the thermal properties of the specific fluid. Substituting estimates of the thickness of the conduction region, this equation matched well with the empirical relationship for LNG found from experimental data. To predict the mass flux through purely theoretical data, will require a theoretical prediction for the thickness of the layer. This will be looked at in chapter 4.

We also briefly discussed a model for the flow in a mixture of two cryogenic fluids in Section 3.2. However, we could not, at this stage, derive a boundary condition to model the preferential evaporation at the surface. This subject will be considered in Chapter 5.

Chapter 4

Instabilities At The Surface

In this chapter we will discuss two instabilities that may occur at the surface of a cryogenic fluid. The first is a thermal instability related to the conduction region of the fluid. In Section 4.2, we focus on temperature fluctuations which have long been noted near the surface of cryogenic liquid mixtures in experiments.

The subject of thermal instability has been of great interest since the beginning of the century, when Bénard(1900) first performed experiments to observe convection cells. Such cells formed when a levelled metallic plate, maintained at a uniform temperature, was placed 1mm deep in a liquid with a free upper surface at a lower temperature. It was observed, with various liquids, that the layer rapidly resolved itself into a number of nearly identical regular convex polygonal cells, of, in general, 4 to 7 sides. The motion in these cells consisted of fluid rising in the middle of the polygons and descending at the common boundary between one cell and its neighbours.

Rayleigh(1916) first formulated the theory of the convective instability of a layer of fluid between horizontal planes based on these experiments, by simplifying Bénard's experiments to two dimensions with an infinitely long strip and choosing relevant equations of motion and boundary conditions. From this, linear equations were derived for the normal modes which showed that convection only occurs when the adverse temperature gradient is so large that a dimensionless parameter, known as the Rayleigh number, exceeds a certain critical value. The Rayleigh number is a characteristic ratio between (i) the destabilising effects of buoyancy, which induces convection due to a temperature difference, and (ii) the stabilising effects of diffusion and dissipation, which attempt to make the temperature distribution more uniform.

The primary aim of the work in our thesis is to understand the mechanisms controlling the evaporation of cryogenic fluids in storage and the effects of this evaporation on the fluid. In Chapter 3 we showed that the evaporation rate is inversely proportional to the thickness of the conduction layer and here we will try to find this thickness theoretically. For simplicity, we consider the layer as a two-dimensional infinitely long strip of fluid.

Rebiai(1985), Agbabi(1987) and Atkinson-Barr(1989) assumed that the thickness of the thin surface layer in cryogenic fluids is restricted to its maximum by the critical Rayleigh number, where $Ra_c = g\beta_T\Delta Td_c^3/\kappa\nu$, with g , the acceleration due to gravity (ms^{-2}), β_T , the thermal expansion coefficient (K^{-1}), ΔT , the temperature difference between the upper and lower boundaries (K), κ , the thermal diffusivity (m^2s^{-1}) and ν , the kinematic viscosity (m^2s^{-1}). The temperature and fluid properties were assumed to be fixed. The thickness of the layer, d , (m) is increased until it reaches its critical thickness at d_c . For Rayleigh numbers greater than the critical value, instabilities begin to occur and convection takes over as the primary form of heat transfer in the layer. This ‘critical thickness’ hypothesis has become widely accepted by experimentalists.

Rebiai(1985) substituted the critical Rayleigh number for the maximum thickness of the layer in the mass flux equation and obtain the modified mass flux equation:

$$\dot{m}^* = \left(\frac{1}{Ra_c}\right)^{1/3} \Delta T^{4/3},$$

where \dot{m}^* is defined in terms of the mass flux as

$$\dot{m}^* = \dot{m}L \left(\frac{\nu}{\kappa^2 g \beta_T \rho^3 c^3}\right).$$

Here ρ is the density of the fluid (kgm^{-3}), c is the specific heat capacity of the fluid ($\text{Jkg}^{-1}\text{K}^{-1}$). Both \dot{m}^* and ΔT were measured experimentally and Ra_c was found using a least squares fit across a number of experiments. The correlation was confirmed by Atkinson-Barr(1989) for LIN, LOX and LAr, with the critical Rayleigh number for LIN calculated to be 33, but was found not to apply to LNG and LCH₄. Berg *et al.*(1966) similarly obtained experimental values of the critical Rayleigh number of the same order of magnitude as LIN, for other fluids such as *n*-Heptane and Methyl alcohol by assuming that the critical Rayleigh number can be determined from the depth at which convection begins to occur in the layer.

Howard(1966) described the convective flow in fluid with large Rayleigh numbers (of

the order of 10^7) as intermittent and characterised the system by the following cyclic process:

1. A thermal boundary layer is formed by diffusion.
2. The layer increases in thickness until, at a 'critical thickness' defined by the critical Rayleigh number, instability sets in.
3. The layer is destroyed by convective flow.
4. The convection reduces in strength because liquid mixes and loses heat.
5. The thermal boundary layer reforms by conduction.

Naturally there is a characteristic period associated with this process and this was investigated by Foster (1971) for the problem of two free surfaces with a Rayleigh numbers of the order of 10^7 . It was found that the periodicity was independent of the depth of the fluid layer but dependent on the rate of cooling and the properties of the fluid.

Experiments in superheated cryogenic fluids (see Chapter 1) have shown that the liquid away from the surface is well mixed by convection. The effect of a horizontal velocity below the conduction layer may be modelled by a shear. This is known as Couette flow. Some calculations of the critical Rayleigh number in the presence of a Couette flow have already been performed. Gallagher and Mercer(1965) investigated the stability of plane Couette flow to small disturbances, for a two-dimensional model of a fluid held between two flat plates, situated at $y = \pm 1$ in non-dimensionalised form, which are held at constant temperatures T_0 and T_1 and move with equal and opposite velocities parallel to the x -axis. It was assumed that the disturbance velocities are sufficiently small to allow the Navier-Stokes equations to be linearised and a similar analysis was performed to that of earlier studies by Gallagher and Mercer(1962,1964), in which the stability of Couette flow without a temperature gradient (leading to the Orr-Sommerfield equation) was examined. For disturbances transverse to the flow in the unperturbed state, i.e. causing longitudinal rolls, Gallagher and Mercer(1965) showed that all fluids will become unstable at the same value of the Rayleigh number irrespective of whether shear is present or not.

Deardorff(1965) examined a similar problem to that of Gallagher and Mercer(1965) of flow between two horizontal plates but with only the upper plane moving with a

constant shear velocity. The results agreed with those of the latter authors, that for disturbances in a vertical plane transverse to the flow in the unperturbed state, the stability criterion with shear becomes the same as that for pure convection. However, this work also shows the stabilising effect of increasing the Reynolds and Prandtl numbers for disturbances in a vertical plane aligned in the direction of the unperturbed flow.

More recently, interest has been shown in predicting the types of convection rolls that form at the onset of instability. Clever and Busse(1992) examined the stability of three-dimensional flows, again between two horizontal rigid plates, which arise from wavy disturbances perpendicular to the axis of longitudinal rolls at Prandtl numbers of order unity or less for fluid heated from below and subjected to a mean shear. Through numerical computations of the stability of these disturbances, it was concluded that at sufficiently low Reynolds numbers, the effect of shear on this type of convection is minimal. The shear may even contribute to the efficiency of the heat transport by delaying the onset of instabilities which usually tend to decrease the efficiency of convection. The steady, wavy roll solutions are shown to be stable with respect to disturbances which do not change the horizontal periodicity interval, for only a limited range of Rayleigh numbers.

Yahata(1994) analytically examined the dominant pattern of convection rolls developing in the presence of a vertical thermal gradient and a horizontal Couette flow on a fluid between two infinitely extended horizontal plates, near the onset of convection for a small rate of shear. The amplitude equations are derived in order to study growth competition between longitudinal rolls and transverse rolls whose axes are in the direction parallel to and perpendicular to the Couette flow respectively. The results indicate that the system is in the longitudinal roll state up to a numerically calculated Rayleigh number, $(Ra)_{TS}$, (1803 for a Prandtl number of 0.7 and a Reynolds number of 10), above which it is in a multiple steady state consisting of both longitudinal and transverse roll states, the dominant state depending on the initial conditions. The numerical calculations of $(Ra)_{TS}$ in this paper show that the Rayleigh number increases with both increasing Prandtl number and Reynolds number.

In the first section, we shall calculate the critical Rayleigh number for a typical cryogenic fluid, by forming a model describing the thin conduction layer, which lies between the convective bulk fluid and the vapour surroundings. This will be used

to investigate whether the working assumption is an accurate and useful model of the conduction layer. Thus our model will consist of a layer of viscous fluid resting between two free boundaries, with the surface maintained at the saturation temperature (below the temperature of the bulk of the fluid) as the problem undertaken by Rayleigh(1916). In order to describe the motion of a single convection cell, we shall take the lower layer to be moving with a constant speed in the direction of the plane, as shown in Figure 4.1. This problem is similar to that solved by Deardorff(1965) except that the lower rather than the upper boundary will be moved horizontally and the two boundaries are free, rather than rigid. This model will be solved numerically and the ‘critical’ thickness compared to those found experimentally.

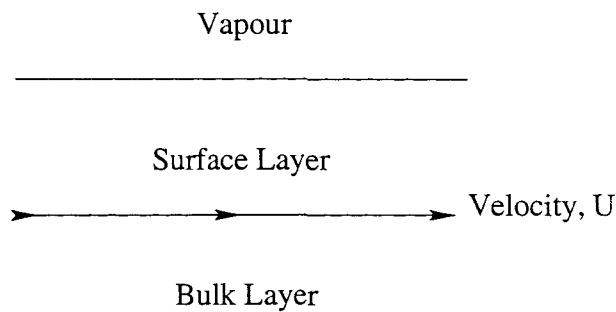


Figure 4.1: Diagram depicting shear effect caused by convection in the bulk liquid on the surface layer.

Temperature fluctuations are seen as spikes in the temperature profile near the surface and those found in a LIN/LOX mixture are shown in Figure 4.2, which has been taken from a recent report, by Beduz and Scurlock(1996). The temperature profile in the thin layer was measure using a micrometer made of $25\mu\text{m}$ thermocouple wires. The position of the thermocouple was fixed and the temperature measured as the liquid surface moved downward due to evaporation. It suggested that the spikes seen in the temperature profile may be due to micro-convection eddies generated by local inversions accompanying liquid evaporation. Two types of thermal spikes were seen, the larger ones being cold spikes and the smaller ones hot. The largest cold spikes were seen adjacent to the thermal conduction region and are thought to correspond to a downward moving element of a convection cell or closed loop which has the function of carrying 'spent' evaporated and cooled liquid down into the bulk liquid. The hot spikes bring superheated liquid up to the surface from the bulk as a heat source of evaporation.

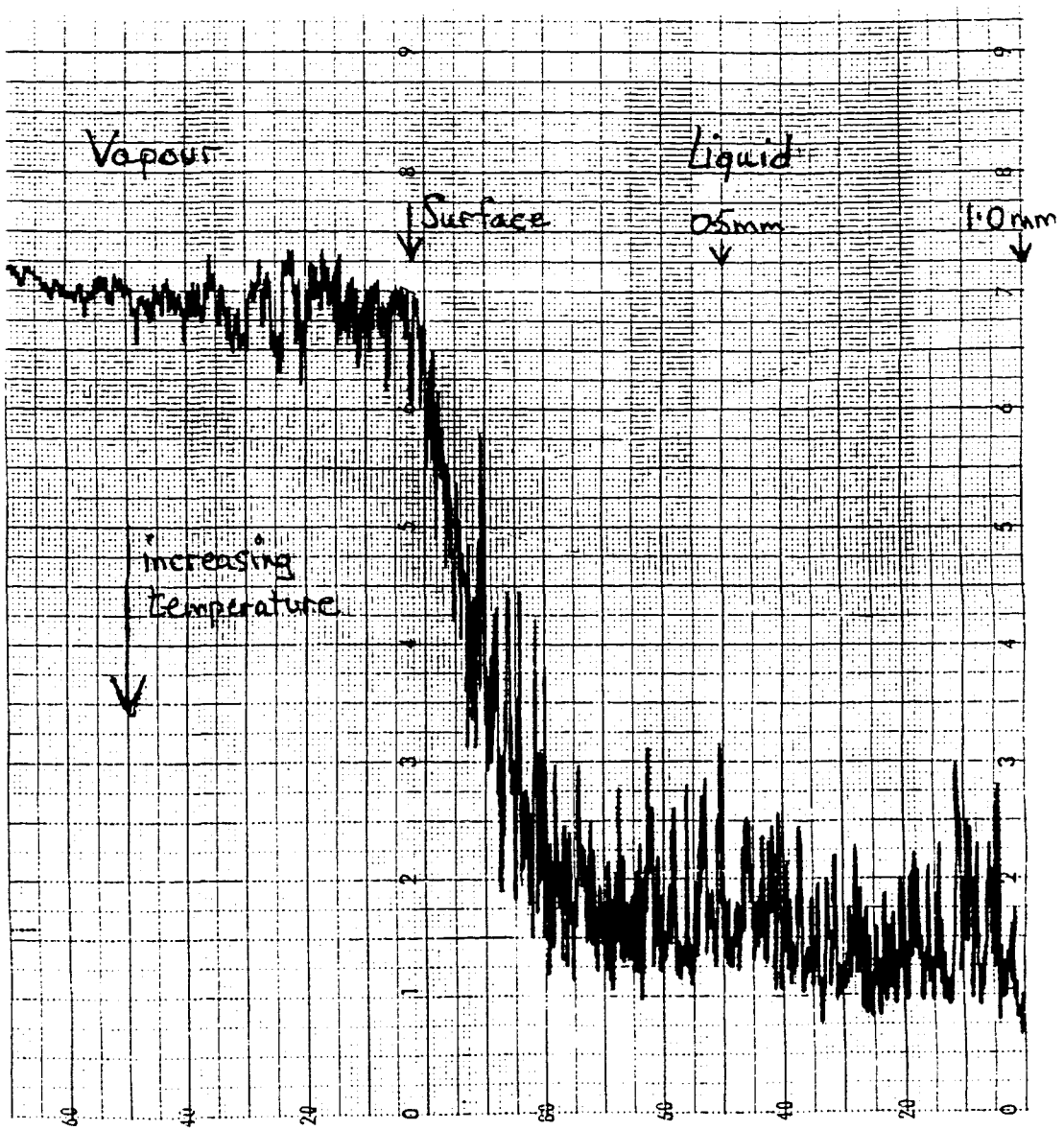


Figure 4.2: Typical temperature profile through the surface of a cryogenic mixture reproduced from Beduz and Scurlock(1996).

In Section 4.2, we shall verify the explanation for these spikes, by constructing a simple model of micro-convection eddies for a LIN/LOX mixture. It will be assumed that each micro-convection occurs when all the LIN has evaporated from the surface. Thermal effects on the density will be ignored. The number density of these thermal fluctuations will be calculated and compared to those observed experimentally.

4.1 Model of Convective Instability with Couette Flow

We will now construct an analytical model to test the supposition derived empirically from experiments that the thin surface layer is restricted to a certain thickness determined by the critical Rayleigh number, by finding the critical Rayleigh number for a heat-conducting fluid confined between two horizontal free or rigid boundaries, the lower of which is moving in the direction of the plane. We will then examine the behaviour of the fluid in this layer.

4.1.1 Governing differential equations

The equations of motion of a heat-conducting viscous fluid under the action of gravity are well known. The continuity equation is used to express the conservation of mass:

$$\frac{\partial \rho}{\partial t} + \frac{\partial(\rho q_j)}{\partial x_j} = 0, \quad (4.1)$$

where ρ is the density (kgm^{-3}) of the liquid, and q_j is the component in the j -direction of the vector \underline{q} , which is the velocity (ms^{-1}) of the fluid flow. The Navier-Stokes equations describe the behaviour of the fluid:

$$\rho \frac{Dq_i}{Dt} = -g\rho\delta_{i3} + \frac{\partial\sigma_{ij}}{\partial x_j}, \quad (4.2)$$

where $D/Dt = \partial/\partial t + \underline{q}\cdot\nabla$, g is the acceleration (ms^{-2}) due to gravity, δ_{ij} is the Kronecker delta defined by $\delta_{ij} = \{1 \text{ if } i=j, 0 \text{ if } i \neq j\}$ and σ_{ij} is the stress tensor (Nm^{-2}) defined by

$$\sigma_{ij} = -p\delta_{ij} + \mu \left(\frac{\partial q_i}{\partial x_j} + \frac{\partial q_j}{\partial x_i} - \frac{2}{3} \frac{\partial q_k}{\partial x_k} \delta_{ij} \right) + \lambda \frac{\partial q_k}{\partial x_k} \delta_{ij},$$

where p is the pressure (Nm^{-2}) in the fluid, μ is the coefficient of dynamic viscosity ($\text{kgm}^{-1}\text{s}^{-1}$) (assumed to be constant and independent of temperature) and λ is the

coefficient of the bulk viscosity (or second viscosity) ($\text{kgm}^{-1}\text{s}^{-1}$). Finally we have the heat conduction equation:

$$\frac{DT}{Dt} = \kappa \Delta T, \quad (4.3)$$

where T is the temperature (K) in the liquid, Δ is the Laplacian operator, given by $\Delta = \partial^2/\partial x_j \partial x_j$ and $\kappa = k/\rho c$ is the thermal diffusivity (m^2s^{-1}) of the liquid where k is the thermal conductivity ($\text{Wm}^{-1}\text{K}^{-1}$) and c is the specific heat capacity ($\text{Jkg}^{-1}\text{K}^{-1}$) of the liquid.

To these general equations of motion, we shall apply the Boussinesq approximation, following Rayleigh(1916). This assumes that density variations are small compared to the standard density and so may be neglected in so far as they affect inertia but must be retained in the buoyancy terms. This is a reasonable assumption since the density varies only minutely with pressure and temperature in cryogenic fluids. The equation for the density variation which is to be used in the buoyancy term is:

$$\rho = \rho_{\text{bulk}} \{1 - \beta_T(T - T_{\text{bulk}})\},$$

where ρ_{bulk} is the density (kgm^{-3}) of the fluid at T_{bulk} , the maintained temperature (K) of the bottom plane and β_T is the constant coefficient of thermal expansion (K^{-1}).

Typically $\beta_T \ll 1$ and if, as in the experiments with cryogenic fluids, $T_{\text{bulk}} - T \leq 10\text{K}$, then $(\rho - \rho_{\text{bulk}})/\rho_{\text{bulk}} = \beta_T(T_{\text{bulk}} - T) \ll 1$. So the derivatives of density in the continuity equation (4.1) are of order β_T and to leading order

$$\frac{\partial q_j}{\partial x_j} = 0, \quad (4.4)$$

as for an incompressible fluid. Then the stress tensor is given by

$$\sigma_{ij} = -p\delta_{ij} + \mu \left(\frac{\partial q_i}{\partial x_j} + \frac{\partial q_j}{\partial x_i} \right).$$

So, on treating ρ as a constant, ρ_{bulk} , in every term other than the buoyancy, the Navier-Stokes equations (4.2) become

$$\frac{Dq_i}{Dt} = -\frac{\partial}{\partial x_i} \left(\frac{p}{\rho_{\text{bulk}}} \right) - \beta_T g(T_{\text{bulk}} - T)\delta_{i3} + \nu \Delta q_i, \quad (4.5)$$

where ν is the coefficient of kinematic viscosity (m^2s^{-1}).

4.1.2 Linearising the governing differential equations

Suppose that the two horizontal planes are situated at $z = 0$ and $z = d$, and are at temperatures (K) T_{bulk} , as stated before, and T_{sat} respectively, where $T_{\text{bulk}} > T_{\text{sat}}$. In the unperturbed state with the lower plane moving at a constant velocity U and the upper plane maintained stationary, the velocity in the fluid is

$$Q = \left(U \left(1 - \frac{z}{d} \right), 0, 0 \right).$$

The temperature in the unperturbed state, $T_0(z)$, must satisfy equation (4.3), so that

$$0 = \kappa \frac{d^2 T_0}{dz^2}.$$

It follows that

$$T_0(z) = T_{\text{bulk}} - \frac{z}{d}(T_{\text{bulk}} - T_{\text{sat}}).$$

Also, equation (4.5) gives

$$0 = -\frac{1}{\rho_{\text{bulk}}} \frac{\partial P}{\partial z} - \beta_{\text{T}} g (T_{\text{sat}} - T).$$

But since $T = T_0(z)$ in the basic state of motion, the basic hydrostatic pressure distribution is simply

$$P = -\frac{g\beta_{\text{T}}\rho_{\text{bulk}}(T_{\text{bulk}} - T_{\text{sat}})}{d} \frac{z^2}{2} + p_{\text{bulk}},$$

where p_{bulk} is the pressure (Nm^{-2}) of the fluid at the temperature T_{bulk} .

In this state, the fluid flows horizontally due to the shear movement of the lower plane and conducts heat upwards as if it were a conducting solid. We shall now disturb the system slightly to see the effects of adding a perturbation to the flow, by writing

$$\begin{aligned} \underline{q} &= \left(U \left(1 - \frac{z}{d} \right), 0, 0 \right) + \tilde{q}(x, y, z, t) \\ T &= T_{\text{bulk}} - a_{\text{T}} z + \tilde{T}(x, y, z, t) \\ p &= -g\beta_{\text{T}}\rho_{\text{bulk}} a_{\text{T}} \frac{z^2}{2} + p_{\text{bulk}} + \tilde{p}(x, y, z, t) \end{aligned}$$

where $a_{\text{T}} = (T_{\text{bulk}} - T_{\text{sat}})/d$ and the variables \tilde{q} , \tilde{T} and \tilde{p} are assumed small. Linearisation of equations (4.4), (4.5) and (4.3) then gives

$$\frac{\partial \tilde{q}_j}{\partial \tilde{x}_j} = 0, \tag{4.6}$$

$$\begin{aligned} \frac{\partial \tilde{q}_j}{\partial t} + U \left(1 - \frac{z}{d} \right) \frac{\partial \tilde{q}_j}{\partial x} - \frac{U \tilde{w}}{d} \delta_{i1} &= -\frac{\partial}{\partial x_i} \left(\frac{\tilde{p}}{\rho_{\text{bulk}}} \right) + g\beta_{\text{T}} \delta_{i3} \tilde{T} \\ &+ \nu \Delta q_i, \end{aligned} \tag{4.7}$$

$$\frac{\partial \tilde{T}}{\partial t} + U \left(1 - \frac{z}{d} \right) \frac{\partial \tilde{T}}{\partial x} - a_{\text{T}} d \tilde{w} = \kappa \Delta \tilde{T}. \tag{4.8}$$

4.1.3 Non-dimensionalisation of the governing equations

Next, we shall non-dimensionalise the equations in order to be able to compare the important parameters in the problem. Scaling distances with the height of the fluid, d , time and velocity with the thermal diffusivity κ , and d , pressure with the density at a temperature of T_{bulk} , ρ_{bulk} , together with κ and d , and temperature with $T/(a_{\text{T}}d)$, the dimensionless form for all variables may be obtained:

$$\left. \begin{aligned} \underline{x}^* &= \underline{x}/d & , & & t^* &= \kappa t/d^2 & , & & \underline{q}^* &= d\bar{q}/\kappa, \\ p^* &= d^2\bar{p}/(\rho_{\text{bulk}}\kappa^2) & , & & T^* &= \bar{T}/(a_{\text{T}}d) \end{aligned} \right\} \quad (4.9)$$

Substituting the dimensionless variables into equations (4.6), (4.7) and (4.8) and rearranging gives

$$\frac{\partial q_j^*}{\partial x_j^*} = 0, \quad (4.10)$$

$$\frac{\partial q_i^*}{\partial t^*} + \text{Pe}(1 - z^*)\frac{\partial q_i^*}{\partial x^*} - \text{Pe}w^*\delta_{i1} = -\frac{\partial p^*}{\partial x_1^*} + \text{RaPr}\delta_{i3}T^* + \text{Pr}\Delta q_i^*, \quad (4.11)$$

$$\frac{\partial T^*}{\partial t^*} + \text{Pe}(1 - z^*)\frac{\partial T^*}{\partial x^*} - w^* = \Delta T^*, \quad (4.12)$$

where the Peclet number, showing which of the convection and the conduction is the more dominant method of heat transfer, is defined by

$$\text{Pe} = \text{RePr}.$$

The Rayleigh number, which measures the buoyancy of the fluid against the stabilising effects of thermal conductivity and viscosity, is given by

$$\text{Ra} = \frac{g\beta_{\text{T}}(T_{\text{bulk}} - T_{\text{sat}})d^3}{\nu\kappa},$$

the Prandtl number, showing the relative measure of the rates of viscosity and thermal diffusivity, is defined by

$$\text{Pr} = \frac{\nu}{\kappa},$$

and the Reynolds number, which gives an indication of the relative magnitudes of the inertia and viscous terms by

$$\text{Re} = \frac{Ud}{\nu}.$$

For simplicity *'s will not henceforth be shown in non-dimensional quantities.

4.1.4 Boundary conditions

To solve this set of differential equations, we now need to consider the boundary conditions. Here, conditions for both rigid and free boundaries will be discussed since initially we shall model the problem between two rigid planes in order to validate our work with that of Deardorff(1965). The conditions are discussed in more detail by Drazin and Reid(1981).

Boundary conditions at a rigid surface

For a rigid surface the no-slip condition may be applied, giving (in non-dimensionalised form):

$$u = v = w = 0. \quad (4.13)$$

The first two of these conditions together with equation (4.10) imply that

$$\frac{\partial w}{\partial z} = 0. \quad (4.14)$$

Also, since the temperature is assumed fixed at both boundaries there are no perturbations of temperature at the planes. Thus

$$T = 0. \quad (4.15)$$

Boundary conditions at a free surface

The normal component of the velocity must again vanish on the surface giving (in non-dimensionalised form):

$$w = 0.$$

Since a free surface behaves as a rigid surface with tangential slip but without any tangential stress, we have the following non-dimensionalised condition on the free surface:

$$\sigma_{xz} = \sigma_{yz} = 0, \quad (4.16)$$

and since the isotropic term $-p\delta_{ij}$ has no transverse components, the condition (4.16) now reduces to

$$\frac{\partial u}{\partial z} + \frac{\partial w}{\partial x} = 0 \quad (4.17)$$

$$\text{and} \quad \frac{\partial w}{\partial y} + \frac{\partial v}{\partial z} = 0 \quad (4.18)$$

Since w vanishes (for all x and y) on the bounding surface, it follows from equations (4.17) and (4.18) that

$$\frac{\partial u}{\partial z} = \frac{\partial v}{\partial z} = 0 \quad (4.19)$$

and together with the equation (4.10), this gives

$$\frac{\partial^2 w}{\partial z^2} = 0 \quad (4.20)$$

Note that we require a further boundary condition for both types of boundaries and this will be found later.

4.1.5 Simplification of the main equations

We shall now obtain, by elimination, an equation for the vertical component of velocity, w , alone. Taking the curl of equation (4.11) gives

$$\frac{\partial \beta_i}{\partial t} + \text{Pe}(1-z)\frac{\partial \beta_i}{\partial x} + \text{Pe}\varepsilon_{ij3}\frac{\partial q_j}{\partial x} - \text{Pe}\varepsilon_{ij1}\frac{\partial w}{\partial x_j} = \text{RaPr}\varepsilon_{ij3}\frac{\partial T}{\partial x_j} + \text{Pr}\Delta\beta_i, \quad (4.21)$$

where

$$\beta_i = \varepsilon_{ijk}\frac{\partial q_k}{\partial x_j}.$$

Taking the curl of equation (4.21) gives,

$$\begin{aligned} \frac{\partial}{\partial t}\Delta q_i + \text{Pe} \left\{ 2 \left(-\frac{\partial^2 q_i}{\partial x \partial z} + \frac{\partial^2 w}{\partial x_i \partial x} \right) + (1-z)\frac{\partial}{\partial x}\Delta q_i - \Delta w \delta_{i1} \right\} \\ - \text{Pr}\Delta^2 q_i = \text{RaPr} \left(\Delta T \delta_{i3} - \frac{\partial^2 T}{\partial x_i \partial z} \right), \end{aligned} \quad (4.22)$$

and on taking the z -component, the result is

$$\frac{\partial}{\partial t}\Delta w + \text{Pe}(1-z)\frac{\partial}{\partial x}\Delta w - \text{Pr}\Delta^2 w = \text{RaPr}\Delta_1 T$$

where

$$\Delta_1 = \frac{\partial^2}{\partial x^2} + \frac{\partial^2}{\partial y^2}.$$

This gives

$$\left(\frac{1}{\text{Pr}}\frac{\partial}{\partial t} + \text{Re}(1-z)\frac{\partial}{\partial x} - \Delta \right) \Delta w = \text{Ra}\Delta_1 T. \quad (4.23)$$

We shall now find the final boundary condition required to solve for w . Substituting equation (4.15) into (4.23) gives the boundary condition:

$$\left(\frac{1}{\text{Pr}}\frac{\partial}{\partial t} + \text{Re}(1-z)\frac{\partial}{\partial x} - \Delta \right) \Delta w = 0. \quad (4.24)$$

From equation (4.12)

$$w = \left(\frac{\partial}{\partial t} - \Delta + \text{Pe}(1-z) \frac{\partial}{\partial x} \right) T.$$

So finally

$$\left(\frac{\partial}{\partial t} - \Delta + \text{Pe}(1-z) \frac{\partial}{\partial x} \right) \left(\frac{1}{\text{Pr}} \frac{\partial}{\partial t} + \text{Re}(1-z) \frac{\partial}{\partial x} - \Delta \right) \Delta w = \text{Ra} \Delta_1 w \quad (4.25)$$

This is identical to the sixth-order differential equation for the evolution of purely gravitational instabilities as given, for example by Acheson(1992), except for the two appearances of the operator $\text{Pe}(1-z)\partial/\partial x$ which arise from the presence of the Couette flow. We shall now search for wave type solutions of the form

$$w = \hat{w}(z) \exp [i(\alpha_x x + \alpha_y y - \alpha_x \text{Pe}ct)] \quad (4.26)$$

where α_x is the non-dimensionalised wavenumber in the x -direction, α_y is the non-dimensionalised wavenumber in the transverse y -direction and $c = c_r + ic_i$ is the non-dimensionalised complex wave speed.

If $c_i > 0$ the flow is unstable and the disturbance grows exponentially with time; if $c_i < 0$ the flow is stable and any small disturbance damps out. Upon substitution of equation (4.26) into (4.25), the determining equation for $\hat{w}(z)$ becomes

$$\left\{ \left(i\alpha_x \text{Pe}(c - (1-z)) + \frac{d^2}{dz^2} - \alpha_x^2 - \alpha_y^2 \right) \left(i\alpha_x \text{Re}(c - (1-z)) + \frac{d^2}{dz^2} - \alpha_x^2 - \alpha_y^2 \right) + \text{Ra}(\alpha_x^2 + \alpha_y^2) \right\} \hat{w} = 0 \quad (4.27)$$

The complete set of boundary conditions for a rigid surface are:

$$\hat{w} = 0, \quad (4.28)$$

$$\frac{d\hat{w}}{dz} = 0, \quad (4.29)$$

$$T = 0 \quad (4.30)$$

$$\text{and } \frac{d^4 \hat{w}}{dz^4} - \left[2(\alpha_x^2 + \alpha_y^2) - i\alpha_x \text{Re}(c - (1-z)) \right] \frac{d^2 \hat{w}}{dz^2} = 0, \quad (4.31)$$

and the complete set of boundary conditions for a free surface are:

$$\hat{w} = 0, \quad (4.32)$$

$$\frac{d^2 \hat{w}}{dz^2} = 0, \quad (4.33)$$

$$T = 0 \quad (4.34)$$

$$\text{and } \frac{d^4 \hat{w}}{dz^4} = 0. \quad (4.35)$$

4.1.6 Numerical procedure

We shall initially consider the problem with two rigid boundaries in order to validate our code with the results of Deardorff(1965). Following his discretisation, we divide the distance between the horizontal surfaces into $n + 1$ intervals. Equation (4.27) and the three boundary conditions for \hat{w} can be split into real and imaginary parts, with $\hat{w} = w_r + iw_i$ and written in finite difference form. Space-centred finite-difference formulations are used in the representation of the derivatives of the real and imaginary parts of \hat{w} . So, the derivatives of $\hat{w}_r(j)$, for example, would be as follows:

$$\frac{\partial \hat{w}_r(j)}{\partial z} = \frac{\hat{w}_r(j+1) - \hat{w}_r(j-1)}{2dz}$$

and

$$\frac{\partial^2 \hat{w}_r(j)}{\partial z^2} = \frac{\hat{w}_r(j+1) - 2\hat{w}_r(j) + \hat{w}_r(j-1)}{dz^2}$$

The finite difference formulation of equation (4.27) may be applied at each of the n interior grid points and, similarly, the boundary conditions at each of the boundary grid points. To minimise errors introduced by setting up the finite difference scheme we designed an automated procedure in Maple to produce the finite difference scheme (and boundary conditions), simplify and then output optimised Fortran code to evaluate it. The finite difference representation of equation (4.27) consists of several hundred terms of coefficients, which becomes more than a hundred lines of Fortran code. The length of the Fortran code is partly due to the optimised Fortran output from Maple, which (for efficiency) attempts to collect together common terms to be pre-computed. This automated procedure also allowed for minor corrections to the equations to be converted into Fortran code in a single easy step.

The finite difference scheme representation yields a matrix, A , representing a system of $2n + 12$ linear, homogeneous equations for which a non-trivial solution exists only if the characteristic determinant vanishes. Since we want to find the critical thickness of the thin layer, our task will be to find the minimum Rayleigh number such that this determinant vanishes:

$$\text{Minimise Ra subject to } |A(\text{Ra}, \alpha_x)| = 0 \quad (4.36)$$

Since $|A| \geq 0$ from the finite difference form of equation (4.27), we can also consider this to be ‘minimise Ra and $|A(\text{Ra}, \alpha_x)|$ ’.

The eigenvalues c_i are set to zero to provide the case of neutral stability, and we choose to seek solutions for which $c_r = 0.5$ such that the disturbances move with the same velocity as the fluid midway between the horizontal plates in the basic state. We shall look at transverse rolls so $\alpha_y = 0$. Note that longitudinal rolls ($\alpha_x = 0$) will result in the simple thermal instability problem with no shear.

Initially a simple Matlab program (which actually used C code generated by our automated Maple method) was written to plot the determinant as a function of α_x and Ra, for small n (about 10). Although we will not use this to solve (4.36), it is crucial to plot the objective function and constraints if possible before attempting to design or choose an efficient algorithm to perform the minimisation.

The surface plots of $\log(|A|)$ as a function of α_x and Ra using $n = 50, 60$ shown in Figures 4.3 - 4.6 were produced in Matlab using output from the Fortran code. The closer the determinant is to zero, the darker the grey is in the plots. As can be seen, the surface is fairly flat except for a parabola in the middle of the plot where the determinant quickly decreases to zero. Along this parabola, a minimum Rayleigh number may be found. By comparing Figures 4.4 and 4.6 we can see that this parabola shifts to the right with increasing grid points.

From Figures 4.3 - 4.6 it is now immediately clear that the naive solution of 4.36 using a black box or library minimisation routine is almost guaranteed to fail spectacularly due to the small region over which $|A| = 0$ (note that these figures show $\log(|A|)$). A quick check using the simplex method confirmed this.

However, for a fixed value of α_x (within a range empirically found to be between 0 and 6), we *know* that there will be a value of Ra for which $|A| = 0$. Once this is found, we can contour around the valley keeping $|A| = 0$ to find the minimum value of Ra. The plots also reveal that the valley in which $|A| = 0$ is roughly parabolic in shape. We can exploit this in designing our minimisation routine. By fitting a parabola through any 3 points in the valley, we should be able to take a single step which takes us (very nearly) to the minimum.

These observations led us to use Brent's algorithm which consists of a slow-but-sure golden section search which will switch over to exploit the parabolic structure when possible.

We now describe each of these components (based on Press *et al.*, 1992):

1. Golden Section Search. Given at each stage, a bracketing triplet of points, the

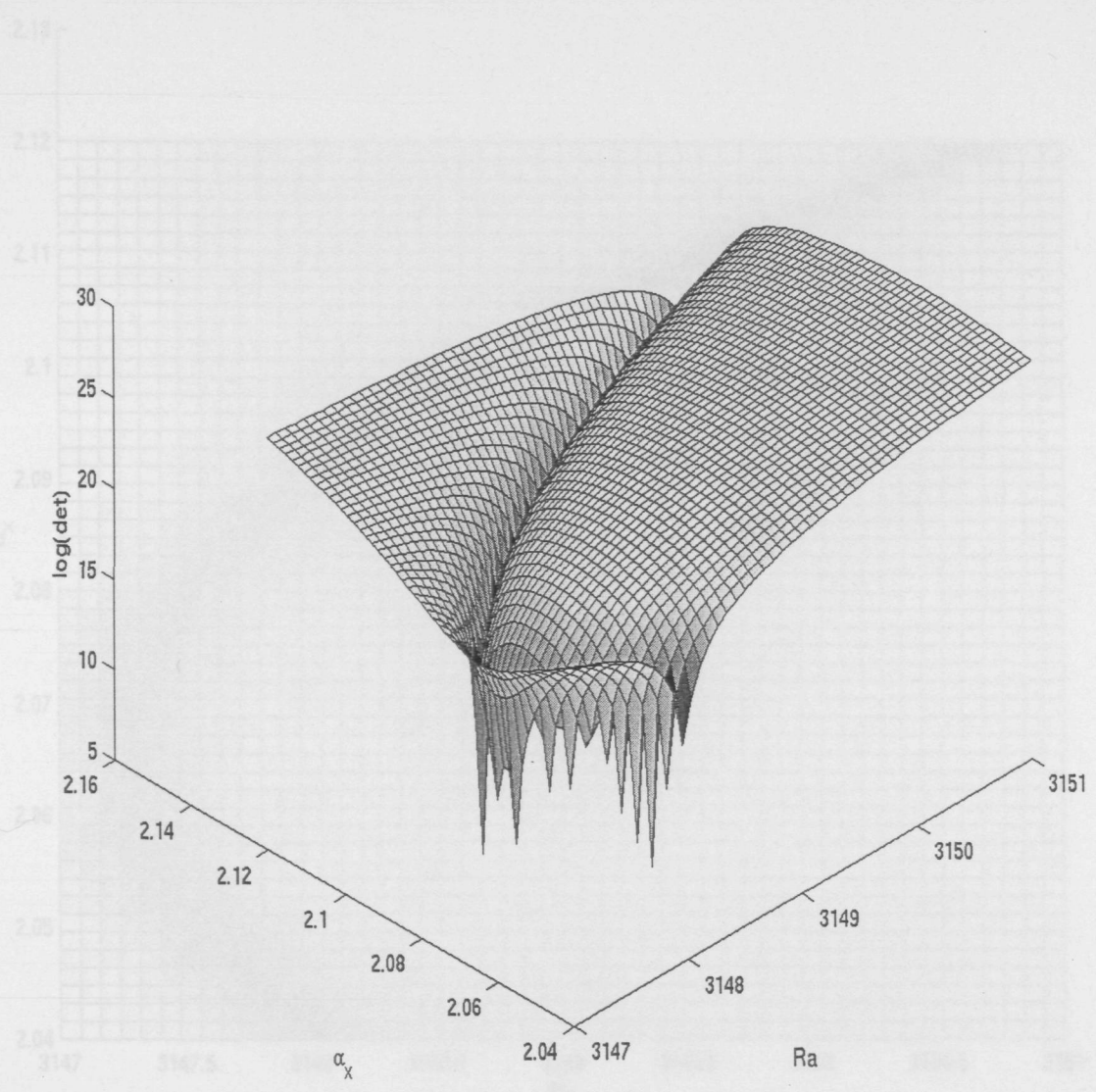


Figure 4.3: Surface plot of the log of the determinant (\det) as α_x and Ra vary with $Pr=0.0$, $Re=200$ and $n=50$.

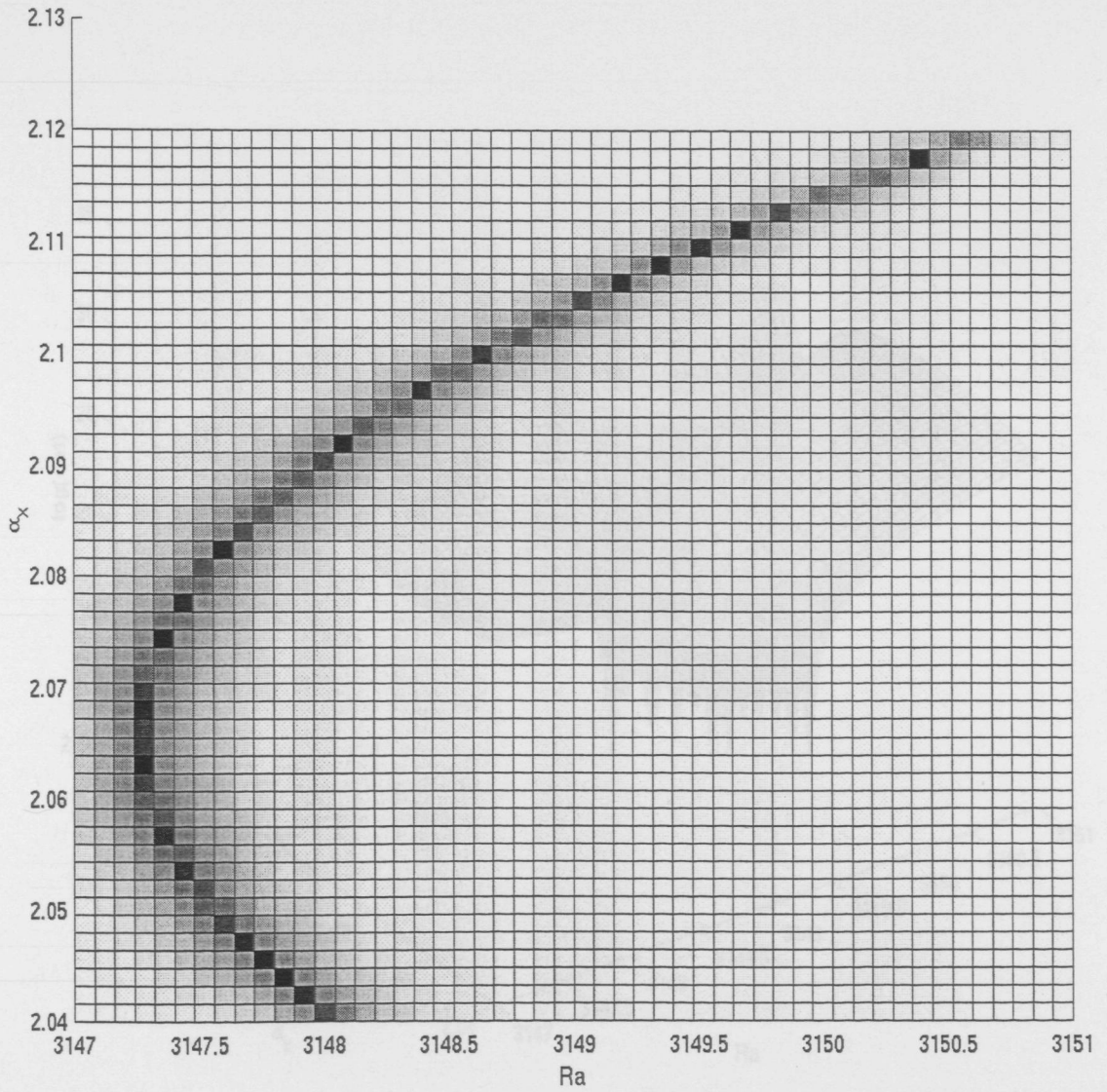


Figure 4.4: Plan view of Figure 4.3.

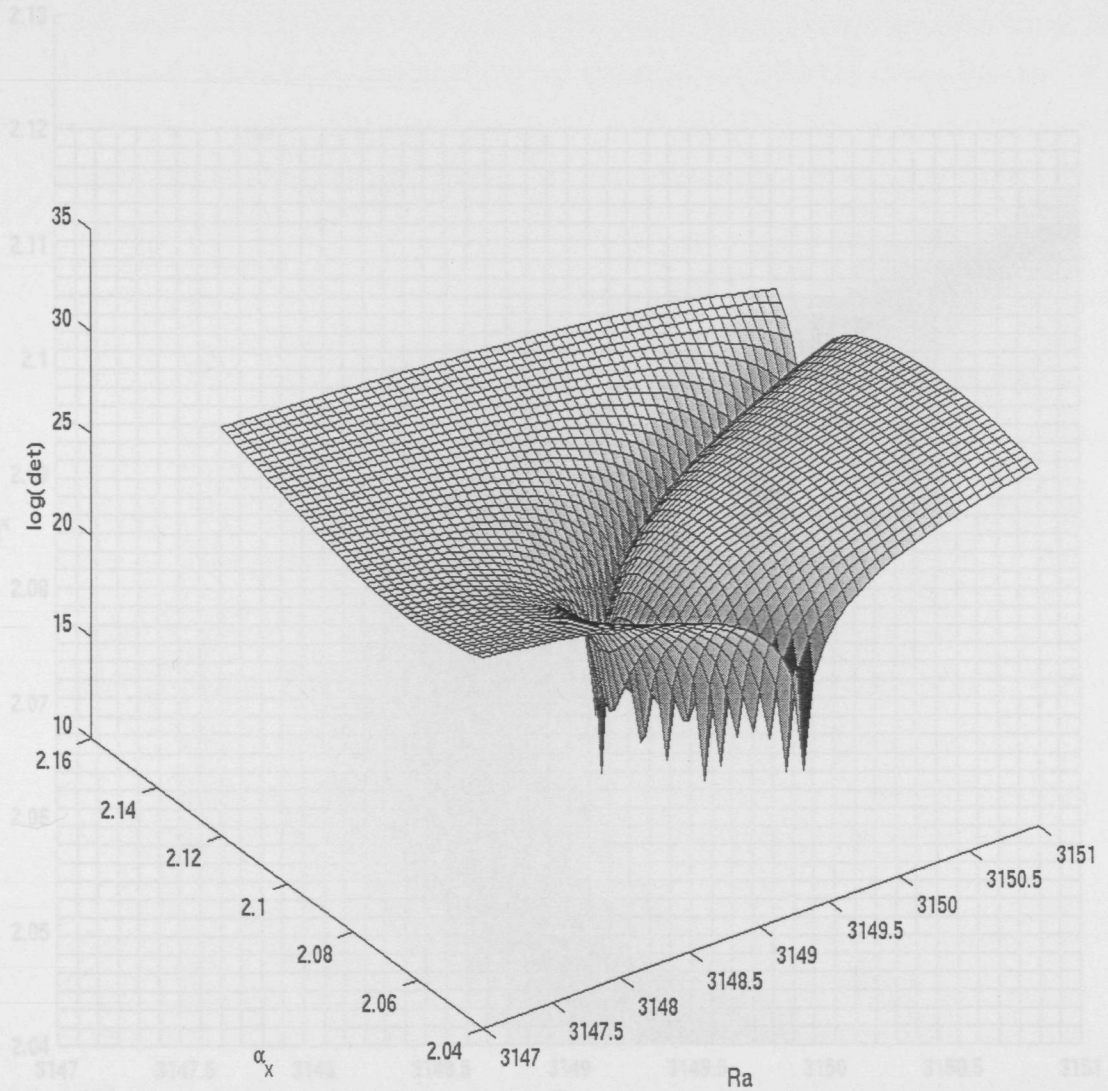


Figure 4.5: Surface plot of the log of the determinant (\det) as α_x and Ra vary with $Pr=0.0$, $Re=200$ and $n=60$.

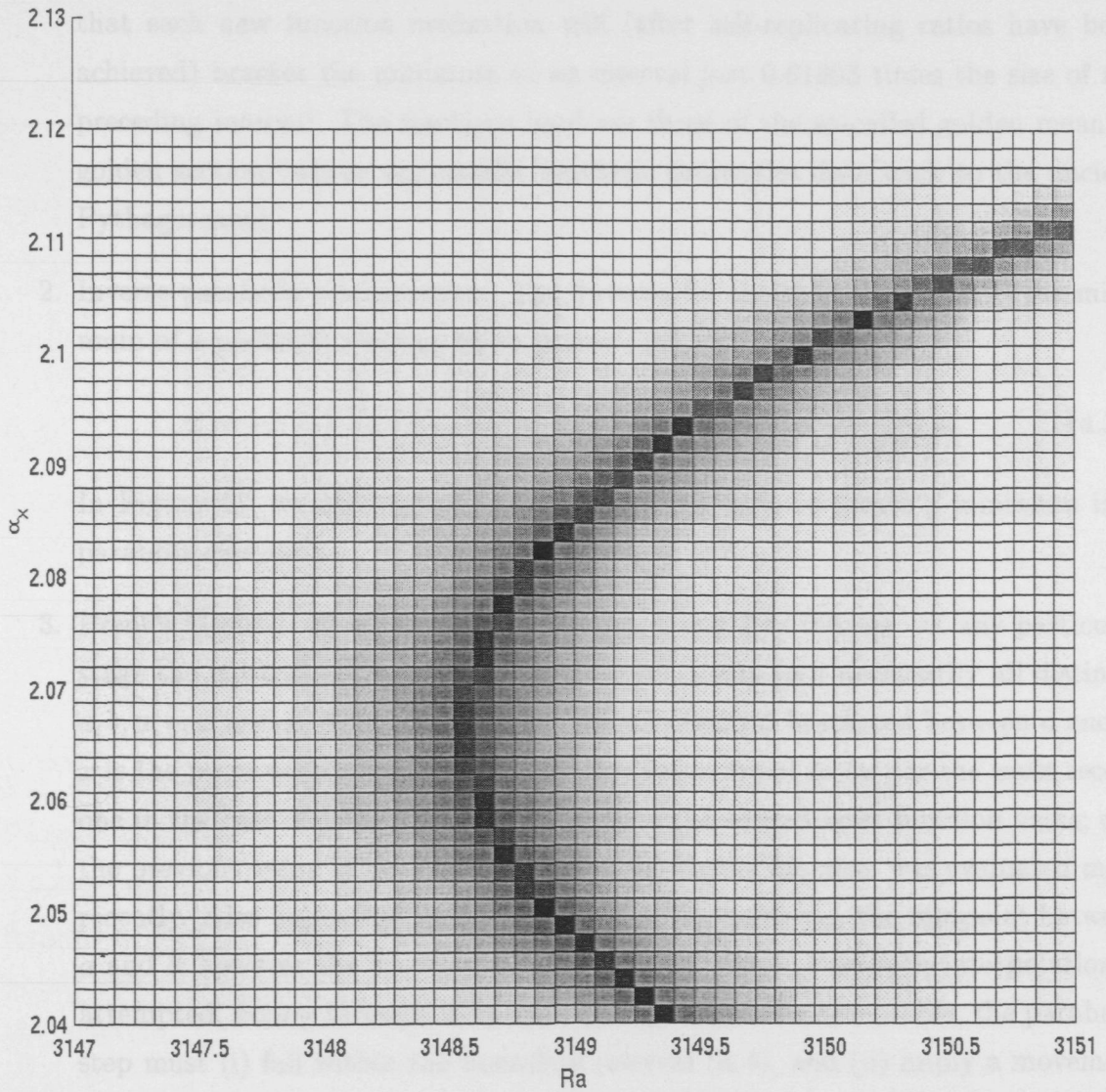


Figure 4.6: Plan view of Figure 4.5.

next point to be tried is that which is a fraction 0.38197 into the larger of the two intervals (measuring from the central point of the triplet). If the bracketing triplet is not initially in the golden ratio, the procedure of choosing successive points at the golden mean point of the larger segment will quickly converge you to the proper, self-replicating ratios. The golden section search guarantees that each new function evaluation will (after self-replicating ratios have been achieved) bracket the minimum to an interval just 0.61803 times the size of the preceding interval. The fractions used are those of the so-called golden mean or golden section (whose supposedly aesthetic properties date back to the ancient Pythagoreans).

2. Inverse parabolic interpolation. The formula for the abscissa x that is the minimum of a parabola through three points $f(a)$, $f(b)$ and $f(c)$ is

$$x = b - \frac{1}{2} \left(\frac{(b-a)^2[f(b) - f(c)] - (b-c)^2[f(b) - f(a)]}{(b-a)[f(b) - f(c)] - (b-c)[f(b) - f(a)]} \right). \quad (4.37)$$

In Figure 4.7 we demonstrate how this can be used to locate a minimum in a parabola efficiently.

3. Brent's Method. Brent's method combines 1 and 2 as follows. At any particular stage the method keeps track of six function points (not necessarily all distinct) a, b, u, v, w and x , defined as follows: the minimum is bracketed between a and b ; x is the point with the very least function value found so far (or the most recent one in the case of a tie); w is the point with the second least function value; v is the previous value of w ; u is the point at which the function was evaluated most recently. Also appearing in the algorithm is the point x_m , the midpoint between a and b ; however the function is not evaluated there. Parabolic interpolation is attempted, fitting through the points x, v and w . To be acceptable, the parabolic step must (i) fall within the bounding interval (a, b) , and (ii) imply a movement from the best current value x that is less than half the movement of the step before last. This second criterion insures that the parabolic steps are actually converging to something, rather than, say, bouncing around in some non-convergent limit cycle. In the worst possible case, where the parabolic steps are acceptable but useless, the method will approximately alternate between parabolic steps and golden sections, converging in due course by virtue of the latter. The reason for comparing to the step before last seems essentially heuristic: experience shows

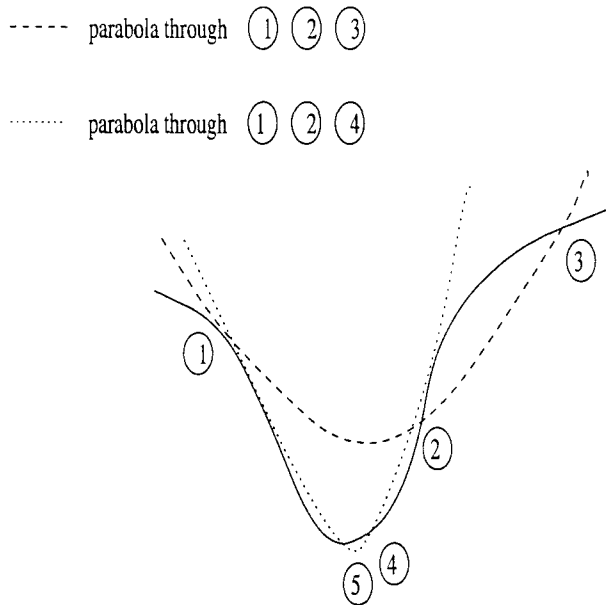


Figure 4.7: Convergence to a minimum by inverse parabolic interpolation taken from Press *et al.*(1992). A parabola (dashed line) is drawn through the three original points 1,2,3 on the given function (solid line). The function is evaluated at the parabola's minimum, 4, which replaces point 3. A new parabola (dotted line) is drawn through points 1,4,2. The minimum of this parabola is at 5, which is close to the minimum of the function.

that it is better not to punish the algorithm for a single bad step if it can make it up on the next one.

Our procedure performs the minimisation of Ra subject to $|A| = 0$ by employing two one-dimensional minimisations which use Brent's method. The first ensures that the constraint is satisfied and the second minimises Ra:

1. Choose three initial values of α_x which bracket the minimum (e.g. 0, 3.14, 6);
2. Find the corresponding value(s) of Ra for which $|A| = 0$ using a one-dimensional minimisation of $|A|$ at fixed α_x (remember $|A| \geq 0$ so minimisation of $|A|$ is equivalent to ensuring that the constraint is satisfied);
3. Based on our value(s) of Ra for each α_x , perform a one-dimensional minimisation of Ra over α_x ;
4. Using the new value of α_x repeat from 2 and stop once the value of Ra does not change significantly between iterations.

We chose $n = 100$ and repeated the computation for various values of Re and Pr and for the cases of two free boundaries and one rigid/one free boundary. The procedure converges within a few iterations in (almost) all cases. Graphs showing the critical Rayleigh number against Reynolds numbers are shown in Figures 4.8 - 4.10 for various boundaries on the upper and lower boundary of the fluid and for three Prandtl numbers, including that of LIN.

4.1.7 Numerical results for the critical Rayleigh number

Validation

The graphs of the critical Rayleigh number against the Reynolds number for the case of fluid between two rigid surfaces with a shear movement at the lower boundary are identical to those of Deardorff(1965) with a moving upper layer for $Pr=0.0$ and 0.71 . Thus the problem is symmetrical whether the upper or lower layer is in motion. This can be seen more clearly by comparing equation (4.27) to the equation that we would have obtained had the lower layer been moving, given by Deardorff(1965) as:

$$\left\{ \left(i\alpha_x Pe (c - z) + \frac{d^2}{dz^2} - \alpha_x^2 - \alpha_y^2 \right) \left(i\alpha_x Re (c - z) + \frac{d^2}{dz^2} - \alpha_x^2 - \alpha_y^2 \right) \right.$$

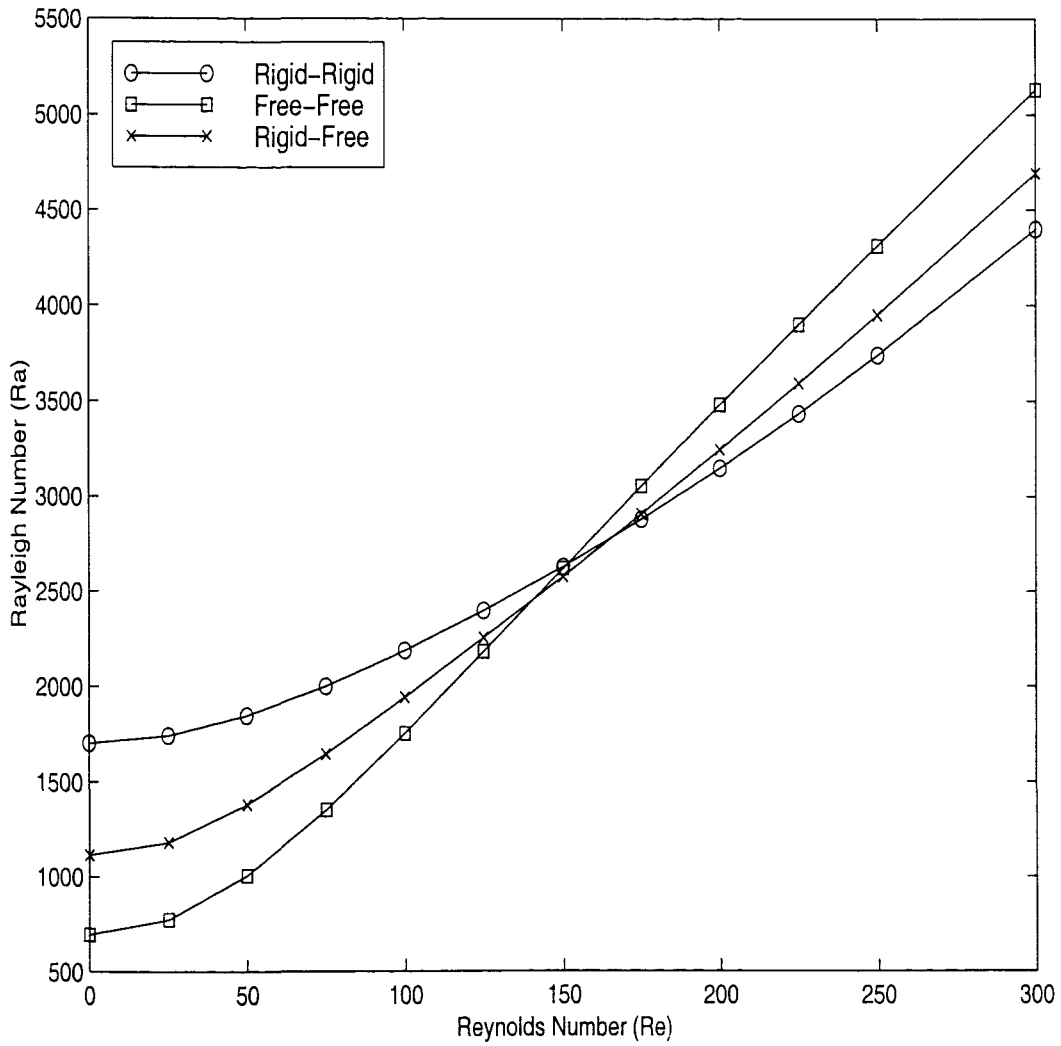


Figure 4.8: Graph of the critical Rayleigh number against the Reynolds Number for $Pr=0.0$, for various boundary conditions on the upper and lower boundary of the fluid.

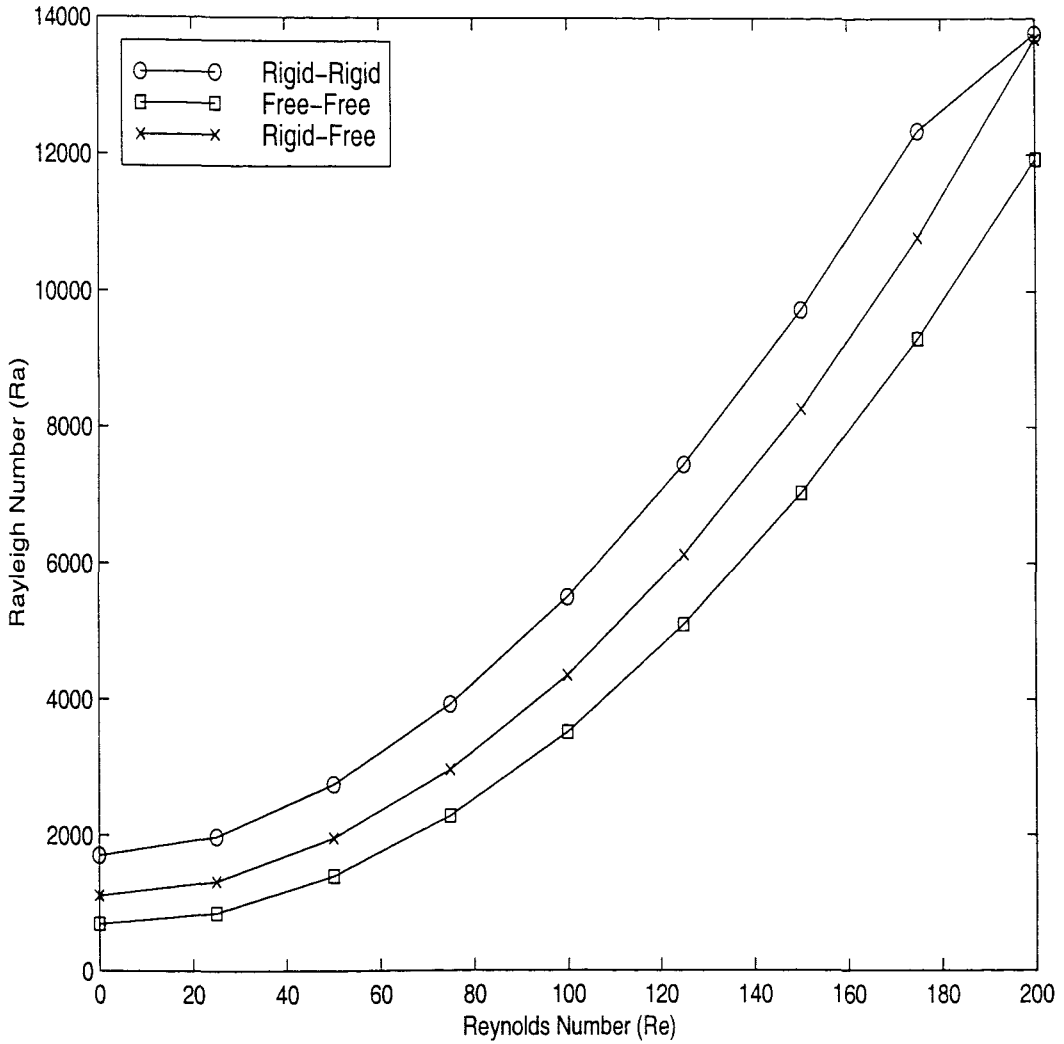


Figure 4.9: Graph of the critical Rayleigh number against the Reynolds number for $Pr=0.71$ (air), for various boundary conditions on the upper and lower boundary of the fluid.

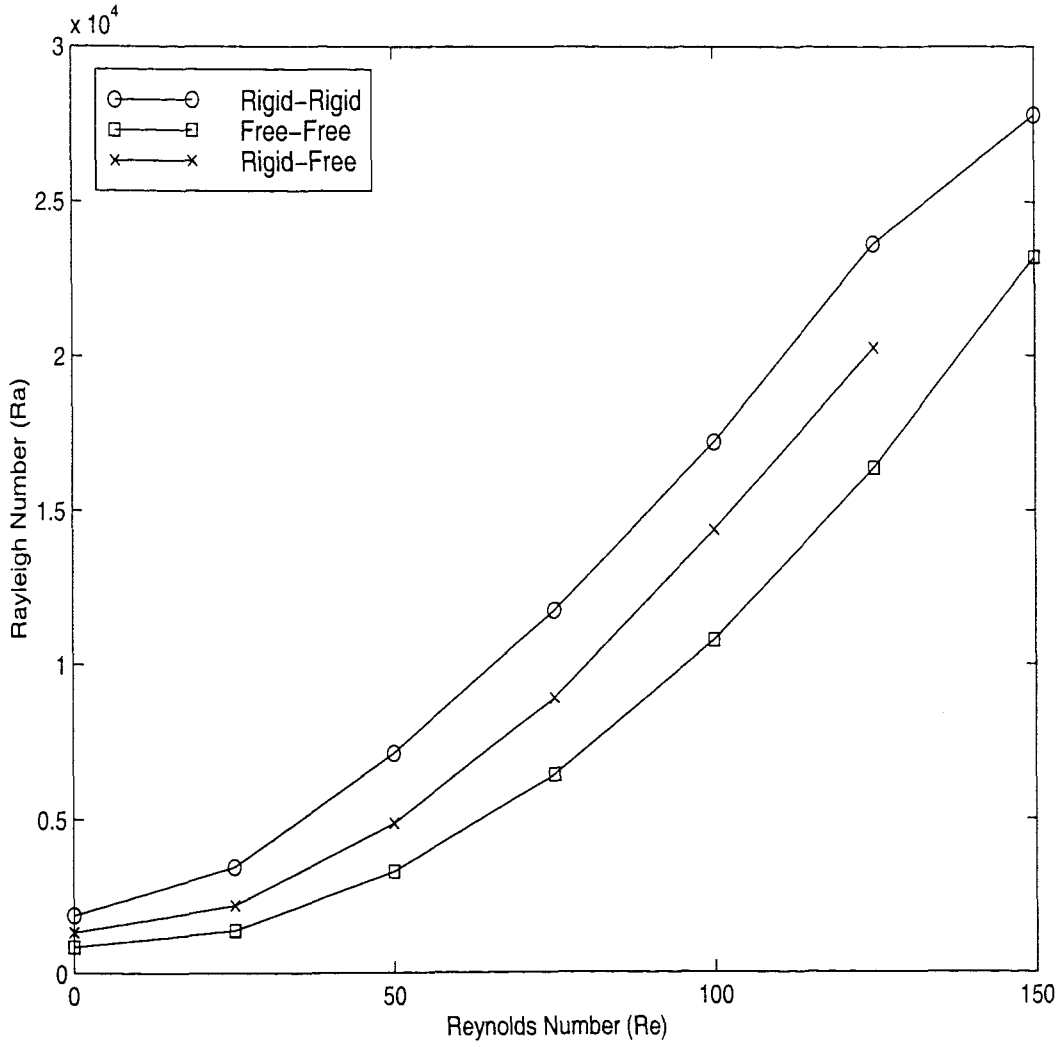


Figure 4.10: Graph of the critical Rayleigh number against the Reynolds Number for $Pr=2.32$ (LIN), for various boundary conditions on the upper and lower boundary of the fluid.

$$\left(\frac{d^2}{dz^2} - \alpha_x^2 - \alpha_y^2 \right) + \text{Ra}(\alpha_x^2 + \alpha_y^2) \Big\} \hat{w} = 0$$

The only difference between our equation (4.27) and the equation above is that $(c - z)$ is replaced by $(c - (1 - z))$ in our equation and so the problem is symmetrical whether the upper or lower boundary be moving. In contrast to Deardorff, our procedure yielded at least 6 figures of accuracy and worked without manual intervention for each of the cases considered.

Estimating the critical thickness of the layer

The thin surface layer at the top of cryogenic fluids may be assumed to lie between two free surfaces since it has a deep layer of fluid underneath and vapour above. The stabilising effect of shear, however, is seen to become increasingly strong with increasing Pr for all boundary conditions, i.e. the critical Rayleigh number increases with increasing Re and Pr. Note that the point at Re=200 in Figure 4.9 where the plots for the rigid-rigid and rigid-free boundaries meet represents a cross-over of the two plots, similar to Figure 4.8 at Re \approx 170. The case of two free boundaries can be seen to have the lowest critical Rayleigh number for all Reynolds numbers at all Prandtl numbers, of all three boundary conditions, except above a Reynolds number of 125, for Pr=0.0, when the Rayleigh number becomes the highest of all three conditions.

In order to find the minimum 'critical' thickness of the surface layer, we must obtain the smallest critical Rayleigh number for the condition of two free boundaries. For this it can be seen that we must assume that the fluid below this layer is stationary and so neglect the effect of convection on the lower boundary. The critical Rayleigh number, Ra_c, for LIN, with a Prandtl number of 2.32, is then 657.5. So with this Ra_c, the thickness of the layer is restricted to a maximum of 300 μ m if the temperature gradient of the conduction region is 7.1K. Although such temperature gradients are possible in cryogenic fluids, it is more usual to find a temperature gradient of 1K in the conduction region. This suggests that the minimum 'critical' thickness of the layer is 578 μ m, almost a factor of three larger than the maximum thickness of the layer observed from experiments. Also in our calculations, we have neglected the shear effect at the lower boundary caused by convection which increases this thickness. Thus, although we have obtained the correct order of magnitude for the thickness of the region, the critical Rayleigh number obtained from these calculations suggests that

it could in principle be substantially larger and so the model in which the thickness of the layer is restricted to a maximum of approximately $200\mu\text{m}$ by the critical Rayleigh number is not supported. In conclusion: although the thickness of the surface layer could be constrained to that found from the critical Rayleigh number there must be some other property of the fluid which further restricts its thickness to that observed experimentally.

4.1.8 Predicted velocity and temperature profiles above the critical Rayleigh number

As stated previously, although the critical Rayleigh number cannot be used to predict the thickness of the surface region, the theory has not been disproved. Therefore, we shall now examine the temperature and velocity profiles through a cross-sectional depth of the fluid at a Rayleigh number which exceeds the critical value in order to examine the behaviour of the surface layer above our theoretical ‘critical’ thickness and to study whether this layer possesses any special features at the surface which can explain the conduction layer seen to exist. Naturally, below the critical Rayleigh number, the velocities and temperature profiles will follow the basic steady state solutions.

Numerical results of the velocity and temperature profiles above the critical Rayleigh number

Again, the specific problem that we will consider shall be that of a layer of LIN with a Prandtl number of 2.32, resting between two free boundaries, the lower of which is moving in the axis parallel to the plane. We shall choose an average velocity for the shear such that the Reynolds number is 100. The critical Rayleigh number for this situation is found, using the previous calculations, to be $Ra_c = 10796$ so we shall choose a Rayleigh number greater than this critical value for which the characteristic determinant of equation (4.27) is zero, $Ra = 17038$. Equation (4.27) can be solved numerically in its matrix form, using inverse iteration, for the case of two free boundaries to give a component of the perturbation of the vertical velocity, \hat{w} , as an eigenvector with an unknown constant. The basic idea behind inverse iteration is quite simple. Suppose \underline{y} is the solution of the linear system

$$(\underline{A} - \tau \underline{I}) \cdot \underline{y} = \underline{b} \quad (4.38)$$

where $\underline{b} = 0$ and τ is close to some eigenvalue λ of \underline{A} . Then the solution \underline{y} will be close to the eigenvector corresponding to λ . The procedure can be iterated by replacing \underline{b} with \underline{y} and solving for a new \underline{y} , which will be even closer to the true eigenvector. We stop when successive iterates are sufficiently close together. Note that the solution of the singular equation (4.38) for \underline{y} can be found stably using the LU method (Press *et al.*, 1992), so long as successive iterates are renormalised. The advantage of using LU decomposition (over, say, Gaussian elimination) is that once the decomposition is computed, successive solutions for new right hand vectors only require a simple backsubstitution. Since the determinant of A is zero, we will pick the eigenvalue $\tau = 0$. From the calculations, the non-dimensionalised vertical velocity can then be found using:

$$\begin{aligned}\bar{w} &= \Re \{(w_r + iw_i) \exp[i(\alpha_x x + \alpha_y y - \alpha_x c_r t \text{Pe})]\} \\ &= \{w_r \cos(\alpha_x x - \alpha_x c_r t \text{Pe}) - w_i \sin(\alpha_x x - \alpha_x c_r t \text{Pe})\},\end{aligned}$$

since we shall consider transverse rolls ($\alpha_y = 0$). The unknown constant in the eigenvector \hat{w} is resolved by picking the length of the eigenvector such that the perturbation makes a discernible effect on the basic steady state and such that the solution for the temperature found with these results is physically reasonable.

Similarly, solutions for temperature are sought for which

$$T = \hat{T}(z) \exp [i (\alpha_x x + \alpha_y y - \alpha_x c t \text{Pe})]$$

where $\hat{T} = T_r + iT_i$. Equation (4.12) may then be split into real and imaginary parts, written in finite difference form, as before, and applied on the n interior grid points with the boundary condition on temperature, (4.34) at both $\bar{x} = 0$ and 1. Using the calculated values of \hat{w} it is possible to solve this matrix equation numerically using the LU-decomposition method to give the $(2n + 4)$ eigenvector component of the perturbation of temperature, \hat{T} . From this, the non-dimensionalised temperature could be found using

$$\begin{aligned}\bar{T} &= \frac{T_0}{(T_0 - T_{\text{sat}})} - z + \Re \{(T_r + iT_i) \exp[i(\alpha_x x + \alpha_y y - \alpha_x c_r t \text{Pe})]\} \\ &= \frac{T_0}{(T_0 - T_{\text{sat}})} - z + \{T_r \cos(\alpha_x x - \alpha_x c_r t \text{Pe}) - T_i \sin(\alpha_x x - \alpha_x c_r t \text{Pe})\}.\end{aligned}$$

The temperature profiles through the cross-sectional depth of the liquid at four fixed points in the fluid are shown in Figures 4.11 - 4.16 for non-dimensionalised times

between $t = 0.0$ and $t = 1.0$ where $z = 1$ represents the free surface. Our first observation from the temperature profiles is that, as expected from the wave-type solution used, the temperature follows a pattern with period $t = 1$ i.e. the profiles at $t = 0.0$ and $t = 1.0$ are the same. Also, though the shape of the temperature profile changes throughout the time of each period, there is always a section in the profile where the temperature remains fairly constant, although the actual position of this section alters. This is the convective part of the fluid. At some time steps we also observe a section of the profile at the surface of the layer where the temperature varies greatly over a small depth. This section, however, is not consistent at all time steps or at all positions and so cannot be interpreted as the conduction layer at the top of the fluid.

Finally from equation (4.22) with $i=1$, we can obtain an equation for the horizontal velocity, u :

$$\frac{\partial}{\partial t} \nabla^2 u + \text{Pe} \left\{ 2 \left(-\frac{\partial^2 u}{\partial x \partial z} + \frac{\partial^2 w}{\partial x^2} \right) + (1-z) \frac{\partial}{\partial x} \nabla^2 u - \nabla^2 w \right\} - \text{Pr} \nabla^4 u = -\text{RaPr} \frac{\partial^2 T}{\partial x \partial z}. \quad (4.39)$$

Solutions are sought for the horizontal velocity with the same form as before, such that

$$u = \hat{u}(z) \exp [i(\alpha_x x + \alpha_y y - \alpha_x c t \text{Pe})]$$

where $\hat{u} = u_r + iu_i$. Again, equation (4.39) can be split into real and imaginary parts, written in finite difference form and applied on the n interior grid points with the conditions $u = \frac{\partial u}{\partial x} = 0$ on both boundaries. Using the calculated values of \hat{w} and $\hat{\theta}$ it is possible to solve this matrix equation numerically using the LU-decomposition method to give the eigenvector component of the perturbation of the horizontal velocity, \hat{u} . The non-dimensionalised horizontal velocity can then be found using:

$$\bar{u} = \text{Pe}(1-z) + \text{Pe} \{ u_r \cos(\alpha_x x - \alpha_x c_r t \text{Pe}) - u_i \sin(\alpha_x x - \alpha_x c_r t \text{Pe}) \}.$$

So velocity profiles of the fluid through a cross-section can be plotted using arrows, at fixed times, where at a point (x_0, z_0) , the angle the arrow makes with the horizontal is $\tan^{-1}(\bar{w}(x_0, z_0)/\bar{u}(x_0, z_0))$ and the length of the arrow is $\sqrt{\bar{u}^2(x_0, z_0) + \bar{w}^2(x_0, z_0)}$. These profiles are shown in Figures 4.17 - 4.20. Similarly to the temperature, the velocity profile is shown to have a period of 1. We have shown fewer time steps for the graphs of the velocity as they do not vary much. However we do note that the fluid

appears to rise slightly at one time step and then fall slightly at the next (this can be seen more clearly by examining the arrows near the surface). Thus the velocity profile follows a wave solution.

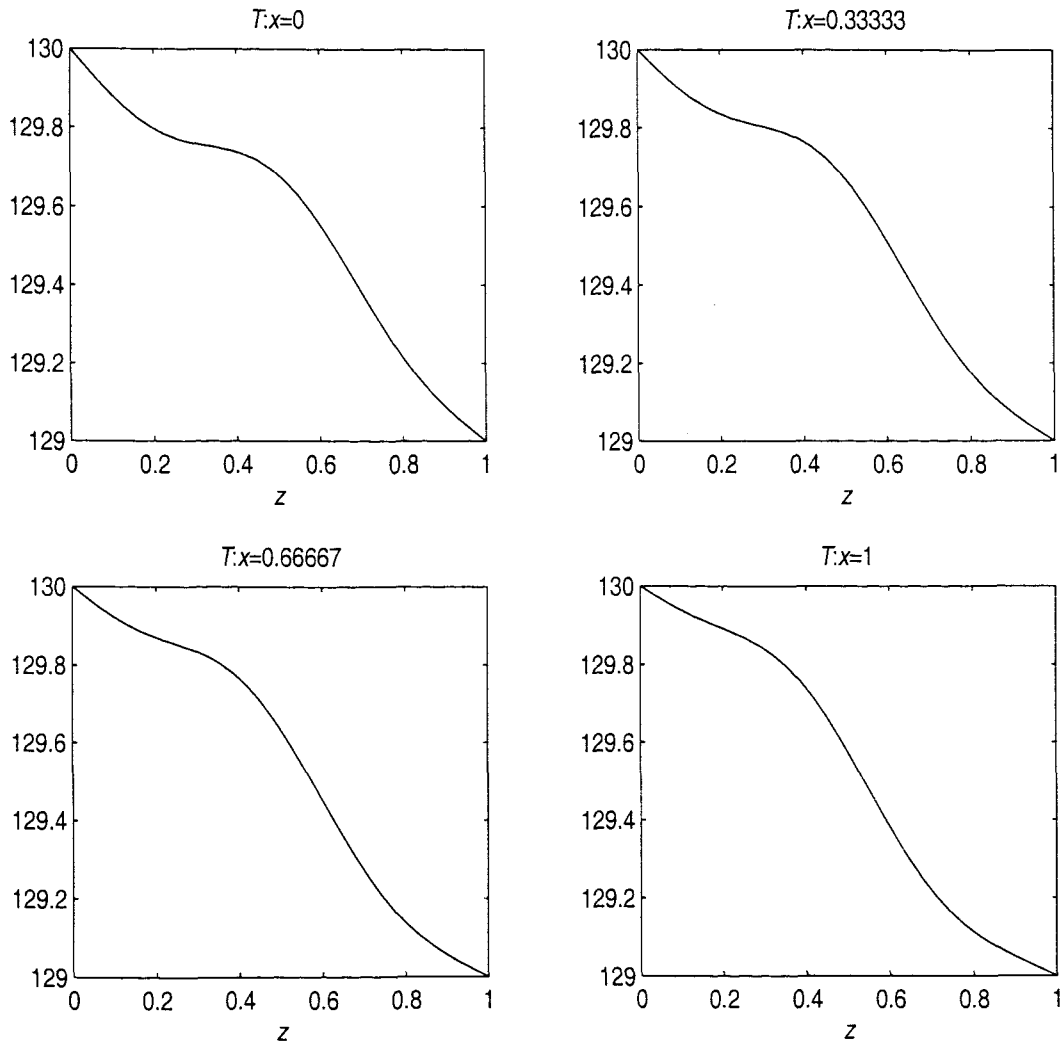


Figure 4.11: Temperature profile through a cross-section at four fixed points of the fluid at $t=0.0$.

4.1.9 Discussion of thermal instability

In this section, we modelled the thin conduction region between two free surfaces. We modelled the effect of one convecting cell by adding a shear flow to the lower boundary. The critical Rayleigh number was calculated for this problem and from this, the maximum thickness of the layer was found. This model, however, suggested that

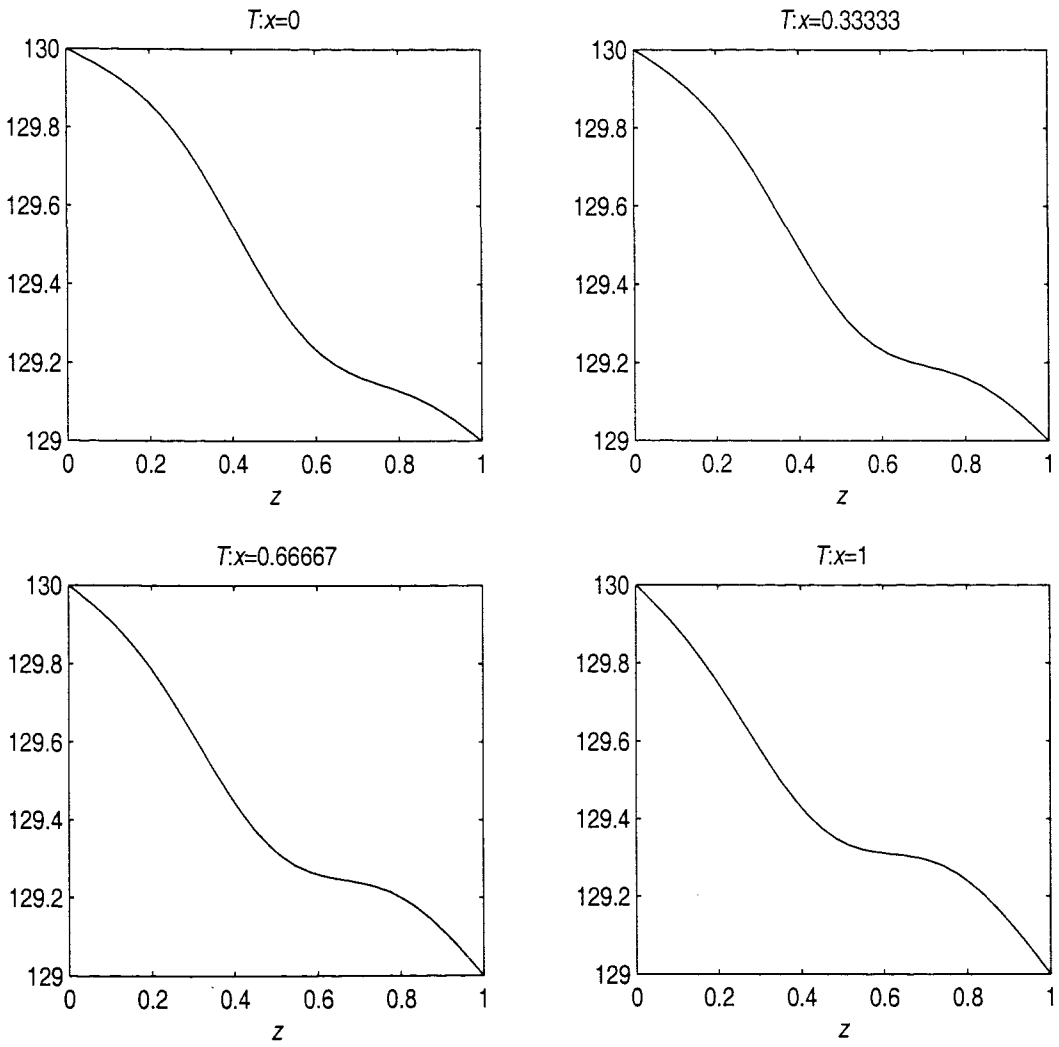


Figure 4.12: Temperature profile through a cross-section at four fixed points of the fluid at $t=0.2$.

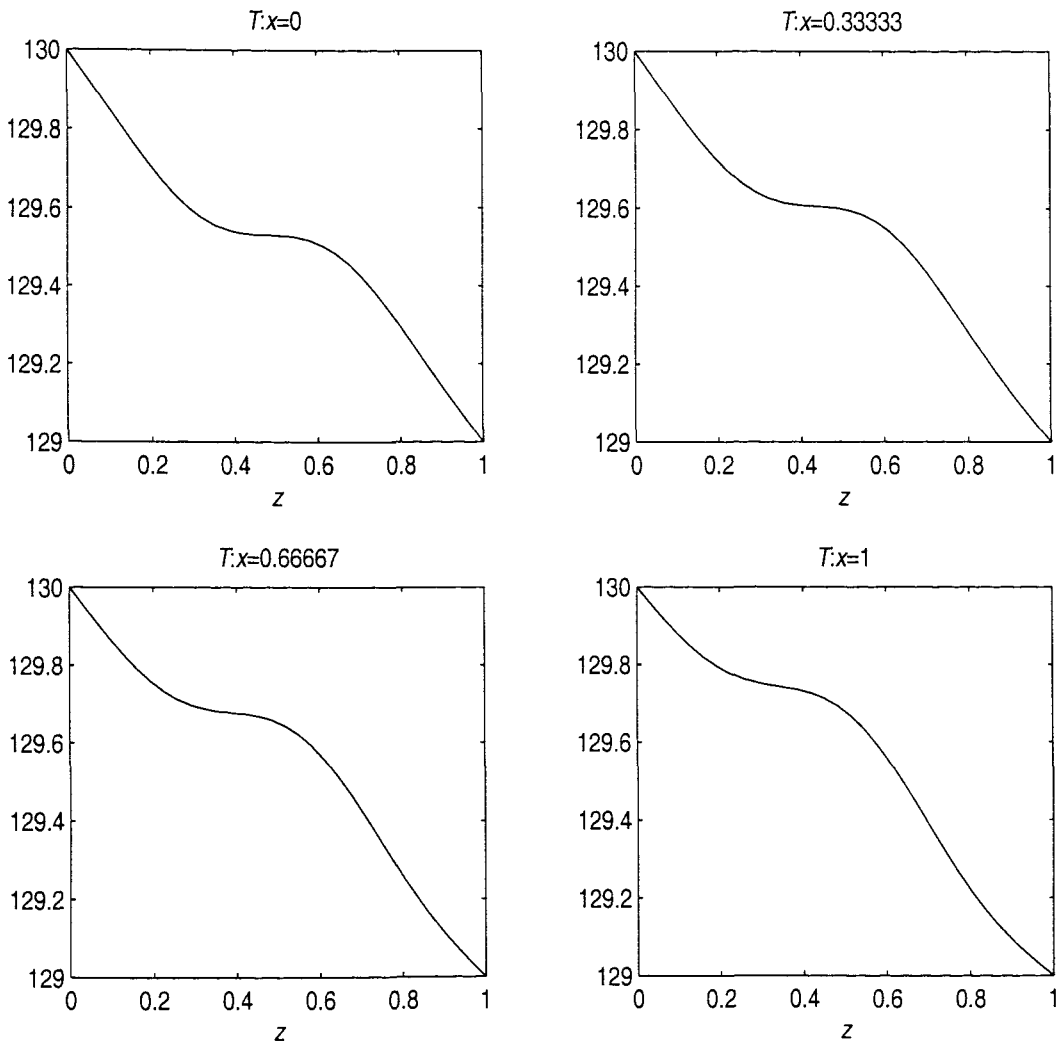


Figure 4.13: Temperature profile through a cross-section at four fixed points of the fluid at $t=0.4$.

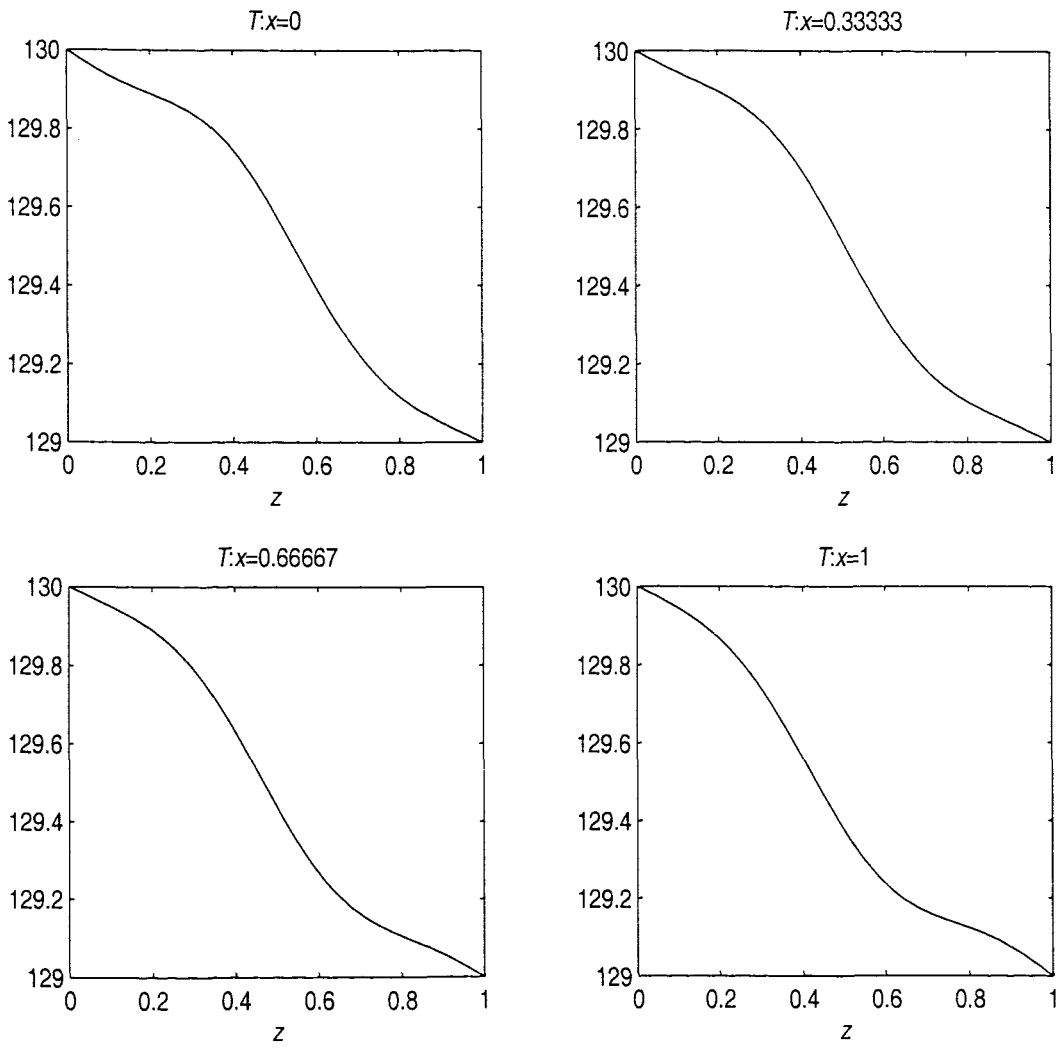


Figure 4.14: Temperature profile through a cross-section at four fixed points of the fluid at $t=0.6$.

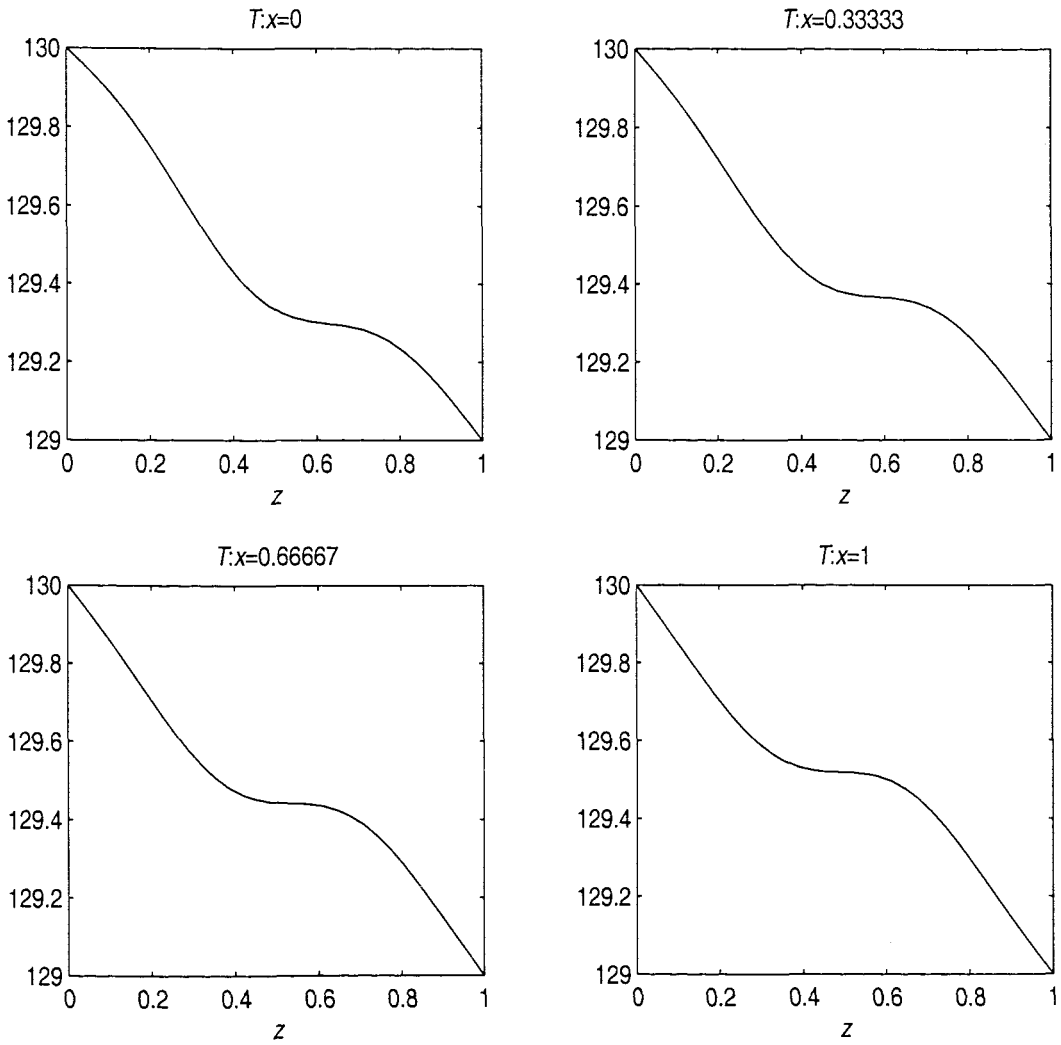


Figure 4.15: Temperature profile through a cross-section at four fixed points of the fluid at $t=0.8$.

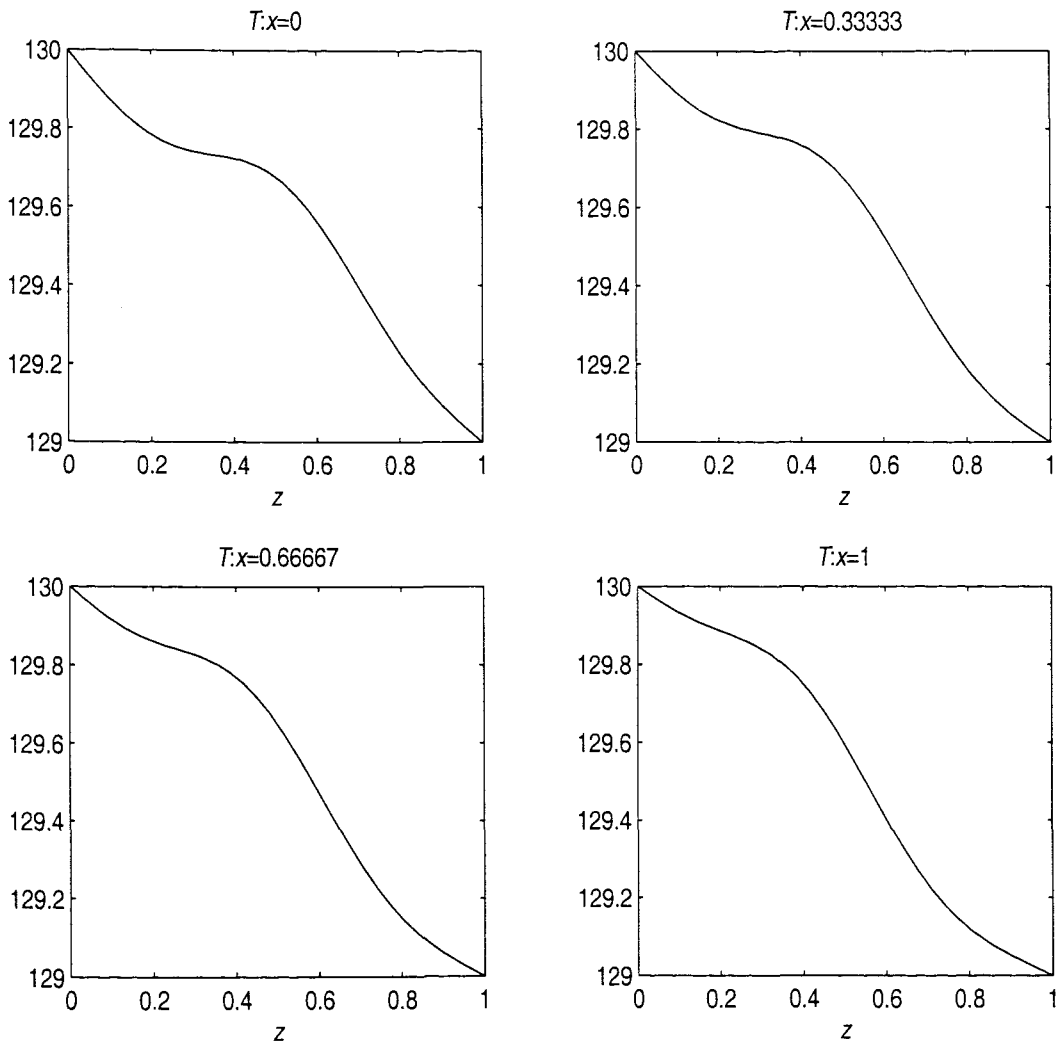


Figure 4.16: Temperature profile through a cross-section at four fixed points of the fluid at $t=1.0$.

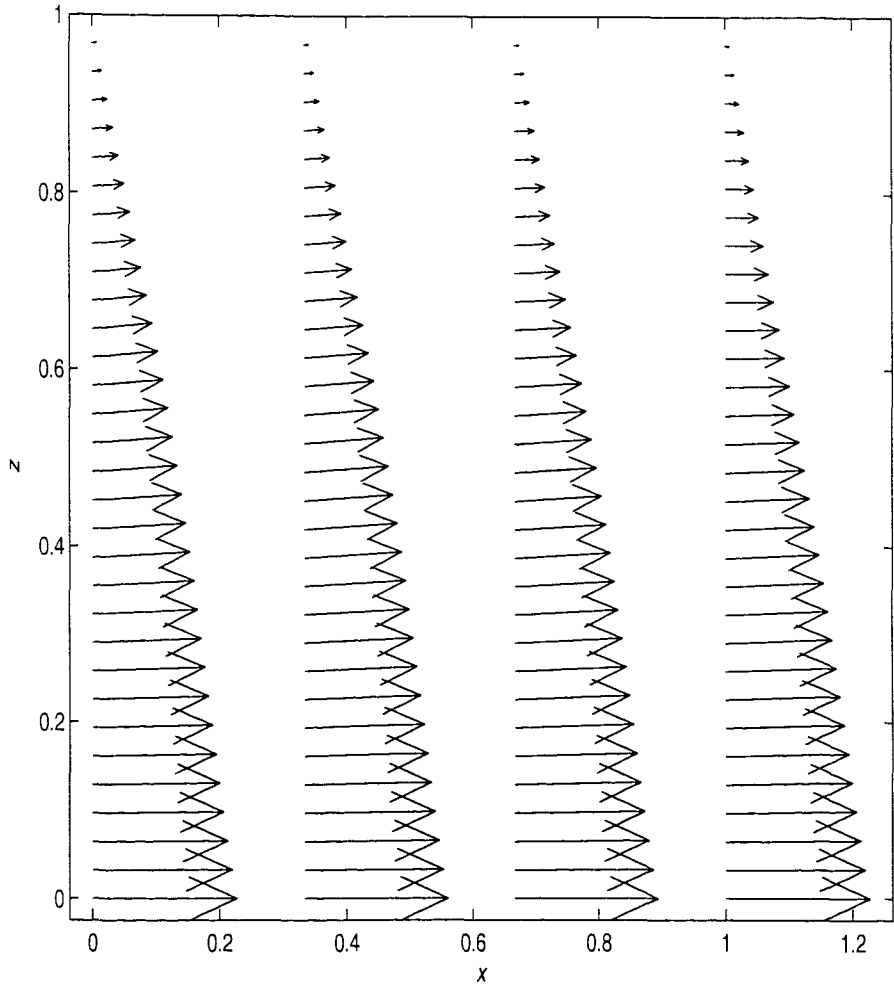


Figure 4.17: Velocity profile at $t=0.0$. The length and direction of the arrows represent the magnitude and direction of the velocity respectively.

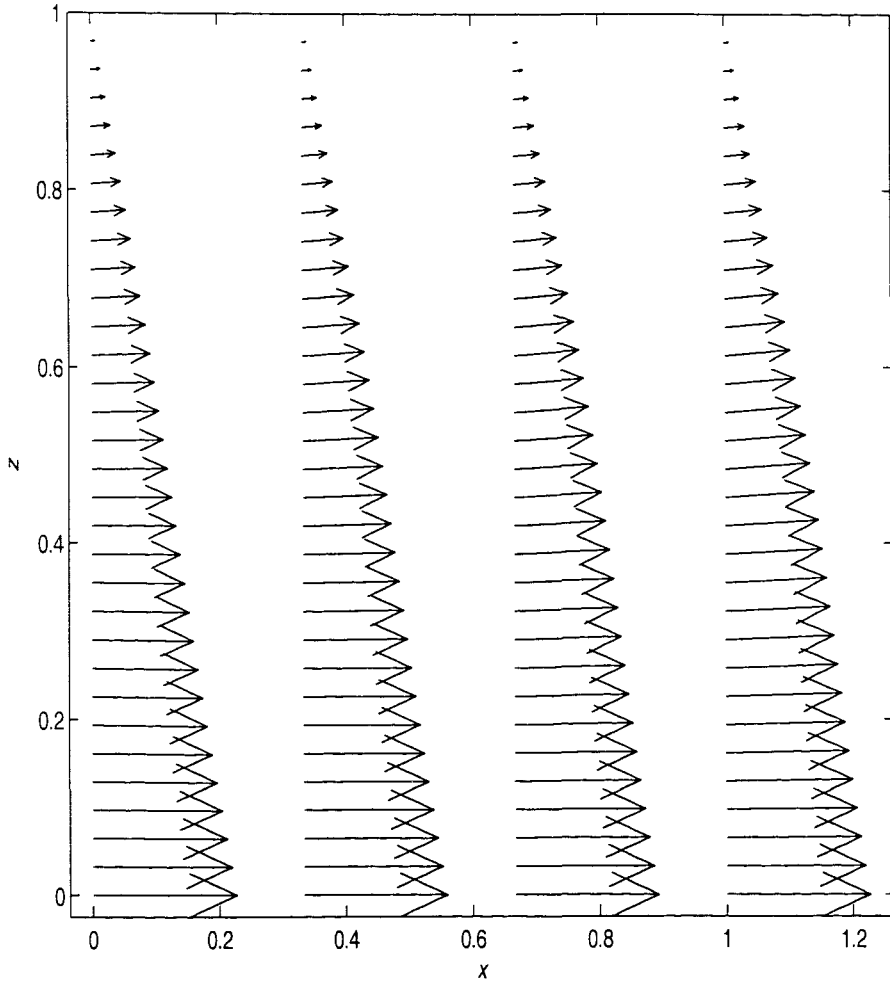


Figure 4.18: Velocity profile at $t=0.4$.

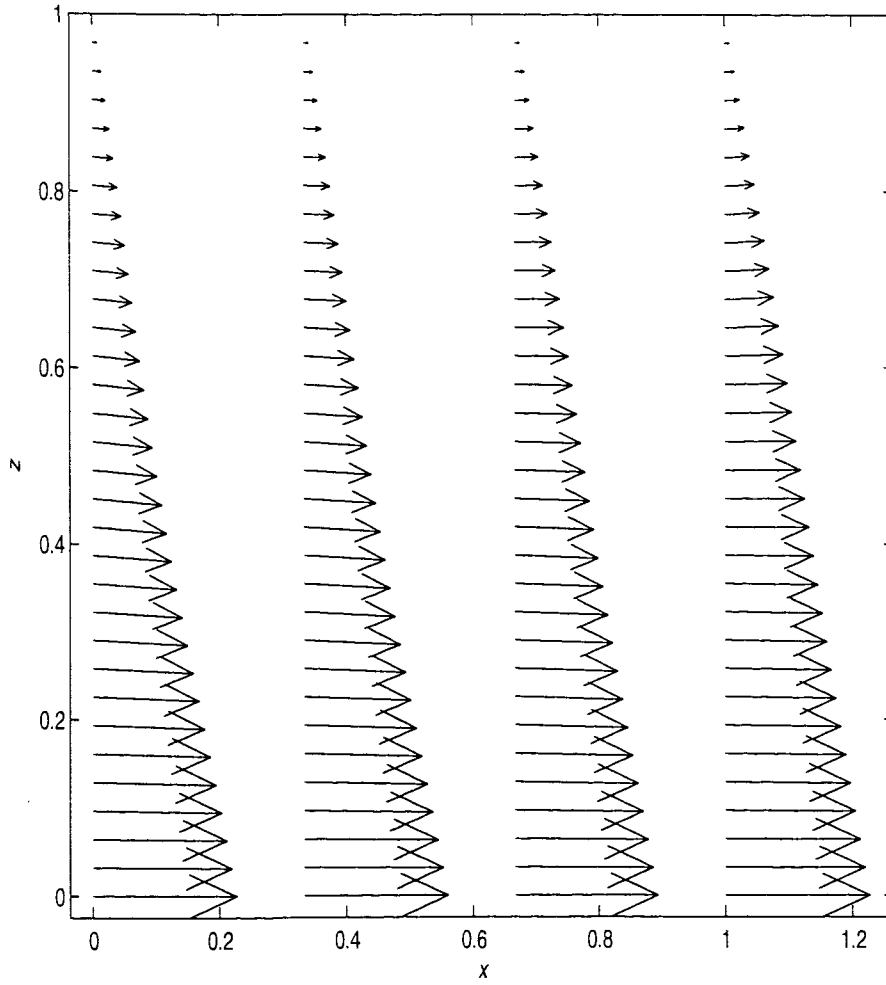


Figure 4.19: Velocity profile at $t=0.8$.

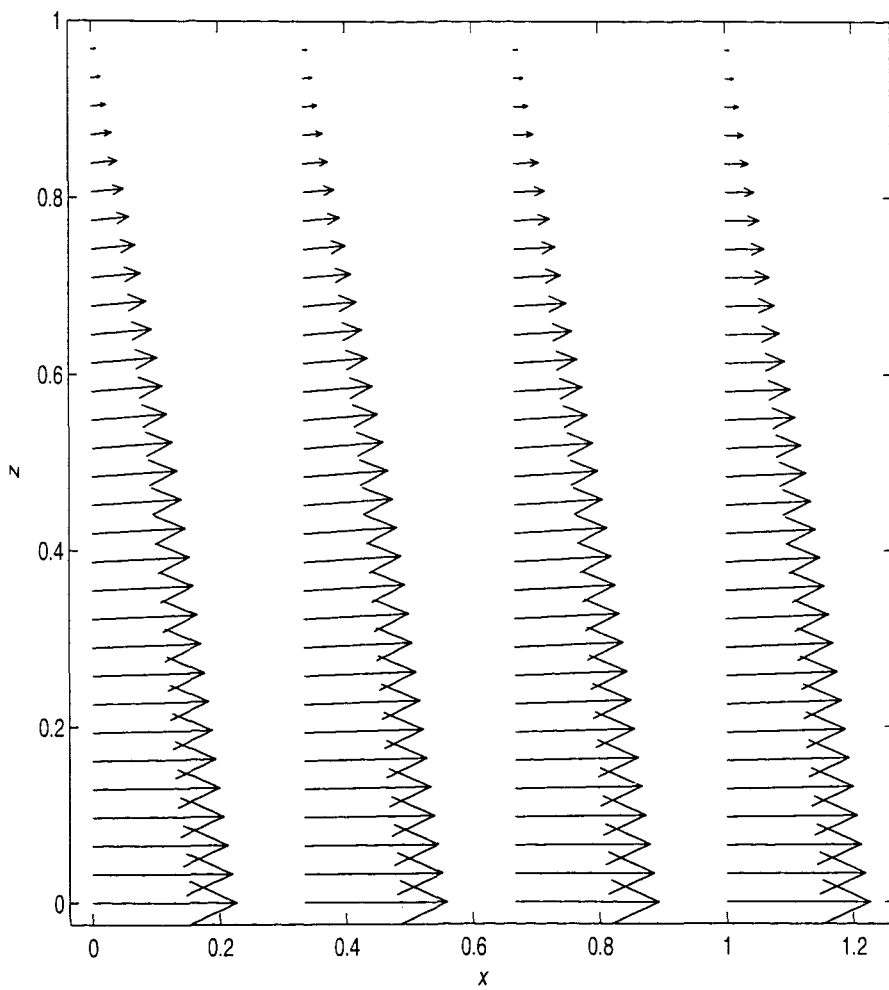


Figure 4.20: Velocity profile at $t=1.0$.

the layer could be three times larger than that observed experimentally and therefore does not corroborate the theory that the conduction layer thickness is determined by the working assumption.

We proceeded to examine the same layer with a supercritical Rayleigh number, so that convection existed, in order to see whether the conduction layer could then be observed in the fluid and to examine the temperature profile. Although a large temperature gradient could be seen in the profile at certain time periods, this was not consistent throughout. Also a stationary layer at the top of the fluid could not be observed. Therefore we conclude that with this model, we are neither able to support the working assumption nor observe a region near the surface with properties similar to those described for the conduction layer.

4.2 Micro Convection Eddies near the Surface

In this section we shall test the second conjecture given at the beginning of the chapter, namely that the temperature fluctuations observed at the surface of cryogenic mixtures are due to micro-convection eddies. This will be done by constructing a simple analytical model of micro-convection eddies for a LIN/LOX mixture. We will ignore any thermal effects on the density which are known to cause this rollover and assume that each micro-convection event occurs when all the LIN has evaporated from the surface. Thermal fluctuations observed to a lesser extent in pure LIN suggest that this assumption is not strictly true. However, we shall prove that the concentration change in mixtures has a far greater effect on the density at the surface. The frequency of these thermal fluctuations will be calculated and compared to those observed experimentally.

Thermal fluctuations in a LIN/LOX mixture

For our calculations, we shall consider a LIN/LOX mixture with only LIN evaporating. This is a reasonable assumption since the surface is at its saturation temperature, assumed a constant. This temperature is between the boiling points of LIN, at 77.4K and LOX, at 90.2K. Thus the LIN in the mixture will evaporate far more readily than the LOX although some LOX will evaporate by virtue of the Maxwellian distribution (see Figure 4.21). This distribution is calculated using statistical mechanics and shows that at any temperature, some molecules of LOX will have a great enough speed to

evaporate out of the mixture. This small fraction can, however, be ignored to a first approximation. To begin the mathematical model, we shall consider a tank, initially

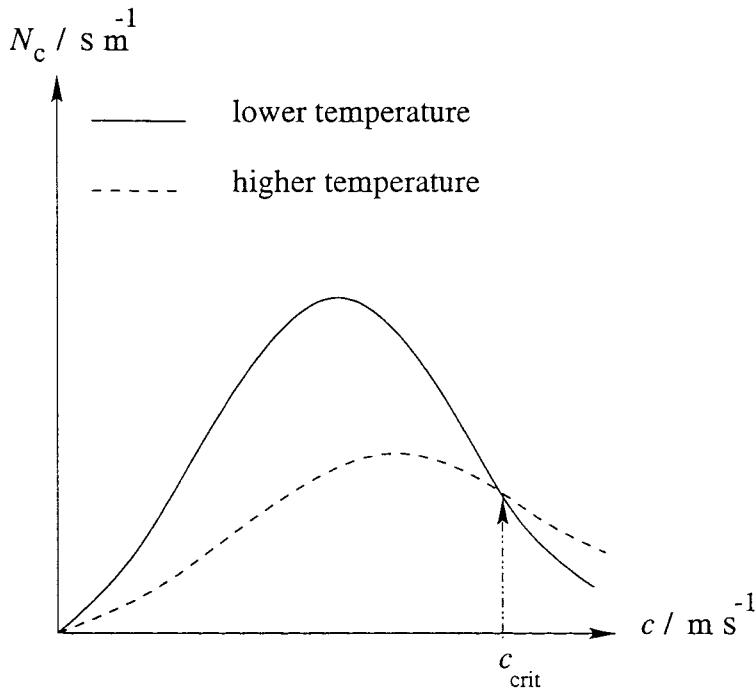


Figure 4.21: The Maxwellian distribution. N is defined so that $N_c \delta c$ is the number of molecules with speeds between c and $(c + \delta c)$ at a particular temperature. c_{crit} is the critical velocity for a particle to escape from the surface of the liquid.

of volume V_0 (m^3), containing 20% LOX and 80% LIN, the same values as those used in the experiments performed by Beduz and Scurlock(1996). Suppose f is the rate at which the volume leaves the system (m^3s^{-1}) through evaporation and that there is no other means of fluid loss. $Q(t)$ will be taken as the mass of nitrogen (kg) in the tank at any one time. Then the time taken for all the LIN to evaporate from the thin surface layer, up to the stage when it is replenished from below, is the time between each spike in the temperature profile. We shall calculate and compare our results to experimental data, which suggests that the frequency of these thermal fluctuations is 1-2 per second.

So, in order to find the time taken for this process to occur, we need to find the rate of change of LIN and then integrate this between the initial mass of LIN in the tank and the mass of LIN in the tank when the molecules in the thin surface layer have evaporated.

The volume of the fluid (LIN and LOX) in the tank at any one time = $V_0 - ft$.

So the density of nitrogen in the tank at any one time = $\frac{Q(t)}{V_0 - ft}$.

Now the rate of change of Q with time, $\frac{dQ(t)}{dt}$ = rate at which LIN enters the tank
 (= 0) – rate at which it
 leaves the system.

So

$$\frac{dQ(t)}{dt} = \frac{-Q(t)}{V_0 - ft}f. \quad (4.40)$$

At $t = 0$, $Q = a$, where $a = 4\rho_{\text{LIN}}V_0/5$ is the mass (kg) of the LIN in the whole tank initially.

So integrating equation (4.40):

$$\int_a^b \frac{dQ}{Q} = \int_0^t \frac{-f}{V_0 - ft} dt,$$

where $b = a - 4Ad\rho_{\text{LIN}}/5$ is the mass (kg) of the LIN in the tank when all the LIN has evaporated from the thin surface layer, with $A = \pi r^2$, as the surface area (m^2) of the mixture in contact with the vapour, r being the radius (m) of the cylinder and d being the depth (m) of the thin surface layer, gives

$$\begin{aligned} t &= \frac{V_0}{f} \left(1 - \frac{b}{a}\right), \\ &= \frac{V_0 d}{fh_0} \end{aligned} \quad (4.41)$$

with h_0 as the initial height (m) of the mixture in the tank so $V_0 = \pi r^2 h_0$.

Note that here the quantity evaporating is calculated as the rate of change of volume (m^3s^{-1}). In experiments and previous models, we have considered the mass flux lost through evaporation ($\text{kgm}^{-2}\text{s}^{-1}$). We find that the rate at which volume leaves the system is

$$f = \frac{4\dot{m}A}{5\rho_g} \quad (4.42)$$

where \dot{m} is the mass flux ($\text{kgm}^{-2}\text{s}^{-1}$) and ρ_g is the density (kgm^{-3}) of nitrogen gas.

So the time between each spike in the temperature profile is

$$t = \frac{5\rho_g d}{4\dot{m}} \quad (4.43)$$

To find a numerical value of the time, we need to calculate the mass flux through evaporation. Atkinson-Barr(1989) finds the modified mass flux for LIN, \dot{m}^* , experimentally as:

$$\dot{m}^* = \left(\frac{1}{33}\right)^{(1/3)} \delta T^{1.085} \quad (4.44)$$

with the modified mass flux defined by

$$\dot{m}^* = \dot{m}L \left(\frac{\nu}{\kappa^2 g \beta_T \rho_{\text{LIN}}^3 c^3} \right) \quad (4.45)$$

where $\delta T = T_{\text{bulk}} - T_{\text{sat}}$, is the difference in temperature (K) between the bulk and the surface layers; L is the latent heat of vaporisation (Jkg^{-1}); ν is the kinematic viscosity (m^2s^{-1}); $\kappa = k/\rho_{\text{LIN}}c$ is the thermal diffusivity (m^2s^{-1}) of LIN, k is the thermal conductivity ($\text{Wm}^{-1}\text{K}^{-1}$), ρ is the density (kgm^{-3}) of LIN and c is the specific heat capacity ($\text{Jkg}^{-1}\text{K}^{-1}$); g is the acceleration (ms^{-2}) due to gravity and β_T is the thermal expansion coefficient (K^{-1}).

For LIN:

$$L = 199 \times 10^5 \text{Jkg}^{-1}, \nu = 1.943 \times 10^{-7} \text{m}^2\text{s}^{-1}, \kappa = 6.03 \times 10^{-8} \text{m}^2\text{s}^{-1}, g = 9.81 \text{ms}^{-2}, \beta_T = 5.63 \times 10^{-3} \text{K}^{-1}, \rho_{\text{LIN}} = 808 \text{kgm}^{-3} \text{ and } c = 2.051 \times 10^3 \text{Jkg}^{-1}\text{K}^{-1}.$$

Substituting this data into equations (4.44) and (4.45), yields

$$\dot{m} = 2.6119 \times 10^{-3} \delta T^{1.085} \text{kgm}^{-2}\text{s}^{-1}$$

Also $\rho_g = 1.18 \text{kgm}^{-3}$, $d = 200 \mu\text{m}$ and $\delta T = 0.21 \text{K}$.

Substituting this into equation (4.43), we find that:

$$t = 0.61 \text{s}$$

This agrees with experimental data that these thermal fluctuations have a frequency of 1-2 per second (refer to Figure 4.2).

4.2.1 Discussion of temperature fluctuations

This simple calculation to find the time taken for each thermal fluctuations agrees with experimental data. This is not enough to prove beyond doubt the conjecture that the temperature fluctuations observed at the surface of cryogenic mixtures are due to micro-convection eddies which replenish the proportion of LIN at the surface is correct. However, it does support the theory.

4.3 Conclusions of the Instabilities at the Surface

In the first section of this chapter we discussed the approximation made in previous experimental studies that the thickness of the conduction layer observed at the surface of cryogenic fluids is due to the restriction made by the critical Rayleigh number, above which the fluid in the layer will start convecting. We set up an analytical model for the Bénard convection in the conduction region of the fluid, which we solved computationally (validating it in a simple case against existing work). We then showed that although this theory gives the correct order of magnitude, it would allow the thickness to be a factor of three larger than seen to exist and therefore this approximation could not be justified in our model. Although this approximation may still hold, in that the thickness can never exceed such a thickness, there must be some other property of the fluid which restricts the thickness to that seen experimentally. At this stage, therefore, we are unable to theoretically predict the thickness of the layer which appears to be an important factor in the evaporation rate. We shall return to this subject in Chapter 5.

In the second section we constructed a simple model which supported the theory that the thermal fluctuations seen to exist at the surface are due to micro-convection eddies which replenish the LIN lost through evaporation. Thus the surface may be considered to 'rollover' with the rest of the fluid frequently. This model, however, neglects the heat entering the system from the side walls. This flux of heat, and the isothermal condition at the surface of the fluid would lead to density differences particularly at the surface and this could be another factor which induces micro-convection.

Chapter 5

Numerical Modelling Of An Evaporative Mixture

In this chapter, we will numerically analyse the behaviour of mixtures of cryogenic fluids in a two-dimensional rectangular vessel with natural convection and evaporation.

A number of investigations have been carried out on convection of Newtonian fluids in such vessels. De Vahl Davis(1968) examined the behaviour of a one-component fluid in a rectangular cavity, insulated on its horizontal boundaries and with the side walls at temperatures of T_c and T_h respectively, for values of the Rayleigh number up to 2×10^5 (in a square cavity), above which flow becomes turbulent. The equations were written in finite difference form, with forward differences used for time derivatives and second-order central differences for all space derivatives. The resulting finite difference approximations were solved by an alternating-direction implicit algorithm. It was found that high Prandtl numbers exert a stabilising influence on the numerical solution. De Vahl Davis(1983) later published benchmark solutions to this problem. This was closely followed by the work of Markatos and Pericleous(1984) who studied the same problem and included benchmark solutions for turbulent flow.

More recently, papers have been written which include the effects of a concentration gradient added to the classical problem, causing double-diffusive convection. Gebhart and Pera(1971) were amongst the first to numerically study double-diffusion for cases of vertical laminar fluid motion along surfaces and in plumes. Their work focused on the influence of non-dimensional parameters relevant to the process, namely the Prandtl number and the Schmidt number, defined as the ratio of the kinematic viscosity to the



molecular diffusivity, on the heat and mass transport. A fundamental study of the scale analysis relative to heat and mass transport processes within cavities, subjected to horizontal temperature and concentration gradients, was given by Bejan(1985). Béghein *et al.*(1992) considered steady-state double-diffusion in a square cavity filled with air. The temperature conditions used by De Vahl Davies(1968), were placed on the boundaries and either augmenting or opposing concentration buoyancy forces were added. The upper and lower horizontal walls were both adiabatic and impermeable as before. The numerical procedure was based on the SIMPLER algorithm. The effects of varying the solutal Rayleigh number on the concentration and temperature flows were shown.

Shi(1990) modelled convection and rollover in mixtures of nitrogen and oxygen in a two layer system with each layer having a different concentration. This system was contained within a rectangular vessel that was subjected to a uniform heat flux through the two vertical walls. Again all sides of the box were assumed to be impermeable and the base to be insulated, but here the top free surface of the fluid was assumed to be isothermal, at the saturation temperature. The predicted concentration and temperature distributions throughout the process was examined.

No previous studies of double-diffusive convection consider the effects of preferential evaporation at the surface. This constitutes a major omission in the case of Shi's model, in that preferential evaporation of LIN would leave an enriched and therefore heavier layer at the surface. In this chapter, we will derive an expression for the rate of evaporation of the solute and include this term in a model for the double-diffusive convection of one layer of a fluid in a vessel similar to that described by Shi, in order to understand the effects of this process. The way in which to include this process in a model of rollover is then examined.

5.1 One-Component Model in Cartesian Coordinates

5.1.1 Construction of problem and basic assumptions

We will initially develop our code to model the same problem as De Vahl Davis(1968, 1983) and use his published results to validate our code. This problem considers a square vessel containing a one-component fluid, insulated on the horizontal boundaries

and with the vertical walls $y = 0$ and $y = d$ at temperatures T_c and T_h respectively. The no-slip boundary condition applies at all four wall boundaries. The thermal-induced convective flows in a plane including the two walls at fixed temperatures are of interest, and assuming the cavity is infinite in the perpendicular direction, these flows may be regarded as two-dimensional. The solution domain is shown in Figure 5.1. In order to

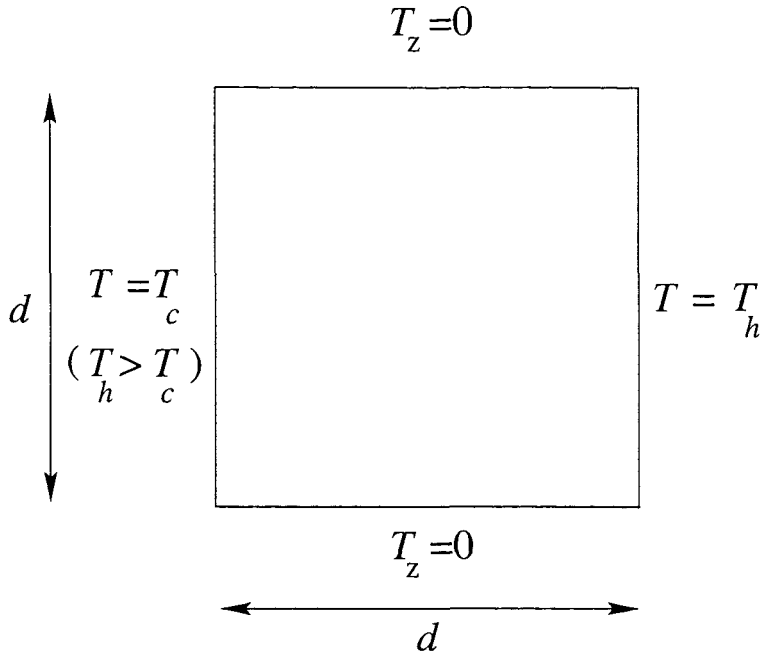


Figure 5.1: Solution domain for problem studied by De Vahl Davis(1968,1983).

model the flow, some basic assumptions are made about the fluid.

1. It is Newtonian.
2. It is incompressible.
3. We will also use the Boussinesq approximation, which states that if density variations are small, they can be neglected in so far as they affect inertia but must be retained in the buoyancy terms. The rigorous proof of this assumption is given in Acheson(1992).

5.1.2 Governing differential equations

The Navier-Stokes equations which describe Newtonian, incompressible fluid are

$$\frac{\partial u}{\partial t} + u \frac{\partial u}{\partial x} + w \frac{\partial u}{\partial z} = -\frac{1}{\rho} \frac{\partial p}{\partial x} + \nu \left(\frac{\partial^2 u}{\partial x^2} + \frac{\partial^2 u}{\partial z^2} \right) \quad (5.1)$$

$$\rho \left(\frac{\partial w}{\partial t} + u \frac{\partial w}{\partial x} + w \frac{\partial w}{\partial z} \right) = -\frac{\partial p}{\partial z} + \mu \left(\frac{\partial^2 w}{\partial x^2} + \frac{\partial^2 w}{\partial z^2} \right) - \rho g; \quad (5.2)$$

and the conservation of mass is

$$\frac{\partial u}{\partial x} + \frac{\partial w}{\partial z} = 0. \quad (5.3)$$

Finally the energy equation (ignoring viscous dissipation) in conservative form is

$$\frac{\partial T}{\partial t} + \frac{\partial(uT)}{\partial x} + \frac{\partial(wT)}{\partial z} = \kappa \left(\frac{\partial^2 T}{\partial x^2} + \frac{\partial^2 T}{\partial z^2} \right) \quad (5.4)$$

where $u(x, z, t)$ is the horizontal component of the velocity (ms^{-1}), $w(x, z, t)$ is the vertical component of the velocity (ms^{-1}), ρ is the density of the fluid (kgm^{-3}), $p(x, z, t)$ is the pressure (Pa), ν is the kinematic viscosity (assumed constant) (m^2s^{-1}), μ is the dynamic viscosity ($\text{kgm}^{-1}\text{s}^{-1}$), g is the acceleration due to gravity (ms^{-2}), T is the temperature (K) and κ is the thermal diffusivity (m^2s^{-1}). Applying the Boussinesq approximation, $\rho = \rho_0(1 - \beta_T(T - T_0))$, where ρ_0 is the density (kgm^{-3}) when $T = T_0$, T_0 is the temperature (K) in a reference state of hydrostatic equilibrium and β_T is the thermal expansion coefficient (K^{-1}), to equation (5.2), gives

$$\frac{\partial w}{\partial t} + u \frac{\partial w}{\partial x} + w \frac{\partial w}{\partial z} = -\frac{1}{\rho_0} \frac{\partial p}{\partial z} + \nu \left(\frac{\partial^2 w}{\partial x^2} + \frac{\partial^2 w}{\partial z^2} \right) + g\beta_T(T - T_0). \quad (5.5)$$

Note that there are four dependent variables in the problem: the velocity components u and w , the pressure p , and the temperature T . The pressure may be eliminated by cross-differentiating equations (5.1) and (5.5) to give the vorticity-transport equation:

$$\frac{\partial \eta}{\partial t} + \frac{\partial(u\eta)}{\partial x} + \frac{\partial(w\eta)}{\partial z} = \nu \left(\frac{\partial^2 \eta}{\partial x^2} + \frac{\partial^2 \eta}{\partial z^2} \right) - g\beta_T \frac{\partial T}{\partial x} \quad (5.6)$$

where η is the vorticity, defined as

$$-\eta = \frac{\partial w}{\partial x} - \frac{\partial u}{\partial z}. \quad (5.7)$$

The velocity components, u and w , may also be expressed as derivatives of the stream function, ψ ,

$$u = \frac{\partial \psi}{\partial z}, \quad w = -\frac{\partial \psi}{\partial x}.$$

Substituting the above expressions into equation (5.7), gives the Poisson equation

$$\frac{\partial^2 \psi}{\partial x^2} + \frac{\partial^2 \psi}{\partial z^2} = \eta.$$

Thus a new set of differential equations, the so-called vorticity-stream formulation, is formed:

$$\frac{\partial \eta}{\partial t} + \frac{\partial \psi}{\partial z} \frac{\partial \eta}{\partial x} - \frac{\partial \psi}{\partial x} \frac{\partial \eta}{\partial z} = \nu \left(\frac{\partial^2 \eta}{\partial x^2} + \frac{\partial^2 \eta}{\partial z^2} \right) - g\beta_T \frac{\partial T}{\partial x} \quad (5.8)$$

$$\frac{\partial T}{\partial t} + \frac{\partial \psi}{\partial z} \frac{\partial T}{\partial x} - \frac{\partial \psi}{\partial x} \frac{\partial T}{\partial z} = \kappa \left(\frac{\partial^2 T}{\partial x^2} + \frac{\partial^2 T}{\partial z^2} \right) \quad (5.9)$$

$$\text{and} \quad \frac{\partial^2 \psi}{\partial x^2} + \frac{\partial^2 \psi}{\partial z^2} = \eta. \quad (5.10)$$

Note that the problem has been reduced to three differential equations in three unknowns.

5.1.3 Non-dimensionalising the governing equations

The problem may now be converted to non-dimensionalised form in order to give an easy comparison of the important parameters in the problem. Scaling using the thermal diffusivity, κ and the height/width of box, d , together with $T - T_c / (T_h - T_c)$ for temperature, the dimensionless form of all variables may be obtained:

$$\left. \begin{aligned} \bar{x} = x/d \quad , \quad \bar{z} = z/d \quad , \quad \bar{t} = t/(d^2/\kappa) \quad , \quad \bar{T} = (T - T_c)/(T_h - T_c) \\ \bar{u} = u/(\kappa/d) \quad , \quad \bar{w} = w/(\kappa/d) \quad , \quad \bar{\psi} = \psi/\kappa \quad , \quad \bar{\eta} = \eta/(\kappa/d^2). \end{aligned} \right\} \quad (5.11)$$

Substituting the dimensionless variables into equations (5.8) and (5.9) and rearranging, gives (dropping the over-bars)

$$\frac{\partial \eta}{\partial \bar{t}} + \frac{\partial \psi}{\partial \bar{z}} \frac{\partial \eta}{\partial \bar{x}} - \frac{\partial \psi}{\partial \bar{x}} \frac{\partial \eta}{\partial \bar{z}} = \text{Pr} \left(\frac{\partial^2 \eta}{\partial \bar{x}^2} + \frac{\partial^2 \eta}{\partial \bar{z}^2} \right) - \text{PrRa}_T \frac{\partial T}{\partial \bar{x}} \quad (5.12)$$

$$\frac{\partial T}{\partial \bar{t}} + \frac{\partial \psi}{\partial \bar{z}} \frac{\partial T}{\partial \bar{x}} - \frac{\partial \psi}{\partial \bar{x}} \frac{\partial T}{\partial \bar{z}} = \left(\frac{\partial^2 T}{\partial \bar{x}^2} + \frac{\partial^2 T}{\partial \bar{z}^2} \right) \quad (5.13)$$

where $\text{Pr} = \nu/\kappa$ is the Prandtl number and Ra_T is the thermal Rayleigh number defined as

$$\text{Ra}_T = \frac{g\beta_T(T_h - T_c)d^3}{\kappa\nu}.$$

The form of the Poisson equation, (5.10), remains unchanged.

5.1.4 Boundary and initial conditions

By initially modelling the problem described, it will be possible to validate the results of our numerical code with benchmark solutions (De Vahl Davis, 1983, Markatos and Pericleous, 1984). The published benchmark solutions for two-dimension natural convection are obtained for the steady state case.

De Vahl Davis(1983) considers a two dimensional flow of a Boussinesq fluid with a Prandtl number of 0.71 (air) in an upright square cavity with the following non-dimensionalised boundary conditions:

At $x = 0$:

$$u = 0 \quad , \quad w = 0 \quad , \quad \psi = 0 \quad , \quad T = 0$$

At $x = 1$:

$$u = 0 \quad , \quad w = 0 \quad , \quad \psi = 0 \quad , \quad T = 1$$

At $z = 0$:

$$u = 0 \quad , \quad w = 0 \quad , \quad \psi = 0 \quad , \quad \frac{\partial T}{\partial z} = 0$$

At $z = 1$:

$$u = 0 \quad , \quad w = 0 \quad , \quad \psi = 0 \quad , \quad \frac{\partial T}{\partial z} = 0$$

The non-dimensionalised initial conditions are:

$$u = 0 \quad , \quad w = 0 \quad , \quad \psi = 0 \quad , \quad T = 0$$

This problem will be solved for velocities and temperature at two Rayleigh numbers and compared with the benchmark solutions.

5.2 Numerical Procedure

5.2.1 Discretisation method

Now that we have a set of differential equations with suitable boundary conditions, we need to use a discretisation method to transform the equations into a set of algebraic equations which may then be solved using an established numerical method.

Here we opt for an explicit scheme whereby a general variable is expressed explicitly in terms of quantities which are known at the beginning of the time step. Although a stability criteria will be required which will restrict the size of the time step, we feel

that the advantage of the computational simplicity of an explicit scheme is more than justification for its use.

The most straightforward approach would be to choose a Forward Time Centred Space (FTCS) representation, as shown in Figure 5.2. The discretisation for a general variable, $\xi(i,l)$, where i is the number of spatial points on a grid of length d , and l is the number of time points, would be as follows:

$$\frac{\partial \xi(i,l)}{\partial t} = \frac{\xi(i,l+1) - \xi(i,l)}{\delta t} \quad \text{forward difference} \quad (5.14)$$

$$\frac{\partial \xi(i,l)}{\partial x} = \frac{\xi(i+1,l) - \xi(i-1,l)}{2\delta x} \quad \text{central difference} \quad (5.15)$$

$$\text{and} \quad \frac{\partial^2 \xi(i,l)}{\partial x^2} = \frac{\xi(i+1,l) - 2\xi(i,l) + \xi(i-1,l)}{(\delta x)^2} \quad \text{central difference} \quad (5.16)$$

where δx is the length step such that $i\delta x = d$, and δt is the time step.

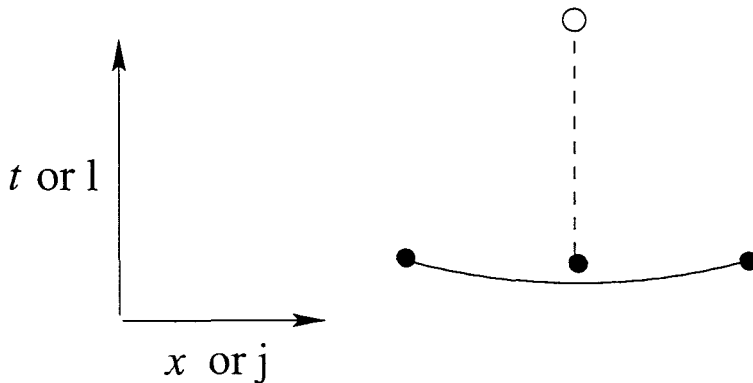


Figure 5.2: Representation of the Forward Time Centred Space (FTCS) differencing scheme reproduced from Press *et al.*(1992). In this and subsequent figures, the open circle is the new point at which the solution is desired; filled circles are known points whose function values are used in calculating the new point; the solid lines connect points that are used to calculate spatial derivatives; the dashed lines connect points that are used to calculate time derivatives.

Stability analysis, however, quickly uncovers the instability of applying central differences to the convection term.

Instead, we will choose an upwind scheme (Morton & Myers, 1994). This uses a forward time step and central differences for the second order derivatives, as with the FTCS scheme, but applies either forward or backward differences for the first derivatives depending on the upstream direction, as follows for a general variable,

$\xi(i, l)$:

$$\frac{\partial \xi(i, l)}{\partial x} = \begin{cases} (\xi(i, l) - \xi(i - 1, l)) / \delta x & \text{if } u(i, l) > 0, \\ (\xi(i + 1, l) - \xi(i, l)) / \delta x & \text{if } u(i, l) < 0. \end{cases} \quad (5.17)$$

This representation is shown in Figure 5.3. The advantage of this method is the ‘fidelity’ (Press *et al.*, 1992) of this scheme to the underlying physics. The numerical stability of this scheme as applied to our problem is discussed in a later subsection.

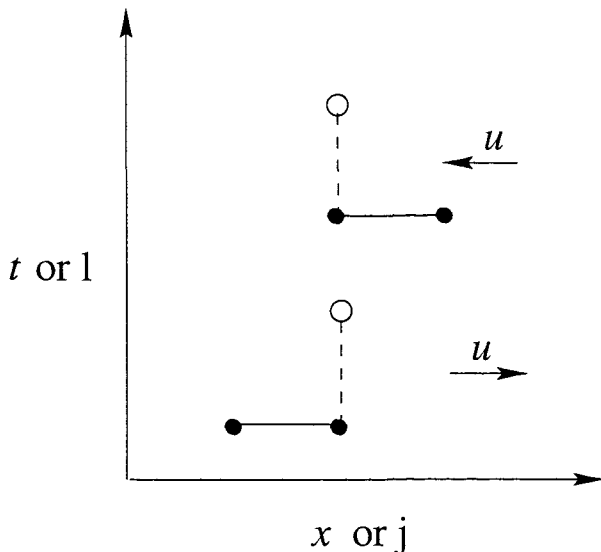


Figure 5.3: Representation of upwind scheme reproduced from Press *et al.*(1992). The upper scheme is stable when the advection constant u is negative, as shown; the lower scheme is stable when the advection constant u is positive, also as shown.

5.2.2 General differential equation

The vorticity and temperature equations (5.12) and (5.13) may both be fitted into the form of the following general differential equation, where ϕ is a general scalar variable:

$$\frac{\partial \phi}{\partial t} + \frac{\partial(u\phi)}{\partial x} + \frac{\partial(w\phi)}{\partial z} = \Gamma \left(\frac{\partial^2 \phi}{\partial x^2} + \frac{\partial^2 \phi}{\partial z^2} \right) + S_o \quad (5.18)$$

where $\phi = T$, $\Gamma = 1$, $S_o = 0$ for the temperature equation and $\phi = \eta$, $\Gamma = \text{Pr}$, $S_o = -\text{PrRa}_T \partial T / \partial x$ for the vorticity equation.

With the velocity substituted by the stream function and using the conservation of mass, this general equation can be written as:

$$\frac{\partial \phi}{\partial t} + \frac{\partial \psi}{\partial z} \frac{\partial \phi}{\partial x} - \frac{\partial \psi}{\partial x} \frac{\partial \phi}{\partial z} = \Gamma \left(\frac{\partial^2 \phi}{\partial x^2} + \frac{\partial^2 \phi}{\partial z^2} \right) + S_o.$$

Using the upwind scheme described in the last subsection, the general differential equation can then be discretised as

$$\begin{aligned} & \frac{\phi(i, j, l+1) - \phi(i, j, l)}{\delta t} + \frac{\partial\psi(i, j, l)}{\partial z} \frac{\partial\phi(i, j, l)}{\partial x} - \frac{\partial\psi(i, j, l)}{\partial x} \frac{\partial\phi(i, j, l)}{\partial z} = \\ & \Gamma \left(\frac{\phi(i+1, j, l) - 2\phi(i, j, l) + \phi(i-1, j, l)}{(\delta x)^2} + \frac{\phi(i, j+1, l) - 2\phi(i, j, l) + \phi(i, j-1, l)}{(\delta z)^2} \right) \\ & + S_o(i, j, l) \end{aligned} \quad (5.19)$$

where $\partial\psi(i, j, l)/\partial x$, $\partial\psi(i, j, l)/\partial z$, $\partial\phi(i, j, l)/\partial x$ and $\partial\phi(i, j, l)/\partial z$, may be discretised in the same way as equation (5.17). Similarly, the elliptic Poisson equation may be discretised to give

$$\begin{aligned} & \frac{\psi(i+1, j, l) - 2\psi(i, j, l) + \psi(i-1, j, l)}{(\delta x)^2} + \frac{\psi(i, j+1, l) - 2\psi(i, j, l) + \psi(i, j-1, l)}{(\delta z)^2} \\ & = \eta(i, j, l). \end{aligned} \quad (5.20)$$

5.2.3 Stability criterion

As explained before, a stability criterion is required when the system is discretised using an explicit scheme. This will give the maximum time step permitted for the numerical scheme to remain accurate. We will look here at the stability of the general equation (5.18). Suppose that θ is an approximate solution to the general equation, regarding it as an equation for ϕ with u , w and S_o known. Then it would satisfy the equation:

$$\begin{aligned} & \frac{\partial\theta(i, j, l)}{\partial t} + \frac{\partial(u(i, j, l)\theta(i, j, l))}{\partial x} + \frac{\partial(w(i, j, l)\theta(i, j, l))}{\partial z} = \\ & \Gamma \left(\frac{\partial^2\theta(i, j, l)}{\partial x^2} + \frac{\partial^2\theta(i, j, l)}{\partial z^2} \right) + S_o(i, j, l) \end{aligned} \quad (5.21)$$

If an exact solution, $\chi(i, j, l)$ was known to exist, the following equation would be satisfied:

$$\begin{aligned} & \frac{\partial\chi(i, j, l)}{\partial t} + \frac{\partial(u(i, j, l)\chi(i, j, l))}{\partial x} + \frac{\partial(w(i, j, l)\chi(i, j, l))}{\partial z} = \\ & \Gamma \left(\frac{\partial^2\chi(i, j, l)}{\partial x^2} + \frac{\partial^2\chi(i, j, l)}{\partial z^2} \right) + S_o(i, j, l) \end{aligned} \quad (5.22)$$

and so the numerical error would be $E(i, j, l) = \theta(i, j, l) - \chi(i, j, l)$, which would satisfy the equation given by (5.21) - (5.22)

$$\frac{\partial E(i, j, l)}{\partial t} + \frac{\partial(u(i, j, l)E(i, j, l))}{\partial x} + \frac{\partial(w(i, j, l)E(i, j, l))}{\partial z} = \Gamma \left(\frac{\partial^2 E(i, j, l)}{\partial x^2} + \frac{\partial^2 E(i, j, l)}{\partial z^2} \right)$$

which eliminates the source term from the stability problem. So we are now concerned with the stability of the general equation with $S_o = 0$.

We shall use von Neumann (also known as Fourier) stability analysis. This analysis is local and we imagine that the coefficients of the difference equations are varying so slowly that they can be considered constant in space and time. In that case, the independent solutions, or eigenmodes, of the difference equations are all of the form

$$\phi(i, j, l) = \lambda^l e^{Ik(i\Delta x + j\Delta z)}$$

where k is a real spatial wave number (which may take any value) and $\lambda = \lambda(k)$ is a complex number which depends on k . Since we are dealing with a grid aspect ratio of one and will use the same size length step in both the x and z directions, this may be re-written as

$$\phi(i, j, l) = \lambda^l e^{Ik\Delta x(i+j)} \quad (5.23)$$

The key fact is that the time dependence of a single eigenmode is nothing more than successive integer powers of the complex number λ . Therefore the difference equations are unstable (have exponentially growing modes) if $|\lambda(k)| > 1$ for some k . The number $\lambda(k)$ is called the amplification factor at a given wave number k .

To find $\lambda(k)$, we simply substitute (5.23) back into the discretised form of (5.18) (with $S_o = 0$), assuming that the velocity is constant and $u, w > 0$. Dividing by $\phi(i, j, l)$, we get

$$\lambda = 1 - \alpha\Delta x(u + w)(1 - e^{-Ik\Delta x}) + 2\Gamma\alpha(e^{Ik\Delta x} - 2 + e^{-Ik\Delta x})$$

where $\alpha = \Delta t / \Delta x^2$. Now

$$e^{Ik\Delta x} = \cos(k\Delta x) + I \sin(k\Delta x).$$

So

$$|\lambda| = \left((1 - 4\alpha\Delta x(u + w) \sin^2(\beta) (1 - \alpha\Delta x(u + w)) + 16\Gamma\alpha \sin^2(\beta) \right. \\ \left. (4\Gamma\alpha \sin^2(\beta) - 1) + 32\alpha^2\Gamma\Delta x(u + w) \sin^4(\beta) \right)^{1/2}$$

where

$$\beta = \frac{k\Delta x}{2}.$$

As mentioned above, for the equation to remain stable $|\lambda| \leq 1$. Since $\alpha > 0$ this may be simplified to

$$\alpha \leq \frac{1}{4\Gamma + \Delta x(u + w)}$$

and so

$$\Delta t \leq \frac{\Delta x^2}{4\Gamma + \Delta x(u + w)}.$$

This procedure is similarly repeated for different combinations of positive and negative components of velocity and, combined, gives the following constraint (Roache, 1976) on the time step:

$$\Delta t \leq \frac{\Delta x^2}{4\Gamma + \Delta x(|u| + |w|)}. \quad (5.24)$$

Thus the time step is restricted by the most tightly constrained differential equation, be it the vorticity, or the temperature equation. The Poisson equation does not require a stability criteria because it is not dependent on time.

5.2.4 Outline of the solution procedure

The solution procedure is a time-marching one. Following a set of initial values for each variable, the final solution is achieved by using the time-marching technique. In each time step the equations are solved in the following way:

1. Determine the time step using equation 5.24.
2. Using a central difference scheme, calculate the velocity from the stream function distribution to find the direction of the components of the velocity.
3. Transform these into an upwind scheme (forward or backward depending on the sign of the velocity component) for use in the equations.
4. Solve the temperature equation (5.12) explicitly for the new time step using the previous step's data.
5. Calculate the source term, $S_o = g\beta_T\partial T/\partial x$, in the vorticity equation, using the temperature solution from the old time step.
6. Solve the vorticity equation for the new time step explicitly.
7. Solve the Poisson equation to obtain the stream function distribution.

The process is repeated until a steady state is reached. This is judged to be achieved when the stream function between two consecutive time steps is less than 10^{-4} . Experimental evidence (Elder, 1968) indicates that provided the Rayleigh number is less than 10^8 , the convection may be assumed to be laminar. In the case of high Rayleigh numbers (greater than $10^7 - 10^8$) flow may become turbulent and so it may be difficult to reach a steady state.

5.2.5 Solution of the discretised Poisson equation - the multigrid method

We will solve the differential equation (5.10) using the multigrid method as implemented in Press *et al.*(1992). The method was first introduced in the 1970s by Brandt(1977) and is $O(N)$ in the number of grid points used, compared to standard relaxation methods which are typically $O(N^2)$ or $O(N^{3/2})$. The key idea is to introduce a hierarchy of grids. Methods such as Gauss-Seidel relaxation (Stoer and Bulirsch, 1993) tend to stall, since they do not attenuate smooth error modes. However a smooth error mode on a fine grid looks less smooth on a coarser grid and will be attenuated by further Gauss-Seidel iterations. The values on the coarser grid are then fed back onto the fine grid and by alternating between fine and coarse grids, the system relaxes more quickly. For further details of the application of multigrid methods to the solution of differential equation see Biggs(1988), Hackbusch(1985), Wesseling(1992), or Zwillinger(1997). Standard grid refinement is used to determine that, for Rayleigh numbers of the order of $10^3 - 10^7$, the solution is sufficiently accurate when 128 points are used. The coarse grid solution is derived by Gauss-Seidel relaxation.

The multigrid method can be understood by considering the simplest case of a two-grid method (based on Press *et al.*, 1992). Suppose we are trying to solve the linear elliptic problem

$$\mathcal{L}u = f \tag{5.25}$$

where \mathcal{L} is some linear elliptic operator and f is the source term. Discretising equation (5.25) on a uniform grid with mesh size h , the resulting linear algebraic equations may be written as

$$\mathcal{L}_h u_h = f_h. \tag{5.26}$$

Let \tilde{u}_h denote some approximate solution to equation (5.26). We will use u_h to denote

the exact solution to the difference equations (5.26). Then the error in \tilde{u}_h or the correction is

$$v_h = u_h - \tilde{u}_h.$$

The *residual* or *defect* is

$$d_h = \mathcal{L}_h \tilde{u}_h - f_h. \quad (5.27)$$

Since \mathcal{L}_h is linear, the error satisfies

$$\mathcal{L}_h v_h = -d_h. \quad (5.28)$$

At this point we need to make an approximation to \mathcal{L}_h in order to find v_h . The classical iteration methods, such as Jacobi or Gauss-Seidel, do this by finding, at each stage, an approximate solution of the equation

$$\hat{\mathcal{L}}_h \hat{v}_h = -d_h$$

where $\hat{\mathcal{L}}_h$ is a ‘simpler’ operator than \mathcal{L}_h and d_h has been modified. For example, $\hat{\mathcal{L}}_h$, is the diagonal part of \mathcal{L}_h for Jacobi iteration, or the lower triangle for Gauss-Seidel iteration. The next approximation is generated by

$$\tilde{u}_h^{\text{new}} = \tilde{u}_h + \hat{v}_h.$$

Now, let us consider, as an alternative, a completely different type of approximation to \mathcal{L}_h , one in which we ‘coarsify’ rather than ‘simplify’. That is, we form some appropriate approximation \mathcal{L}_H of \mathcal{L}_h on a coarser grid with mesh size H (we will take $H = 2h$). The residual equation (5.28) is now approximated by

$$\mathcal{L}_H v_H = -d_H. \quad (5.29)$$

Since \mathcal{L}_H has smaller dimensions, this equation will be easier to solve than equation (5.28). To define the defect d_H on the coarse grid, we need a restriction operator \mathfrak{R} that restricts d_h to the coarse grid:

$$d_H = \mathfrak{R}d_h. \quad (5.30)$$

The restriction operator is also called the *fine-to-coarse operator* or the *injection operator*. Once we have a solution \tilde{v}_H to equation (5.29), we need a *prolongation operator* \wp that prolongates or interpolates the correction to the fine grid:

$$\tilde{v}_h = \wp \tilde{v}_H. \quad (5.31)$$

The prolongation operator is also called the *coarse-to-fine operator* or the *interpolation operator*. Both \mathfrak{R} and \wp are chosen to be linear operators. Finally the approximation \tilde{u}_h can be updated:

$$\tilde{u}_h^{\text{new}} = \tilde{u}_h + \tilde{v}_h \quad (5.32)$$

One step of this *coarse-grid correction scheme* is thus:

Coarse-grid correction

1. Compute the defect on the fine grid from equation (5.27).
2. Restrict the defect by equation (5.30).
3. Solve equation (5.29) exactly on the coarse grid for the correction.
4. Interpolate the correction to the fine grid by equation (5.31).
5. Compute the next approximation by equation (5.32).

We will now examine the advantages and disadvantages of relaxation and the coarse-grid correction scheme. Consider the error v_h expanded into a discrete Fourier series. We shall call the components in the lower half of the frequency spectrum the *smooth components* and the high-frequency components the *nonsmooth components*. Relaxation becomes very slowly convergent in the limit $h \rightarrow 0$, i.e., when there are a large number of mesh points. The reason turns out to be that the smooth components are only slightly reduced in amplitude on each iteration. However, many relaxation methods reduce the amplitude of nonsmooth components by large factors on each iteration: they are good *smoothing operators*.

For instance a Gauss-Seidel iteration attenuates oscillatory components much faster, and this means that the contribution of the latter is almost eliminated after only a few iterations. The non-oscillatory terms, however, are left and they account for the slower rate of attenuation in the asymptotic regime. In other words the Gauss-Seidel scheme is a ‘smoother’: its effect after a few iterations is to filter out high frequencies from the ‘signal’ (Iserles, 1996).

For the two-grid iteration, on the other hand, components of the error with wavelengths $\leq 2H$ are not even representable on the coarse grid and so cannot be reduced to zero on this grid. But it is exactly these high-frequency components that can be

reduced by relaxation on the fine grid. This leads us to combine the ideas of relaxation and coarse-grid correction:

Two-grid iteration

1. Pre-smoothing: Compute \tilde{u}_h by applying $\nu_1 \geq 0$ steps of a relaxation method to \tilde{u}_h .
2. Coarse-grid correction: As above, using \tilde{u}_h to give \tilde{u}_h^{new} .
3. Post-smoothing: Compute \tilde{u}_h^{new} by applying $\nu_2 \geq 0$ steps of the relaxation method to \tilde{u}_h^{new} .

It is only a short step from the above two-grid method to a multigrid method. Instead of solving the coarse-grid defect equation (5.29) exactly, we can get an approximate solution of it by introducing an even coarser grid and using the two-grid iteration method. If the convergence factor of the two-grid method is small enough, we will need only a few steps of this iteration to obtain a good enough approximate solution. We denote the number of such iterations by γ . Obviously we can apply this idea recursively down to some coarsest grid. There the solution is found easily, for example by direct matrix inversion or by iterating the relaxation scheme to convergence.

One iteration of a multigrid method, from finest grid to coarser grids and back to finest grid again, is called a *cycle*. The exact structure of a cycle depends on the value of γ , the number of two-grid iterations at each intermediate stage. The case $\gamma = 1$ is called a V-cycle, while $\gamma = 2$ is called a W-cycle (see Figure 5.2.5). These are the most important cases in practice.

So far we have described multigrid as an iterative scheme, where one starts with some initial guess on the finest grid and carries out enough cycles (V-cycles, W-cycles, ...) to achieve convergence. This is the simplest way to use multigrid: simply apply enough cycles until some appropriate convergence criterion is met. However, efficiency can be improved by using the *Full Multigrid Algorithm* (FMG), also known as the *nested iteration*.

Instead of starting with an arbitrary approximation on the finest grid (e.g., $u_h = 0$), the first approximation is obtained by interpolating from a coarse-grid solution:

$$u_h = \wp u_H \tag{5.33}$$

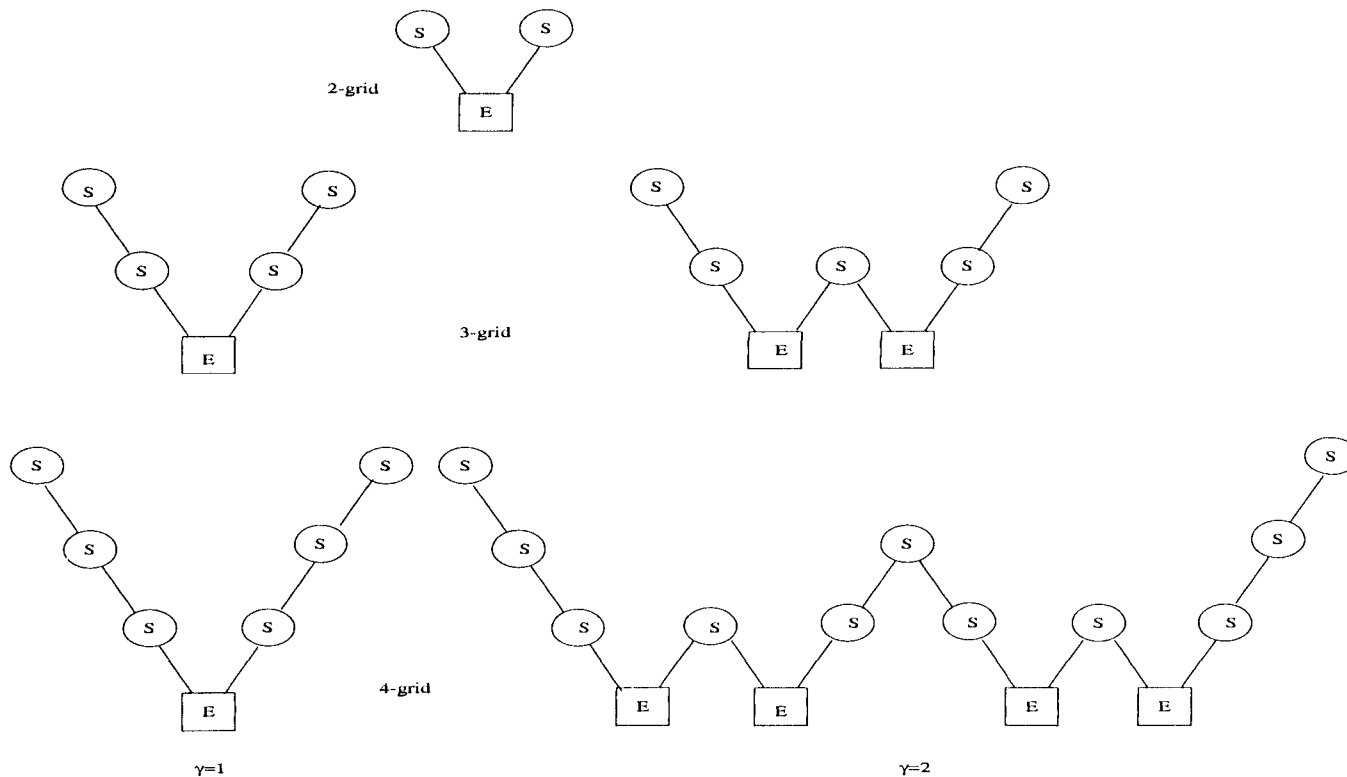


Figure 5.4: Structure of multigrid cycles reproduced from Press *et al.*(1992). S denotes smoothing, while E denotes exact solution on the coarsest grid. Each descending line, \backslash , denotes restriction (\mathfrak{R}) and each ascending line, $/$, denotes prolongation (\wp). The finest grid is at the top level of each diagram. For the V-cycles ($\gamma = 1$) the E step is replaced by one 2-grid iteration each time the number of grid levels is increased by one. For the W-cycles ($\gamma = 2$), each E step gets replaced by two 2-grid iterations.

The coarse-grid solution itself is found by a similar FMG process from even coarser grids. At the coarsest level, you start with the exact solution. Rather than proceed as in Figure 5.2.5, FMG gets to its solution by a series of increasingly tall ‘N’s’, each taller one probing a finer grid (see Figure 5.2.5). Note that ρ in equation (5.33) need not be

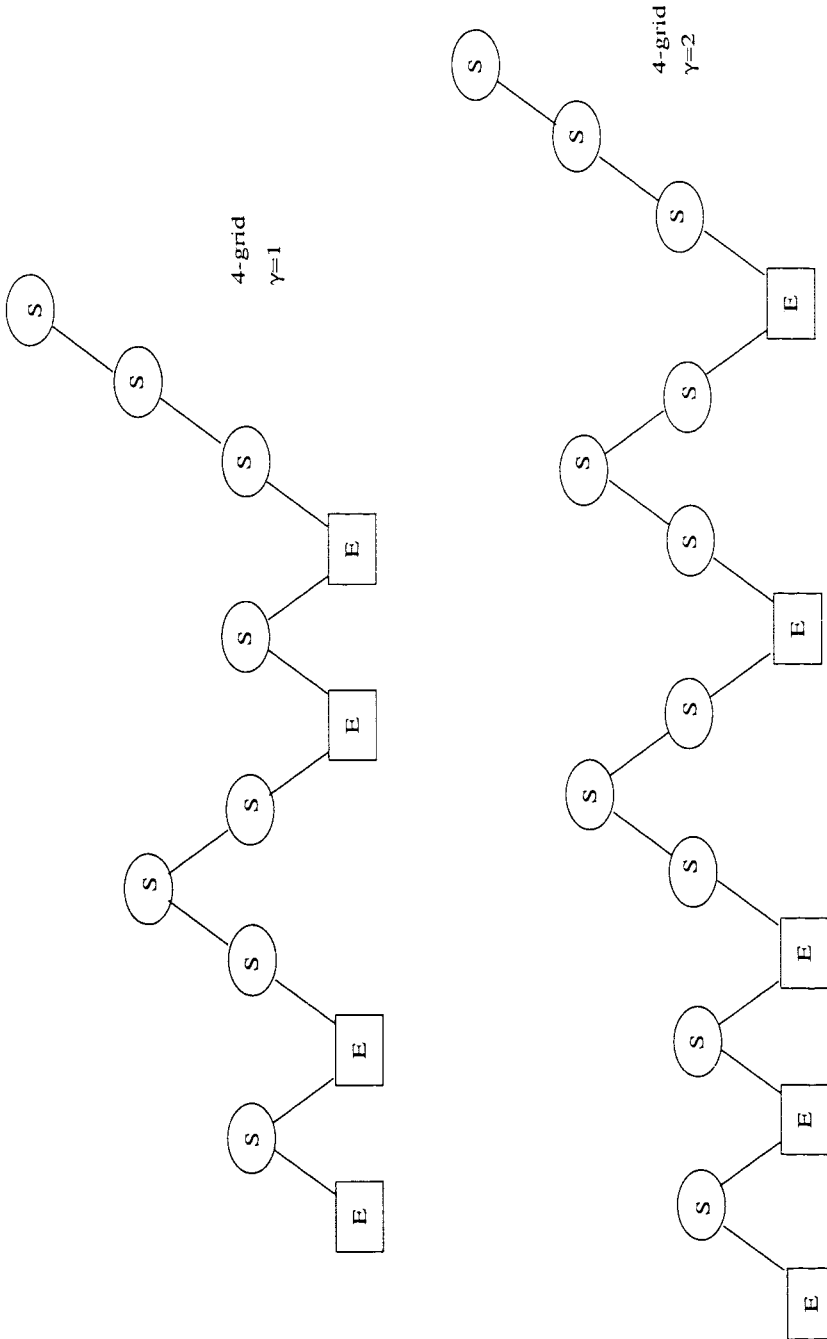


Figure 5.5: Structure of cycles for the full multigrid (FMG) method reproduced from Press *et al.*(1992). This method starts in the coarsest grid, interpolates, and then refines (by ‘V’s’), the solution onto grids of increasing fineness.

the same ρ used in the multigrid cycles. It should be at least of the same order as the

discretisation \mathcal{L}_h , but sometimes a higher-order operator leads to greater efficiency.

Usually only a couple of multigrid cycles are used at each level. We use $\gamma = 2$ throughout and apply one Gauss-Seidel smoothing iteration to each grid.

The simplest multigrid iteration (cycle) needs the right-hand side f only at the finest level. FMG needs f at all levels. If the boundary conditions are homogeneous, you can use $f_H = \mathfrak{R}f_h$. Note that the FMG algorithm produces the solution on all levels.

5.2.6 Validation of code for thermal induced convection

Table 5.1 shows a comparison between numerical solutions from the present model and that found from De Vahl Davis(1983) who used uniform meshes of 11×11 and 41×41 for Rayleigh numbers of 10^3 and 10^4 and finer meshes up to 81×81 for higher Rayleigh numbers. For our work, for Rayleigh numbers up to 10^5 , a 64×64 uniform grid is found adequate. However, at $Ra_T = 10^5$, a finer grid of 128×128 is needed for the system to reach a steady state. As can be seen, all results are accurate to within 5% of the benchmark solutions.

	ψ_{mid}	ψ_{max}	u_{max}	w_{max}	\bar{Nu}
$Ra_T = 10^3 (64 \times 64)$					
B.M.	1.174	-	3.649	3.697	1.118
P.M.	1.210	-	3.740	3.773	1.069
$\epsilon(\%)$	3.1	-	2.5	2.1	4.6
$Ra_T = 10^4 (64 \times 64)$					
B.M.	5.071	-	16.178	19.617	2.243
P.M.	5.213	-	16.594	19.776	2.172
$\epsilon(\%)$	2.8	-	2.6	0.8	3.2
$Ra_T = 10^5 (128 \times 128)$					
B.M.	9.111	9.612	34.73	68.59	4.519
P.M.	9.284	9.804	35.58	68.39	4.474
$\epsilon(\%)$	1.9	2.0	2.4	0.3	1.0

Table 5.1: Comparison of present model (P.M.) to benchmark solutions(B.M.).

A comparison between the contour maps and the isotherms obtained from our code

and those by De Vahl Davis(1968) is shown for the two cases: $Ra_T = 1.2 \times 10^4$ and 5×10^4 in Figures 5.6 and 5.7 respectively. The small differences could be due to the contour plotting routine. Also there is some evidence that the steady state has not quite been attained. However, overall they agree well. The development of the motion may be seen in the contour maps whilst the isotherms show the distortion of the temperature distribution from that of conduction alone showing a fairly constant temperature in the bulk of the fluid and sharp temperature gradients near the two side walls.

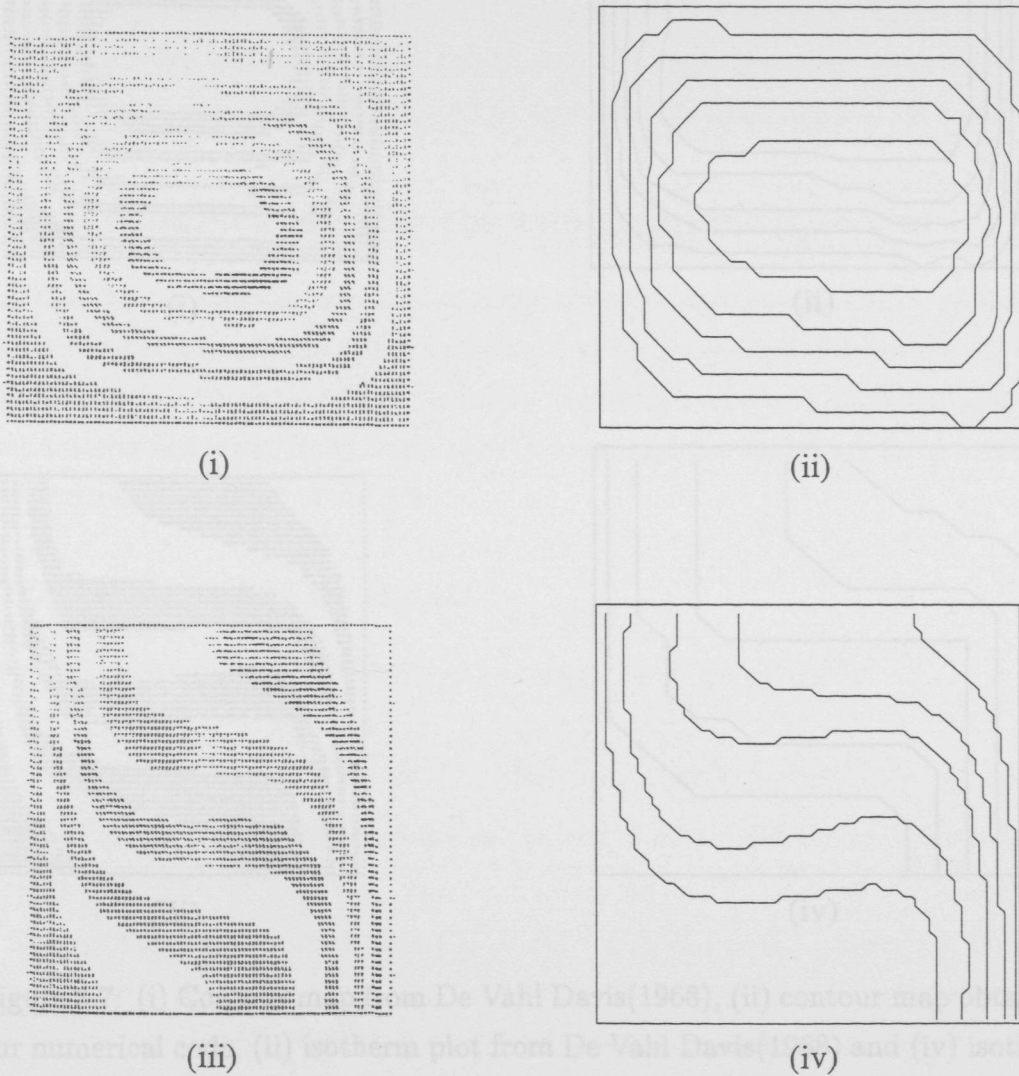


Figure 5.6: (i) Contour map from De Vahl Davis(1968), (ii) contour map obtained from our numerical code, (iii) isotherm plot from De Vahl Davis(1968) and (iv) isotherm plot obtained from our numerical code for $Pr = 10^3$ and $Ra = 1.2 \times 10^4$.

5.3 Two-Component Model in Cartesian Coordinates

We have so far developed the one component model. This model will now be expanded to deal with heterogeneous flows where the fluid contains more than one miscible component. Here for simplicity, only two-component flows will be considered, but multi-component systems can be dealt with in just the same manner. We refer to the major constituent in the vessel as the ‘solvent’ whilst the other will be referred to as the ‘solute’. We will again apply the Boussinesq approximation requiring the density variations due to composition as well as temperature differences to be small.

5.3.1 Modifications for the two-component model

In order to incorporate the solute, there are only two modifications required in the mathematical formulation of the problem. Firstly, a differential equation for the solute concentration and appropriate boundary conditions must be included and secondly, the vorticity equation, (5.8), must take into account the buoyancy force resulting from the horizontal gradient of the solute.

Differential equation for the solute

The differential equation governing the behaviour of the solute is

$$\frac{\partial C}{\partial t} + \frac{\partial(uC)}{\partial x} + \frac{\partial(wC)}{\partial z} = D \left(\frac{\partial^2 C}{\partial x^2} + \frac{\partial^2 C}{\partial z^2} \right) \quad (5.34)$$

where C is the concentration of the solute and D is the diffusivity of the solute in the solvent (m^2s^{-1}).

Scaling the concentration using $\bar{C} = (C - C_c)/(C_h - C_c)$, where C_h is the higher concentration of the two fixed concentrations on the two side walls and C_c is the lower concentration on the other side wall, and using the scales in (5.11), we can readily non-dimensionalise equation (5.34), giving (dropping the over-bars)

$$\frac{\partial \bar{C}}{\partial t} + \frac{\partial(u\bar{C})}{\partial x} + \frac{\partial(w\bar{C})}{\partial z} = \frac{1}{\text{Le}} \left(\frac{\partial^2 \bar{C}}{\partial x^2} + \frac{\partial^2 \bar{C}}{\partial z^2} \right) \quad (5.35)$$

where Le , the Lewis number is the ratio of the thermal diffusivity to the molecular diffusivity and is defined by $\text{Le} = \kappa/D$. Note that this is identical with the result

of assuming that $\Gamma = 1/Le$ and $S_o = 0$ in the general differential equation (5.18). Therefore, the stability criteria for this equation is the same as that used for the temperature and vorticity equations.

Boundary and initial conditions for the solute

Initially we shall validate this modification to our model by using it to model the problem described by Béghein *et al.*(1992) of steady-state thermosolutal convection in a square cavity subject to horizontal temperature and concentration gradients.

The physical model is a square two-dimensional cavity, whose upper and lower horizontal walls are adiabatic and impermeable; the vertical walls are maintained at different temperatures and concentrations in order to generate fluid motion, as shown in Figure 5.8.

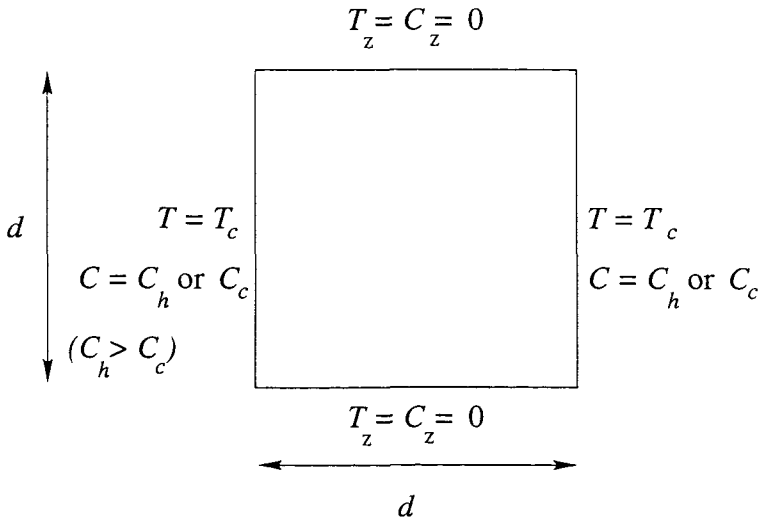


Figure 5.8: Solution domain for problem studied by Béghein *et al.*(1992).

Thus the boundary conditions remain the same as in the previous section but with the addition of the following boundary conditions for the concentration on the four walls:

$$\frac{\partial C}{\partial z} = 0 \quad \text{at } z = 0 \text{ and } d.$$

With the opposing flow (working in the opposing direction to temperature)

$$C = C_h \text{ at } x = 0 \text{ and } C = C_c \quad \text{at } x = d$$

or the aiding flow (working in the same direction as temperature)

$$C = C_c \text{ at } x = 0 \text{ and } C = C_h \text{ at } x = d.$$

Thus the non-dimensionalised boundary conditions are

$$\begin{aligned} \frac{\partial C}{\partial z} &= 0 & \text{at } z = 0 \text{ and } 1 \\ C &= 1 & \text{at } x = 0 \text{ or } 1 \\ \text{and } C &= 0 & \text{at } x = 1 \text{ or } 0. \end{aligned}$$

The initial conditions remain the same as in the previous section but with the additional condition:

$$C = 0 \quad \text{at } t = 0$$

Vorticity transportation equation

Owing to the presence of the solute, equation (5.8) must be rewritten as

$$\frac{\partial \eta}{\partial t} + \frac{\partial \psi}{\partial z} \frac{\partial \eta}{\partial x} - \frac{\partial \psi}{\partial x} \frac{\partial \eta}{\partial z} = \nu \left(\frac{\partial^2 \eta}{\partial x^2} + \frac{\partial^2 \eta}{\partial z^2} \right) - g\beta_T \frac{\partial T}{\partial x} - g\beta_S \frac{\partial C}{\partial x}$$

where β_S is the solutal expansion coefficient. Normalising the above equation, using the same scales as before (dropping the over-bars) yields

$$\frac{\partial \eta}{\partial t} + \frac{\partial \psi}{\partial z} \frac{\partial \eta}{\partial x} - \frac{\partial \psi}{\partial x} \frac{\partial \eta}{\partial z} = \text{Pr} \left(\frac{\partial^2 \eta}{\partial x^2} + \frac{\partial^2 \eta}{\partial z^2} \right) - \text{PrRa}_T \frac{\partial T}{\partial x} - \text{PrRa}_S \frac{\partial C}{\partial x}$$

where $\text{Ra}_S = g\beta_S(C_h - C_c)d^3/(\nu\kappa)$ is the Rayleigh solutal number and Ra_T is the thermal Rayleigh number as defined before. This can again be fitted into the general equation (5.18) with $\Gamma = \text{Pr}$ and $S_o = -\text{PrRa}_T \partial T / \partial x - \text{PrRa}_S \partial C / \partial x$. The two new equations are discretised in the same way as before.

5.3.2 Solution procedure

Since values for the solute are required to determine the source term in the modified vorticity equation, the differential equation for the solute is solved before equation (5.8). The problem is now complete and the procedure is repeated until a steady state is reached which is judged in the same way as for the previous section.

5.3.3 Validation of code for double-diffusive convection

Figure 5.9 shows a comparison between the streamlines, isotherms and isopleths of concentration from Béghein *et al.*(1992) and those obtained from our numerical results, for the case:

$$Le = 1 \quad , \quad Ra_T = 10^7 \quad , \quad Ra_S = 10^6 \quad , \quad \text{opposing flows.}$$

Note that the box around the plots does not represent the walls of the vessel. Also, when plotting contour maps, small changes in the distribution or in the chosen contour values can make a significant difference to the resulting plot. Differences in the location of a contour line in regions with few contour lines can easily occur.

With a lower solutal Rayleigh number than thermal Rayleigh number, the convection for the above case is thermally dominated and the flow is clockwise. The Lewis number of unity means that the diffusion of concentration is the same as the diffusion of temperature. As a result, the isopleths of concentration and temperature should be similar. This is not the case for our plots of the isopleths of concentration and temperature, which are slightly asymmetrical. This may be due to the flow not quite having attained a steady state. Thus our results do not quite agree with those obtained from Béghein *et al.*(1992).

Figure 5.10 shows a comparison between the streamlines and isotherms from Béghein *et al.*(1992) and those obtained from our numerical results, for the case:

$$Le = 1 \quad , \quad Ra_T = 10^7 \quad , \quad Ra_S = 5 \times 10^7 \quad , \quad \text{opposing flows.}$$

The flow is shown to be very similar to the latter case.

Figure 5.11 shows the isopleth of concentration for the case when

$$Le = 5 \quad , \quad Ra_T = 10^7 \quad , \quad Ra_S = 10^6 \quad , \quad \text{opposing flows.}$$

With this Lewis number, the major mass transfer process is mass diffusion rather than the process being dominated by thermal diffusion. We can see that the fingers on either side of the vessel are present in both plots. Away from the boundary detailed agreement is not so good in regions with weaker convection. The other plots compare well, allowing us to proceed with our studies.

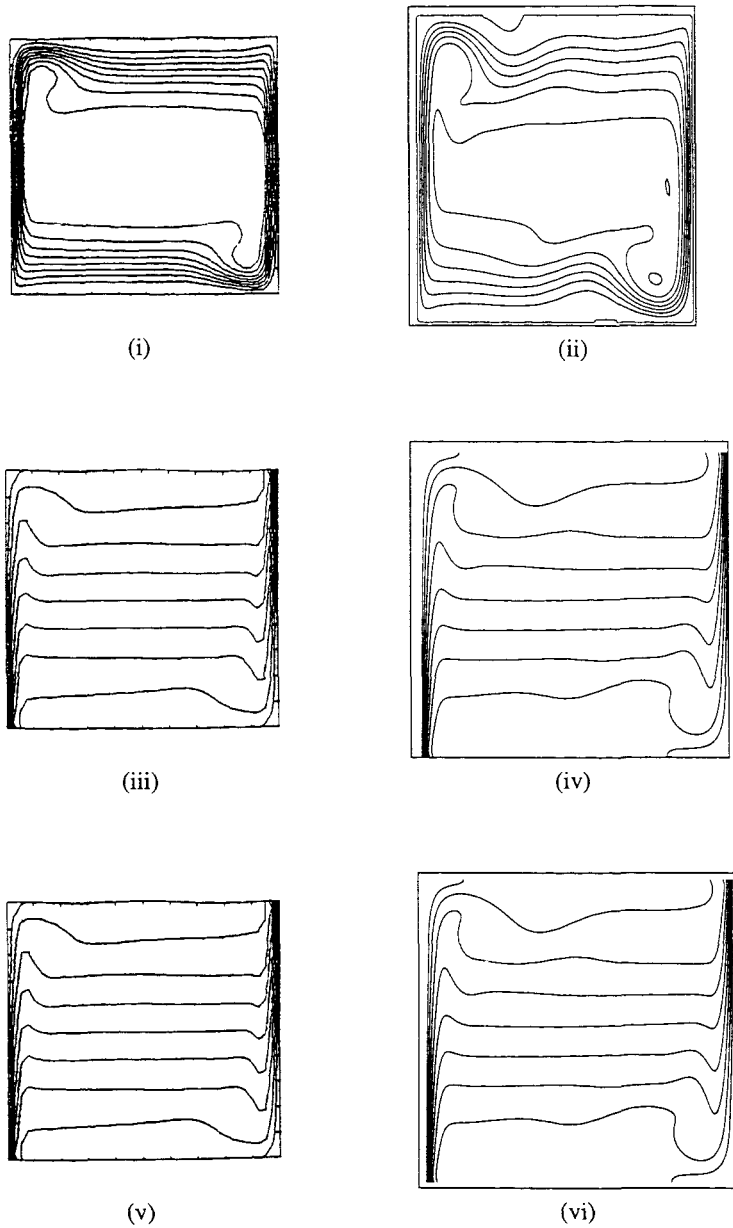
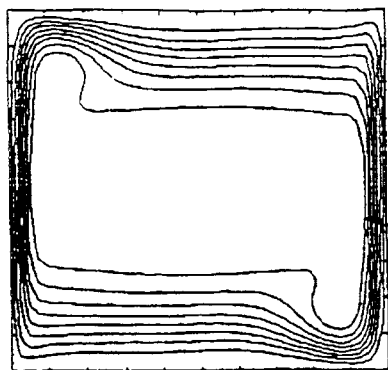
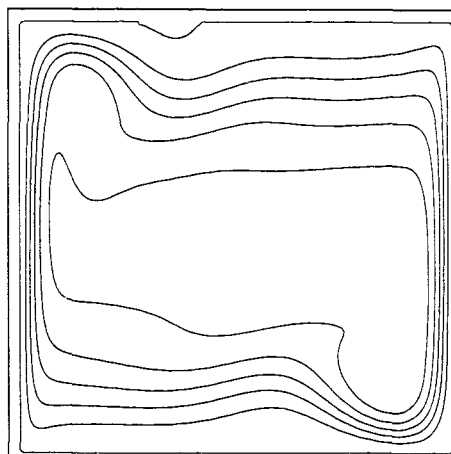


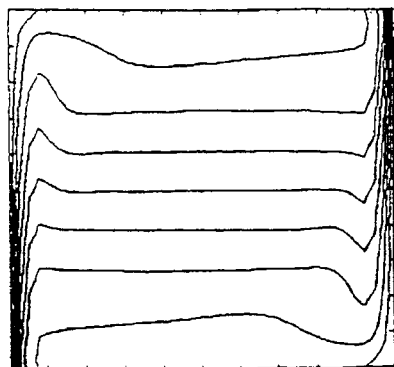
Figure 5.9: (i) Streamlines from Béghein *et al.*(1992), (ii) streamlines obtained from our numerical code, (iii) isotherms from Béghein *et al.*(1992),(iv) isotherms obtained from our numerical code, (v) isopleths of concentration from Béghein *et al.*(1992) and (vi) isopleths of concentration obtained from our numerical code, for $Le = 1$, $Ra_T = 10^7$, $Ra_S = 10^6$.



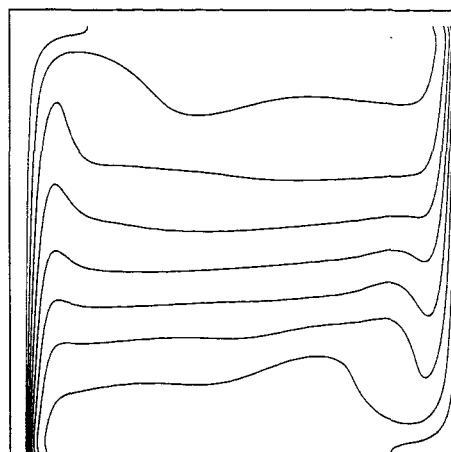
(i)



(ii)



(iii)



(iv)

Figure 5.10: (i) Streamlines from Béghein *et al.*(1992), (ii) streamlines obtained from our numerical code, (iii) isotherms from Béghein *et al.*(1992) and (iv) isotherms obtained from our numerical code, for $Le = 1$, $Ra_T = 10^7$, $Ra_S = 5 \times 10^7$.

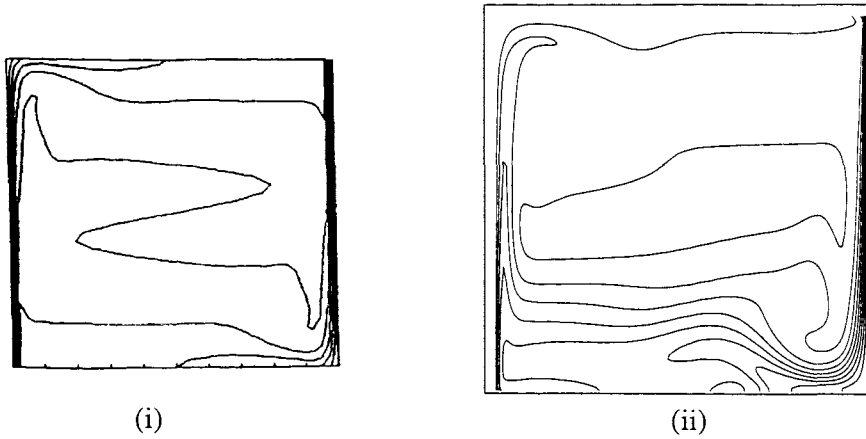


Figure 5.11: (i) Isoleths of concentration from Béghein *et al.*(1992) and (ii) isopleths of concentration obtained from our numerical code, for $Le = 5$, $Ra_T = 10^7$, $Ra_S = 10^6$.

5.4 Rollover Model

We will now adapt the code to follow the work of Shi(1990) in which a numerical model of rollover with a LIN/LOX mixture is studied. Our results for this problem can be compared with those of Shi before developing the model further to include preferential evaporation. Shi considers two layers of cryogenic fluid with a free top surface contained in a square vessel subjected to a uniform heat flux along two opposing vertical walls as shown in Figure 5.12. Since experiments show that the temperature variation within stored cryogenic fluids is usually less than ten degrees Kelvin, the change in fluid density caused would be less than five per cent. Therefore the Boussinesq approximation may still be used.

5.4.1 Governing differential equations

Although the governing equations remain the same as in the previous section, the temperature is scaled by $T - T_{\text{sat}} = \bar{T}\dot{q}d/k$, where \dot{q} is the wall heat flux (Wm^{-2}) and T_{sat} is the saturation temperature (K). All other variables are non-dimensionalised in the same way as before. This only alters the thermal Rayleigh number which is replaced by the modified thermal Rayleigh number, defined as follows:

$$Ra_T^* = \frac{g\beta_T\dot{q}d^4}{k\kappa\nu}.$$

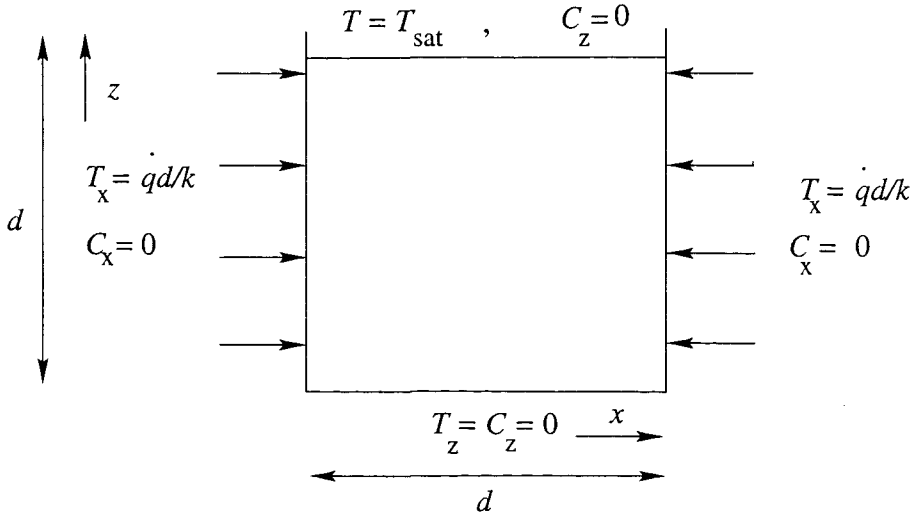


Figure 5.12: Solution domain for problem studied by Shi(1990).

5.4.2 Boundary and initial conditions

Shi(1990) argues that the liquid surface can be considered as non-evaporating, i.e. stationary, since the vessels are well insulated, such that the daily loss of liquid (of the order of 0.5%) may be neglected. Therefore

$$w = 0$$

Also

$$\frac{\partial C}{\partial n} = 0$$

holds at all four boundaries, where \vec{n} is the direction normal to the boundary. The base of the vessel is considered to be adiabatic, whilst the surface, under atmospheric pressure, is taken to be isothermal, at the saturation temperature. The side walls are heated giving the temperature gradient as

$$\frac{\partial T}{\partial x} = -\frac{\dot{q}}{k} \text{ at } x = 0$$

and

$$\frac{\partial T}{\partial x} = \frac{\dot{q}}{k} \text{ at } x = d$$

The surface is considered to be stress free, i.e. a free surface, which dictates that there are no external forces acting on the surface. This means that the gradient of the horizontal velocity is zero at the surface. From the definition of vorticity and stream function, it follows that the vorticity and stream function are zero and constant at the surface. All walls have the no-slip boundary condition implying that the components

of velocity, u and w , are zero and the stream function, ψ , is a constant. ψ is set as zero at all four boundaries. These conditions on T , C and ψ at the boundaries are non-dimensionalised to give:

At $x = 0$:

$$u = 0 \Rightarrow \frac{\partial \psi}{\partial x} = 0, \quad w = 0, \quad \psi = 0, \quad \frac{\partial T}{\partial x} = -1, \quad \frac{\partial C}{\partial x} = 0;$$

At $x = 1$:

$$u = 0 \Rightarrow \frac{\partial \psi}{\partial x} = 0, \quad w = 0, \quad \psi = 0, \quad \frac{\partial T}{\partial x} = 1, \quad \frac{\partial C}{\partial x} = 0;$$

At $z = 0$:

$$u = 0 \Rightarrow \frac{\partial \psi}{\partial z} = 0, \quad w = 0, \quad \psi = 0, \quad \frac{\partial T}{\partial z} = 0, \quad \frac{\partial C}{\partial z} = 0;$$

At $z = 1$:

$$\frac{\partial u}{\partial z} = 0 \Rightarrow \frac{\partial^2 \psi}{\partial z^2} = 0, \quad w = 0, \quad \psi = 0, \quad T = 0, \quad \frac{\partial C}{\partial z} = 0.$$

Note that these conditions are symmetrical about $x = 0.5$. Shi(1990) utilises this symmetry and applies the following boundary conditions at $x = 0$:

$$u = 0 \Rightarrow \frac{\partial \psi}{\partial z} = 0, \quad \frac{\partial w}{\partial x} = 0, \quad \psi = 0, \quad \frac{\partial T}{\partial x} = 0, \quad \frac{\partial C}{\partial x} = 0$$

and solves the equations for half the vessel (from $x = 0$ to $x = 0.5$). This will give accurate predictions if the heat flux is low enough to maintain laminar convection. However, we will solve the problem for the full vessel in order to clearly observe any instability to the symmetry, which may be indicative of the flow becoming turbulent.

The numerical simulations are performed on a LIN/LOX two-layer system. All variables are initially set to zero except the concentration of LOX. The profile of this is stepwise across the interface; the concentration is zero in the upper layer of the vessel and the fluid is assumed to have a concentration of C_h in the bottom layer. The depth of the two layers are equal. Thus the non-dimensionalised initial conditions are:

$$u = 0, \quad w = 0, \quad \psi = 0, \quad T = 0, \quad C = 1 \text{ for } z \leq \frac{1}{2}, \quad C = 0 \text{ for } z > \frac{1}{2}.$$

All that is left to complete the problem is the specification of the boundary conditions on the vorticity, η .

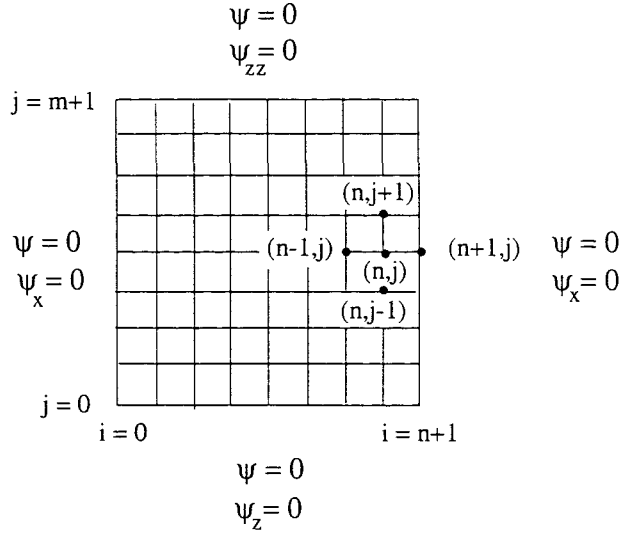


Figure 5.13: Diagram depicting the cavity flow in the vessel which is used to calculate the wall vorticity.

The wall vorticity may be derived using the Taylor expansion (Chow, 1983). Let us consider an arbitrary grid point $(n+1, j)$ on the right-hand wall of the cavity. Our aim is to calculate the vorticity at this point based on the local velocity and on the information of ψ at four neighbouring grid points marked in Figure 5.13. We assume the following form for vorticity at $(n+1, j)$

$$\begin{aligned}
 \eta(n+1, j) &= \left(\frac{\partial^2 \psi(n+1, j)}{\partial x^2} + \frac{\partial^2 \psi(n+1, j)}{\partial z^2} \right) \\
 &= \alpha_1 \psi(n, j) + \alpha_2 \psi(n-1, j) + \alpha_3 \psi(n, j+1) + \alpha_4 \psi(n, j-1) \\
 &\quad + \alpha_5 \left(\frac{\partial \psi(n+1, j)}{\partial x} \right) \tag{5.36}
 \end{aligned}$$

Substituting from the Taylor's series expansions,

$$\psi(n+1-N, j) = \psi(n+1, j) - Nh \left(\frac{\partial \psi(n+1, j)}{\partial x} \right) + \frac{N^2 h^2}{2} \left(\frac{\partial^2 \psi(n+1, j)}{\partial x^2} \right) + O(h^3)$$

$$\begin{aligned}
 \psi(n, j \pm 1) &= \psi(n+1, j) - h \left(\frac{\partial \psi(n+1, j)}{\partial x} \right) + \frac{h^2}{2} \left(\frac{\partial^2 \psi(n+1, j)}{\partial x^2} \right) \\
 &\quad \pm h \left(\frac{\partial \psi(n+1, j)}{\partial z} \right) + \frac{h^2}{2} \left(\frac{\partial^2 \psi(n+1, j)}{\partial z^2} \right) + O(h^3)
 \end{aligned}$$

where h is the width of each square mesh, and retaining only terms up to $O(h^2)$,

equation (5.36) becomes

$$\begin{aligned}
\left(\frac{\partial^2 \psi(n+1, j)}{\partial x^2} + \frac{\partial^2 \psi(n+1, j)}{\partial z^2} \right) &= (\alpha_1 + \alpha_2 + \alpha_3 + \alpha_4) \psi(n+1, j) \\
&+ (-\alpha_1 - 2\alpha_2 - \alpha_3 - \alpha_4 + \frac{\alpha_5}{h}) h \left(\frac{\partial \psi(n+1, j)}{\partial x} \right) \\
&+ (\alpha_1 + 4\alpha_2 + \alpha_3 + \alpha_4) \frac{h^2}{2} \left(\frac{\partial^2 \psi(n+1, j)}{\partial x^2} \right) \\
&+ (\alpha_3 - \alpha_4) h \left(\frac{\partial \psi(n+1, j)}{\partial z} \right) \\
&+ (\alpha_3 + \alpha_4) \frac{h^2}{2} \left(\frac{\partial^2 \psi(n+1, j)}{\partial z^2} \right)
\end{aligned}$$

The constants α_i are determined by equating the coefficients of like terms on the two sides of this equation. Substitution of these values into (5.36) gives

$$\eta(n+1, j) = \frac{1}{h^2} \left(-\psi(n, j-1) + \frac{8}{3}\psi(n, j) - \psi(n, j+1) - \frac{2}{3}\psi(n-1, j) \right)$$

where the second boundary condition of ψ , i.e. $\psi_x = 0$, is employed. By analogy we can write down the expressions for vorticity at the bottom and the left wall as

$$\begin{aligned}
\eta(0, j) &= \frac{1}{h^2} \left(-\psi(1, j-1) + \frac{8}{3}\psi(1, j) - \psi(1, j+1) - \frac{2}{3}\psi(2, j) \right) \\
\eta(i, 0) &= \frac{1}{h^2} \left(-\psi(i-1, 1) + \frac{8}{3}\psi(i, 1) - \psi(i+1, 1) - \frac{2}{3}\psi(i, 2) \right)
\end{aligned}$$

The vorticity on the top surface can be found from the boundary conditions on the stream function to be

$$\eta(i, m+1) = 0.$$

The problem is now complete. The equations and boundary conditions are discretised and solved in the same way as previously.

5.5 Properties of Liquid Nitrogen and Liquid Oxygen

Table 5.2 lists the properties of LIN and LOX, which we will use in our modelling. T_{sat} denotes the saturation temperature. For mixtures of fluids, we assume that the properties are linear combinations of the initial concentrations of each fluid.

	LIN	LOX
$\rho(\text{at } T_{\text{sat}})(\text{kgm}^{-3})$	807.3	1141.0
$c(\text{kJkg}^{-1}\text{K}^{-1})$	2.051	1.695
$k(\text{Wm}^{-1}\text{K}^{-1})$	0.1396	0.1514
$\kappa(\text{m}^2\text{s}^{-1})$	8.43×10^{-8}	7.83×10^{-8}
$L(\text{kJkg}^{-1})$	199.3	213
$\beta_T(\text{K}^{-1})$	5.77×10^{-3}	4.2×10^{-3}
$\nu(\text{m}^2\text{s}^{-1})$	1.957×10^{-7}	1.665×10^{-7}
Pr	2.32	2.13

Table 5.2: Comparison of properties of LIN and LOX.

5.5.1 Validation of code for rollover model

The code was run for the same conditions as used by Shi(1990), with $Le= 31.25$, $Pr=2.32$, $Ra_T = 1 \times 10^7$ and $Ra_S = -3 \times 10^6$ until a preset time. Figures 5.14, 5.15, 5.16, 5.17 and 5.18 show reasonable comparisons between the temperature, concentration and stream function obtained from our numerical code and those from the work of Shi(1990) at the non-dimensionalised times $t = 0.005$, $t = 0.01$, $t = 0.02$, $t = 0.04$ and $t = 0.06$ respectively. Note that the box around the plots, again, does not represent the sides of the vessel and that the aspect ratio for our plots differs from that of Shi's because our results were obtained for the complete cavity whereas Shi modelled only one half of the cavity.

At $t = 0.005$, the stream function contour shows temperature driven convective loops (rising at the sides and descending in a central plume) in both the upper and lower layers. The upward boundary layer flow in the lower layer is unable to overcome the density difference at the interface and so it spreads inwardly after impinging on the interface. It is evident that more heat is retained in the lower layer than in the upper layer which means that more heat is removed at the surface than is replenished from the lower layer showing poor heat transfer between the layers. The concentration contour spreads out on both sides of the interface through diffusion. At $t = 0.01$, a dramatic reduction in the number of streamlines in the lower layer is observed, reflecting a decrease in the velocity field. This is due to the substantial decrease in the temperature gradient in the lower layer, making the buoyancy force, which induces

convection, much smaller, i.e. the lower layer is mostly isothermal. There is evidence at this stage that some oxygen rich liquid from the lower layer becomes entrained in the upper layer's convective flow.

The convective loop becomes increasingly stronger in the upper layer at $t = 0.02$ due to a new buoyant force, resulting from the concentration gradient across the core of the interface. In contrast, the lower layer is almost uniform in its temperature distribution. The concentration contour shows that more solute is swept away at the interface by the increasingly stronger convective current in the upper layer. At $t = 0.04$, the core flow in the upper layer starts to penetrate downward, where it entrains heavier liquid from the interface into the upper layer, before spreading out. The concentration contour pattern in the upper layer closely follows that of the stream function, suggesting that the mixing is mainly due to advection. The steady downward movement of the interface, due to the entrainment mentioned before, is observed at $t = 0.06$. The temperature of both layers increases, the lower layer at a higher rate than the upper, leading to a greater temperature difference between the layers.

At the non-dimensionalised time $t = 0.1$, the results of our code, shown in Figure 5.19, suggest that the flow becomes asymmetrical and continues to be asymmetrical for the remainder of the numerical run. We believe that the flow has started to become turbulent at this stage. The condition used at the centre of the vessel by Shi(1990) forces his solution to remain symmetrical and this may alter the time until the onset of turbulence. Thus we can only say that our model is valid up until the non-dimensionalised time, $t=0.6$, after which the flow loses symmetry which may be a sign of turbulence, such that the governing equations no longer apply to the fluid. However the results up to this stage satisfy us that the numerical code is correct. Further numerical tests (not shown) suggest that the Rayleigh number for which the flow becomes unstable is greater for one-component flows (around 10^8).

5.6 Preferential Evaporation Model

The mathematical modelling of double-diffusive convection is a comparatively recent development in the field of convection. A review of the developments and applications in double-diffusive convection is given by Huppert and Turner(1981). This type of convection was first associated with salt fingers, long narrow convection cells that are

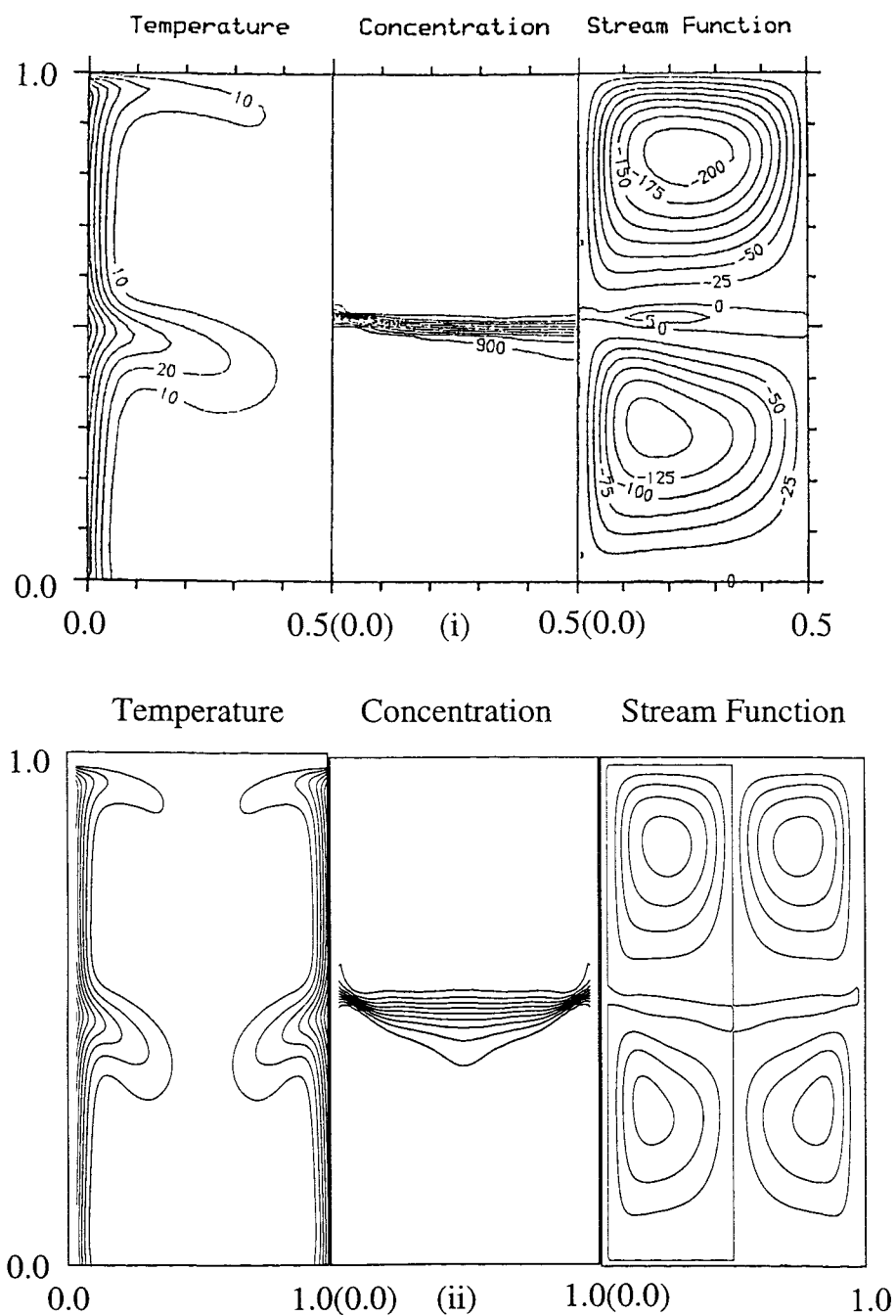


Figure 5.14: (i) Isotherms, isopleths of concentration and contour map from Shi(1990), (ii) isotherms, isopleths of concentration and contour map obtained from our numerical code at non-dimensionalised time, $t=0.005$.

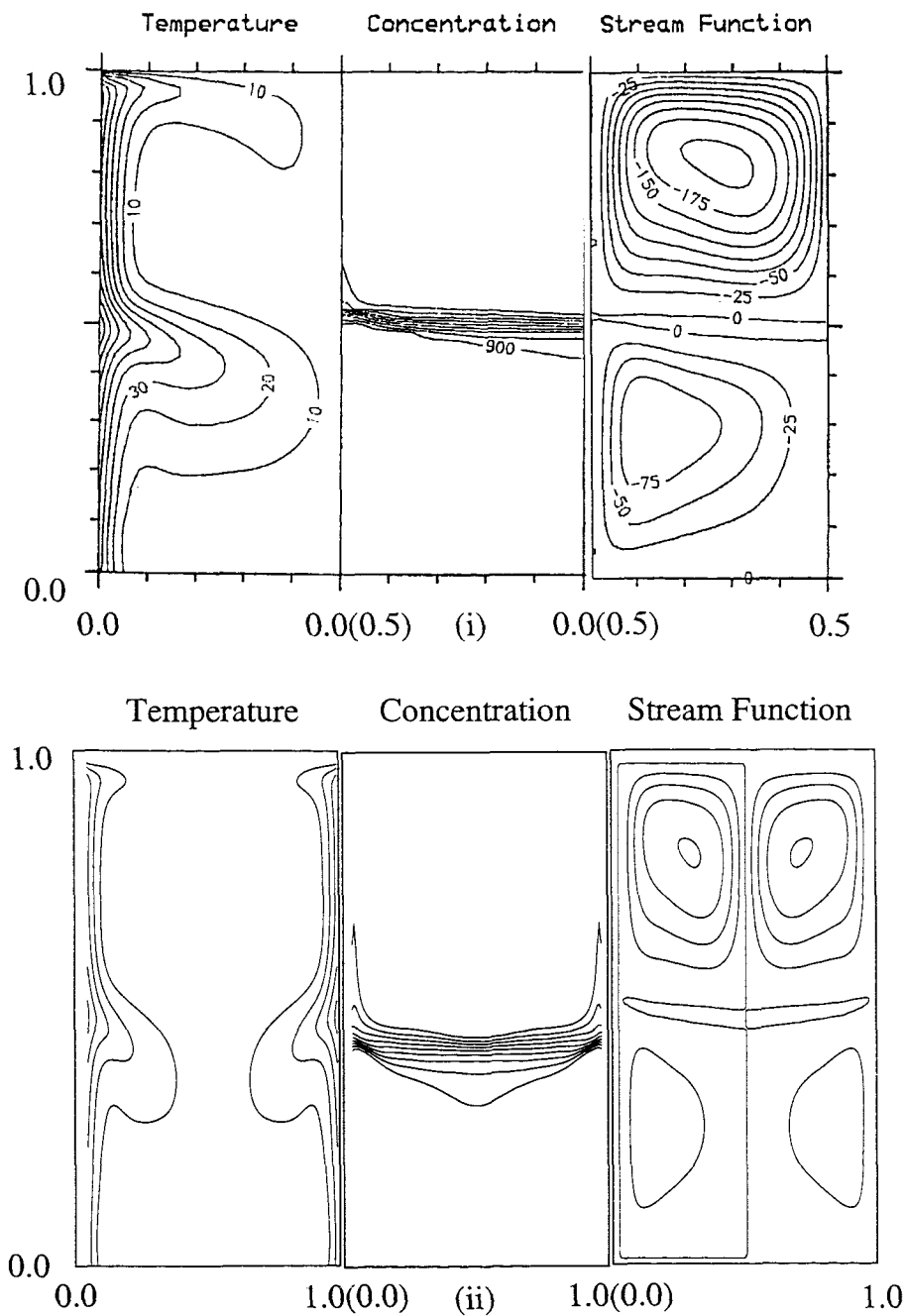


Figure 5.15: (i) Isotherms, isopleths of concentration and contour map from Shi(1990), (ii) isotherms, isopleths of concentration and contour map obtained from our numerical code at non-dimensionalised time, $t=0.01$.

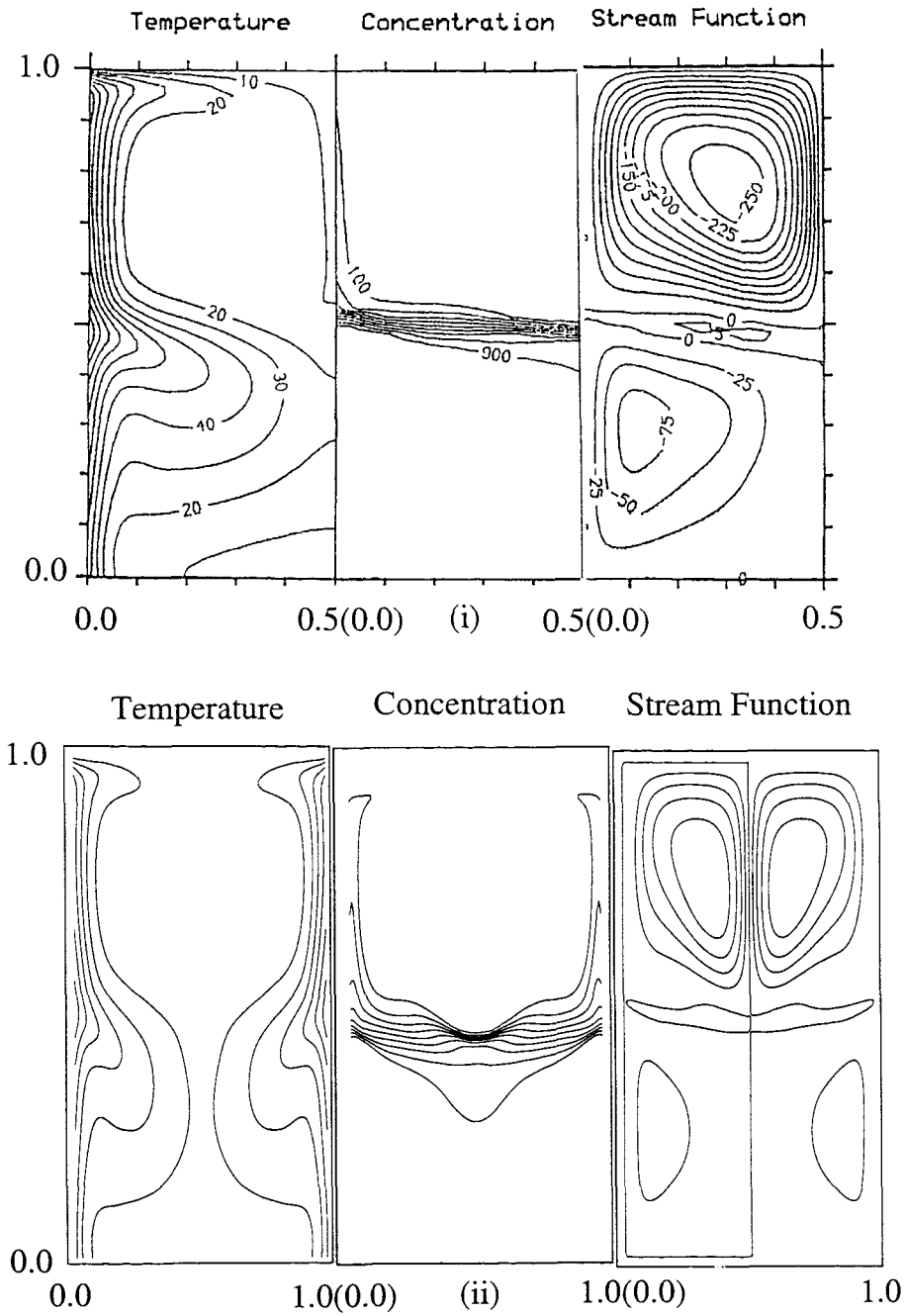


Figure 5.16: (i) Isotherms, isopleths of concentration and contour map from Shi(1990), (ii) isotherms, isopleths of concentration and contour map obtained from our numerical code at non-dimensionalised time, $t=0.2$.

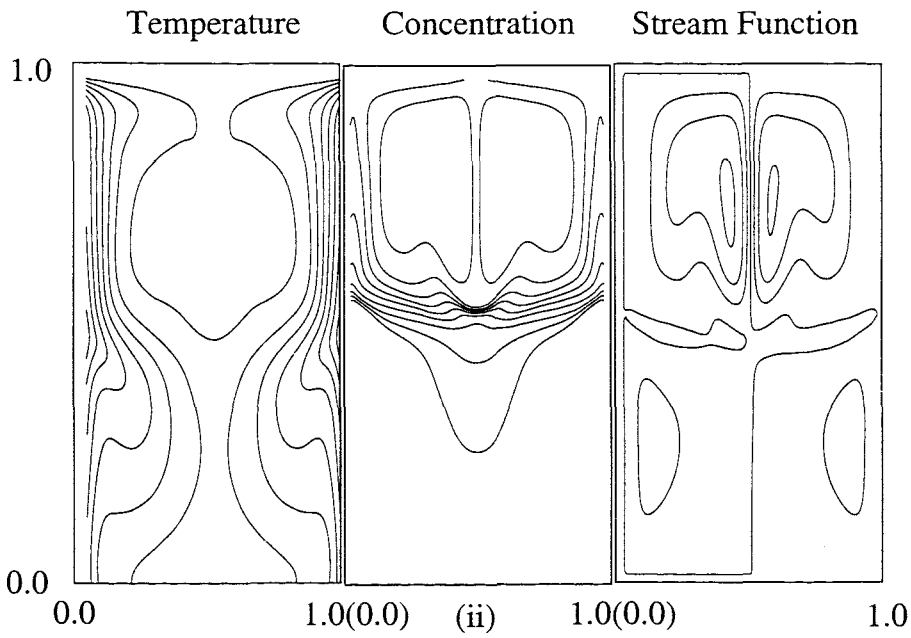
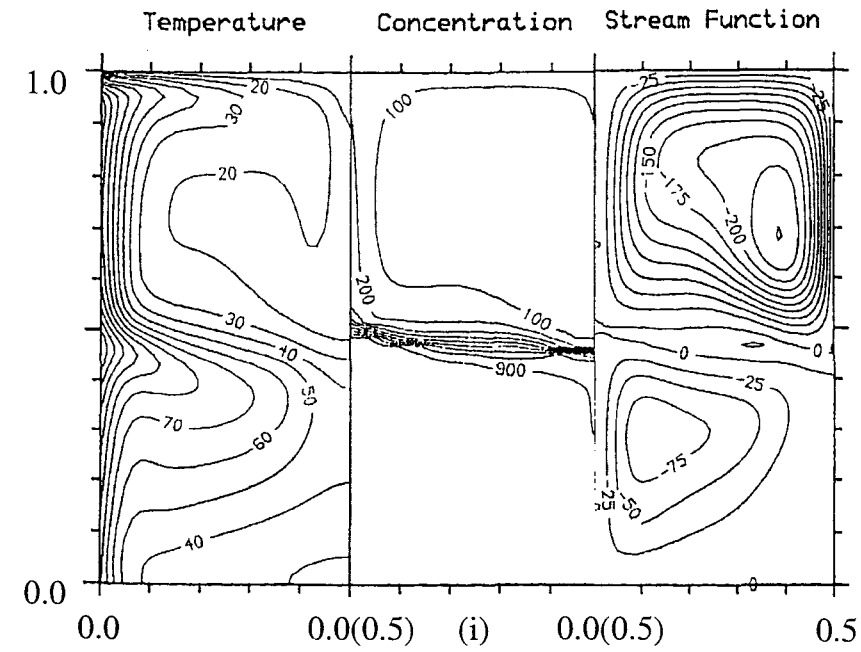


Figure 5.17: (i) Isotherms, isopleths of concentration and contour map from Shi(1990), (ii) isotherms, isopleths of concentration and contour map obtained from our numerical code at non-dimensionalised time, $t=0.04$.

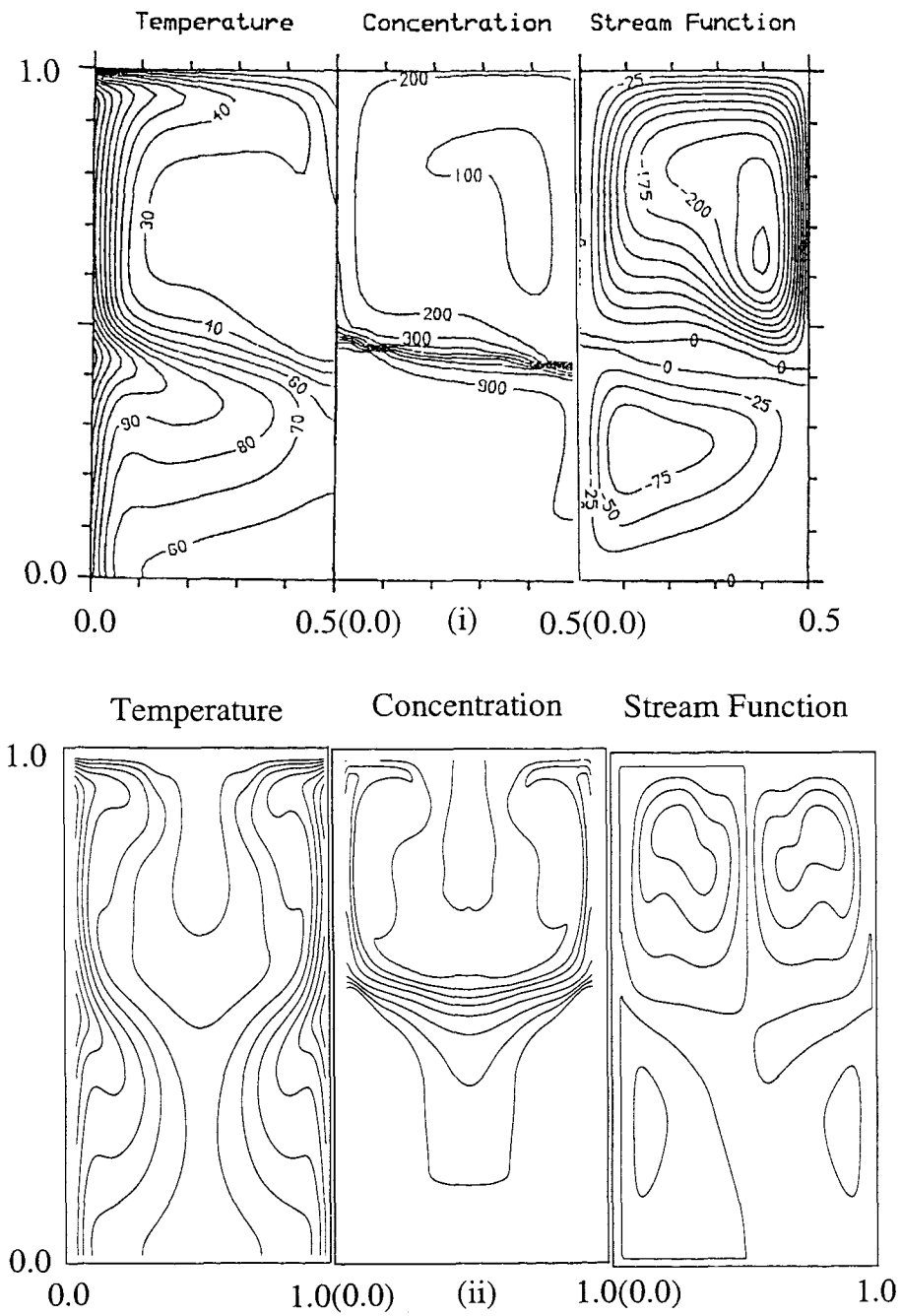


Figure 5.18: (i) Isotherms, isopleths of concentration and contour map from Shi(1990), (ii) isotherms, isopleths of concentration and contour map obtained from our numerical code at non-dimensionalised time, $t=0.06$.

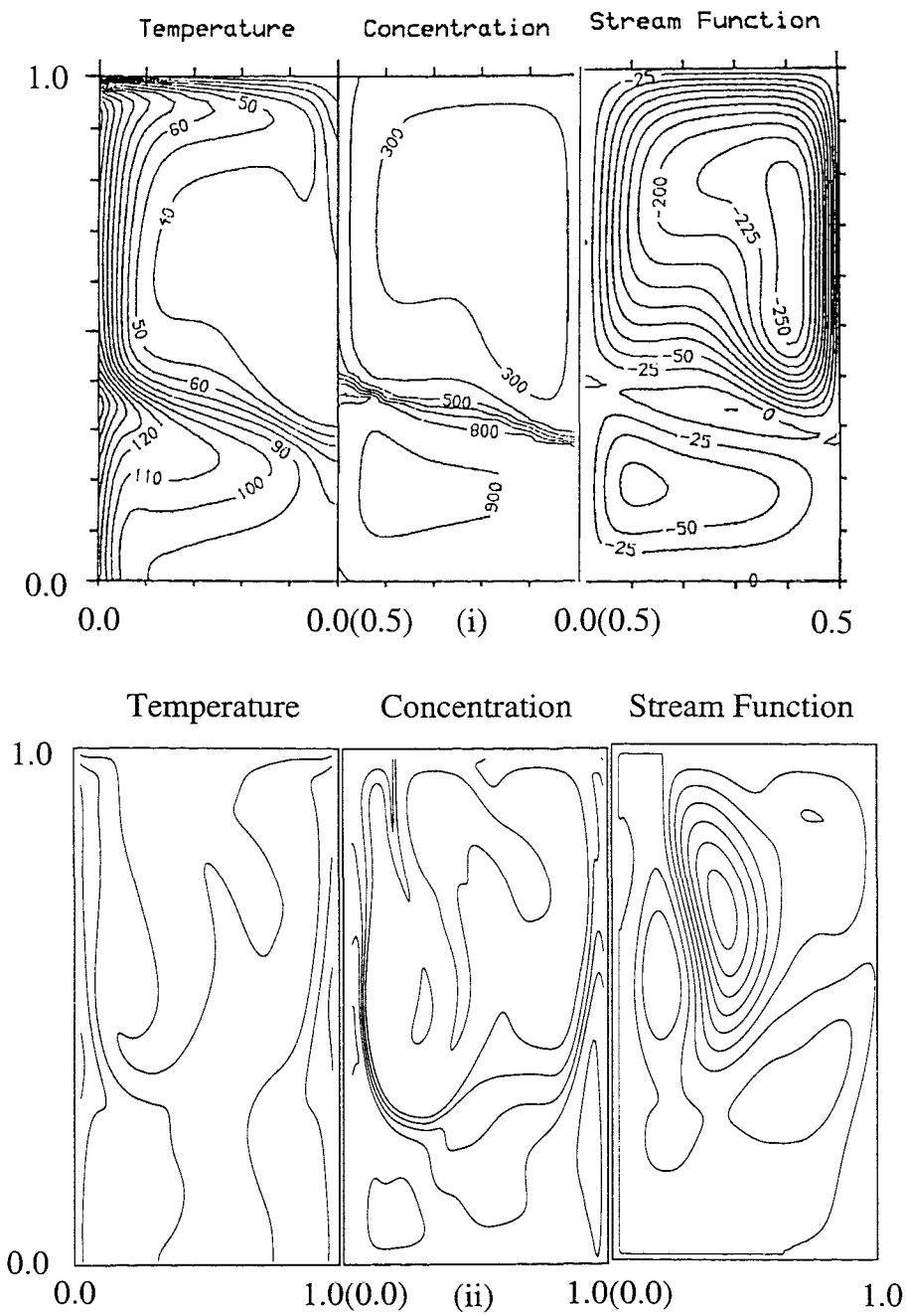


Figure 5.19: (i) Isotherms, isopleths of concentration and contour map from Shi(1990), (ii) isotherms, isopleths of concentration and contour map obtained from our numerical code at non-dimensionalised time, $t=0.10$.

set up when warm salt water lies above cold fresh water. Renardy and Schmitt(1996) explore the influence of non-linear profiles of salinity, as might arise due to surface evaporation, on the linear stability problem in a salt-fingering regime. Asymmetry is observed experimentally in the salt fingers and is attributed to evaporation due to a dry atmosphere leading to a salty layer at the top with the salinity varying little over the rest of the fluid. A model is constructed of double-diffusive convection with a sharp, non-linear concentration gradient applied at the upper boundary, to model the surface evaporation of the solute. This gradient is found to drive a motion that is confined to a depth of a few boundary layers. No significant motion is found lower in the layer. The instability which operates in the boundary is stabilised by the temperature gradient in the bulk. However no previous work has considered the effects of preferential evaporation on the concentration in the fluid.

Preferential evaporation will result in the surface becoming richer in the less volatile phase. This will have an effect on the subsequent convection patterns in the fluid. We shall include this whilst still using Shi's assumption that evaporation rates in a well insulated tank are low, in order to justify a constant volume of liquid and a stationary interface in the model.

5.6.1 Modifications for the evaporation model

There are two possible ways of adding evaporation to our model: either by changing the concentration boundary condition at the surface or by adding a source term to the main differential equation for the solute, (5.34). We choose to add the source term to the main differential equation as this will be the simplest change to make to the numerical code.

Differential equation for solute with evaporation

The differential equation governing the behaviour of the solute (5.34) remains the same as before except at the surface where a source term is added to represent the increase or decrease in solute concentration through evaporation. Our present boundary condition assumes no loss of liquid at the surface (since $w = 0$ at the surface) so the source term, S_{evap} , at the surface will represent the true concentration change through the evaporative mass loss at the surface. The molecular diffusion through the surface is negligible

due to the high interfacial impedance. The concentration of the evaporated fluid, C_{vap} , is in equilibrium with that of the well-mixed vapour. An experimental correlation between the concentration in the vapour, C_{vap} , based on the concentration at the surface is found using data from Barron(1985). A graph displaying this relationship is shown in Figure 5.21. The following equation for the relationship between the concentration at the surface and that in the vapour may be obtained by fitting an exponential curve to the graph:

$$C_{\text{vap}} = -\frac{1}{3.71} \ln(1 - 0.976C(i, m + 1)).$$

Our implementation of the surface condition will give a surface concentration which varies with x , so we shall take an average concentration at the surface in order to calculate the vapour concentration at that time.

Now let us examine equation (5.34) more closely:

$$\frac{\partial C}{\partial t} + \frac{\partial(uC)}{\partial x} + \frac{\partial(wC)}{\partial z} = D \left(\frac{\partial^2 C}{\partial x^2} + \frac{\partial^2 C}{\partial z^2} \right)$$

The only term that will be lost by using the incorrect vertical velocity at the surface is $w\partial C/\partial z$, so let us say that

$$S_{\text{evap}} = w_{\text{true}}(i, m + 1) \frac{\partial C}{\partial z}(i, m + 1) \quad (5.37)$$

where w_{true} is the true velocity (ms^{-1}) at the surface, i.e. the velocity of the mass flux lost through the surface and C is the concentration at the surface. By assuming that the vessel is always maintained at atmospheric pressure and that the liquid is in equilibrium with the vapour at the vapour/liquid interface, it is possible to eliminate the need to consider partial pressures.

We shall use the finite volume method to examine the source term in more detail. Suppose we consider one element at the surface as shown in Figure 5.20 where C_s is the concentration entering the element from below with velocity w_s and C_n is the concentration leaving the element from the top with velocity w_n . Since the source term only exists at the surface, we will need to use the average change in concentration per unit time over the height of the box. So

$$\begin{aligned} S_{\text{evap}} &= \frac{w_{\text{true}}}{dz} \int \frac{\partial C}{\partial z} dz \\ &= w_{\text{true}} \frac{[C]_s^n}{dz} \\ &= w_{\text{true}} \frac{(C_{\text{vap}} - C(i, m + 1))}{dz}. \end{aligned}$$

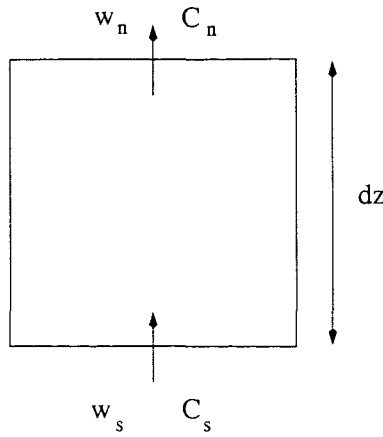


Figure 5.20: An element at the surface of the fluid.

Now we need to find an equation for $w_{\text{true}}(i, m + 1)$. The mass flux per unit area ($\text{kgm}^{-2}\text{s}^{-1}$) of the total liquid leaving the system, out of the surface, can be found using the Stefan condition:

$$\dot{m} = \frac{k}{L} \frac{\partial T}{\partial z}$$

since the temperature gradient in the vapour phase is negligible:

$$\begin{aligned} \text{So the volume flux per unit area of liquid evaporating} &= \frac{k}{\rho L} \frac{\partial T}{\partial z}(i, m + 1) \\ &= w_{\text{true}}(i, m + 1). \end{aligned}$$

Thus the main differential equation for the solute at the surface is

$$\frac{\partial C}{\partial t} + \frac{\partial(uC)}{\partial x} + \frac{\partial(wC)}{\partial z} + S_{\text{evap}} = D \left(\frac{\partial^2 C}{\partial x^2} + \frac{\partial^2 C}{\partial z^2} \right)$$

where

$$S_{\text{evap}} = \frac{k}{\rho L} \frac{\partial T(i, m + 1)}{\partial z} \frac{(C_{\text{vap}} - C(i, m + 1))}{dz}.$$

Let us consider the source term for a moment. If we have a pure LIN liquid, i.e. $C = 0$, then the vapour concentration, $C_{\text{vap}} = 0$. So the source term is eliminated from the problem and the concentration remains unchanged. Similarly with a pure LOX liquid, i.e. $C = 1$, then the vapour concentration, $C_{\text{vap}} = 1$ so the source term is zero and the concentration remains unchanged. Finally, if the vapour concentration is equal to the liquid concentration then the liquid is in equilibrium and so there is no change in concentration again. If there is no evaporation, $\dot{m} = 0$ and there is no effect on the fluid.

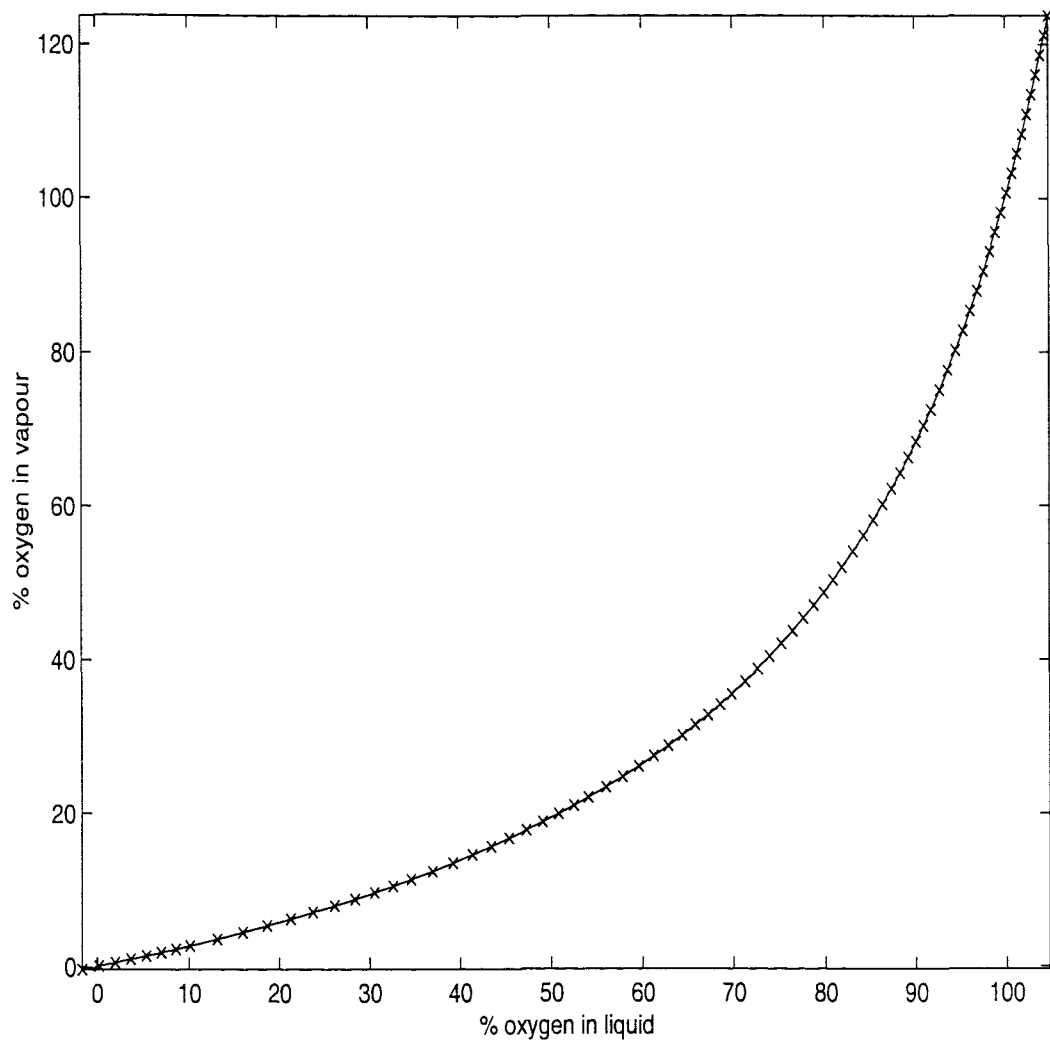


Figure 5.21: Graph showing the relationship between the concentration at the surface of the liquid and the concentration of the vapour where the crosses mark the data points and the line is the best fit line through those points.

5.6.2 Normalisation of the concentration equation

Assuming that the surface of the liquid is in equilibrium with the vapour, the saturation temperature at which the surface is maintained, $T_{\text{sat}}(x)$, is a function of the concentration of the fluid at the surface. So, instead, the temperature is non-dimensionalised in all equations by $T = (\bar{T} - T_{\text{sat}}^{\text{init}})k/(\dot{q}d)$, where $T_{\text{sat}}^{\text{init}}$ is the initial saturation temperature at the surface, calculated from the uniform initial concentration in the fluid. Non-dimensionalising the concentration equation with this and the same dimensional terms as before for the other variables, the equation becomes (dropping the over-bars)

$$\frac{\partial C}{\partial t} + \frac{\partial(uC)}{\partial x} + \frac{\partial(wC)}{\partial z} + S_{\text{evap}} = \frac{1}{\text{Le}} \left(\frac{\partial^2 C}{\partial x^2} + \frac{\partial^2 C}{\partial z^2} \right) \quad (5.38)$$

where

$$S_{\text{evap}} = \frac{\dot{q}d}{\rho L \kappa} \frac{\partial T(i, m + 1)}{\partial z} \frac{(C_{\text{vap}} - C(i, m + 1))}{dz}$$

None of the other equations are altered by this change in scales.

5.6.3 Boundary and initial conditions

As mentioned before, changing the boundary conditions is avoided by adding a source term for evaporation in the main solute equation and so they remain the same as in the previous section.

The data for the correlation for the saturation temperature based on the concentration for a mixture of LIN and LOX was again found from Barron(1985) and is shown in Figure 5.22. We are only interested in mixtures with concentrations of below 60% LOX and it is possible to fit a straight line to this part of the graph such that

$$T_{\text{sat}}(i) = -9.78(1 - C(i, m + 1)) + 86.71.$$

This is non-dimensionalised and replaces the fixed saturation temperature at the surface. Thus the non-dimensionalised saturation temperature is given by:

$$T(i, m + 1) = (-9.78(1 - C(i, m + 1)) + 86.71 - T_{\text{sat}}^{\text{init}}) \frac{k}{\dot{q}d}.$$

All other boundary conditions remain the same.

The initial conditions for the problem are set as

$$\psi = 0 \quad , \quad \eta = 0 \quad , \quad T = 0 \quad , \quad C = 0.2.$$

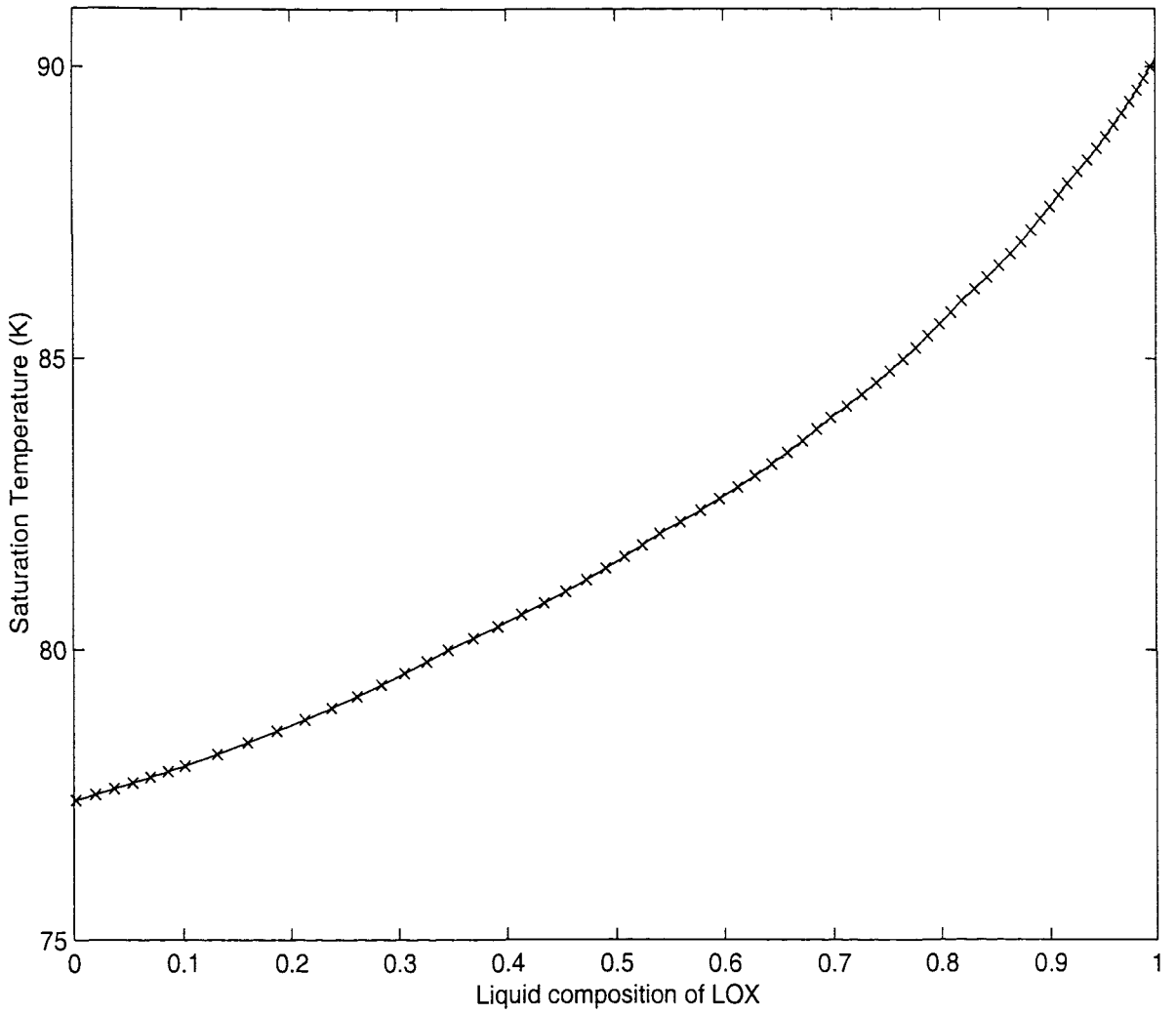


Figure 5.22: Graph showing relationship between the saturation temperature and the concentration where the crosses mark the data points and the line is the best fit line through those points.

5.6.4 Solution procedure

The gradient of the temperature, normal to the surface, is initially set to zero and both the initial vapour concentration and the initial saturation temperature are found from the initial concentration in the fluid. The new equation (5.38) for the surface of the system is solved immediately after the main concentration equation for the rest of the fluid is solved. At the end of each time step, the current gradient of temperature normal to the surface, across the top is found, and an average vapour concentration is calculated which is used in equation (5.38) for the next time step. The saturation temperature is updated using the concentration across the surface. The rest of the solution procedure remains the same.

5.6.5 Results of the preferential evaporation model

The program is solved for a single layer in a square vessel with a height and width, d , of 0.025m. Although this is a fairly small vessel it allows us to have a heat flux of a reasonable magnitude entering the fluid and still maintain laminar convection so that the governing equations are still valid. A grid of size 128×128 is found sufficiently fine to observe the conduction layer, each step of the grid measuring $195 \mu\text{m} \times 195 \mu\text{m}$. We shall take the heat flux, \dot{q} to be 5Wm^{-2} . The thermal conductivity, thermal diffusivity, thermal expansion coefficient and kinematic viscosity are set by taking linear combinations of the properties of nitrogen and oxygen based on the initial concentration, giving the thermal Rayleigh number, $\text{Ra}_T = 5 \times 10^7$. Now to calculate the solutal Rayleigh number, we require the solutal expansion coefficient, defined as

$$\beta_S = \frac{1}{\rho} \frac{\partial \rho}{\partial C}.$$

By taking ρ as the initial density of the mixture, we find that $\beta_S = 0.38$. Assuming that

$$C_h - C_c = C(t=0) - C_{\text{vap}}(t=0)$$

the solutal Rayleigh number is $\text{Ra}_S = -5.2 \times 10^7$. From the properties of the fluid, we also find that the Prandtl number is $\text{Pr} = 2.32$ and the Lewis number is $\text{Le} = 30.77$ (i.e. the flow is dominated by thermal rather than molecular diffusion).

Figures 5.23 - 5.29 show the evolution of the flow with preferential evaporation at the surface at non-dimensionalised times $t = 0.1, 0.5, 0.91.3, 1.7, 2.1$ and 2.3 . Note

again that the box around the plots do not represent the sides of the vessel. At the non-dimensionalised times, $t=0.5$ (64 mins), 1.7 (3.6 hours) and 2.3 (4.9 hours), each graph has three contours, which are labelled. Since the number of contours needs to be restricted for the clarity of the graphs to be unaffected, the labelling has not been included in the graphs for all time steps so the strength of the pattern can be judged by the number of contours in all the other time steps.

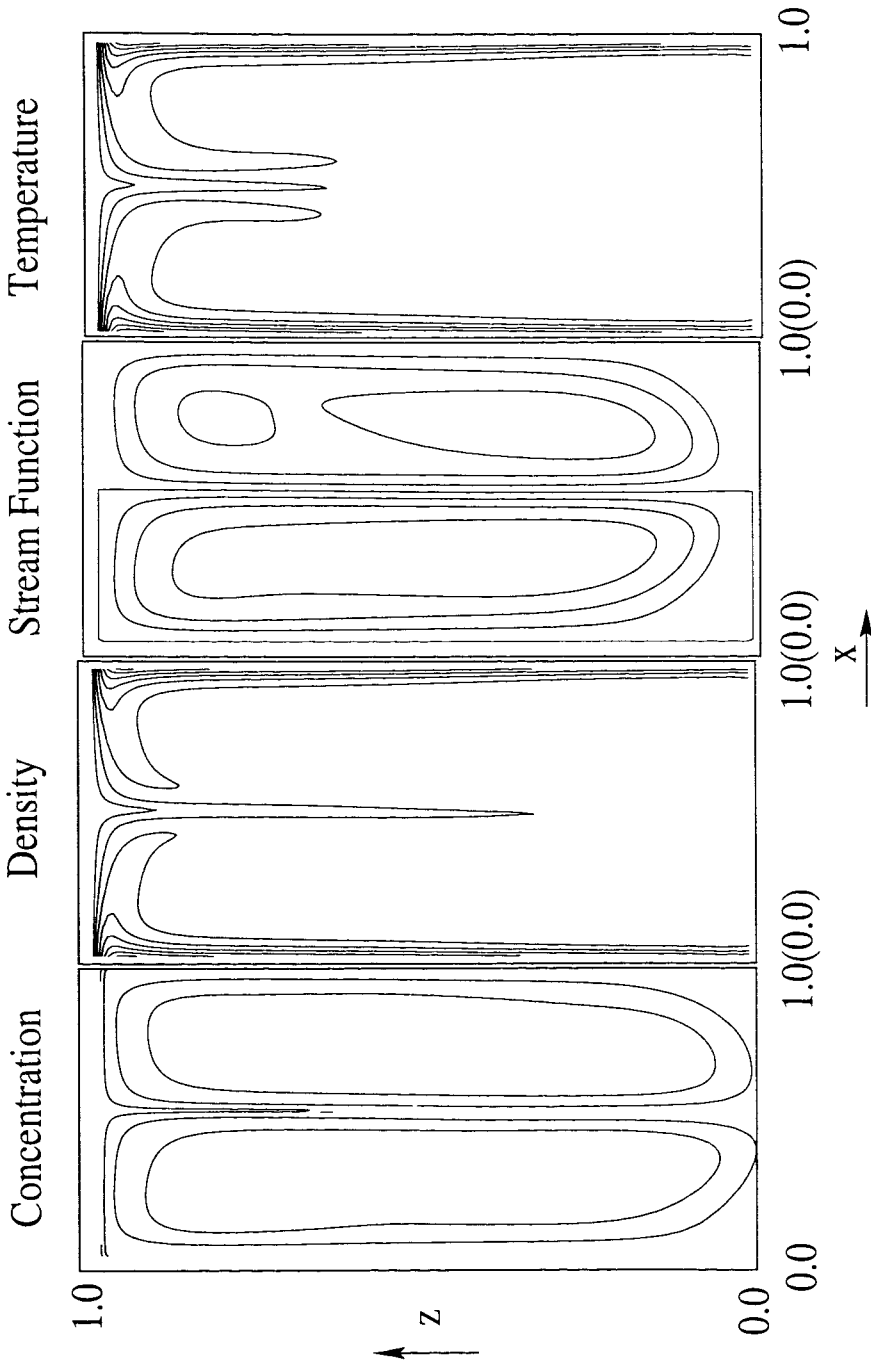


Figure 5.23: Isopleths of concentration, contour maps and isotherms for double-diffusive convection with preferential evaporation at non-dimensionalised time, $t=0.1$ (13 mins).

At time, $t = 0.1$ (13 mins), the preferential evaporation has already affected the fluid, leaving an enriched layer of LOX at the surface. Due to the heat flux on the side walls, the fluid rises at the sides of the vessels to the top surface, where it cools and, due to the preferential evaporation, becomes richer in oxygen. Both processes cause the density of the fluid to increase and a strong downward plume develops at the centre of the cavity. The concentration contours follow the same pattern as the stream function, suggesting that the concentration is distributed through advection.

At the next time step, $t = 0.5$ (64 mins), we see the central plume of denser fluid developing in strength with a sink at the centre of the bottom boundary. We note in this figure that the temperature and concentration differences are only of the order 10^{-2} and 10^{-3} respectively but that this is enough to induce convective loops.

The increase in the number of stream function and concentration contours indicates an increase in strength of the convection at $t = 0.9$ (1.9 hours). This flow entrains the denser fluid, which was seen earlier to be resting at the bottom of the vessel, into the bulk of the fluid. The denser central plume, however, is still noticeable. The convection continues to increase in strength over time with enriched LOX fluid continuously being drawn to the centre of the bottom of the vessel at $t = 1.3$ (2.75 hours) and distributed through advection at $t = 1.7$ (4 hours). The shear force of this convection dominates the temperature distribution. At the end of the run, at time $t = 2.3$ (approximately 5 hours), shown in Figure 5.29, we see that the concentration has increased by 0.01 at the top surface and the temperature by 0.12 at the side walls.

The evolution of the average surface saturation temperature and the average temperature of the bulk of the fluid over time, are shown in Figure 5.30. Although both increase with time, due to the heat flux and preferential evaporation, they do so with the same gradient, such that the surface temperature is, as expected, always approximately 0.02K less than the bulk temperature. Figure 5.31 shows the relationship between the average surface concentration and the concentration of the bulk of the fluid. Again both concentrations increase with the same gradient, with the surface always having a higher concentration of LOX. The total mass flux over time is shown in Figure 5.32. It is noted that the mass flux increases initially with a very sharp gradient, as convection is initiated but then the system reaches an equilibrium state with a constant mass flux.

In previous chapters, we have seen the importance of the thin conduction layer at the

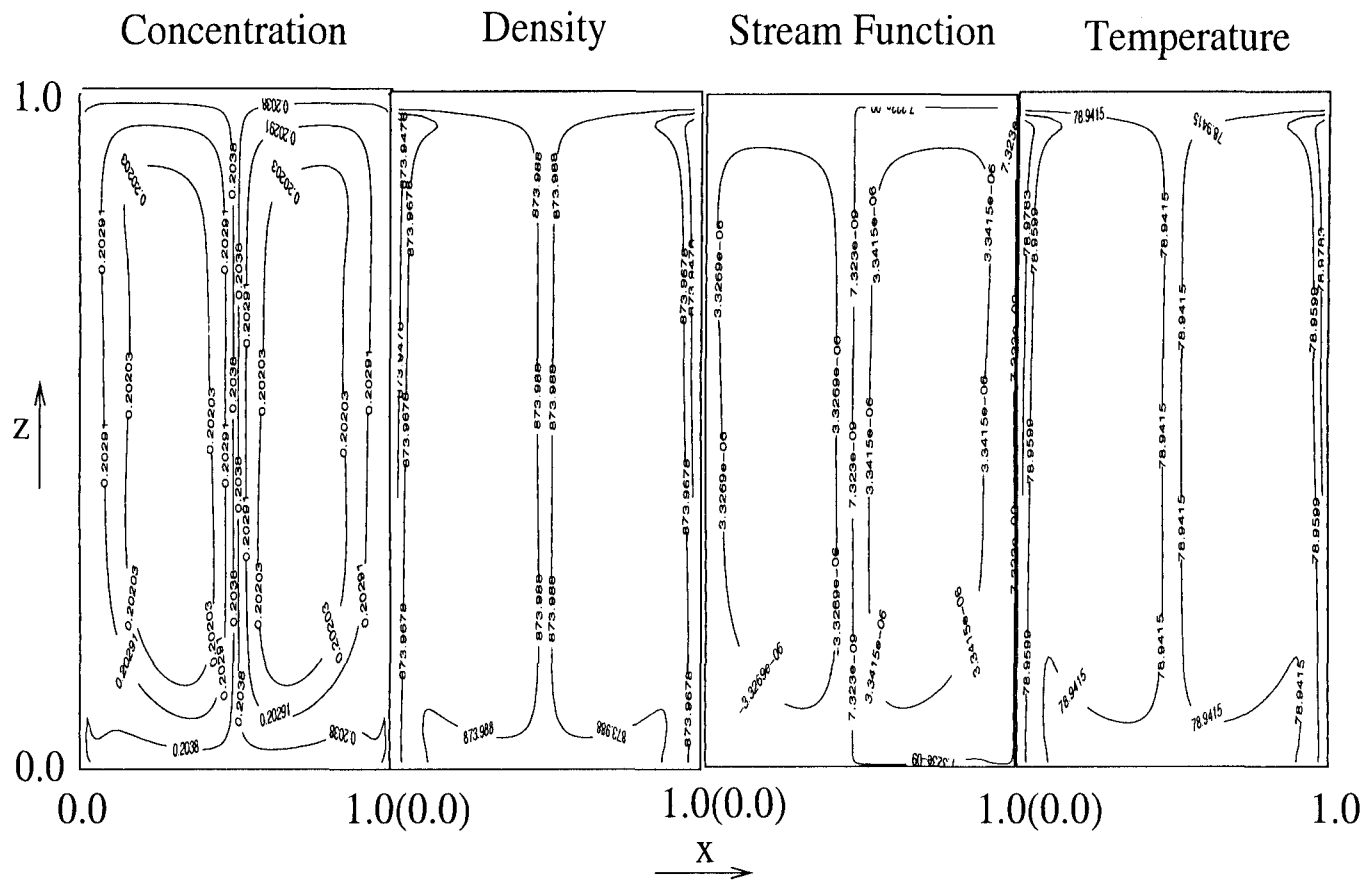


Figure 5.24: Isopleths of concentration, contour maps and isotherms for double-diffusive convection with preferential evaporation at non-dimensionalised time, $t=0.5$ (64 mins).

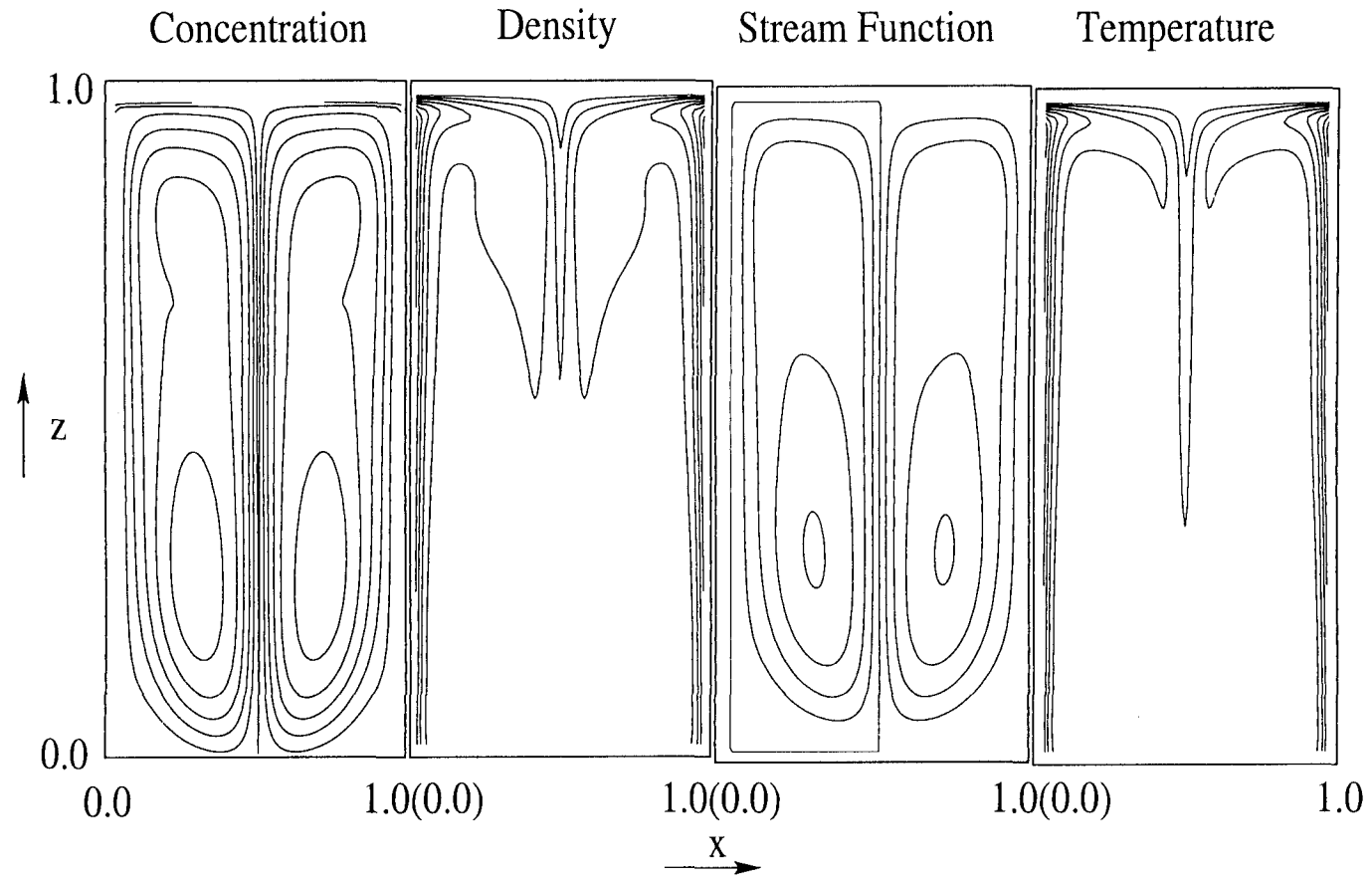


Figure 5.25: Isopleths of concentration, contour maps and isotherms for double-diffusive convection with preferential evaporation at non-dimensionalised time, $t=0.9$ (1.9 hours).

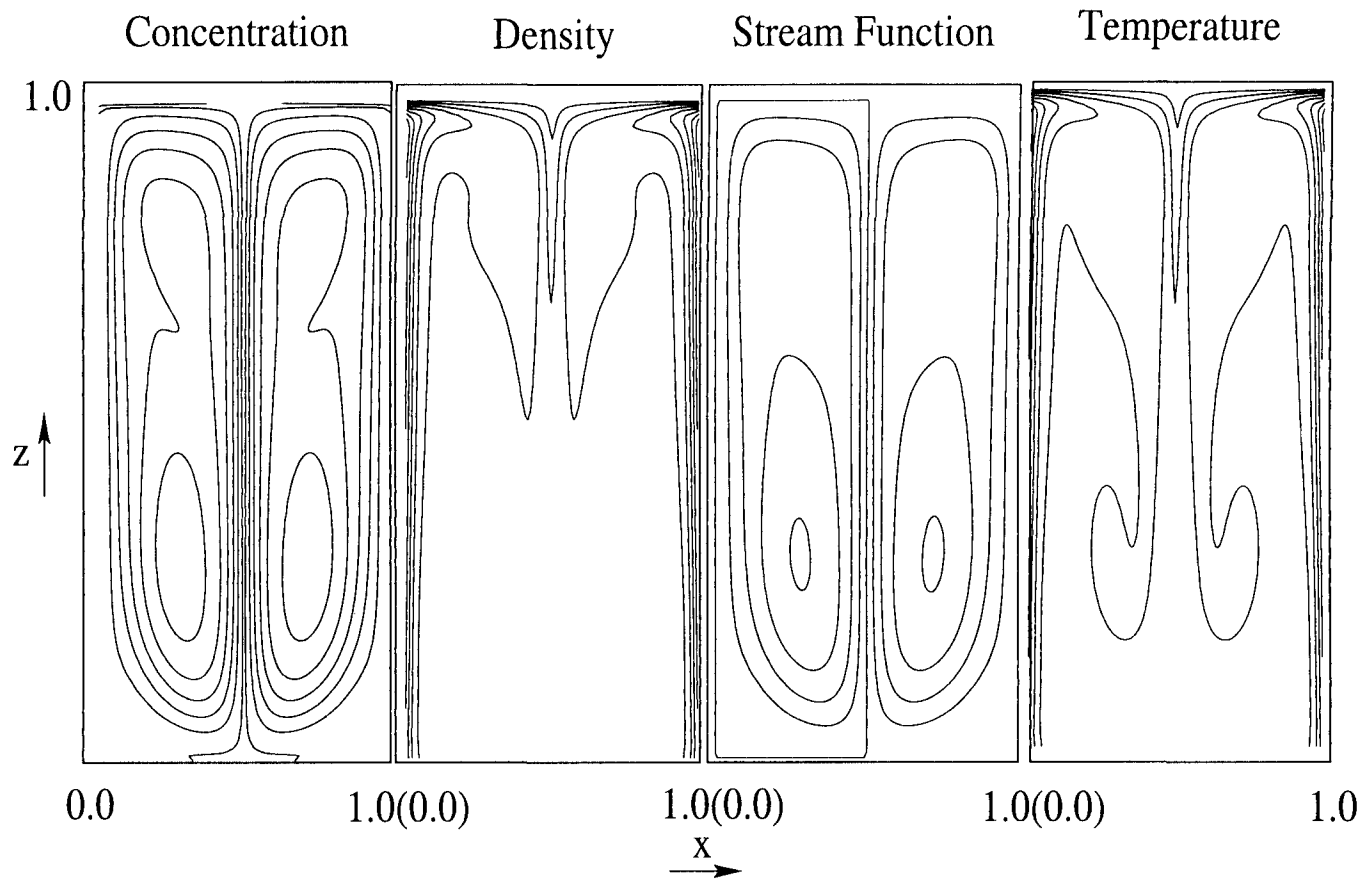


Figure 5.26: Isopleths of concentration, contour maps and isotherms for double-diffusive convection with preferential evaporation at non-dimensionalised time, $t=1.3$ (2.75 hours).

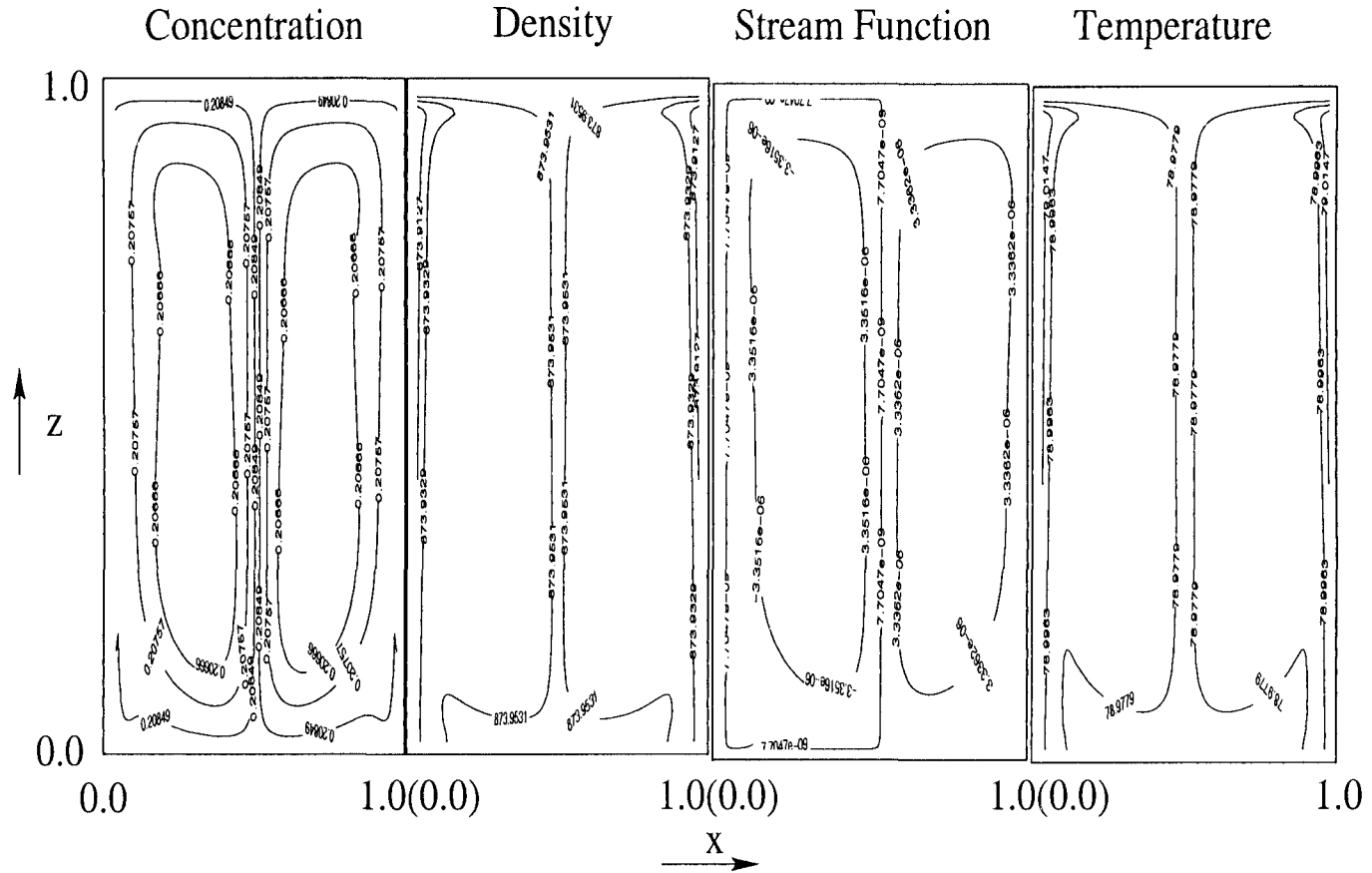


Figure 5.27: Isopleths of concentration, contour maps and isotherms for double-diffusive convection with preferential evaporation at non-dimensionalised time, $t=1.7$ (4 hours).

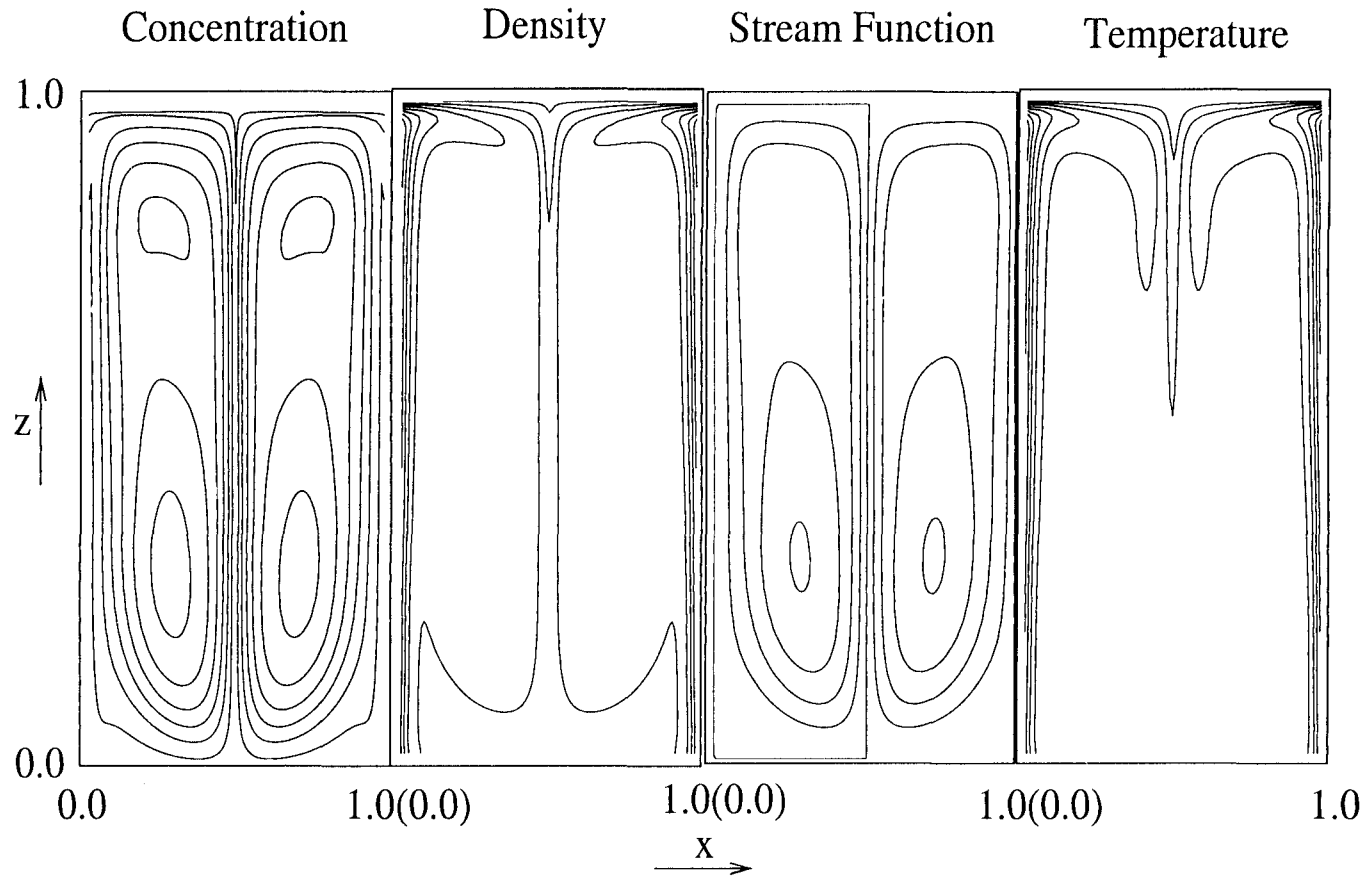


Figure 5.28: Isopleths of concentration, contour maps and isotherms for double-diffusive convection with preferential evaporation at non-dimensionalised time, $t=2.1$ (4.4 hours).

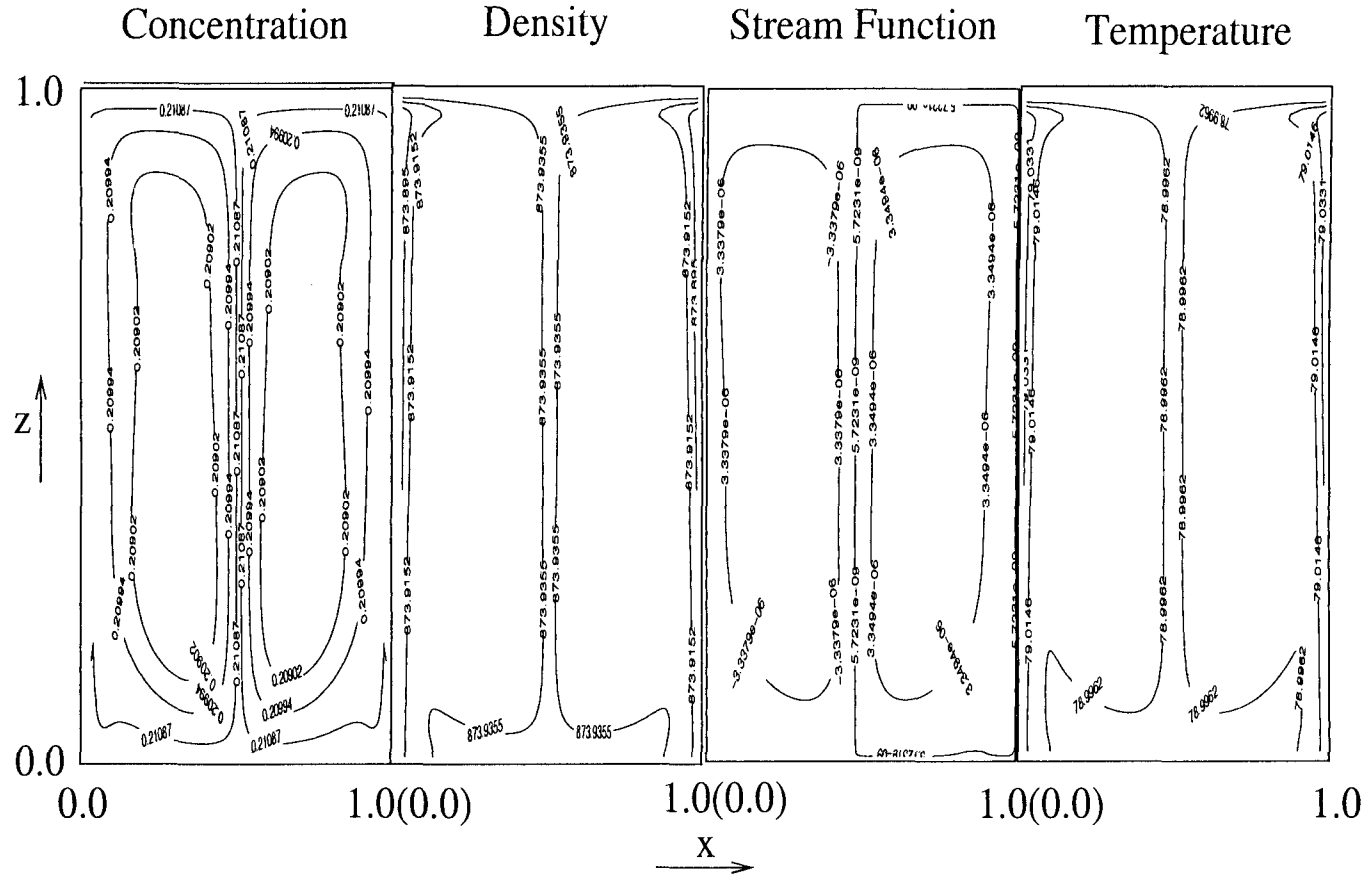


Figure 5.29: Isopleths of concentration, contour maps and isotherms for double-diffusive convection with preferential evaporation at non-dimensionalised time, $t=2.3$ (4.9 hours).

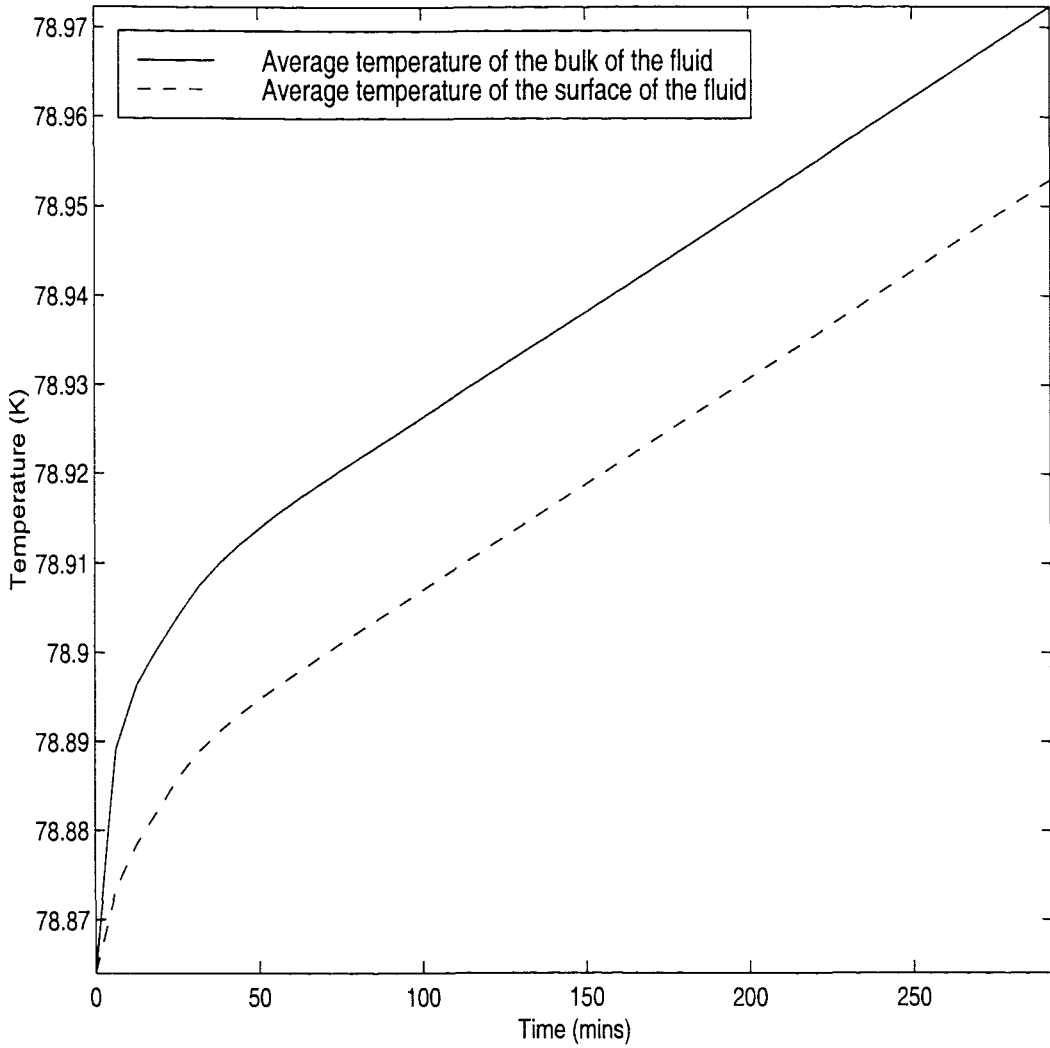


Figure 5.30: Graph showing the average temperature of the bulk of the fluid and the average temperature at the surface of the fluid over time.

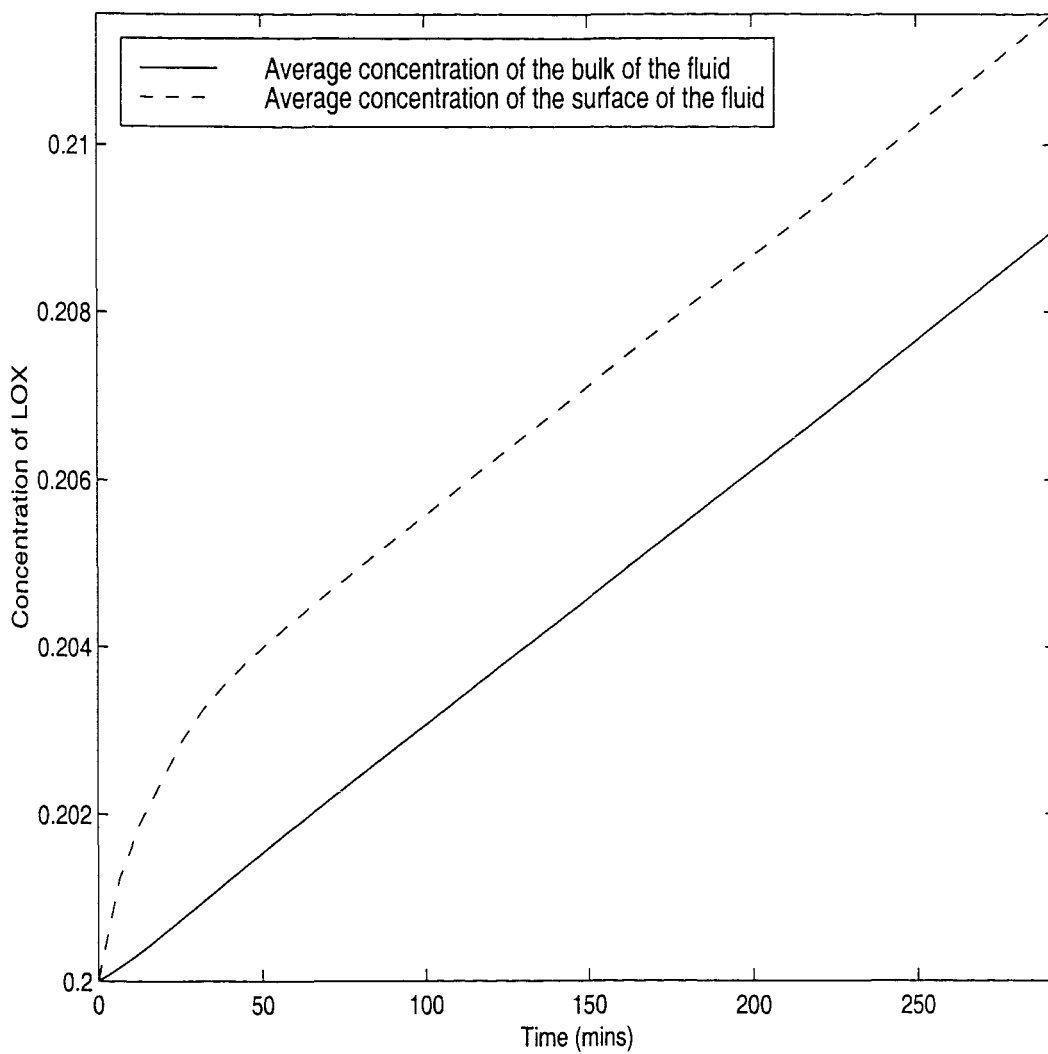


Figure 5.31: Graph showing the average concentration of the bulk of the fluid and the average concentration at the surface of the fluid over time.

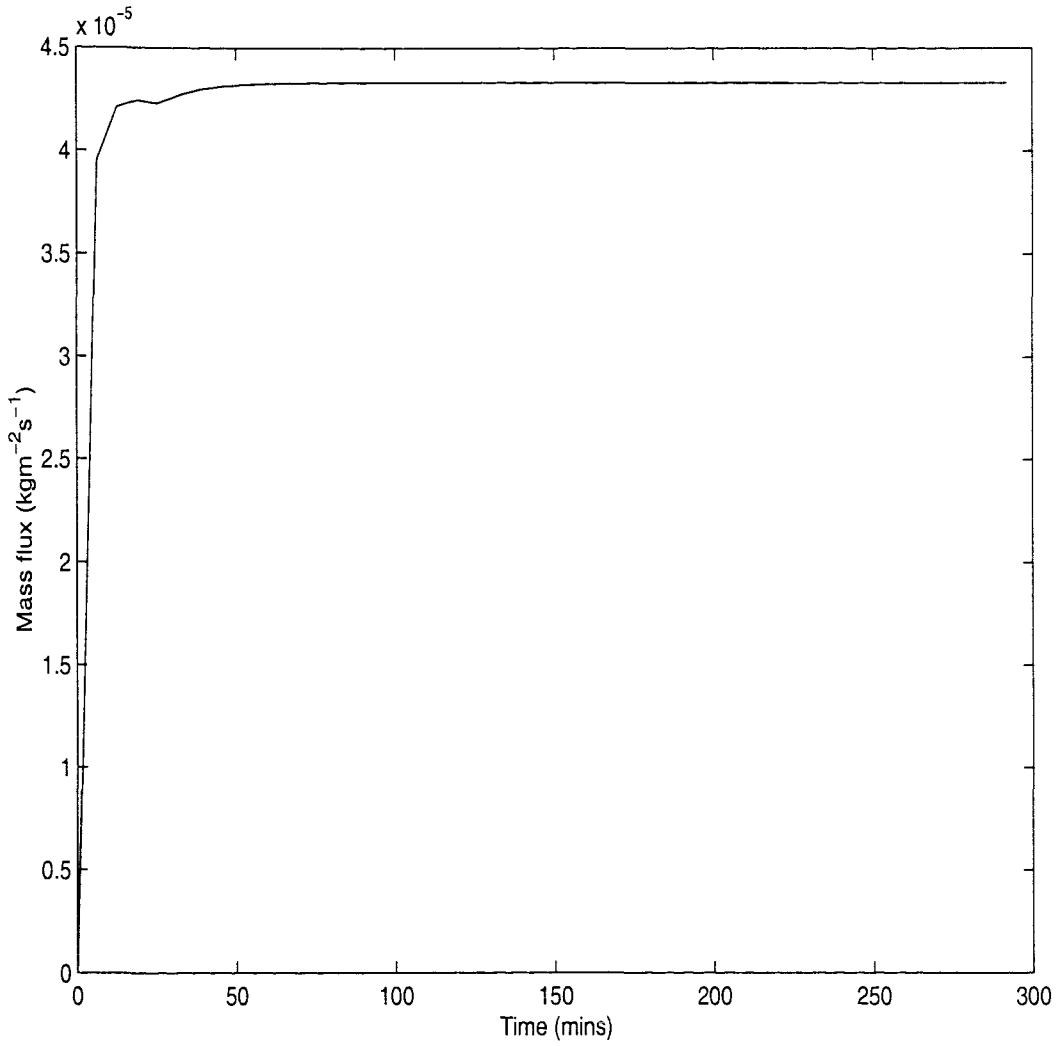


Figure 5.32: Graph showing the total mass flux over time.

surface of the fluid. Here, we will evaluate this thickness from plots of the temperature distribution down the depth of the vessel, and these are shown in Figures 5.33 - 5.35 for non-dimensional times, $t=0.5$ (64 mins), 1.7 (4 hours) and 2.3 (4.9 hours) respectively. These distribution are only shown for half of the vessel, the other half being symmetrical. At $x = 0.0031\text{m}$, close to the side wall, the temperature increases sharply as we enter the fluid from the surface, from the saturation temperature which is a function of the concentration at the surface, to a temperature, T_{hot} , which is close to the temperature of the side walls. It then steadily decreases to a fairly uniform temperature approximately equal to T_{bulk} . The fluid in the centre of the vessel is affected by the central plume preventing the conduction layer from being observed, since the cooler fluid is convected down along this line. Finally we have a plot of the temperature distribution a quarter of the way in from the wall (at $x = 0.0063\text{m}$). Although this, too, can be seen to be slightly affected by the hot temperature of the walls, due to the size of the vessel, this appears to be the distribution which is least influenced by effects other than those caused by the layer. Although the temperature in the bulk of the fluid and the saturation temperature both increase as time progresses, the temperature distribution maintains the same shape. The temperature profile through the vessel at $x=0.0063\text{m}$, for the non-dimensionalised times $t=0.5$, $t=1.7$ and $t=2.3$ are shown in Figure 5.36.

We will use data from the final time step to calculate the thickness of the conduction layer. Let us assume that the thickness of the conduction layer, d_{crit} , is defined from the surface of the fluid to the point where the temperature is T_{est} , where $T_{\text{est}} = T_{\text{sat}} + .99(T_{\text{bulk}} - T_{\text{sat}})$. Due to the size of the vessel, it is difficult to find part of the fluid whose temperature distribution is completely unaffected by the heated boundary layer near the side walls, the cold central plume or the centre of the convection cell. We will examine the temperature distribution at $x = 0.0031\text{m}$, where the fluid is more than the boundary layer away from the side wall. From Figure 5.30 we find that at $t = 2.3$, $T_{\text{bulk}} = 79.00\text{K}$ and $T_{\text{sat}} = 78.98\text{K}$ and so we find that $T_{\text{est}} = 79.00\text{K}$. There are two points where $T = T_{\text{est}}$ along the distribution since it is influenced by the temperature at the wall. However we shall assume that the end of the layer is defined by the first point at which it reaches T_{est} . Thus the thickness of the conduction layer is found to be approximately $400\mu\text{m}$. This fits experimental results (Scurlock and Beduz, 1994), which suggests that the conduction layer has a thickness of $100\text{-}500\mu\text{m}$.

With this conduction layer and with the temperature difference, $T_{\text{bulk}} - T_{\text{sat}} = 0.02\text{K}$,

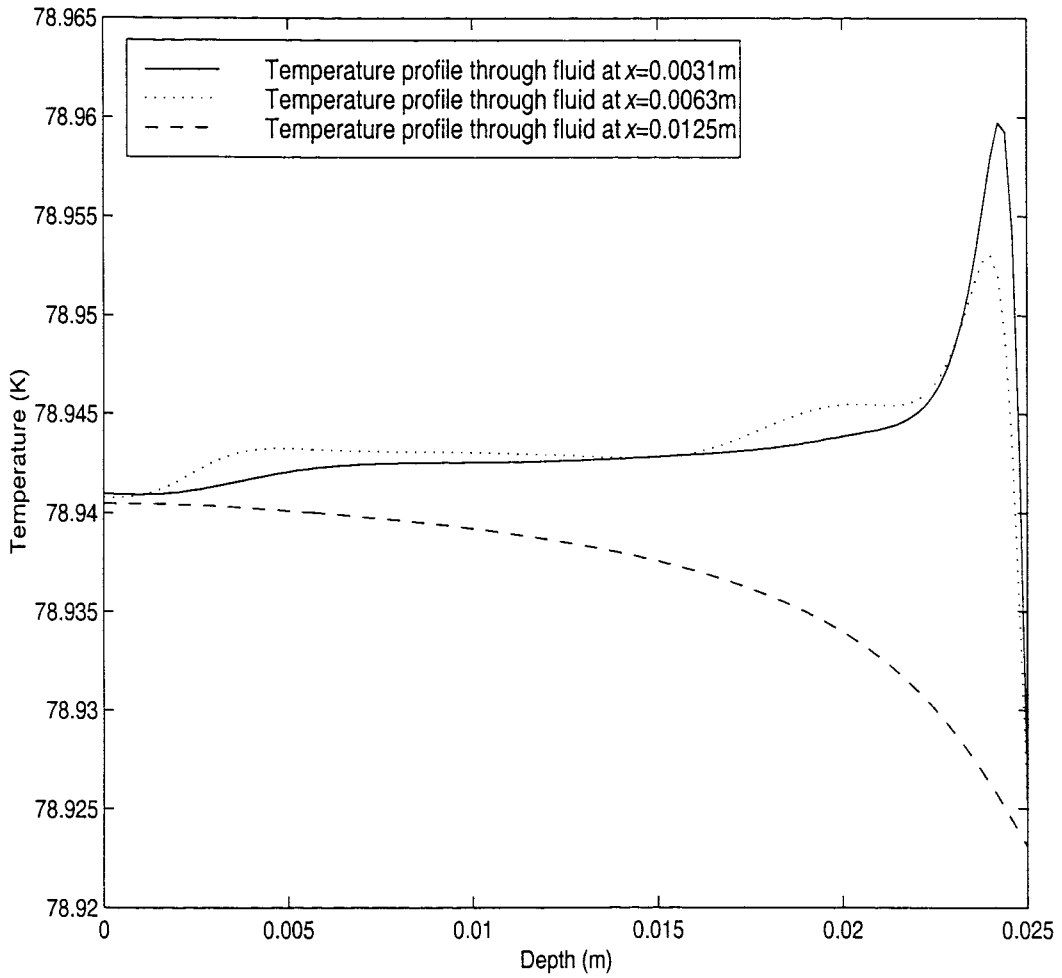


Figure 5.33: Graph showing the temperature distribution down the depth of the vessel at $x=0.0031\text{m}$, $x=0.0063\text{m}$ and $x=0.0125\text{m}$ at non-dimensionalised time, $t=0.5$.

found from Figure 5.30, we find that the critical Rayleigh number for this region is

$$\begin{aligned} Ra_c &= \frac{g\beta_T(T_{\text{bulk}} - T_{\text{sat}})d_{\text{crit}}^3}{\kappa_l\nu} \\ &= 3.28. \end{aligned}$$

Atkinson-Barr(1989) found the critical Rayleigh number calculated from experimental data to be 33 for LIN and 25 for LOX. However, this data is for pure liquids and our studies are with mixtures. The only critical Rayleigh numbers for mixtures that we have are those for LNG and liquid methane, LCH₄, which are found in the same work to be 4 and 5 respectively. These values are much lower than those with pure liquids and agree well with our numerical results. Thus we can finally substantiate the working assumption described in Chapter 4.

5.7 Rollover with Preferential Evaporation

We are now able to include preferential evaporation in the model of evaporation. It would be useful if we could compare our results to the work of, say, Agbabi(1987). However his experiments are performed in cylindrical dewars and our model is only valid for a square vessel. Therefore in order to make a reasonable comparison we will need to ensure that the rate of increase of the bulk temperature is the same for both vessels. We will begin by examining a simplified model of the effect of the heat flux on the fluid in the cylindrical dewar. Now the heat flux which enters the vessel either acts to heat the bulk of the fluid or to evaporate the fluid at the surface so

$$q_c A_{Sc} = \rho c V \frac{\partial T_{\text{bulk}}}{\partial t} + k A_{Tc} \left. \frac{\partial T}{\partial z} \right|_{x=\text{surface}}$$

where q_c is the heat flux (Wm⁻²) entering the dewar, A_{Sc} is the area (m²) of the side walls in contact with the heater, A_{Tc} is the surface area (m²) at the top of the fluid, T is the temperature (K) of the fluid, T_{bulk} is the average temperature (K) of the bulk fluid, ρ is the density (kgm⁻³), c is the specific heat capacity (Jkg⁻¹K⁻¹) and k is the thermal conductivity (Wm⁻¹K⁻¹) of the fluid. Therefore

$$q_c A_{Sc} = \rho c A_{Tc} h \frac{\partial T_b}{\partial t} + \frac{k A_{Tc}}{\delta} (T_{\text{bulk}} - T_{\text{sat}})$$

where h is half the height of the vessel (assuming that the stratified layers are equal in height), δ is the depth (m) of the conduction layer and T_{sat} is the saturation temperature

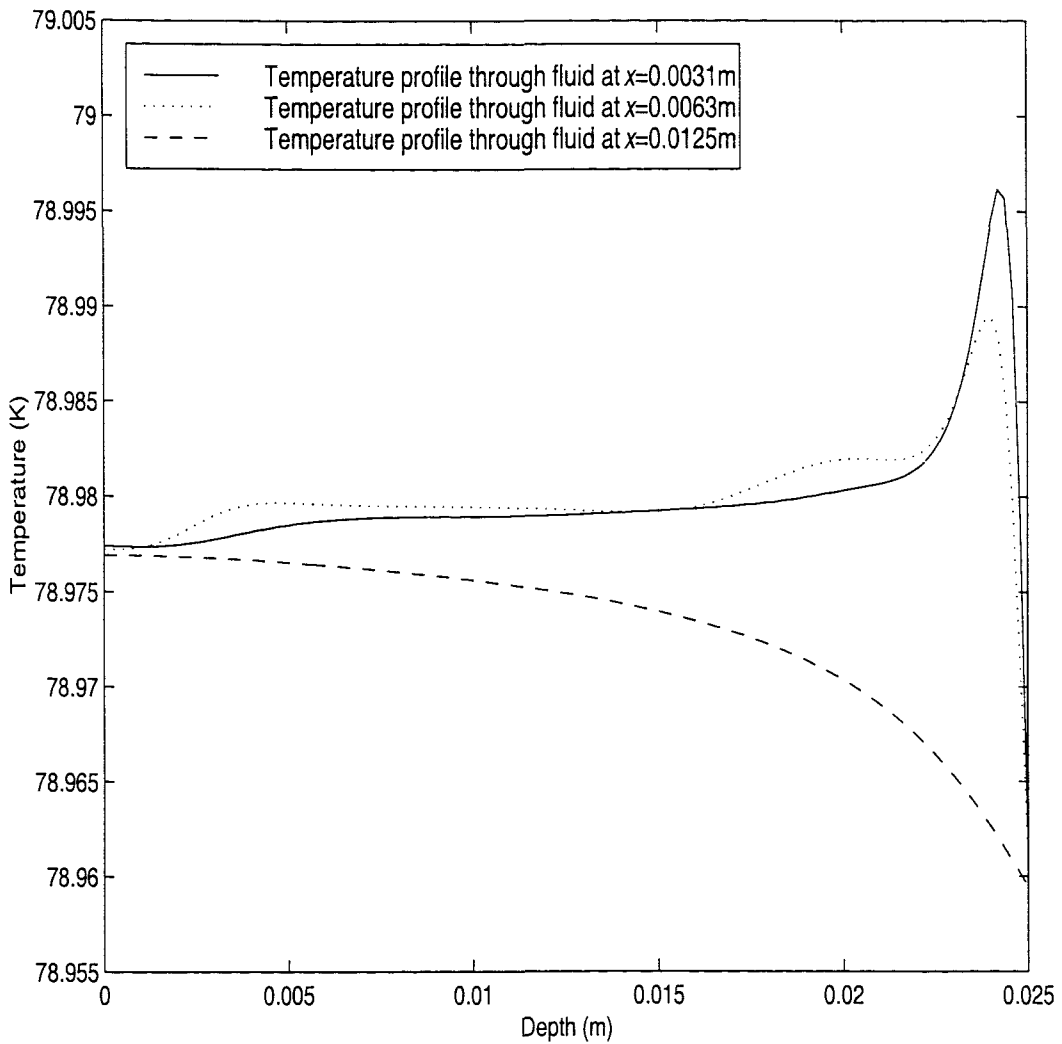


Figure 5.34: Graph showing the temperature distribution down the depth of the vessel at $x=0.0031\text{m}$, $x=0.0063\text{m}$ and $x=0.0125\text{m}$ at non-dimensionalised time, $t=1.7$.

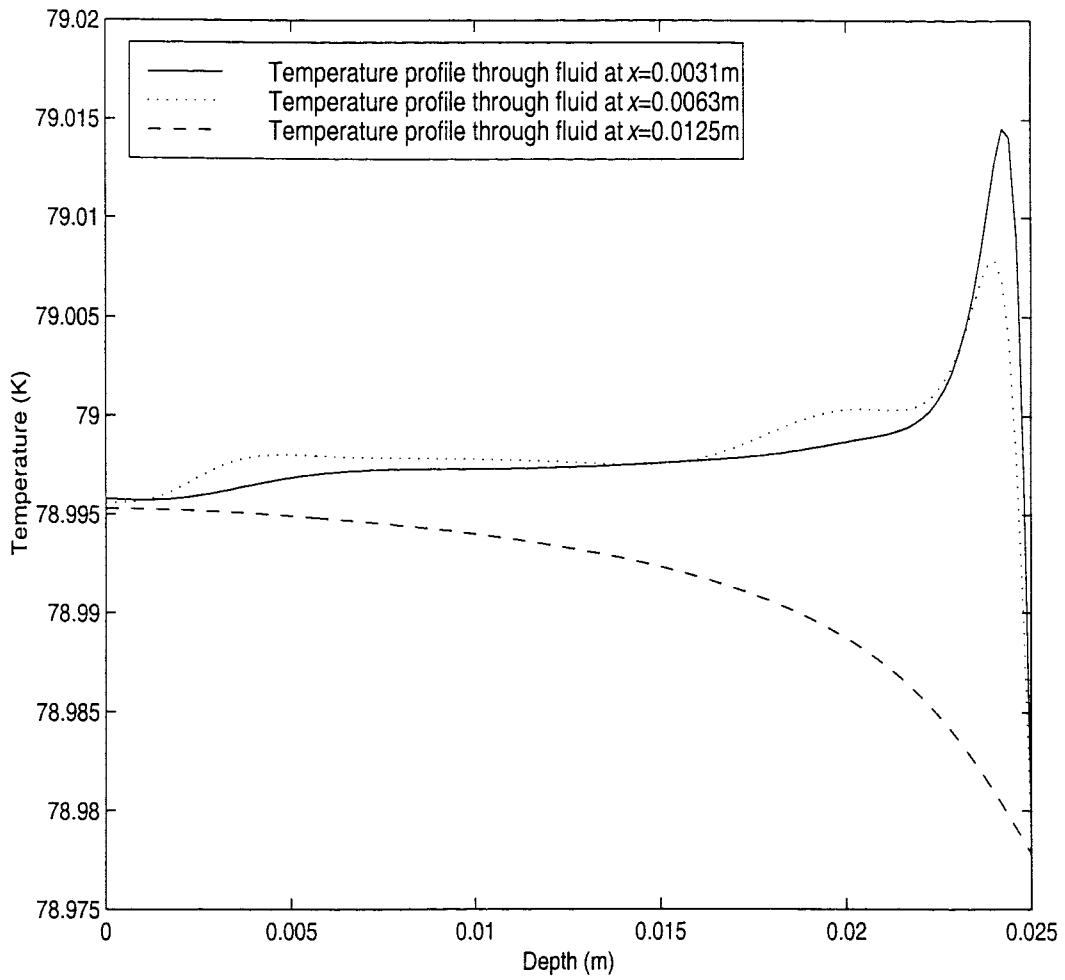


Figure 5.35: Graph showing the temperature distribution down the depth of the vessel at $x=0.0031\text{m}$, $x=0.0063\text{m}$ and $x=0.0125\text{m}$ at non-dimensionalised time, $t=2.3$.

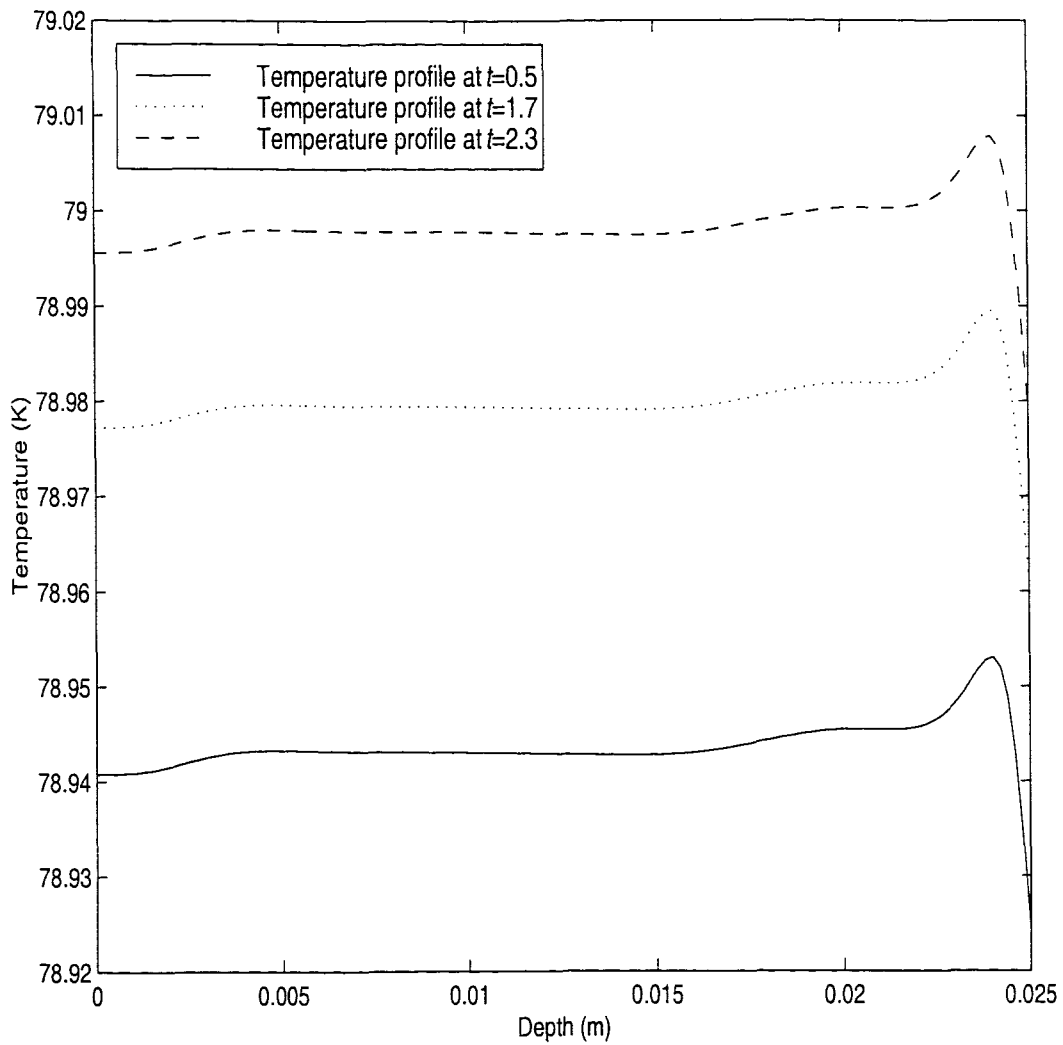


Figure 5.36: Graph showing the temperature profile through the vessel at $x=0.0063\text{m}$ for the non-dimensionalised times $t=0.5$, $t=1.7$ and $t=2.3$.

(K) at the surface of the fluid. This gives the first order differential equation

$$\frac{\partial T_{\text{bulk}}}{\partial t} + \frac{k}{\delta \rho c h} T_{\text{bulk}} = \frac{q_c A_{Sc}}{\rho c h A_{Tc}} + \frac{k}{\delta \rho c h} T_{\text{sat}}.$$

Solving this, using the initial condition that

$$T_{\text{bulk}} = T_{\text{sat}} \text{ at } t = 0,$$

gives

$$T_{\text{bulk}} = T_{\text{sat}} + \frac{q_c A_{Sc} \delta}{A_{Tc} k} \left(1 - \exp \left(-\frac{k}{\delta \rho c h} t \right) \right).$$

Therefore the temperature of the fluid in our square vessel will increase at the same rate as the fluid in the experiments, as long as h in the exponential, and the ratio of $q_c A_{Sc}/A_{Tc}$ in the multiplier, remain the same for both vessels.

Now the square vessel has two layers of equal height, h , so the surface area (m^2) at the top of this vessel must be given by

$$A_{T_s} = 4h^2$$

and the surface area (m^2) in contact with the heater around two side walls is

$$A_{S_s} = 8h^2.$$

Thus the heat flux into the square vessel must be

$$q_s = \frac{2h}{d} q_c.$$

Since $h > d$ for the cylindrical dewar used, the heat flux must be larger in our numerical work than in the experiments for it to have the same effect on the fluid. Unfortunately even the experiment with the lowest value of the heat flux, gives a Rayleigh number of $O(10^{11})$ which is too high for laminar convection to be maintained. Also, as mentioned before, the same h must be used in our code as in the experimental work. The resolution of the grid must be high, in order to observe the conduction layer at the surface. We do not have the computational power to solve this problem within a reasonable time but believe it would be possible to do so using parallel computers if the code were developed further to include turbulence.

5.8 Conclusions from Numerical Modelling an Evaporative Mixture

In this chapter, we started by solving the equations of a one-component model in Cartesian coordinates to model the convection patterns in a vessel with one side wall maintained at a temperature below that of the other. The results were found to agree well with De Vahl Davis(1968,1983), showing the distortion of the temperature distribution by the convection driven flows, giving a fairly constant temperature in the bulk of the fluid and sharp temperature gradients near the two side walls.

We then expanded the model to deal with heterogeneous flows by including a solute into the problem. The numerical code was validated with the work of Béghein *et al.*(1992) in which steady-state thermosolutal convection in a square cavity filled with air and subjected to horizontal temperature and concentration gradients, is studied. The results agreed and showed that if the solutal Rayleigh number is less than the thermal Rayleigh number, convection is thermally dominated.

We then adapted the code to follow the work of Shi(1990), which numerically models rollover with a LIN/LOX mixture. The results agreed up until the non-dimensionalised time $t = 0.1$ (over half the total time) when the flow in our model became non-symmetric. This was not observed in Shi's predictions due to the assumption of symmetry, however, the excellent agreement up to this stage satisfied our validation exercise.

Finally in this chapter, we proposed a term in the main equation for concentration to model preferential evaporation. This term used the relationship for liquid and vapour concentrations at equilibrium from published experimental data to obtain the concentration of the liquid removed given the concentration at the fluid surface. With this, we were able to study the effect of evaporation on the fluid. The total mass flux was found to reach an equilibrium over time.

Further to Chapter 4, we also found the thickness of the conduction layer, which compares well to experimental work by Beduz and Scurlock(1994). Moreover the critical Rayleigh number found using this thickness agreed well with the experimental calculated critical Rayleigh number (Atkinson-Barr, 1989) for various mixtures. Thus, the working assumption used by experimentalists could finally be substantiated.

Although our work has only been developed for a small vessel, in order to have a

heat flux of a reasonable magnitude and still maintain laminar convection, this is the first work that examines such types of evaporation on mixtures.

Chapter 6

Discussion

In this thesis we have constructed and solved (both analytically and computationally) new models for the phenomena which occur in superheated cryogenic fluids. In Chapter 2, we proposed and solved a simple model, dependent only on time, for two stratified layers in a dewar, in order to understand rollover. The model examined the increase in temperature of both layers due to heat leak in through the sides of the dewar and a small effect of heat loss/gain through conduction between the layers. This was further developed in Section 2.2 by the addition of a term for the heat loss at the surface through evaporation. The final model provides us with a good understanding of temperature up to the point at which rollover occurs, where the model no longer applies, suggesting that other effects begin to influence the system.

In the storage of cryogenic fluids, heat leak from the surroundings is impossible to avoid, since the saturation temperatures of the fluids are generally over 200K below room temperature. When the storage containers are clean, with few nucleation sites, the heat leak may cause the fluids to become superheated. Experiments (e.g. Atkinson-Barr, 1989) show that there is a high temperature gradient over a small depth at the surface of these superheated fluids, with the surface evaporating at the saturation temperature. The vertical velocity over this depth is close to zero since the vertical velocity at the surface is zero. This in turn suggests that the only important type of heat transfer is conduction.

In Chapter 3 we modelled this thin 'conduction layer' using the Stefan condition at the surface to describe the loss of fluid through evaporation. A travelling wave was found as a solution and we obtained a temperature dependent evaporation rate which,

using knowledge of the thickness of the conduction layer (found experimentally to be between 100-500 μm), compared well to the experimental correlation for LNG (Rebiai, 1985). The main drawback of this model is that the evaporation rate is dependent on the thickness of the conduction region in the fluid which we only know approximately through experiments and which may vary from fluid to fluid.

We also proposed a model to describe the flow in a LIN/LOX mixture using the volume fractions of each liquid, in Chapter 3. The Stefan condition was placed at the surface but our model assumed that only LIN evaporated. Although a larger proportion of LIN does evaporate, the distribution of the kinetic energy of individual molecules, given in Section 4.2, suggests that there will always be some LOX evaporating. Since we were not able to derive a boundary condition which correctly modelled this evaporation, we decided not to pursue the model at this stage. However, it would be useful, as further work, to compare numerical solutions obtained from this model, to those obtained in Chapter 5.

We obtained a numerical prediction for the thickness of the conduction layer in Chapter 4. This model was constructed using the assumption made in previous experimental studies that the thickness of the conduction layer is restricted by a Bénard-type instability criterion, characterised by a critical Rayleigh number. Equations were formed which modelled convective instability in the surface layer with Couette flow at the bottom boundary to describe the convection of a cell below on the conduction region. The finite difference equations were formed using an automated procedure and we validated our results against other cases in the literature.

We then went on to investigate the effect of previously unstudied boundary conditions on the top and bottom surface of the fluid. Numerical results obtained with the model suggested that the minimum thickness of the layer would be three times as large as that observed in experiments. So, although the conjecture that the conduction layer must be less than that evaluated from the critical Rayleigh number may be true, our model did not predict the thickness of the layer to be the same as that observed experimentally. Thus there must either be a different limiting mechanism which restricts the thickness of the layer or our assessment of this layer without the full inclusion of the rest of the fluid does not provide us with a complete picture of the problem. Also in this chapter, we constructed a simple model to investigate the theory that thermal fluctuations observed at the surface of cryogenic fluids, particularly mixtures, could be due to

micro-convection eddies, which replenish the fluid lost at the surface. The comparison between our estimated frequency and experimental results supported such a theory.

Finally, in Chapter 5, we proposed a model for laminar natural convection within a mixture of two cryogenic fluids, in a square vessel with preferential evaporation at the surface. To our knowledge, this is the first time that preferential evaporation has been included. We began this work by constructing a model for the laminar natural convection within a one-component fluid. The equations from this model were discretised by an upwind scheme and solved numerically, with the Poisson equation being solved using the multigrid method.

An important aspect of setting up and solving a new model is ensuring that it reproduces results from the literature in simple limiting cases. We carefully validated our code in three independent ways:

1. with benchmark results of laminar convection with a one-component fluid;
2. against published results from a model of double-diffusive convection within a two-component liquid;
3. against the results of Shi(1990) for a two layer system, up to and including rollover.

Finally we derived a new term for the preferential evaporation of the mixture which was added as a source term to the equation describing the concentration at the surface.

The equations used in the model were solved numerically to obtain the first plots of the evolution of this type of evaporation. It was found that convection became stronger when preferential evaporation was included in the model, with both a concentrated surface layer and a concentrated central plume carrying the denser fluid to the bottom of the vessel. It was also noted that the concentration of both the bulk of the fluid and the surface increased with time with a uniform difference between the two. Further, by examining the temperature profiles near the surface, we were able to estimate a thickness for the conduction layer which agreed well with experimental data (Scurlock and Beduz, 1994). We were not able to observe the micro-convection eddies described in Section 4.2 but this was presumably because we had a very low temperature difference to keep the flow laminar.

The results are extremely encouraging, allowing convection to be investigated and

the effect of preferential evaporation on the bulk of the fluid to be studied. Our method of including preferential evaporation is stable and robust.

At present we require further experimental results to examine the distribution of concentration in mixtures of cryogenic fluids under the conditions modelled, to determine the accuracy of our model. It would also be interesting to compare the flow in vessels with different aspect ratios, which could be done by allowing the height and width of the vessel to vary independently in the computation.

Much of the previous experimental work has focused on the process of rollover involving Rayleigh numbers greater than 10^{11} , which is in the range of turbulent flow. An important development to this work would be to include turbulence in the model. This would allow simulations to be carried out with higher heat fluxes and in vessels with larger dimensions. It is expected that such work would be considerably more computationally intensive requiring more computing power and memory, suggesting the use of parallel computing.

The preferential evaporation condition could be developed further to model a closed container where the pressure is allowed to vary. By including the variations of saturation temperature with pressure into the model, predictions could be obtained for closed containers with differing vapour spaces.

References

- Acheson D.J. (1992) *Elementary Fluid Dynamics*, Clarendon Press, Oxford, U.K.
- Agbabi T. (1987) Ph.D. Thesis, University of Southampton, U.K.
- Agbabi T., Beduz C., Scurlock R.G. and Shi J.Q. (1990) Evaporation Stability of Cryogenic Liquids under Storage, *L.T.E.C.*, Southampton, U.K.
- Atkinson-Barr M.C.M. (1989) Ph.D. Thesis, University of Southampton, U.K.
- Atkinson M.C.M., Beduz C., Rebiai R. and Scurlock R.G. (1984) Heat and Evaporative Mass Transfer Correlation at the Liquid-Vapour Interface of Cryogenic Liquids, *Int. Cryog. Eng. Conf.*, Helsinki, Finland.
- Barron R.F. (1985) *Cryogenic Systems*. Second edition, Oxford University Press.
- Bates S. and Morrison D.S. (1997) Modelling the Behaviour of Stratified Liquid Natural Gas in Storage Tanks: a Study of the Rollover Phenomenon, *Int. J. Heat Mass Transfer*, **40** 1875-1884.
- Beduz C., Rebiai R. and Scurlock R.G. (1984) Thermal Overfill, and the Surface Vaporisation of Cryogenic Liquids under Storage Conditions, *Adv. Cryog. Eng.*, **29** 795-803.
- Beduz C. and Scurlock R.G. (1994) Evaporation Mechanisms and Instabilities in Cryogenic Liquids, *Adv. Cryog. Eng.*, **39** 1749-1757.
- Beduz C. and Scurlock R.G. (1995) priv. comm.
- Beduz C. and Scurlock R.G. (1996) Stratification Of Cryogenic Liquid Mixtures, Report Cau 96/102, Institute of Cryogenics, University of Southampton, U.K.
- Béghein C., Haghghat F. and Allard F. (1992) Numerical Study of Double-Diffusive Natural Convection in a Square Cavity, *Int. J. Heat Mass Transfer*, **35** 833-846
- Bejan A. (1985) Mass and Heat Transfer by Natural Convection in a Vertical Cavity, *Internat. J. Heat Fluid Flow*, **6** 149-159.

- Bénard H. (1900) Les Tourbillons Cellulaires dans une Nappe Liquide, *Revue Gen. Sci. Pur. Appl.*, **11** 1261-1271.
- Berg J.C., Acrivos A., and Boudart M. (1966) Evaporative Convection, *Adv. Chem. Eng.*, **6** 61-123.
- Biggs W.L. (1988) A Multigrid Tutorial, SIAM, Philadelphia, PA
- Bose A. and Palmer H.J. (1983) Interfacial Stability of Binary Mixtures Evaporating at Reduced Pressure, *J. Fluid Mech.*, **126** 491-506.
- Brandt A. (1977) Multi-Level Adaptive Solutions to Boundary-Value Problems, *Math. Comp.*, **31** 333-390.
- Chadam J. and Ortoleva P. (1983) The Stabilizing Effects of Surface Tension on the Development of the Free Boundary in a Planar, One-dimensional, Cauchy-Stefan Problem, *IMA J. Appl. Math.*, **30** 57-66.
- Chatterjee N. and Geist J.M. (1972), The Effects of Stratification on Boil-Off Rates in LNG tanks, *P. & G. Jour.*, **199** 40- 45.
- Chatterjee N. and Geist J.M. (1976), Spontaneous Stratification in LNG Tanks containing Nitrogen, Paper 76-WA/PID-6, ASME Winter Annual Meeting, New York
- Chow C. (1983) An Introduction to Computational Fluid Mechanics, Seminole Publishing Company, Boulder, Colorado, U.S.A.
- Clever R.M. and Busse F.H. (1992) Three-Dimensional Convection in a Horizontal Fluid Layer subjected to a Constant Shear, *J. Fluid Mech.*, **234** 551-527.
- Deardorff J.W. (1965), Gravitational Instability between Horizontal Plates with Shear, *Phys. Fluids*, **8** 1027-1030.
- De Vahl Davis G. (1968) Laminar Natural Convection in an Enclosed Rectangular Cavity, *Int. J. Heat Mass Transfer*, **11** 1675-1693.
- De Vahl Davis G. (1983) Natural Convection of Air in a Square Cavity: a Benchmark Numerical Solution, *Int. J. Numer. Methods Fluids*, **3** 249-264.
- Dewynne J.N., Howison S.D., Ockendon J.R. and Xie W. (1989) Asymptotic Behaviour of Solutions to the Stefan Problem with a Kinetic Condition at the Free Boundary, *J.*

Austral. Math. Soc. Ser. B, **31** 81-96.

Drake E.M. (1976) LNG rollover-update, *Hydrocarbon Process.*, **55** 119-122.

Drazin P.G. and Reid W.H. (1981) *Hydrodynamic Instability*, Cambridge University Press, U.K.

Elder J.W. (1968) The Unstable Thermal Interface, *J. Fluid Mech.*, **32** 69-96.

Foster T.D. (1971) Intermittent Convection, *Geophys. Fluid Dyn.*, **2** 201-217.

Gallagher A.P. and Mercer A.McD. (1962) On the Behaviour of Small Disturbances in Plane Couette Flow, *J. Fluid Mech.*, **13** 91-100.

Gallagher A.P. and Mercer A.McD. (1964) On the Behaviour of Small Disturbances in Plane Couette Flow Part 2. The Higher Eigenvalues, *J. Fluid Mech.*, **18** 350-352.

Gallagher A.P. and Mercer A.McD. (1965) On the Behaviour of Small Disturbances in Plane Couette Flow with a Temperature Gradient, *Proc. Roy. Soc. London Series A*, **286** 117-128.

Gebhart B. and Pera L. (1971) The Nature of Vertical Natural Convection Flows resulting from the Combined Buoyancy Effects of Thermal and Mass Diffusion, *Int. J. Heat Mass Transfer*, **14** 2025-2050.

Germeles A.E. (1975) A Model for LNG Tank Rollover, *Adv. Cryog. Eng.*, **21** 326-336.

Hackbusch W. (1985) *Multi-Grid Methods and Applications*, Springer-Verlag, New York.

Hashemi H.T. and Wesson H.R. (1971), Cut LNG Storage Costs, *Hydrocarbon Process.*, **50** 117-120.

Heestand J., Shipman C.W. and Meader J.W. (1983), A Predictive Model for Rollover in Stratified LNG Tanks, *AIChE*, **29** 199-207.

Howard L.N. (1966), Convection at High Rayleigh Number, *Proceedings of the Eleventh International Congress of Applied Mechanics*, Munich, Germany.

Huppert H.E. and Turner J.S. (1981), Double-Diffusive Convection, *J. Fluid Mech.*, **106** 299-329.

- Iserles A. (1996) A First Course in the Numerical Analysis of Differential Equations, Cambridge University Press, Cambridge, U.K.
- Kamakura K. and Ozoe H. (1993), Experimental and Numerical Analyses of Double Diffusive Natural Convection Heated and Cooled from Opposing Vertical Walls with an Initially Condition of a Vertically Linear Concentration Gradient, *J. Fluid Mech.*, **106** 299-329.
- Keary A., Beduz C. and Richardson R.N. (1998) Synthetic Liquid Air Research, Report ME/98/02, Institute of Cryogenics, Department of Mechanical Engineering, University of Southampton, U.K.
- Lin T.F., Huang C.C. and Chang, T.S. (1990) Transient Binary Mixture Natural Convection in Square Enclosures, *Int. J. Heat Mass Transfer*, **33** 287-299.
- MacKenzie D. (1986) Chemical Disasters Need not Happen, *New Sci.*, **110** 42-45.
- Maher J.B. and Van Gelder L.R. (1972) Roll-Over and Thermal Overfill in Flat Bottom LNG Tanks, *P. & G. Jour.* **199** 46-48.
- Markatos N.C. and Pericleous K.A. (1984) Laminar and Turbulent Natural Convection in an Enclosed Cavity, *Int. J. Heat Mass Transfer*, **27** 755-772.
- Milne-Thomson L.M. (1968) Theoretical Hydrodynamics. Fifth edition, Macmillan, London, U.K.
- Morrison D.S. and Richardson A. (1990) An Experimental Study on the Stability of Stratified Layers and Rollover in LNG Storage Tanks, *LTEC*, Southampton, U.K.
- Morton K.W. and Mayers D.F. (1994) Numerical Solution of Partial Differential Equations, Cambridge University Press, Cambridge, U.K.
- Nakano R., Sugawara Y., Yamagata S. and Nakamura J. (1982) An Experimental Study on the Mixing of Stratified Layers using Liquefied Freon, *Gastech Sess* **6**.
- Nishimura T., Wakamatsu M. and Morega A.M. (1998) Oscillatory Double-Diffusive Convection in a Rectangular Enclosure with Combined Horizontal Temperature and Concentration Gradients, *Int. J. Heat Mass Transfer* **41** 1601-1611.
- Press W.H., Teukolsky S.A., Vetterling W.T. and Flannery B.P. (1992) Numerical

Recipes in Fortran - the Art of Scientific Computing. Second edition, Cambridge University Press, Cambridge, U.K.

Rayleigh (1916) On Convection Currents in a Horizontal Layer of Fluid, when the Higher Temperature is on the Under Side, *Phil. Mag* **32** 529-546.

Rebiai R. (1985) Ph.D. Thesis, University of Southampton, U.K.

Renardy Y.Y. and Schmitt R.W. (1996) Linear Stability Analysis of Salt Fingers with Surface Evaporation or Warming, *Phys. Fluids* **8** 2855-2867.

Roache P.J. (1976) Computational Fluid Dynamics, Hermosa Publishers, Albuquerque, New Mexico.

Rubinstein L.(1982) Global Stability of the Neumann Solution of the Two-Phase Stefan Problem, *IMA J. Appl. Math.* **28** 287-299.

Sarsten J.A. (1972) LNG Stratification and Rollover, *P. & G. Jour.* **199** 37-39.

Sévédér V. and Petit J.P. (1989) Flow Structures Induced by Opposing Heat and Mass Transfer in a Cavity, *Numer. Heat Transfer* **15** 431-444.

Shi J.Q.(1990) Ph.D. Thesis, University of Southampton, U.K.

Smith G.D. (1965) Numerical Solution of Partial Differential Equations: Finite Difference Methods, Oxford University Press, Oxford, U.K.

Stoer J. and Bulirsch R. (1993) Introduction to Numerical Analysis. Second edition, Springer-Verlag, New York.

Strain J. (1988) Linear Stability Of Planar Solidification Fronts, *Phys. D*, **30** 297-320.

Sugawara Y., Kubota A. and Muraki S. (1983) Rollover Test in LNG Storage Tank and Simulation Model, *Adv. Cryog. Eng.*, **29** 805-811.

Taylor A.B. (1986) Mathematical Models in Applied Mechanics, Clarendon Press, Oxford, U.K.

Turner J.S. (1965) The Coupled Turbulent Transports of Salt and Heat Across a Sharp Density Interface, *Int. J. Heat Mass Transfer*, **8** 759-767.

Turner J.S. (1973) Buoyancy Effects in Fluids, Cambridge University Press, Cambridge,

U.K.

Wesseling P. (1992) An Introduction to Multigrid Methods, Wiley, New York.

Yahata H. (1994) Convection Rolls with a Small Rate of Shear slightly above the Onset Point, *Fluid Dyn. Res.*, **14** 135-148.

Younglove B.A. (1982) Thermophysical Properties of Fluids.1.Argon, ethylene, parahydrogen, nitrogen, nitrogen trifluoride, and oxygen, *J. Phys. Chem. Ref. Data Suppl.*, Volume II, Supplement No.1.

Zwillinger D. (1997) Handbook of Differential Equations. Third edition, Academic Press, New York.